



# MONASH University

## **Designed Polymer-Based Nanoparticles for Drug Delivery and Imaging**

***Lars Esser***

*Master of Science in Biomedical Engineering  
Eindhoven University of Technology*

A thesis submitted for the degree of **Doctor of Philosophy** at  
Monash University in 2016

Drug Delivery, Disposition and Dynamics  
Monash Institute of Pharmaceutical Sciences  
Monash University (Parkville Campus)  
381 Royal Parade, Parkville  
Victoria 3052, Australia



## Copyright notice

© Lars Esser (2016). Except as provided in the Copyright Act 1968, this thesis may not be reproduced in any form without the written permission of the author.

I certify that I have made all reasonable efforts to secure copyright permissions for third-party content included in this thesis and have not knowingly added copyright content to my work without the owner's permission.

## Table of contents

ABSTRACT	5
DECLARATION	6
PUBLICATIONS	7
COMMUNICATIONS	9
ACKNOWLEDGEMENTS	11
LIST OF ABBREVIATIONS	14
CHAPTER 1: AN INTRODUCTION INTO POLYMER-BASED NANOPARTICLES FOR DRUG DELIVERY AND IMAGING	17
<b>1.1 Nanoparticles for drug delivery</b>	<b>18</b>
1.1.2 Nanoparticle drug delivery systems	23
1.1.3 Bio-nano interactions of nanoparticles	23
1.1.4 Polymer-based nanoparticles	26
1.1.5 Controlled/living radical polymerization techniques	26
1.1.6 Synthesis of polymer-based nanoparticles	31
<b>1.2 Nanoparticles for diagnostics</b>	<b>39</b>
1.2.1 Magnetic resonance imaging	42
1.2.2 X-ray computed tomography	49
1.2.3 Nuclear medicine: SPECT	52
1.2.4 Nuclear medicine: PET	54
1.2.5 Medical ultrasound	57
1.2.6 Fluorescence Imaging	59
1.2.7 Multimodal imaging	60
<b>1.3 Nanoparticles for theranostics</b>	<b>63</b>
1.3.1 Theranostics	63
1.3.2 Theranostic nanoparticles	63
<b>1.4 Aims</b>	<b>66</b>
CHAPTER 2: POLYMERIZATION-INDUCED SELF-ASSEMBLY - CONTROL OVER MORPHOLOGY FOR DRUG DELIVERY	78
<b>2.1 Introduction</b>	<b>79</b>
<b>2.2 Experimental Section</b>	<b>81</b>
2.2.1 Materials	81
2.2.2 Physical and analytical methods	81
2.2.3 Syntheses	84
<b>2.3 Results and discussion</b>	<b>87</b>

<b>2.4 Conclusion</b>	<b>98</b>
<b>2.5 References</b>	<b>99</b>
 <b>CHAPTER 3: POLYMERIZATION-INDUCED SELF-ASSEMBLY - CONTROL OVER SURFACE AND MORPHOLOGY FOR T<sub>1</sub>-WEIGHTED MR IMAGING</b>	 <b>102</b>
<b>3.1 Introduction</b>	<b>103</b>
<b>3.2 Experimental Section</b>	<b>105</b>
3.2.1 Materials	105
3.2.2 Physical and analytical methods	105
3.2.3 Syntheses	109
<b>3.3 Results and discussion</b>	<b>113</b>
3.3.1 Preparation of PGMA surface-functional block	113
3.3.2 Preparation of chain extended hydrophilic macro-CTA	114
3.3.3 Preparation of surface-functional block copolymer with various morphologies	115
3.3.4 <i>Investigating versatility of surface functionality</i>	118
3.3.5 Preparation of T <sub>1</sub> -weighted MR contrast agents with different morphologies	124
<b>3.4 Conclusion</b>	<b>130</b>
<b>3.5 References</b>	<b>131</b>
 <b>CHAPTER 4: DESIGNED NANOPARTICLES FOR DUAL-MODALITY IMAGING AND DRUG/RADIOPHARMACEUTICAL DELIVERY: COMBINING SPECT/PET AND MRI</b>	 <b>133</b>
<b>4.1 Introduction</b>	<b>134</b>
<b>4.2 Experimental Section</b>	<b>138</b>
4.2.1 Materials	138
4.2.2 Physical and analytical methods	138
4.2.3 Syntheses	141
<b>4.3 Results and discussion</b>	<b>147</b>
4.3.1 Preparation of P(VBC-co-OEGA) arm polymer	147
4.3.2 Preparation of core-cross-linked star polymer	148
4.3.3 Preparation of azide-functional polymers	149
4.3.4 Investigation of three-component reaction for iodine labelling	151
4.3.5 Radiochemistry - Investigation of three-component reaction for radio-iodine labelling	155
4.3.6 Preparation of gadolinium-DOTA / (radio)iodine labelled polymers	160
<b>4.4 Conclusion</b>	<b>165</b>
<b>4.5 References</b>	<b>166</b>
 <b>CHAPTER 5: CONCLUSIONS AND FUTURE WORKS</b>	 <b>168</b>
<b>5.1 Conclusions</b>	<b>169</b>
<b>5.2 Future Works</b>	<b>170</b>
<b>5.3 References</b>	<b>174</b>

## Abstract

Nanomedicine has emerged as a novel field in medicine integrating nanoscale technologies with materials sciences, chemistry and biology. Nano-sized particles are able to deliver otherwise insoluble drugs and simultaneously improve the kinetics of drug delivery. Furthermore, they have been able to enhance diagnostic capacities by improved disease detection.

Polymer chemistry has proven to be a very versatile technique for nanomedicine, as it allows the synthesis of nanoparticles with a wide range of architectures, sizes and surface chemistry. Most commonly, spherical nanoparticles have been employed. However, recent studies showed that the shape of nanoparticles also affects the bio-nano interactions.

The overall objective of this dissertation was to develop novel methods to synthesize polymer-based nanoparticles with enhanced properties for both drug delivery and diagnostics with an emphasis on shape. Furthermore, a dual-modality PET/MRI agent was developed to exploit the benefits of multimodal PET/MRI imaging and to enable high-resolution, high-sensitivity investigation of biological activity.

Firstly, in **chapter 1**, the current state of research in nanoparticles for drug delivery and imaging is discussed with a special focus on polymer-based nanoparticles and the importance of design.

In **chapter 2**, polymerisation-induced self-assembly was exploited to create a library of polymer-based nanoparticles with different sizes and shapes, and their efficacy as drug delivery vehicle was assessed to determine the optimal morphology. The results indicated that flexible worm-like nanoparticles have a higher tumour cell uptake and drug toxicity than spherical nanoparticles.

In **chapter 3**, a method was developed to synthesize novel epoxide surface-functional nanoparticles by polymerization-induced self-assembly, and the versatility of the functional group was investigated. In the second part of the chapter, the use of the different shaped nanoparticles as positive MRI contrast was investigated by successfully conjugating a gadolinium chelate onto the self-assembled nanoparticles. The worm-like nanoparticles showed a high MR contrast enhancement and have a great potential as imaging agent.

Finally, in **chapter 4**, a novel bimodal MRI/PET imaging probe was designed containing both gadolinium (for MRI) and radioiodine (for PET) by combining novel multicomponent chemistry with a core-cross-linked functional star polymer to optimally exploit the synergy between MRI and PET.

## Declaration

This thesis contains no material which has been accepted for the award of any other degree or diploma at any university or equivalent institution and that, to the best of my knowledge and belief, this thesis contains no material previously published or written by another person, except where due reference is made in the text of the thesis.

This thesis includes one original paper published in a peer reviewed journal and two unpublished manuscripts. The core theme of the thesis is the design of polymer-based nanoparticles with enhanced properties for drug delivery and diagnostics. The ideas, development and writing up of all the papers in the thesis were the principle responsibility of myself, the candidate, working within the theme of Drug Delivery, Disposition and Dynamics, under the supervision of Professor Thomas Davis and Dr. Michael Whittaker.

Signature:

A handwritten signature in black ink, appearing to read 'Lars Esser', with a stylized, cursive script.

Print Name: **Lars Esser**

Date: **25/08/2016**

## Publications

1. Basuki, J. S.; **Esser, L.**; Zetterlund, P. B.; Whittaker, M. R.; Boyer, C.; Davis, T. P., *Grafting of P(OEGA) Onto Magnetic Nanoparticles Using Cu(0) Mediated Polymerization: Comparing Grafting “from” and “to” Approaches in the Search for the Optimal Material Design of Nanoparticle MRI Contrast Agents*. *Macromolecules* 2013, 46 (15), 6038-6047.
2. Basuki, J. S.; Duong, H. T. T.; Macmillan, A.; Erlich, R. B.; **Esser, L.**; Akerfeldt, M. C.; Whan, R. M.; Kavallaris, M.; Boyer, C.; Davis, T. P., *Using Fluorescence Lifetime Imaging Microscopy to Monitor Theranostic Nanoparticle Uptake and Intracellular Doxorubicin Release*. *ACS Nano* 2013, 7 (11), 10175-10189.
3. Basuki, J. S.; **Esser, L.**; Duong, H. T. T.; Zhang, Q.; Wilson, P.; Whittaker, M. R.; Haddleton, D. M.; Boyer, C.; Davis, T. P., *Magnetic nanoparticles with diblock glycopolymer shells give lectin concentration-dependent MRI signals and selective cell uptake*. *Chemical Science* 2014, 5 (2), 715-726.
4. Karagoz, B.; **Esser, L.**; Duong, H. T.; Basuki, J. S.; Boyer, C.; Davis, T. P., *Polymerization-Induced Self-Assembly (PISA) - control over the morphology of nanoparticles for drug delivery applications*. *Polymer Chemistry* 2014, 5 (2), 350-355.
5. Li, Y.; Laurent, S.; **Esser, L.**; Elst, L. V.; Muller, R. N.; Lowe, A. B.; Boyer, C.; Davis, T. P., *The precise molecular location of gadolinium atoms has a significant influence on the efficacy of nanoparticulate MRI positive contrast agents*. *Polymer Chemistry* 2014, 5 (7), 2592-2601.
6. Basuki, J. S.; Jacquemin, A.; **Esser, L.**; Li, Y.; Boyer, C.; Davis, T. P., *A block copolymer-stabilized co-precipitation approach to magnetic iron oxide nanoparticles for potential use as MRI contrast agents*. *Polymer Chemistry* 2014, 5 (7), 2611-2620.
7. Karagoz, B.; Yeow, J.; **Esser, L.**; Prakash, S.M.; Kuchel, R.P.; Davis, T.P.; Boyer, C., *An efficient and highly versatile synthetic route to prepare iron oxide nanoparticles/nanocomposites with tunable morphologies*. *Langmuir* 2014, 30 (34), 10493-10502.

8. **Esser, L.**; Truong, N.P.; Karagoz, B.; Moffat, B.A.; Boyer, C.; Quinn, J.F.; Whittaker, M.R.; Davis, T.P., *Gadolinium-functionalized nanoparticles for application as magnetic resonance imaging contrast agents via polymerization-induced self-assembly*. *Polymer Chemistry*, 2016, 7, 7325 – 7337.

## Communications

1. Esser, L.; Basuki, J.S.; Li, Y.; Duong, H.; Whittaker, M.R.; Boyer, C.; Davis, T.P., *Polymeric MRI contrast agents*, oral presentation, 9.4T MRI Opening Symposium, Sydney, March 2013.
2. Esser, L.; Karagoz, B.; Duong, H. T.; Basuki, J. S.; Boyer, C.; Davis, T. P., *Polymerization-Induced Self-Assembly in One-Pot Fashion: Various Shapes, Cross-Linking, and Drug Loading*, poster presentation, 4<sup>th</sup> International NanoMedicine Conference, Sydney, July 2013.
3. Esser, L.; Karagoz, B.; Duong, H. T.; Basuki, J. S.; Boyer, C.; Davis, T. P., *Polymerization-Induced Self-Assembly - Control over the Morphology of Nanoparticles for Drug Delivery Applications*, 9<sup>th</sup> Annual Postgraduate Symposium, poster presentation, Monash Institute of Pharmaceutical Sciences, Parkville, November 2014.
4. Esser, L.; Karagoz, B.; Duong, H. T.; Basuki, J. S.; Boyer, C.; Davis, T. P., *Polymerization-Induced Self-Assembly - Control over the Morphology of Nanoparticles for Drug Delivery Applications*, poster presentation, Nanotechnology & Medicines for Tomorrow Symposium, Parkville, November 2014.
5. Esser, L.; Quinn, J.F.; Whittaker, M.R.; Davis, T.P., *Tuning Nanoparticle Shape, Size, and Surface by Polymerisation Induced Self-Assembly for Biomedical Applications*, poster presentation, PolymerVic 2015, Parkville, July 2015.
6. Esser, L.; Quinn, J.F.; Whittaker, M.R.; Davis, T.P., *Polymeric Nanoparticles for Drug Delivery and Imaging*, oral presentation, Bionano@Monash Workshop, Clayton, June 2015.
7. Esser, L.; Karagoz, B.; Quinn, J.F.; Whittaker, M.R.; Boyer, C.; Davis, T.P., *Polymeric Nanoparticles for Drug Delivery and Imaging*, oral presentation, 35th Australasian Polymer Symposium, Gold Coast, July 2015.
8. Esser, L.; Quinn, J.F.; Whittaker, M.R.; Davis, T.P., *Polymeric Nanoparticles for Dual-Modality Imaging and Radiopharmaceutical Delivery*, oral presentation, AINSE Roadshow Melbourne University, Parkville, August 2015.
9. Esser, L.; Quinn, J.F.; Whittaker, M.R.; Davis, T.P., *Polymeric Nanoparticles for Dual-Modality Imaging and Radiopharmaceutical Delivery*, oral presentation, AINSE Roadshow Monash, Clayton, August 2015.

10. Esser, L.; Truong, T.P.; Quinn, J.F.; Whittaker, M.R.; Davis, T.P., *Tuning Nanoparticle Size, Shape and Surface by Polymerization-Induced Self-Assembly for Biomedical Applications*, oral presentation, Monash Parkville 10th Annual Postgraduate Symposium, Parkville, October 2015.
11. Esser, L.; Quinn, J.F.; Whittaker, M.R.; Davis, T.P., *Polymeric Imaging Agents*, *Centre for Bio-Nano Science Annual Workshop*, oral presentation, Lorne, December 2015.
12. Esser, L.; Truong, T.P.; Quinn, J.F.; Whittaker, M.R.; Davis, T.P., *Polymeric filomicelles as T1-weighted MRI contrast agent*, oral presentation, PolymerVic 2016, Parkville, July 2016.

## Acknowledgements

First, I would like to express my sincere gratitude to my main supervisor, Prof. Tom Davis, for showing his trust in me by first employing me as a research assistant at ACN and then as a PhD candidate at Monash University. I am very thankful for the many opportunities that I have been given during my PhD to evolve my research skills.

I would also like to thank my co-supervisor Michael Whittaker for all his valuable advice during my PhD and for initiating the collaboration with ANSTO via AINSE. I hope that we can be Facebook friends again now that you are not my supervisor anymore.

John, thank you for your guidance and for editing several chapters of my thesis even though you are not officially my supervisor.

As I spent the first year of my PhD at UNSW, I would like to thank Cyrille Boyer for his advice during this time and for letting me be part of his group. Johan, thank you very much for all your help. I have learnt a lot from you and we had some great results together. Unforeseen we both moved to Melbourne, and it's great that we were able to carry on our friendship. I would also like to thank Daniel for teaching me the basics of RAFT polymerization, and Hien for her valuable advice. In addition, I would like to thank Andre Bongers and Carl Power at the Biological Resources Imaging Laboratory of UNSW for teaching me how to use the 9.4 T MRI scanner and for trusting the instrument in my hands. Rabeya, thank you for carrying out ICP-AES measurements for me over the years.

Thank you to Ben for introducing me to PISA, it has become a large part of my thesis. I would also like to thank all PhD students at CAMD, including Ka Wai, Joey, Ray, Manuela, Alice, Ted, Alexandre, and everyone else.

I really enjoyed the dynamics at ACN and the seminars together with the groups of Prof. Maria Kavallaris and Prof. Justin Gooding. Finally, my 'Sydney thank you' would be incomplete without mentioning Carla, I really enjoyed our conversations over morning tea and I was always welcome to drop by your office.

When the labs were operational I moved south to Melbourne, which became my new favourite city in Australia. I was warmly welcomed by Tom, Mikey, Fran, Nghia, Kristian, Jinming, Daniel and the first cohort of students: Elly, James, Joanne, Song, Christine, Catherine, and Patrick. Some people left while others started, and it's great that most of you are still here and we still have our lunch together more than two years later. Thanks for all the fun times and support.

I would also like to thank everyone else for the great working environment, including Jeroen, Ximo, Thomas, Adrian, Qiuming, Sadik, Pu-Chun, Alex, David and May, and all PhD students who commenced later: Cheng, Emily, Mai, Marvin, Paulina and all honours and exchange students over the years. I would especially like to mention Jun and Amanda. It was great to be your supervisor, and I hope that I was able to teach you a bit about nanomedicine.

One of the best things about my PhD was being part of the Centre of Excellence in Convergent Bio-Nano Science and Technology. It has opened up many opportunities for collaborations, and it's a great to see that different research groups are now working together on many interesting projects towards a better understanding of what happens to nanoparticles in the body, and how to advance the field of nanomedicine. This would not be possible without the hard work of Katrina and Gaby. Katrina, thank you for your kindness, you really are like a mother for us students.

During my PhD I was fortunate to collaborate with several other groups next to UNSW:

I would like to thank Ivan Greguric and Nigel Lengkeek at ANSTO for their advice and for facilitating my one-month stay. I have learnt a lot about radiochemistry during this time. Nigel, thank you for all your help.

I am very grateful for the financial support from AINSE. It has helped a lot to support my research and my living.

Although the responsive MRI project did not eventuate in the way we envisioned, I would like to thank Prof. Thomas Nann, Melissa Dewi, Emilie Nehlig and Prof. Nico Voelcker for all discussions and for introducing me into the world of inorganic chemistry.

Brad, thank you for facilitating the MRI measurements, taking the time to write a matlab-file for me and for your advice. I hope we can continue our collaboration.

Here at MIPS, I would like to thank my PhD panel for their advice and promoting critical thinking: Ben Boyd, Colin Poulton, Chris Porter, and Roger Nation. Furthermore I would to thank Karen M and Karen D for their help with my enrolment; and Win, Liz and Tika for all their help with ordering chemicals.

During my PhD I have also been part of the Parkville Postgraduate Association. And I was fortunate to meet a lot of people from other parts of the faculty. It was a lot of fun to help organising the trivia night, student symposium and other events, and to be treasurer for a year.

Foremost I would like to thank my parents Lei and Marjo, and my brother Tim for their unconditional support over the years and for always being there for me. I am very fortunate to have you all in my life.

Finally, to my Emilia. Although I have only met you this year, it's like you've been part of my life for much longer. I am sincerely grateful for your kindness, your unconditional support when I was writing my thesis and for loving me. We will have an amazing future together.

Lars

## List of Abbreviations

$^1\text{H}$ NMR	Proton nuclear magnetic resonance
AGET	Activators generated by electron transfer
AIBN	Azobis(isobutyronitrile)
API-ES	Atmospheric pressure ionization electrospray
ARGET	Activators regenerated by electron transfer
ATR-FTIR	Attenuated total reflectance-Fourier transform infrared spectroscopy
ATRP	Atom transfer radical polymerization
AuNP	Gold nanoparticle
BOLD	Blood-oxygen-level dependent
BSPA	3-(Benzyl sulfanyl thiocarbonyl sulfanyl)-propanoic acid
$\text{CDCl}_3$	Deuterated chloroform
CEST	Chemical exchange saturation transfer
cRGDY	Cyclic arginine-glycine-aspartate-tyrosine
CPADB	4-Cyanopentanoic acid dithiobenzoate
CPMG	Carr-Purcell-Meiboom-Gill (MR spin echo sequence)
CT	X-ray computed tomography
CTA	Chain transfer agent
CuAAC	Copper(I)-catalysed azide-alkyne cycloaddition
$\text{D}_2\text{O}$	Deuterium oxide
DLS	Dynamic light scattering
DMAc	<i>N,N</i> -Dimethylacetamide
DMF	<i>N,N</i> -Dimethylformamide
DMSO	Dimethylsulfoxide
$\text{DMSO-d}_6$	Deuterated dimethyl sulfoxide
DNA	Deoxyribonucleic acid
DOTA	1,4,7,10-Tetraazacyclododecane-1,4,7,10-tetraacetic acid
DOX	Doxorubicin
$\text{DP}_n$	Number-average degree of polymerization
DTPA	Diethylenetriaminepentaacetic acid
eATRP	Electrochemically-mediated ATRP
EDTA	Ethylenediaminetetraacetic acid
EEO	Electroendosmosis
EMA	European Medicines Agency

EPR	Enhanced permeability and retention effect
FAm	5(6)-Fluoresceinamine
FDA	USA food and drug administration
FDG	Fludeoxyglucose
FLT	3-Deoxy-3-fluorothymidine
FMISO	Fluormisonidazole
FOV	Field of view
FRI	Fluorescence reflectance imaging
GMA	Glycidyl methacrylate
Her2	Human epidermal growth factor receptor 2
HPDO3A	10-(2-Hydroxypropyl)-1,4,7-tetraazacyclododecane-1,4,7-triacetic acid
HPLC	High Performance Liquid Chromatography
ICAR	Initiators for continuous activator regeneration
ICG	Indocyanine green
ICP-OES	Inductively coupled plasma optical emission spectroscopy
IV	Intravenously
KS	HIV-related Kaposi's sarcoma
LC-MS	Liquid chromatography-mass spectrometry
MCF-7	Michigan cancer foundation-7, breast cancer cell line
M <sub>n</sub>	Number-average molecular weight
mPEG	Methoxypoly(ethylene glycol)
MPS	Mononuclear phagocyte system; also known as reticuloendothelial system
MRA	Magnetic resonance angiography
MRI	Magnetic resonance imaging
M <sub>w</sub>	Weight-average molecular weight
MWCO	Molecular weight cut-off
NIR	Near-infrared
NMP	Nitroxide mediated polymerization
NMR	Nuclear magnetic resonance
NOTA	1,4,7-Triazacyclononane-1,4,7-triacetic acid
NP	Nanoparticle
OEGMA	Oligo(ethylene glycol) methyl ether methacrylate
$\pi$ -ATRP	Photoinduced ATRP
PEG	Polyethylene glycol

PET	Positron emission tomography
PISA	Polymerization-induced self-assembly
PMDTA	N,N,N',N'',N'''-Pentamethyl-diethylenetriamine
POEGMA	Poly(oligo(ethylene glycol) methyl ether methacrylate)
ppm	Parts per million
PRINT	Particle replication in non-wetting templates
PTFE	Polytetrafluoroethylene
RAFT	Reversible addition fragmentation chain transfer polymerization
RCY	Radiochemical yield
RNA	Ribonucleic acid
RPM	Revolutions per minute
SC	Subcutaneously
SEC	Size-exclusion chromatography
shRNA	Small hairpin RNA
siRNA	Short-interfering RNA
SPECT	Single-photon emission computed tomography
ST	Styrene
TAE	Buffer solution containing a mixture of tris base, acetic acid and EDTA
TE	Echo time
TFA	Trifluoroacetic acid
THF	Tetrahydrofuran
TR	Repetition time
Tris	Tris(hydroxymethyl)aminomethane
UV/Vis	Ultraviolet–visible
VBA	3-Vinylbenzaldehyde
VBC	4-Vinylbenzyl chloride

## Chapter 1: An introduction into Polymer-Based Nanoparticles for Drug Delivery and Imaging

## 1.1 Nanoparticles for drug delivery

It is estimated that around 40 % of all active substances identified through combinatorial screening programs are difficult to use as a pharmaceutical due to their lack of significant solubility in water. [1] Furthermore, most pharmacologically active agents are not inherently clinically active as their efficacy is linked to how they are administered, including drug pharmacokinetics, absorption, distribution, metabolism, duration of metabolic effect, excretion, and toxicity. [2] Drug delivery systems, such as nanoparticles, have therefore been designed to overcome these limitations. Nano-sized drug delivery vehicles (1 to 1000 nm) have been developed to improve the efficacy of delivering therapeutic and imaging agents by improving *in vivo* solubility and stability, carrying drugs across barriers such as cellular membranes, providing high payload and/or targeting moieties, and controlled delivery and release. [3-6]

The first FDA-approved nanoparticle-drug was Doxil in 1995. Doxil is a PEGylated liposome that has a prolonged drug circulation time and avoids the mononuclear phagocyte system (MPS). It has a high and stable loading of doxorubicin (an anticarcinogen) driven by a transmembrane ammonium sulphate gradient, which also allows for drug release at the tumour. [7] Several other nanomedicines have also been clinically approved for cancer, such as liposomal daunorubicin (DaunoXome) and albumin-bound paclitaxel (Abraxane). [8] These have all shown to reduce toxicity compared with conventional chemotherapeutics, for example in peripheral toxicity or cardiotoxicity. [9] However, they only modestly improve the overall survival of patients in phase-III trials. [9] Other clinically-approved nanoparticles for drug delivery are amongst others: iron oxide nanoparticles for solid tumour hyperthermia (NanoTherm), PEGylated antibodies for hepatitis C or neutropenia, NanoCrystal based oral tablets that increase solubility and dissolution, and polymer-based nanoparticles. [10] All currently clinically approved nanoparticles are summarized in Table 1.1.

In nanomedicine, there is a noticeable focus on development of nanoparticles for cancer applications. [8] As the efficacy is often limited by physiological barriers posed by the tumour microenvironment, the next generation of nanoparticles is directed towards a more customized nanomedicine design: by tuning size, surface chemistry (e.g. introducing active targeting), shape, and formulation. [11, 12] An interesting example is paclitaxel poliglumex (Opaxio) that is currently in phase III trial for advanced ovarian cancer. [8] It is a biologically enhanced chemotherapeutic that links paclitaxel to a biodegradable polyglutamate polymer that is preferentially distributed to tumours and activated after enzymatic metabolism in tumour cells.

Table 1.1: Clinically-approved nanoparticles for drug delivery. Adapted from Weissig *et al.* [13] and Anselmo and Mitragotri. [14]

Name	Description	Mechanism of action	Approval/indication
<b>1) Liposomes</b>			
AmBisome®	Amphotericin B encapsulated in liposomes (60–70 nm)	Mononuclear phagocyte system (MPS) targeting. selective transfer of drug from lipid complex to target fungal cell with minimal uptake into human cells	FDA 1997 Systemic fungal infections
DaunoXome®	Daunorubicin citrate encapsulated in liposomes (45 nm)	Passive targeting via enhanced permeability and retention (EPR) effect: concentration liposomal drug in tumours exceeds that of free drug; persists at high levels for several days	FDA 1996 HIV-related Kaposi's sarcoma (KS), intravenously (IV)
Doxil®	Doxorubicin hydrochloride encapsulated in Stealth® liposomes (100 nm)	Passive targeting via EPR effect: enhanced accumulation in lesions of AIDS-associated KS	FDA 1995 AIDS-related KS, multiple myeloma, ovarian cancer
Epaxal®	Liposome with hepatitis A virus	Hepatitis A vaccine	Some of Europe 2007 Hepatitis A vaccine
Inflexal®	Influenza virus antigens (hemagglutinin, neuraminidase) on surface (150 nm)	Mimicking native antigen presentation: allowing for cellular entry and membrane fusion and high immunogenicity	Switzerland 1997 Influenza vaccine
Marqibo®	Vincristine sulphate encapsulated in sphingo-myelin/cholesterol (60/40, molar) 100 nm liposomes	Passive targeting via EPR effect: Extravasation of liposomes through fenestra in bone marrow endothelium	FDA 2012 Acute lymphoid leukaemia in specific conditions
Mepact™	Mifamurtide incorporated into large multilamellar liposomes	MPS targeting: drug, an immune stimulant, is anchored in liposomal bilayer membrane	Europe 2009 Non-metastasizing resectable osteosarcoma
Myocet®	Doxorubicin encapsulated 180 nm oligolamellar liposomes	MPS targeting: slow release into blood circulation resembles prolonged infusion	Europe 2000 Metastatic breast cancer (IV)
Onivyde MM 398®	Liposomal irinotecan (PEGylated)	Topoisomerase inhibitor	FDA 2015 Metastatic pancreatic cancer (secondary)
Visudyne®	Verteporfin in liposomes (negatively charged)	Drug solubilisation	FDA 2000 Photodynamic therapy of wet age-related macular degeneration, myopia, ocular histoplasmosis syndrome (IV)
<b>2) Lipid-based (non-liposomal) formulations</b>			
Abelcet® / Amphocil®	Amphotericin B complex 1:1 with lipids > 250 nm, ribbon like structures of a bilayered membrane	MPS targeting: selective transfer of drug from lipid complex to fungal cell with minimal uptake into human cells	FDA 1995 / 1996 Systemic fungal infections (IV)
Amphotec®	Amphotericin B complex with cholesteryl sulphate. Colloidal dispersion of disc-like particles, 122 nm × 4 nm	MPS targeting	FDA 1996 Indicated for aspergillosis in specific cases

Name	Description	Mechanism of action	Approval/indication
<b>3) Polymer-based nanoparticles</b>			
Copaxone®	Polypeptide (average MW 6.4 kDa) composed of four amino acids (glatiramer)	Based on its resemblance to myelin basic protein, glatiramer is thought to divert as a “decoy” an autoimmune response against myelin	FDA 1996/2014 Multiple sclerosis, subcutaneously (SC)
Eligard®	Leuprolide acetate incorporated in nanoparticles composed of PLGH copolymer (DL-lactide/glycolide)	Sustained release	FDA 2002 Advanced prostate cancer (SC)
Genexol®	Paclitaxel in 20–50 nm micelles composed of block copolymer poly(ethylene glycol)- poly(D,L-lactide)	Passive targeting via EPR effect	South Korea 2001 Metastatic breast cancer, pancreatic cancer (IV)
Opaxio®	Paclitaxel covalently linked to solid nanoparticles composed of polyglutamate	Passive targeting via EPR effect: drug release inside solid tumour via enzymatic hydrolysis of polyglutamate	FDA 2012 Glioblastoma
Renagel®	Cross-linked poly allylamine hydrochloride, 40 MW variable	No mechanism attributable to nano-size. Phosphate binder	FDA 2000 Hyperphosphatemia (oral)
Zinostatin stimalamer®	Conjugate protein or copolymer of styrene-maleic acid and an anti-tumour protein neocarzinostatin	Passive targeting via EPR effect	Japan 1994 Primary unresectable hepatocellular carcinoma

#### 4) Protein–drug conjugates

Abraxane®	Nanoparticles (130 nm) formed by albumin with conjugated paclitaxel	Passive targeting via EPR effect: dissociation into individual drug-bound albumin molecules may mediate endothelial transcytosis of paclitaxel via albumin-receptor mediated pathway	FDA 2005 Metastatic breast cancer, non-small-cell lung cancer (IV)
Kadcyla®	Immunoconjugate. Monoclonal antibody–drug (a cytotoxin acting on microtubule) conjugate, linked via thioether	No mechanism attributable to nano-size	FDA 2013 Metastatic breast cancer
Ontak®	Recombinant fusion protein of fragment A of diphtheria toxin and subunit binding to interleukin-2 receptor	Fusion protein binds to interleukin-2 receptor, followed by receptor-mediated endocytosis; fragment A released into cytosol where it inhibits protein synthesis	FDA 1994/2006 Primary cutaneous T-cell lymphoma, CD25-positive, persistent or recurrent disease

Name	Description	Mechanism of action	Approval/indication
<b>5) PEGylated proteins, polypeptides, aptamers</b>			
Adagen®	PEGylated adenosine deaminase	Increased circulation time and reduced immunogenicity	FDA 1990 Adenosine deaminase deficiency
Cimzia®	PEGylated antibody (Fab' fragment of a humanized anti-TNF-alpha antibody)	See above	FDA 2008 Crohn's disease, rheumatoid arthritis
Macugen®	PEGylated anti-VEGF aptamer		FDA 2004 Neovascular age-related macular degeneration
Mircera®	PEGylated epoetin beta		FDA 2007 Anaemia associated with chronic renal failure in adults
Neulasta®	PEGylated filgrastim (granulocyte colony-stimulating factor)		FDA 2002 Febrile neutropenia
Oncaspar®	PEGylated L-asparaginase		FDA 1994 Acute lymphoblastic leukaemia
Pegasys®	PEGylated interferon alfa-2b		FDA 2002 Hepatitis B and C
PegIntron®	PEGylated interferon alfa-2b		FDA 2001 Hepatitis C
Somavert®	PEGylated human growth hormone receptor antagonist		FDA 2003 Acromegaly, second-line therapy
<b>6) Nanocrystals</b>			
Emend®	Aprepitant as nanocrystal	Increased bioavailability due to increased dissolution rate	FDA 2003 Emesis, antiemetic (oral)
Megace ES®	Megestrol acetate as nanocrystal		FDA 2005 Anorexia, cachexia (oral)
Rapamune®	Rapamycin (sirolimus) as nanocrystals formulated in tablets		FDA 2002 Immunosuppressant (oral)
Tricor®	Fenofibrate as nanocrystals		FDA 2004 Hypercholesterolemia, hypertriglyceridemia (oral)
Triglide®	Fenofibrate as insoluble drug-delivery microparticles		FDA 2005 Hypercholesterolemia, hypertriglyceridemia (oral)

Name	Description	Mechanism of action	Approval/indication
<b>7) Metal-based nanoparticles</b>			
CosmoFer® / INFeD® / Ferrisat®	Iron dextran colloid	Iron deficient anaemia	FDA 1992 Iron deficient anaemia
DexFerrum® / DexIron®	Iron dextran colloid	Iron deficient anaemia	FDA 1996 Iron deficient anaemia
Diafer®	5 % Iron isomaltoside 1000 colloid	Iron deficient anaemia	Some of Europe (2013) Iron deficient anaemia
Feraheme™	Superparamagnetic iron oxide nanoparticles coated with dextran, > 50 nm	MPS targeting: Iron released inside macrophages, enters into intracellular storage iron pool, or transferred to plasma transferrin	FDA 2009 Treatment of iron deficiency anaemia in adults with chronic kidney disease
Ferlecit®	Iron gluconate colloid	Iron replacement for anaemia treatment in patients with chronic kidney disease	FDA 1999 Iron deficient anaemia
Injectafter® / Ferinject®	Iron carboxymaltose colloid	Iron deficient anaemia	FDA 2009 Iron deficient anaemia
Monofer®	10 % Iron isomaltoside 1000 colloid	Treating iron deficiency and anaemia	Some of Europe 2009 Iron deficient anaemia
NanoTherm®	Aminosilane-coated superparamagnetic iron oxide 15 nm nanoparticles	Thermal ablation: exposed to alternating magnetic field causing the nanoparticles to oscillate, generating heat directly within the tumour tissue	Europe 2013 Local ablation in glioblastoma, prostate, and pancreatic cancer
Venofer®	Iron sucrose colloid Iron	Iron replacement for anaemia treatment in patients with chronic kidney disease	FDA 2000 Iron deficient anaemia. Following autologous stem cell transplantation
<b>8) Surfactant-based nanoparticles</b>			
Fungizone®	Lyophilized powder of amphotericin B with sodium deoxycholate. Micellar dispersion.	Drug solubilisation: make drug biocompatible and enhancing ease of IV administration.	FDA 1966 Systemic fungal infections (IV)
Diprivan®	Oil-in-water emulsion of propofol	Drug solubilisation	FDA 1989 Sedative–hypnotic agent for anaesthesia (IV)
Estrasorb™	Emulsion of estradiol in soybean oil, polysorbate 80, ethanol, and water	Drug solubilisation	FDA 2003 Hormone replacement therapy during menopause
<b>9) Virosomes</b>			
Gendicine®	Recombinant adenovirus expressing wildtype-p53	Infects tumour target cells and delivers the adenovirus genome	People's Republic of China 2003 Head and neck squamous cell carcinoma
Rexin-G®	Gene stops cell cycle, inserted into retroviral core (replication-incompetent retrovirus) devoid of viral genes. About 100 nm particle	Particle targets specifically exposed collagen, which is a common histopathological property of metastatic tumour formation.	Philippines 2007 For all solid tumours

### 1.1.2 Nanoparticle drug delivery systems

Numerous nano-scale platforms have emerged to improve drug delivery: 1) organic, such as liposomes, dendrimers, polymeric nanoparticles, or micelles, and 2) inorganic nanocarriers like mesoporous silica, magnetic nanoparticles, gold particles, or quantum dots (see Figure 1.1). [15] Furthermore, also hybrid nanoparticles have been developed combining for example an inorganic core and an organic coating. For instance, the aforementioned Feraheme contains an iron oxide nanoparticle core and a dextran coating. Each nanoparticle system has its advantages and disadvantages regarding control of size, introduction of functionalities, ease of synthesis and costs. [8, 16, 17]

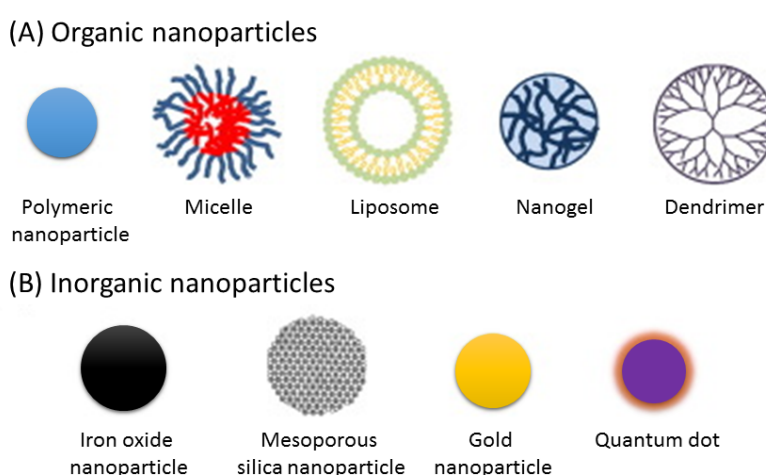


Figure 1.1: Representative structures of various nanoparticles for drug delivery and imaging. Adapted from Jia *et al.* [15] with permission from Elsevier.

### 1.1.3 Bio-nano interactions of nanoparticles

#### *Surface*

The interactions of the nanomaterials with biological systems, also known as bio-nano interactions. [18], are determined by the intrinsic properties of the nanoparticles, such as size, shape and surface chemistry. [19] For example, surface coating with polyethylene glycol (PEG) limits clearance by the mononuclear phagocyte system (MPS) and results in better biocompatibility, longer circulation times, and decreased aggregation. [10, 20] Recently, it was revealed that the stealth effect is not a polymer effect only, but a secondary effect. [21] A PEG surface coating results in a distinct reduction and modification of protein adsorption and the formation of a protein corona that contains an abundance of clusterin proteins which limited non-specific cell uptake. [21] Other polymers with enhanced circulation time are poly(glycerol)s, poly(amino acid)s, poly-(vinylpyrrolidone), poly(2-oxazoline)s, and

poly(N-(2-hydroxypropyl)methacrylamide) (PHPMA). [20] The surface of nanoparticles can also be modified using surface-anchored antibodies, aptamers, saccharides, or peptides to enhance site-specific delivery, *viz.* active targeting [10, 22, 23]. In addition, a surface charge can also be introduced to optimize bio-nano interactions. [24] For example cationic nanoparticles facilitate cell uptake and transfection of genetic material, [25] whereas nanoparticles with neutral and negative surface charges have been shown to reduce the adsorption of serum proteins, resulting in longer circulation half-lives (see also Figure 1.2). [26, 27]

### Size

The size of nanoparticles is also an essential factor as it influences the biodistribution, elimination and cell uptake [9, 11, 24] Very small particles (less than 11 nm) are eliminated more quickly by the renal and hepatobiliary clearance. [28] Whereas non-continuous endothelia with vascular fenestrations measuring 50–100 nm are present in the liver, resulting in non-specific accumulation of larger particles in this organ. [27] Nanoparticles over 200 nm are retained in the spleen, due to the 200 - 500 nm size range of splenic interendothelial cell slits (see Figure 1.2). [27] Lastly, particles in the micrometer range (2 - 5  $\mu$ m) readily accumulate within capillaries of the lungs. [27]

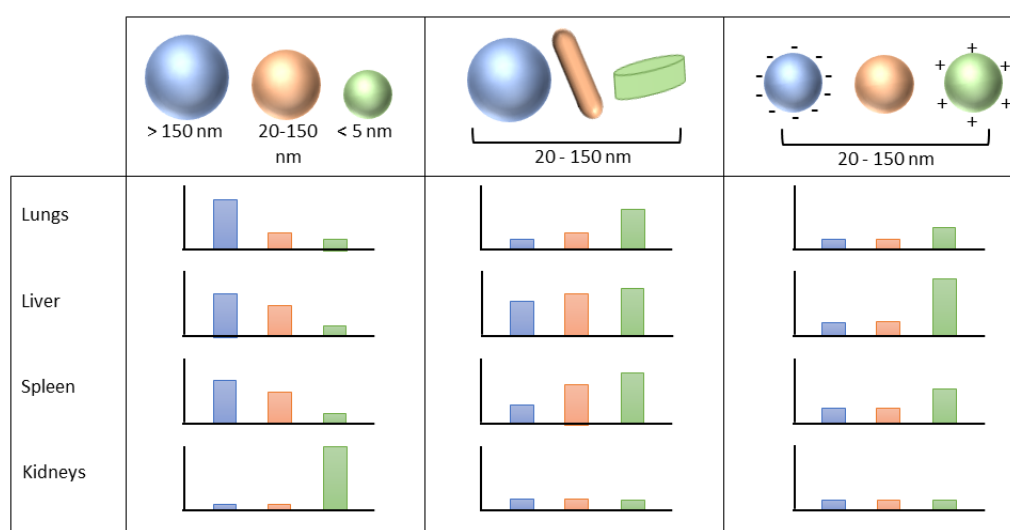


Figure 1.2: *In vivo* fates of nanoparticles, taking into account singular design parameters of size, shape and surface charge. Figure is inspired by Blanco *et al.* [27]

Larger nanoparticles (10 nm - 400 nm [29], N.B. cut-off is tumour dependent [9, 30]) can take advantage of the enhanced permeability and retention (EPR) effect in cancer, *viz.* passive targeting (see Figure 1.3). This is a unique phenomenon of solid tumours due to their anatomical and pathophysiological differences from normal tissues [31], such as extensive angiogenesis and hence hypervascularity, defective vascular architecture, impaired lymphatic drainage/recovery system, and

greatly increased production of a number of permeability mediators. [32] This effect can be further enhanced in clinical settings by increasing systolic blood pressure via slow angiotensin II infusion or using NO-releasing agents such as topical nitroglycerin. [33] However, the EPR effect is often oversimplified as tumours are very heterogeneous. [9] For example, the pore-size distribution of the microvasculature vary substantially by tissue [34], and each tumour type has its own range. [9, 35] As tumour blood vessels are derived from normal microvessels, tumour vessels are influenced by characteristics of the tissue [9], and the exact pore cut-off size fluctuates with the organ site. For instance, the pore cut-off size for a breast or pancreatic tumour can be around 50 – 60 nm versus 5 nm for normal breast or pancreatic tissue [36], while in a brain tumour it might be around 7 nm versus less than 1 nm for normal brain tissue. [9, 35]

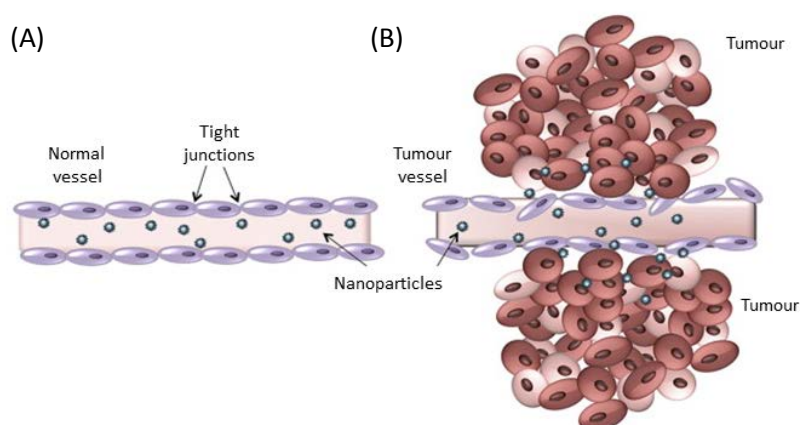


Figure 1.3: Passive accumulation of nanoparticles. (A) Nanoparticles flow through normal blood vessels and cannot pass through the tight junctions between the endothelial cells thereby preventing toxicity in normal tissues. (B) The tumour vasculature is discontinuous with large gaps in the endothelial cell tight junctions resulting in preferential nanoparticle accumulation at the tumour site. Reprinted from Sagnella *et al.* [37] with permission from Elsevier.

Furthermore, the penetrability of tumours is also very heterogeneous due to a low or high stroma content, or pericyte coverage of blood vessels. [38, 39] For example, 100 nm micelles could easily penetrate a hyperpermeable murine colon adenocarcinoma 26 (C26) model characterised by high vascularisation and a slight tumour stroma burden. Whereas only 30 nm micelles could penetrate a human pancreatic adenocarcinoma (BxPC3) characterised by low vascularisation, reduced vascular permeability because of pericyte coverage of blood vessels and thick fibrosis [40] (which are representative properties of some intractable solid tumours [41]). Therefore, nanoparticles have to be engineered with these caveats in mind for their specific applications.

## *Shape*

Next to the size, recent studies showed that the shape of nanoparticles has also important implications on biodistribution, cellular uptake and clearance. [12] For example, spherical micelles are taken up by phagocytes more readily than micelles that have been extended into filaments by shear flow. [42] Moreover, rod-like particles showed a faster transvascular penetration compared to size-matched spheres [43] and displayed a higher cell uptake for nanoparticles over 100 nm, whereas spheres performed better in studies with sub-100-nm particles. [11] At the same time, it was shown that rod like and cubic nanoparticles penetrate dense tumour tissue more efficiently than spheres. [44] The flexibility of rods is also important, as flexible rods clear from plasma much slower than size-matched rigid rods. [43] Non-spherical nanoparticles have therefore exciting potential advantages for drug delivery.

### 1.1.4 Polymer-based nanoparticles

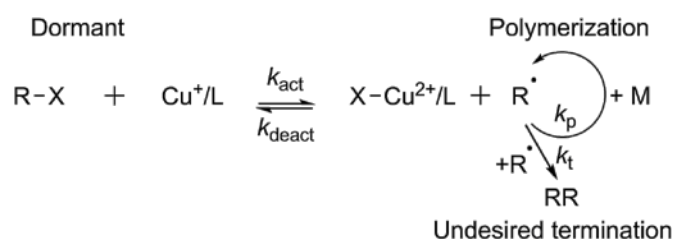
As mentioned above, a wide range of nanoscale platforms have emerged to improve drug delivery. The next part of this review will predominantly focus on polymeric nanoparticles for drug delivery. Polymer chemistry has proven to be a very versatile technique for applications in the field of nanomedicine, as it allows the synthesis of nanoparticles with a wide range of size, shape, and surface chemistry. [45] This is largely made possible by the emergence of controlled/living radical polymerization techniques (also known as reversible-deactivation radical polymerization), including atom transfer radical polymerization (ATRP), reversible addition fragmentation chain transfer polymerization (RAFT) and nitroxide mediated polymerization (NMP) [46, 47], and efficient organic reactions, including copper azide alkyne click chemistry and thiol–ene reactions. [48] These polymerization techniques will be introduced in the next section; followed by an overview of the synthesis of polymeric nanoparticles with a special focus on spherical and non-spherical self-assembled nanoparticles, and hyperbranched / star polymers.

### 1.1.5 Controlled/living radical polymerization techniques

#### ATRP

ATRP is a versatile and effective controlled polymerization technique for a wide range of vinyl monomers including styrenes, (meth)acrylates, acrylonitriles, and dienes. [49-51] ATRP usually uses a transition metal complex as the catalyst with an alkyl halide as the initiator, and has been utilized for amongst others the syntheses of polymers with complex architecture (e.g. brush polymers and multifunctional stars), various hybrids, and bioconjugates. [52] The procedure for basic ATRP is

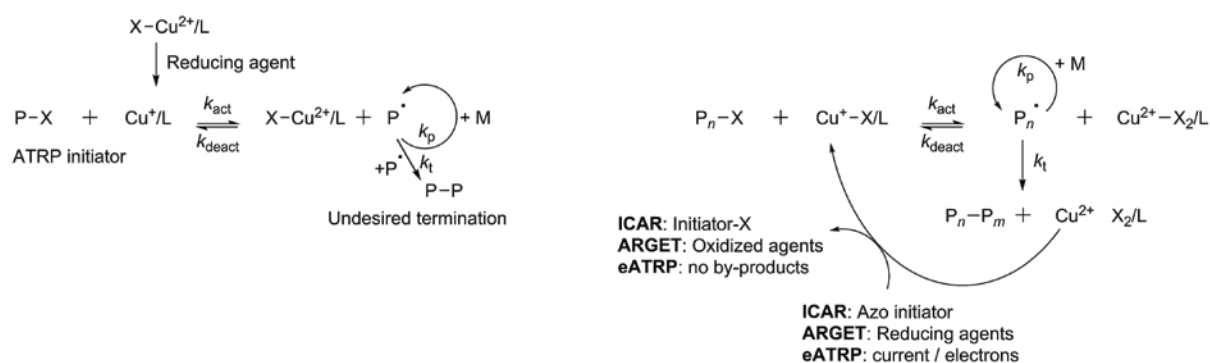
straightforward and includes an initiator, a catalyst, and monomer added to solvent. The equilibration describing the reaction is depicted in Scheme 1.1.



Scheme 1.1: The basic ATRP equilibrium equation. [51]

It consists of three situations: (1) a polymer sitting dormant on the left side of the equilibrium; (2) a polymer reacting with monomer on the right side of the equilibrium; and (3) two radical end groups combining to terminate and end the reaction irreversibly. In ATRP, the reaction is predominantly on the left side of the equation, which minimizes the probability for two radicals to be near each other and therefore minimizes termination. This control over termination is the primary benefit of choosing ATRP. [49, 53] The rate of the polymerization is marked by rate constants ( $k_x$ ) where the rate of activation is  $k_{act}$ , the rate of deactivation is  $k_{deact}$ , the rate of monomer addition is  $k_p$ , and the rate of termination is  $k_t$ . The control over this equilibrium highly depends on the choice of catalyst. [49]

Next generation versions of ATRP have been developed in the last decades. The most important are: (1) reverse ATRP in which catalyst is added in the higher oxidation state [54]; (2) activators generated by electron transfer (AGET) in which a non-radical forming reducing agent is employed to generate the activator from the higher oxidation state transition metal complex (see Scheme 1.2A) [55]; (3) activators regenerated by electron transfer (ARGET) that uses only ppm amounts of Cu-based catalysts by using appropriate reducing agents; (4) initiators for continuous activator regeneration (ICAR), that can be seen as a reverse ARGET where a source of organic free radicals is employed to continuously regenerate the Cu(I) activator which is otherwise consumed in termination reactions when catalysts are used at very low concentrations [56]; (5) electrochemically-mediated ATRP (eATRP) (see Scheme 1.2B) [57] and (6) photoinduced ATRP ( $\pi$ -ATRP). [58]



Scheme 1.2: (A) Mechanism of reverse ATRP, and (B) mechanisms of ICAR, ARGET and eATRP. [55-58]

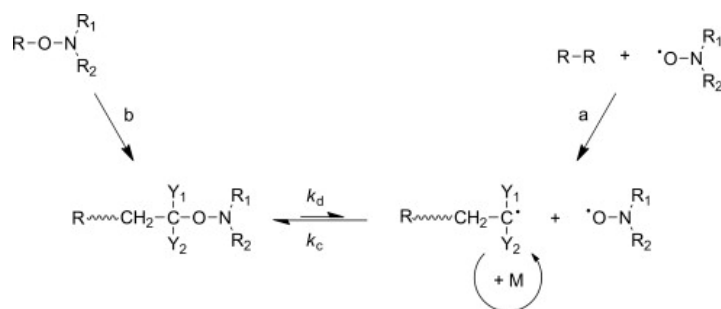
Cu(0)-mediated living radical polymerization [59, 60] is also an efficient polymerization method that provides access to a large variety of materials and complex macromolecular architectures. [50, 61] A wide range of monomers can be utilized for rapid polymerization with narrow molecular weight distributions, including acrylates, methacrylates, and acrylamides. [61] In addition, a very high endgroup functionality is maintained, which is able of undergoing *in situ* chain extensions and block copolymerizations. Moreover, it can be conducted at ambient temperature or below with no need for strict deoxygenating procedures. [59] A limitation is that it cannot currently be used for the polymerization of less activated monomers such as N-vinylpyrrolidone and vinyl acetate, while reports with styrene and methacrylamides are also limited. [61] Furthermore, acidic monomers cannot be directly homopolymerized due to complexation of the catalyst, and the solvent choice is limited (predominantly DMSO and water). [50, 61]

There is still an ongoing debate regarding the exact mechanism of this polymerization method as there are two differing interpretations on the role of the  $\text{Cu}^0$  and  $\text{Cu}^{1+}$  catalyst complexes in the presence of polar solvent. [50, 62, 63] Hence this method is also known as supplemental activator and reducing agent atom transfer radical polymerization (SARA ATRP).

## NMP

Nitroxide-mediated polymerization (NMP) was the first controlled/living radical polymerization technique that enabled the design of well-defined, functional and complex macromolecular architectures. [64] It is based on a reversible termination mechanism between the growing propagating (macro)radical and the nitroxide, which acts as a control agent, to yield a (macro)alkoxyamine. [64, 65] This dormant functionality generates back the propagating radical and the nitroxide by cleavage upon temperature increase. By careful selection of the nitroxide, an equilibrium between dormant and active species is established (see Scheme 1.3). [64] The main advantage is that this equilibrium is thermally initiated in the absence of an external radical source or

a metal catalyst. [65] The polymerization kinetics is governed by both this activation–deactivation equilibrium (with  $K = k_d/k_c$ , the activation–deactivation equilibrium constant) and the persistent radical effect. [66] An important drawback for NMP is the relatively reduced number of monomers that can be controlled, in particular less activated monomers such as vinyl acetate, vinyl chloride and N-vinylpyrrolidone. [64]



Scheme 1.3: Activation–deactivation equilibrium in nitroxide-mediated polymerization. Bicomponent initiating system (a) and monocomponent initiating system (b). Reprinted from Nicolas *et al.* [64] with permission from Elsevier.

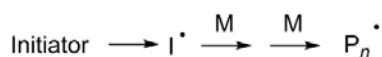
## RAFT

Reversible addition fragmentation chain transfer (RAFT) polymerization [67] is the most versatile method for providing living characteristics to radical polymerization. [68, 69] It has been used to polymerize a wide range of monomers, such as styrenic, (meth)acrylic, (meth)acrylamido, isoprene, vinylic, and diallyl monomers. [68, 70]. RAFT polymerization is adaptable to use in both organic and aqueous media and charged polymers can be successfully polymerized at room [71] or high temperatures. [72]

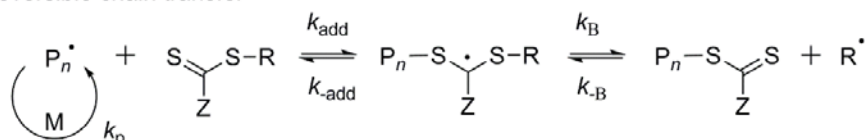
The predominant feature of the RAFT polymerization mechanism is a sequence of addition–fragmentation equilibria as displayed in Scheme 1.4. [73] Initiation and radical–radical termination occur like in conventional radical polymerization. In the initial stages of the polymerization, addition of a propagating radical ( $P_n^\bullet$ ) to the thiocarbonylthio compound followed by fragmentation of the intermediate radical results in a polymeric thiocarbonylthio compound and a new radical. The reaction of the radical with monomer creates a new propagating radical ( $P_m^\bullet$ ). The rapid equilibrium between the active propagating radicals and the dormant polymeric thiocarbonylthio compounds offers equal probability for all chains to grow, and enables the synthesis of polymers with a narrow polydispersity. [67, 73] When the polymerization is finished (or stopped), most of chains retain the thiocarbonylthio end group which can be potentially used for characterization. Furthermore, the end groups can be

modified for bioconjugation of different biomolecules, for instance oligonucleotides, carbohydrates, peptides, [74] and gasotransmitters such as nitric oxide. [75]

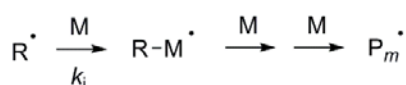
Initiation



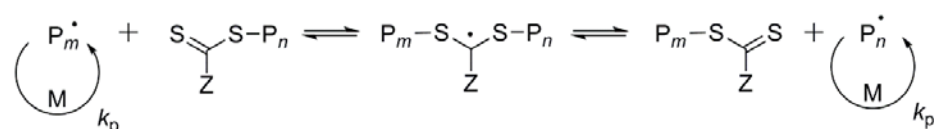
Reversible chain transfer



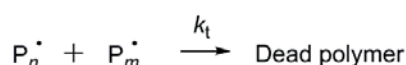
Reinitiation



Chain equilibration



Termination



Scheme 1.4: RAFT mechanism.

The mechanism for achieving control in RAFT polymerization is significantly different compared to other living radical polymerization methods such as NMP and ATRP. [46, 73] In RAFT, the deactivation–activation equilibria are chain-transfer reactions. No radicals are made or destroyed in these steps and an external source of free radicals is needed to start and maintain polymerization. Whereas the other methods contain reversible deactivation of propagating radicals by radical–radical reaction (NMP) and atom transfer (ATRP). [73] The dormant species (the alkoxyamine in NMP or the halo-compound in ATRP) is also the source of radicals. The position of the deactivation–activation equilibria and the persistent radical effect govern the rate of polymerization. [69]

### 1.1.6 Synthesis of polymer-based nanoparticles

As described above, controlled/living radical polymerization techniques, such as RAFT, offer an unprecedented control over material design, architecture, introduction of functionalities; and the preparation of bioconjugates, organic/inorganic composites and self-assembled nanoparticles (see Figure 1.4). A plethora of RAFT-mediated polymer-based nanoparticles have been developed for drug and imaging applications. [68, 70] In this section, the synthesis of spherical and non-spherical self-assembled polymeric nanoparticles, and hyperbranched / star polymers will be discussed.

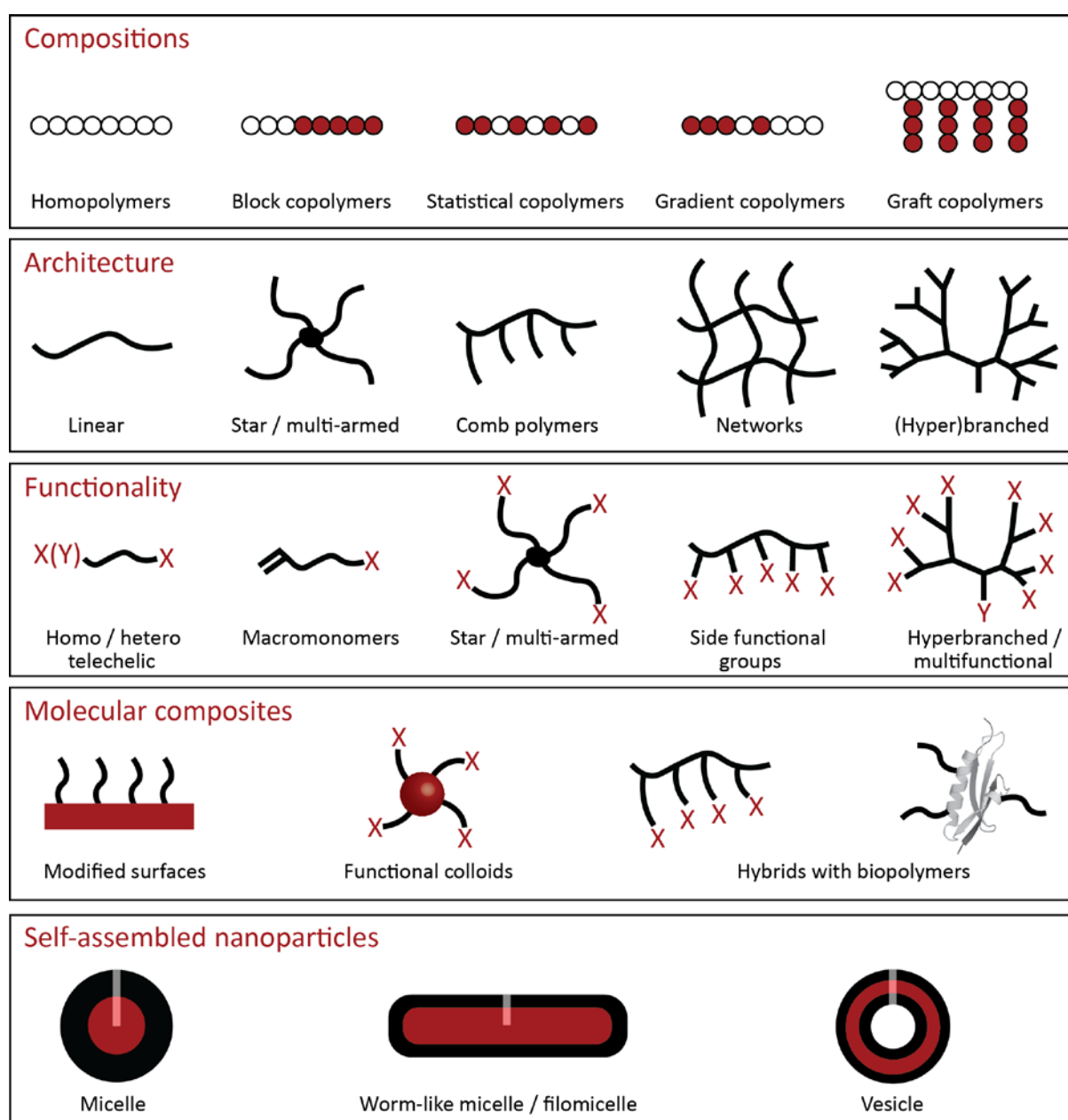


Figure 1.4: overview of structures that can be obtained using RAFT polymerization.

## Self-assembled nanoparticles

Amphiphilic block copolymers can self-assemble into several morphologies, such as micelles, rod-like micelles/filomicelles and vesicles. [76] The morphology is predominantly the result of the inherent molecular curvature, which is influenced by the packing of the copolymer chain. The packing is dependent on the volume of the hydrophobic chains, the area of the head group, and the length of the hydrophobic tail (see Figure 1.5). [77] This process can be quantified using the packing diameter ( $P$ ), which is given by the equation:

$$P = v / a \cdot l \quad (1.1)$$

For an amphiphilic diblock copolymer,  $v$  and  $l$  are the volume and length of the hydrophobic block, respectively, and  $a$  is the interfacial area of the block junction. It is generally accepted that spherical micelles are produced with  $P < 0.33$ , filomicelles when  $0.33 < P < 0.5$ , and vesicles are formed when  $0.5 < P < 1.0$ . [76 - 77]

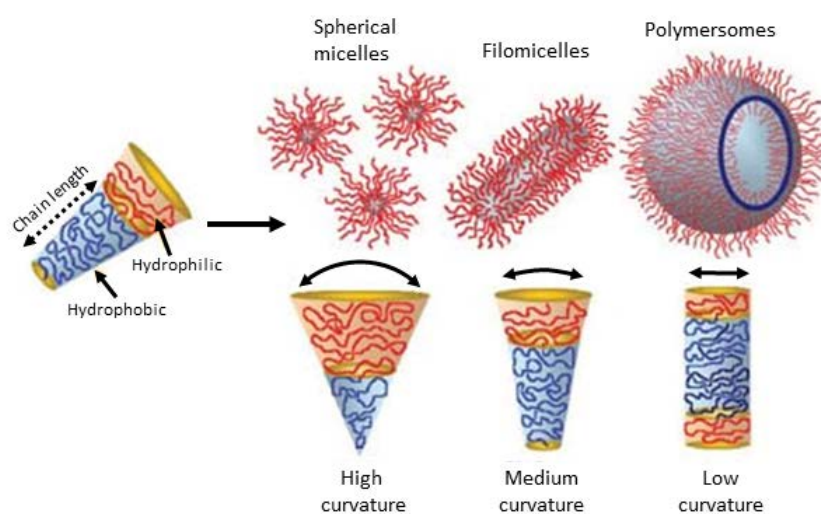


Figure 1.5: Various self-assembled structures formed by amphiphilic block copolymers in aqueous solutions. The morphology is dependent on the inherent curvature of the molecule. Figure is adapted with permission from Blanz et al. [77] Copyright Wiley-VCH Verlag GmbH & Co. KGaA, Weinheim 2009.

## Polymeric micelles

Polymeric micelles are the most utilized self-assembled polymeric nanoparticle for drug delivery. [8] These nano-sized core/shell structures are formed by amphiphilic block copolymers. They were introduced in the early 1990s by Kataoka's group through the development of doxorubicin-conjugated block copolymer micelles [78]. Polymeric micelles have since been used for the delivery of many

anticancer drugs in preclinical and clinical studies due to their high loading capacity, prolonged circulation, biodegradability and passive targeting by the EPR effect. [79, 80] The inner core is usually the hydrophobic part of the block copolymer, which contains the poorly water-soluble drug, while the corona of the hydrophilic block protects the drug from the aqueous environment and recognition by the mononuclear phagocyte system. [81, 82] The encapsulation of the drug can involve a variety of cohesive interactions such as hydrophobic, electrostatic,  $\pi$ - $\pi$  interactions, and hydrogen bonding, however as most drugs are poorly water-soluble, anticancer agents are predominantly encapsulated using hydrophobic interactions. [79, 83] This is usually performed using the dialysis method, oil-in-water emulsion solvent evaporation method, or solid dispersion method. Other methods used are direct dissolution, complexation, chemical conjugation, and various solvent evaporation procedures. [79, 84]

Self-assembly of polymeric micelles occur when the concentration of amphiphilic polymer reaches the threshold concentration named critical micelle concentration (CMC) or critical association concentration (CAC). [81] The micelle formation is entropically driven to minimize energetically unfavourable hydrophobe-water interactions. [79] The CMC of polymeric micelles ( $10^{-6}$ – $10^{-7}$  M) is much lower than the CMC of surfactants ( $10^{-3}$ – $10^{-4}$  M) [79], therefore polymeric micelles are more stable than surfactant-based micelles. In addition, polymeric micelles can be tailored by cross-linking of the core or shell to stabilize the micellar morphology further, and to control the release of encapsulated drug. [82]

At the same time, instability can also be deliberately introduced using responsive amphiphilic block copolymers to promote site-specific drug release. For example, the tumour extracellular pH is slightly lower than normal tissue pH. It ranges from pH 5.7 to 7.8, with a mean value of 7.0, but most of the pH values are below pH 7.2, whereas the blood pH remaining constant at pH 7.4. [85] This resulted in the development of pH-sensitive polymeric micelles that dissociate in tumours using a pH-sensitive polybase [poly(L-histidine)] or introducing titrable groups (e.g. methacrylic acid or ethylazepene) [79, 86-88] into the copolymer. For sub-cellular targeting, micelles have also been designed to be responsive to pH values ranging from 5.0 to 6.0 (endosomal-lysosomal pH) for example using diisopropylamine-based monomers. [87, 89]

## Polymersomes

Polymeric vesicles (polymersomes) exhibit superior mechanical and physical properties compared to phospholipid-based vesicles (liposomes) and are much tougher, sustaining a ten-fold increase in critical areal strain before rupture when compared to liposomes. [90] Therefore polymersomes have

received tremendous attention as versatile drug carrier. [91, 92] Similar to polymeric micelles, polymersomes can be tailored in many ways due to the versatility of controlled/living radical polymerization; and responsiveness and/or active targeting groups can be introduced. [91] The advantage of vesicles is that hydrophilic drugs can be included in the inner aqueous lumen, while hydrophobic drugs can be loaded into the membrane. However, although the larger size of polymersomes results in a higher drug loading capacity, it can limit drug delivery to tumours with a high stroma or lower EPR cut-off. [40] Polymeric vesicles can be prepared using AB diblock copolymers, as well as using a binary mixture of AB and BC diblock copolymers within the membrane (the enhanced curvature drives membrane asymmetry) or an ABC triblock copolymer (where block A has a larger hydrophilic volume than block C). [77]

#### Polymeric filomicelles

Polymeric worm or rod-like micelles, also known as filomicelles, can be seen as an intermediate structure between polymeric micelles and vesicles, as amphiphilic block copolymers with a medium curvature form filomicelles. [77] Polymeric filomicelles are an emerging subclass of materials and receive increasing attention for applications in drug delivery due to their favourable properties. [93, 94] They combine the high drug loading capacity of vesicles with beneficial physical properties such as high surface area and aspect ratios. [93] Discher and co-workers showed that filomicelles have an elongated blood circulation time [95], and a better tissue penetration compared to vesicles. [96] Furthermore, filomicelles have a high accumulation in tumours [97] and the high surface area results in enhanced active targeting. [12]

Polymeric filomicelles can be synthesized using several methods. [93] First of all, filomicelles can be synthesized via self-assembly using either solvent mixing or film dispersing, similar to micelles and polymersomes. Furthermore, particle replication in non-wetting templates (PRINT) can also be used. [98] This is a continuous, roll-to-roll, high-resolution technology that enables the moulding of solid polymers into rod-like nanoparticles by employing a porous template. [93] Self-assembly can also be promoted by crystallization-driven self-assembly, which exploits the crystallization of semicrystalline diblock copolymers as the driving force to form filomicelles. [99] In addition, self-assembly can also be induced by temperature changes in a technology named temperature-induced morphological transformation. [100] In this strategy, filomicelles are prepared from spherical nanoparticle seeds or intermediates (from either nanospheres or nanovesicles). Then a change in temperature is used to trigger an irreversible morphological transformation into filomicelles. [93, 101] Finally, polymeric filomicelles can also be synthesized using polymerization-induced self-assembly (PISA).

## Polymerization induced-self assembly

Polymerization-induced self-assembly (PISA) is based on the preparation of amphiphilic diblock copolymers and the *in situ* formation of filomicelles (and other shapes such as micelles and vesicles) during the living/control radical polymerization polymerization. [102, 103] Typically, first the A block is synthesized by solution polymerization and act as a steric stabilizer. Then block A is chain-extended in a dispersion polymerization, using a second monomer in a solvent that is chosen such that the growing second block (B) gradually becomes insoluble. This drives the *in situ* self-assembly to form AB diblock copolymer nanoparticles (see Figure 1.6). [102] By varying the degree of polymerization of both blocks, either micelles or higher order morphologies such as filomicelles or vesicles are created. [103, 104] Next to these, also other shapes have been obtained, such as lamellae [105], octopi [106], or donuts. [107] PISA has decisive advantages in terms of versatility, efficiency, and cost efficiency. [102] For example, PISA reactions can be carried out with high solid content (25 – 50 % w/w) and very high monomer conversions are often achieved within short reaction times, while the final copolymer concentrations are rather low (< 1.0 % w/w) in almost all self-assembly cases, which precluded many potential commercial applications. [102]

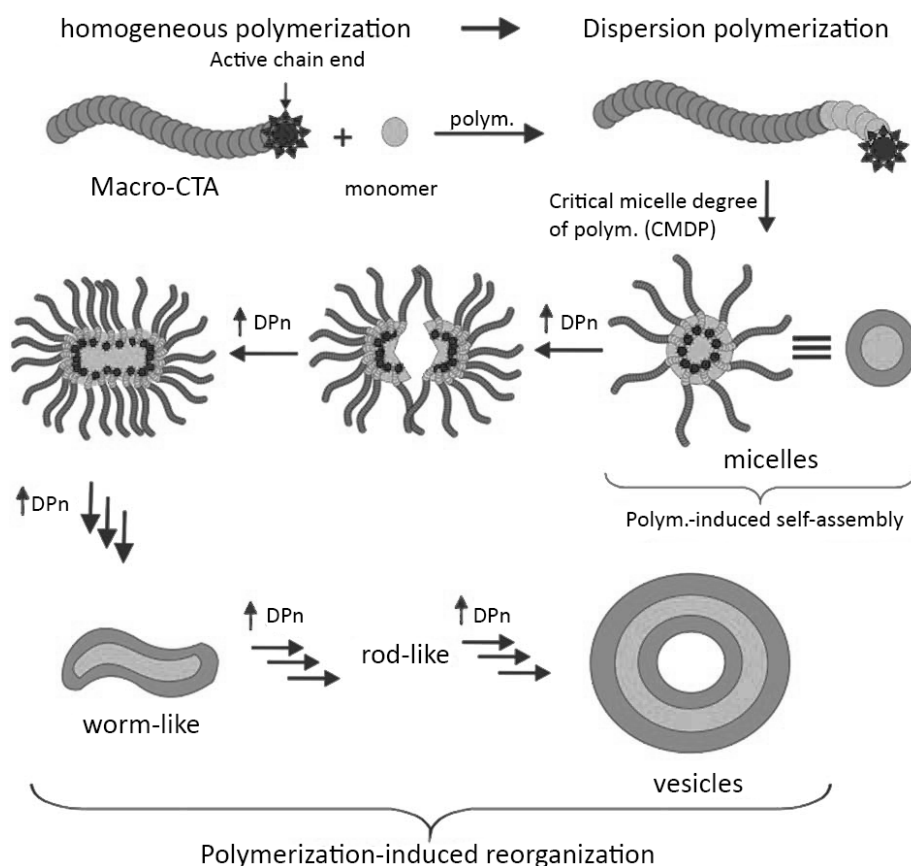


Figure 1.6: Schematic overview of polymerization-induced self-assembly. Adapted from Karagoz *et al.* [108] with permission from The Royal Society of Chemistry.

## Hyperbranched and star polymers

Dendrimers were developed in the 1980s and have become prominent synthetic macromolecules in the field of biomedical sciences. [109] They are a class of macromolecules with a highly branched three-dimensional architecture whose structural elements can be changed to affect both surface and internal properties of the macromolecule and are virtually monodisperse. [110] However, dendrimers require an intricate stepwise synthetic scheme that limits their broad range of applications. [111] This resulted in the development of hyperbranched and star polymers that have architectural similarities to dendrimers. These polymeric dendrimer-like nanoparticles are more facile and versatile regarding the synthesis of complex architectures with controlled dimensions and functionalities. [111] Furthermore, although these polymers are not monodisperse, controlled/living radical polymerization can excellently limit dispersity. [112, 113]

Hyperbranched polymers are highly branched, three-dimensional globular polymeric nanoparticles. [109] They can be facilely prepared using a one-pot polymerization of monomers and macromers, avoiding complicated synthesis and purification procedures. [113] Thanks to the large number of end-groups, hyperbranched polymers provide a platform for conjugation of functional moieties, and have an outstanding biocompatibility and biodegradability, a controlled responsive nature, and the ability to include pharmaceutical agents through covalent or noncovalent approaches. [113-115] However, hyperbranched polymers are less well-controlled and defined as star polymers, and their physicochemical behaviour is in between linear polymers and dendrimers. [111] As such, star polymers have advantages for synthesis, and a wide range of strategies have developed to synthesize functional star polymers for many applications in life sciences and nanotechnologies. [112, 116, 117]

Star polymers consist of numerous linear polymers (arms) fused at a central point (core). A diverse range of star polymers can be synthesized, including miktoarm, block copolymer, network-core, and end-functionalised star polymers. [117] Star polymers can be prepared using three different approaches: (1) core-first, (2) arm-first, and (3) grafting-onto approach. Each approach has its advantages and disadvantages, which will be discussed in the next section. [112, 118]

The core-first approach utilizes a pre-synthesized multifunctional initiator (the core) to form star polymers by divergently growing linear polymers (the arms). [119] The main advantages are the good structural control and excellent yields, as star polymers can be easily purified from the crude reaction mixture. [112, 119] However, the disadvantages are that the number of arms is limited and it has a very small core domain. [112] Although functionalised hyperbranched polymers [120] and dendrimers

[121] have been used as scaffolds to circumvent this problem. Moreover, it is difficult to synthesize miktoarms or to directly determine the molecular weight of each arm. [112]

In the arm-first approach, linear polymers are first synthesized and then stars are formed by cross-linking via a polymerization or coupling reaction in a convergent fashion. [112, 116, 122] These star polymers are better known as core-cross-linked star polymers or star nanogels. [116] The advantages of the arm-first approach are that the arm polymers can be synthesized and characterized in advance, resulting in a higher level of control over the arm polymerization. Furthermore, high molecular weight star polymers can be prepared with a high number of arms. [112, 123] In addition, this approach leads to large core domains that provide a high capacity for the storage of functional compounds via covalent attachments and/or supramolecular interactions. [116, 118] Another attractive feature is that miktoarms can be formed in which different linear arm polymers are simultaneously included. [124] The disadvantages are a broader number of arms distribution, [112] and the arm-first approach often results in a low yield due to incomplete arm-incorporation, requiring a rigorous purification process. [116] The low arm-to-star conversion is caused by disproportionation and bimolecular termination of the propagating (macro)radicals, leading to the formation of “dead” chains, which are responsible for the low arm conversion. [125]

Finally, star polymers can also be synthesized using the grafting-onto approach. [118, 126] This method provides the highest level of structural control as the core and arm of the stars can be synthesized and characterized independently before formation. [112, 127] Moreover, similar to core-cross-linked stars, the grafting-onto approach offers a straightforward method to produce miktoarm star polymers using different types of arm polymers with identical complementary chain ends. [128] However, the grafting-onto approach is usually limited to stars with a low arm number (typically 4–8) and small core size due to the limitations of available compounds in both functionality and dimensions. [112, 118] In addition, the synthesis of stars with a high number of arms and high molecular weight arms is also increasingly difficult due to steric congestion around the core, which results in lower coupling efficiencies. [112]

#### Star polymers for gene and drug delivery

The versatility of star polymers has been exploited for applications in both gene therapy and drug delivery. [112, 116] Gene therapy depends on the delivery of appropriate genetic materials, such as plasmid DNA, short-interfering RNA (siRNA), small hairpin RNA (shRNA), and microRNA, into cells. [129] However, these materials are often negatively charged and hydrophilic, limiting cell uptake. Furthermore, as these nucleic acids can be easily degraded by enzymes before delivery to the nucleus,

encapsulation is required. [129, 130] Therefore, positive charged star polymers have been developed for gene delivery. For example, dimethylaminoethyl methacrylate (DMAEMA) containing core-cross-linked stars (synthesized by RAFT) were able to self-assemble with siRNA and the stars were able to silence target gene expression by 50 % in an *in vivo* tumour setting. [131] In addition, miktostars were developed containing different lengths of cationic poly(DMAEMA) side-arms and varied amounts of poly [oligo(ethylene glycol) methyl ether methacrylate] (POEGMA arms) that showed high accumulation of siRNA to orthotopic pancreatic tumours in mice and silenced  $\beta$ III-tubulin expression by 80 % at the gene and protein levels in pancreatic tumours. [132] Furthermore, star polymers composed of polyhedral oligomeric silsesquioxane or  $\beta$ -cyclodextran cores and polycation arms were prepared by Xu and co-workers with various functional groups, allowing for effective gene therapeutics. [133]

Core-cross-linked star polymers have also been utilized as unimolecular drug delivery vehicles due to their high drug loading capacity and absence of dissociation as is prevalent for micelles upon physiological changes. [83, 112] Drugs can be incorporated by physical encapsulation or chemical conjugation, for example Xu *et al.* developed core-first stars with  $\beta$ -cyclodextran as the initiating core, and the anticarcinogen doxorubicin was loaded into the hydrophobic domain of the unimolecular amphiphilic micelles. The star polymers demonstrated an efficient cell uptake by tumour tissues and exhibited pH-triggered sustained drug. [134] Moreover, Qiao and co-workers prepared a series of core-cross-linked stars where arm-incorporated poly(caprolactone) was utilized as the hydrophobic domain for the encapsulation of pirarubicin and doxorubicin, while PEG was used as the hydrophilic shell. [135] The advantage of this method for core-cross-linked stars is a higher drug loading capacity as the core drug loading capacity is limited due to extensive cross-linking. [112]

Next to via hydrophobic and ionic interactions, drugs can also be incorporated into star polymers via covalent conjugation. For example, Liu *et al.* loaded doxorubicin into the core of core-cross-linked star polymers using pH-sensitive imine (Schiff-base) bonds, resulting in release in slightly acidic conditions. [136] In addition, Sumerlin and co-workers employed poly(*N*-(2-hydroxypropyl)methacryl amide) (PHPMA), a biocompatible and non-immunogenic polymer to form core-cross-linked HPMA star polymers. An HPMA-modified anticancer drug, methotrexate, was introduced by copolymerization during the crosslinking reaction of PHPMA arms, and drug release was induced by esterase. [137] Moreover, active targeting can also be introduced on star polymers. For example, Entezami and co-workers designed folate-decorated thermo-responsive star-shaped amphiphilic block copolymer micelles for targeted cancer therapy with a temperature-regulated release profile of the hydrophobic anticarcinogen paclitaxel. [138]

## 1.2 Nanoparticles for diagnostics

The second part of this chapter will discuss the application of nanoparticles for diagnostics. First, the main advantages for the use of nanoparticles as diagnostic agent will be discussed, followed by a short overview of the current clinically-approved nanoparticulate imaging agents. Next the key clinically used imaging technologies will be introduced and for each modality it will be deliberated in depth how nanoparticles can contribute to improved diagnostics.

In the last decades, a wide range of nanoparticles have been employed as imaging agent to improve diagnostics as they possess unique advantages over many small-molecule imaging probes. [14, 139] The large surface to volume ratio of nanoparticles enables the introduction of multiple functional groups onto the surface for labelling with imaging agents, increasing the local concentration and signal-to-noise ratio. [140] Secondly, modification of the size, shape and surface of nanoparticles results in enhanced blood circulation times, and increased tumour uptake via the enhanced permeability and retention effect. [31] Furthermore, targeting agents, such as antibodies, aptamers or peptides can be incorporated to enable active targeting of specific physiological processes or disease markers to enable early diagnosis and patient-specific treatment. [141]

Several nanoparticulate imaging agents have been approved by regulatory authorities in the USA (FDA) and Europe (EMA). [13, 14, 17] For example, Feridex I.V., a dextran-coated superparamagnetic iron oxide (size 120 – 180 nm) has been approved for magnetic resonance imaging of liver lesions [14] and SonoVue, a phospholipid stabilized microbubble, has been approved for ultrasound. [142] Although the latter can also be described as a microparticle due to its size. The current approved micro/ nanoparticles for imaging are listed in Table 1.2.

In addition, various diagnostic nanoparticles are currently in clinical trials. For example, cornell dots, silica-organic hybrid nanoparticles (7 nm) that consist of near-infrared fluorophores, a polyethylene glycol coating and a  $^{124}\text{I}$ -radiolabelled cRGDY targeting peptide were investigated for the imaging of melanoma and malignant brain tumours. [143] The translation of imaging agents into the clinic has been much slower than was initially anticipated. The reasons for this include regulatory hurdles, market forces, lower profit margins for imaging than for therapeutic drugs, and the lack of reimbursement strategies for newer imaging agents. [144, 145] However, extensive pre-clinical research is being carried out to overcome these hurdles, which is exemplified by the vast array of peer-reviewed publications regarding nanoparticles for imaging applications. [139, 146]

Table 1.2: Clinically approved intravenous micro/nanoparticles for diagnostics, adapted from Anselmo and Mitragotri. [14]

Name	Particle type	Approved application/indication	Approval (year)
Feridex I.V. / Endorem	Iron oxide dextran colloid	MR imaging of liver lesions	FDA (1996)
Ferumoxtran-10 / Combidex / Sinerem	Iron oxide dextran-coated	MR imaging lymph node metastases	Only available in Holland
GastroMARK / Lumirem	Iron oxide siloxane	MR imaging of bowel	FDA (1996)
Resovist / Clivast	Iron carboxydextran colloid	MR imaging of liver lesions	Some of Europe Discontinued (2009)
Definity	Perflutren lipid microspheres	Ultrasound contrast agent	FDA (2001)
Optison	Human serum albumin stabilized perflutren microspheres	Ultrasound contrast agent	FDA (1997) EMA (1998)
SonoVue	Phospholipid stabilized microbubbles	Ultrasound contrast agent	EMA (2001)

Currently, multiple imaging modalities are used for diagnostics in the clinical practice and in pre-clinical research. The main imaging technologies are magnetic resonance imaging (MRI), X-ray computed tomography (CT), positron emission tomography (PET), single-photon emission computed tomography (SPECT), ultrasound (US) and fluorescence. [147] Each modality has its advantages and limitations as can be seen in Table 1.3. In this sub-chapter, each imaging technology will be briefly described, including its pros and cons, the use of modality-specific imaging probes, and the progress in the development of nanoparticle-based imaging agents with a special focus on polymer-based nanoparticles.

Table 1.3 Overview of imaging systems in clinic.

Technique	Resolution <sup>a</sup>	Depth	Time <sup>b</sup>	Examples imaging agents	Sensitivity (M) <sup>c</sup>	Target	Cost <sup>a,d</sup>
MRI	10–100 µm	No limit	Minutes to hours	Paramagnetic chelates, magnetic particles	10 <sup>-6</sup> to 10 <sup>-9</sup>	Anatomical, physiological, molecular	\$\$\$
CT	50 µm	No limit	Minutes	Iodinated molecules	10 <sup>-6</sup>	Anatomical, physiological	\$\$
Ultrasound	50 µm	cm	Seconds to minutes	Microbubbles	10 <sup>-8</sup>	Anatomical, physiological	\$\$
PET	4–6 mm	No limit	Minutes to hours	<sup>18</sup> F-, <sup>64</sup> Cu labelled compounds	10 <sup>-15</sup>	Physiological, molecular	\$\$\$
SPECT	8–12 mm	No limit	Minutes to hours	<sup>99m</sup> Tc- or <sup>111</sup> In-labelled compounds	10 <sup>-14</sup>	Physiological, molecular	\$\$
Fluorescence reflectance imaging	2–3 mm	< 1 cm	Seconds to minutes	Photoproteins, fluorochromes	10 <sup>-12</sup>	Physiological, molecular	\$

<sup>a</sup> For high-resolution, small-animal imaging systems (clinical imaging systems differ). <sup>b</sup> Time for image acquisition. <sup>c</sup> Moles of label detected.

<sup>d</sup> Cost is based on purchase price of imaging systems in the United States: \$, < US\$100,000; \$\$, US\$100,000–300,000; \$\$\$, > US\$300,000 as per 2008. Figure was adapted from Weissleder and Pittet [147] with additional sensitivity data from Lee *et al.* [148] and Janib *et al.* [149]

### 1.2.1 Magnetic resonance imaging

Nuclear magnetic resonance imaging (MRI) is a high resolution, non-invasive imaging technique that relies on the fundamentals of nuclear magnetic resonance. [150-152] MRI has the ability to obtain both anatomical and functional information, such as perfusion and flow, provides a great contrast between different soft tissues and has no radiation harm. [153, 154] As a consequence more than 60 million diagnostic MRI scans are carried out every year [155] and MRI is widely used in neurological, musculoskeletal, cardiovascular, and oncological imaging. [156]

Magnetic resonance imaging (MRI) is based on the interaction between an applied magnetic field and a nucleus with a nuclear magnetic moment or spin. [157] Several nuclei, including  $^1\text{H}$ ,  $^{13}\text{C}$ ,  $^{15}\text{N}$ ,  $^{19}\text{F}$ , and  $^{31}\text{P}$  have nuclear moments with a spin of  $\frac{1}{2}$ . Protons ( $^1\text{H}$ ) are the most studied as they are the most abundant nuclei in living organisms (63 %) and  $^1\text{H}$  has the highest natural abundance of all isotopes of hydrogen (99.985 %), while for example  $^{13}\text{C}$  has only a natural abundance of 1.11 %. [151]

When a group of spins are placed in an external magnetic field ( $B_0$ , 1.5 or 3.0 T for most clinical scanners [158]), each spin aligns along the field, distributed over a low energy state (parallel) and a high energy state (anti-parallel). [150] At room temperature, the number of spins at low energy state slightly outnumbers spins at a high energy state, resulting in a net magnetization rotating around  $B_0$  with the Larmor frequency (related to the energy difference between the spin states). [151]

A second time-dependent magnetic field ( $B_1$ ) is then applied using a radiofrequency (RF) pulse at the Larmor frequency. The magnetization vector will rotate away from  $B_0$  towards the transverse plane. After the RF pulse is turned off, the net magnetization vector will start to return back to its equilibrium state as a result of a process called relaxation. The recovery process along the longitudinal axis is called  $T_1$  relaxation, spin-lattice relaxation or longitudinal relaxation. [151] Whereas the dephasing process in the transverse plane, as each spin experiences a slightly different magnetic field, is referred to as  $T_2$  relaxation, or spin-spin relaxation (see Figure 1.7). [159] The decaying signal, called free induction decay (FID), is detected by a radiofrequency coil placed in the transverse field and is converted to the time-domain by Fourier transformation. [150, 151]

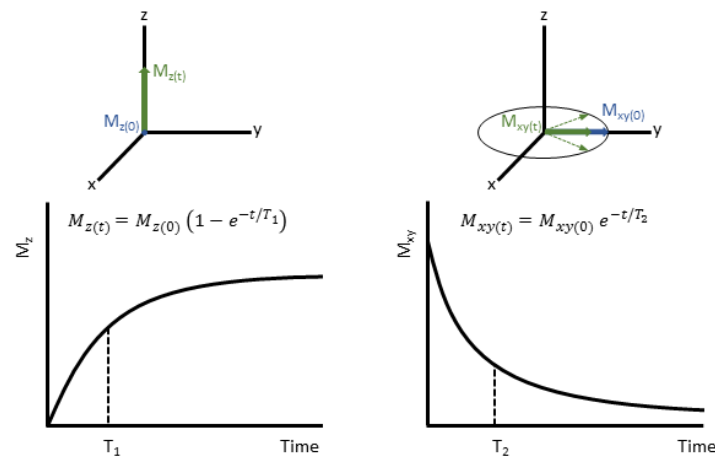


Figure 1.7: Longitudinal ( $T_1$ ) and transverse ( $T_2$ ) relaxation processes.

As  $T_1$  and  $T_2$  relaxation are dependent on the local environment of the spins and field strength, different tissues give a different contrast. [151] For example at 1.5 T,  $T_1$  values are 1500 - 2000 ms for fluids, 400-1200 ms for water based tissues and 100-150 ms for fat based tissues, while  $T_2$  values at 1.5 T are in seconds for fluids, 40-200 ms for water based tissues, 10-100 ms for fat based tissues and a few milliseconds for fluids. [160]

However, as the  $B_0$  field is homogenous, the entire body would only give a single signal. Spatial information is obtained by applying gradients parallel to  $B_0$  to give each spin a different magnetic field strength and an identifiable resonance frequency. [151, 161] The gradient has three components: the slice selection ( $G_z$ ) gradient is used to excite only the spins in the desired cross-section gradient; the frequency-encoding ( $G_x$ ) assigns a different frequency along the x-axis, and the frequency-encoding ( $G_y$ ) applies a specific phase angle to the transverse phase angle. [152] A variety of pulse sequences are used to create MRI scans, such as a spin echo for  $T_2$ -weighted MRI, in which first a  $90^\circ$  pulse is applied, followed by a  $180^\circ$  pulse to partially rephase the magnetization and produce a signal called an echo; or an inversion recovery for  $T_1$ -weighted MRI, in which a  $180^\circ$  pulse is first applied followed by a  $90^\circ$  pulse to measure the  $T_1$  relaxation. A more in-depth description of MRI pulse sequences is out of scope for this chapter, and the reader is referred to the literature. [161]

### *MRI contrast agents*

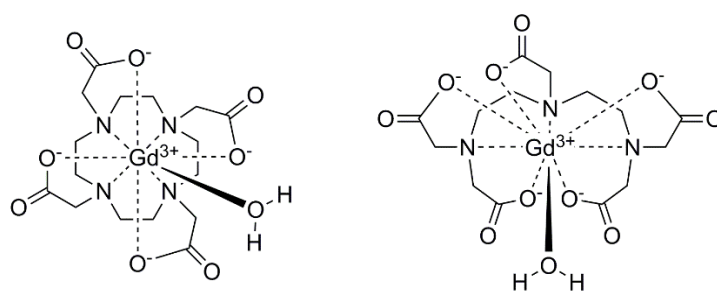
The overriding challenge with MRI is its relatively low sensitivity [162-164] and contrast agents are used to enhance image contrast between normal and diseased tissues, and to indicate the status of organ function or blood flow. [165] Currently, nearly half of all MRI studies are contrast enhanced. [156] Unlike nuclear medicine or CT, where image brightness is determined by the concentration of

radiotracer (for example iodine), MRI relies on water proton relaxation and contrast is enhanced by the use of a so-called contrast agent, that is present in small concentrations relative to the protons that it catalytically influences. [153]

The two main categories of MRI contrast agents are positive contrast agents, which shorten  $T_1$ -relaxation (and thus increase brightness), and negative contrast agents, which shorten  $T_2$ -relaxation (and thus reduce brightness). [156] In addition, there are also contrast agents that use different mechanisms such as chemical-exchange saturation transfer (CEST) [166], using nitric oxide [167] or  $^{19}\text{F}$  [168], and hyperpolarized probes for contrast. [169]

### Positive contrast agents

Positive contrast agents are predominantly based on gadolinium and manganese. [153] The gadolinium ion ( $\text{Gd}^{3+}$ ) couples a large magnetic moment with a long electron spin relaxation time, ensuring an optimum efficiency for nuclear spin relaxation of the interacting nuclei. [170] Due to its toxicity, chelating ligands are used. [162] Currently, only gadolinium-based MRI contrast agents are being used in the clinical practice, such as Gd-DTPA (Magnevist), Gd-DOTA (Gadovist) and Gd-HPDO3A (Gadobutrol) (see Scheme 1.5); [DTPA, diethylenetriaminepentaacetic acid; DOTA, 1,4,7,10-tetraazacyclododecane-1,4,7,10-tetraacetic acid HPDO3A, 10-(2-hydroxypropyl)-1,4,7-tetraazacyclododecane-1,4,7-triacetic acid]. [169]



Scheme 1.5: Examples of clinically used positive MRI contrast agents: Gd-DTPA, a linear chelate, and Gd-DOTA, a cyclic chelate with a higher stability. [155]

However, for applications in molecular MRI, i.e. the detection of molecular and cellular processes *in vivo* (e.g. tumour cell surface receptors), the low intrinsic sensitivity of MRI contrast agents still represents a significant challenge. [164] Therefore, amplification strategies are desired to facilitate the use of Gd-based contrast agents in molecular MRI. [162, 164] Nanoparticles offer a straightforward method of amplification, as large amounts of Gd-chelates can be incorporated, and there is an increased circulation time compared to rapidly renal cleared small-molecule gadolinium-chelates.

[153] For instance, approximately 34,000 Gd-chelates can be incorporated into the lipid bilayer of 100 nm liposomes with enhanced blood circulation times. [16]

Next to this, a lot of research has also been directed to optimize the design of Gd-complexes to maximize contrast enhancement. [163] The efficiency of an MR imaging agent to enhance contrast is expressed as relaxivity ( $r_{1,2}$ )

$$r_{1,2} = \frac{R_{1,2} - R_{1,2(0)}}{[Gd]} \quad (1.2)$$

In the equation,  $R_{1,2}$  is the relaxation rate (in  $s^{-1}$ ) presence of the contrast agent, and  $R_{1,2(0)}$  in absence (e.g. physiological medium only).

According to the Solomon-Bloembergen-Morgan theory,  $T_1$  contrast enhancement is the result of a complex interplay of several structural and dynamic parameters of the gadolinium complex, among which the more relevant factors are the number of coordinated water molecules to the metal ( $q$ ), their residence lifetime at the metal site ( $\tau_M$ ), and the rotational correlation ( $\tau_R$ ) (see Figure 1.8). [162]

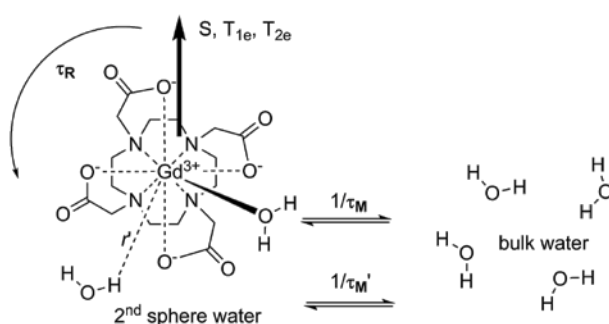


Figure 1.8: Factors influencing solvent water relaxation, adapted from Caravan *et al.* [162] with permission from Royal Society of Chemistry. The metal complex has an inner sphere of nitrogen and oxygen atoms from the DOTA ligand and a coordinated water molecule. There is also a distinct second hydration sphere with Gd–H distance  $r$ , and water molecules from both spheres undergo exchange with bulk water at rates  $1/\tau_M$  and  $1/\tau_M'$  for first- and second-sphere exchange.

The rotational dynamics is the limiting factor at clinical field strength (1.5 T). Small Gd-chelates have a short rotational correlation rate that is suboptimal [163], however the rotation can be slowed down by conjugation to a protein or nanoparticle, which significantly increases the  $T_1$  relaxivity. [171] For example, Gd-DOTA has a  $T_1$  relaxivity of  $5 \text{ mM}^{-1}\text{s}^{-1}$  (at 0.47 T), however when conjugated to a linear

dextran polymer an  $r_1$  of  $10.6 \text{ mM}^{-1}\text{s}^{-1}$  was observed, and when conjugating to a dendrimer an even higher  $r_1$  of  $16.5 \text{ mM}^{-1}\text{s}^{-1}$  [172] was measured as it imposes a more isotropic rotational dynamic. [162]

A wide range of nanoparticles have been functionalized with gadolinium, such as dendrimers, lipid-based nanoparticles (like micelles, emulsions and liposomes), polymeric nanoparticles, and inorganic nanoparticles such as silica, gold or quantum dots. [153, 154, 162, 165, 173] Furthermore, gadolinium has been incorporated into inorganic nanoparticles, such as  $\text{Gd}_2\text{O}_3$  [174] and the more acid-stable  $\text{NaGdF}_4$ . [175] Some polymer-based nanoparticles are presented here as an example, but the reader is pointed to, extensive reviews by Tang *et al.* [165] and Bryson *et al.* [153] for more information.

As example, Gd-DOTA chelates were conjugated to linear, hyperbranched and core-cross-linked star polymers synthesized by RAFT polymerization (see Figure 1.9). [176] Conjugation to the polymers showed a substantially increased relaxivity in comparison to existing commercial Gd-contrast agents. In a follow-up study, the location of the chelate in the star architecture was investigated by conjugating the chelate to the surface, arm polymer or core. [177] Surface incorporation resulted in the highest relaxivity per gadolinium due to a slower rotational dynamics, however arm incorporation resulted in the highest relaxivity per star due to the accessibility of more conjugation groups. Interestingly, the relaxation benefit of macromolecules was partially lost at very high magnetic field (9.4 T) as different rotational dynamics are then required. [163]

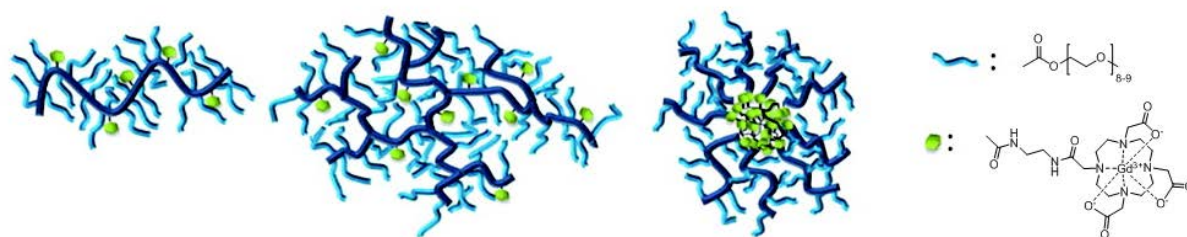


Figure 1.9: (A) linear, (B) hyperbranched, and (C) star polymers were covalently labelled with Gd-chelate. Reprinted with permission from Li *et al.* [176] Copyright 2016 American Chemistry Society.

### Negative contrast agents

Superparamagnetic iron oxide nanoparticles (IONP), consisting of maghemite ( $\text{Fe}_2\text{O}_3$ ) or magnetite ( $\text{Fe}_3\text{O}_4$ ), are the predominant negative contrast agents. [169, 178, 179] Under an external magnetic field, IONPs generate a local perturbing dipolar field in their surroundings. This results in an increased magnetic field fluctuation (inhomogeneity) that accelerates the dephasing rate of surrounding water

molecules (reducing  $T_2$  relaxation), and leads to darkening of the corresponding  $T_2$ -weighted magnetic resonance image [178] in comparison with an image without contrast agent. [180]

Several IONP-based  $T_2$  contrast agents have been approved for clinical use, such as GastroMARK for bowel imaging, Feridex I.V. and Resovist for detection of liver lesions, and Combidex for lymph node metastases imaging (see Table 1.2). [179, 180] To improve the colloidal stability in physiological media, IONPs have been coated with hydrophilic, biocompatible and anti-fouling materials such as polyethylene glycol and dextran to avoid aggregation and extend blood circulation times. [179]

A lot of research has focused on further improving the crystallinity and thus saturation magnetisation, size, and coating. [178, 179] Polymers have attracted a lot of attention as coating due to their versatility in improving hydrophilicity, anti-fouling, size, charge and to introduce targeting groups or drugs. [181] For example, Basuki *et al.* used Cu(0)-mediated living radical polymerization to investigate the effect of grafting methods (grafting from and to) on colloidal stability and  $T_2$  relaxivity, demonstrating that the grafting from method resulted in more stable IONPs due to a higher grafting density, even at lower molecular weight. [182] Furthermore, Basuki *et al.* reported PEG-glycopolymers grafted on IONPs with an enhanced uptake of mannose-functional IONPs in a lung cancer cell line (A549). [183]

#### Fluorine-19

$^{19}\text{F}$  MRI contrast agents have also received a lot of attention in the last decades. [184, 185]  $^{19}\text{F}$  nuclei have similar MRI properties to  $^1\text{H}$ , including a spin of  $\frac{1}{2}$  and 100 % natural isotopic abundance. The most attractive feature of  $^{19}\text{F}$  is its physiological rarity. This limits undesirable background noise in imaging as the concentration of endogenous  $^{19}\text{F}$  nuclei in body is negligible (usually less than  $10^{-3}$   $\mu\text{mol/g}$  wet tissue weight) and barely detectable by  $^{19}\text{F}$  MRI. [184]

$^{19}\text{F}$  MRI contrast agent can be categorised as  $^{19}\text{F}$  salts,  $^{19}\text{F}$ -containing small molecules, perfluorocarbon (PFC) emulsions and  $^{19}\text{F}$ -containing macromolecules. [186] Polymer-based  $^{19}\text{F}$  contrast agents have considerable advantages, such as tailored architectures and functionalities, long circulation times, and the capability to carry functional sites for incorporating multimodal imaging modalities, targeting moieties and therapeutic agents. [186] Therefore numerous polymeric nanoparticles, such as linear polymers, dendritic polymers, hyperbranched polymers and hydrogels have been reported in literature. [184, 186]

## CEST

Chemical exchange saturation transfer (CEST) imaging is a relatively new magnetic resonance imaging contrast approach. Exogenous or endogenous compounds containing either exchangeable protons or exchangeable molecules are selectively saturated in this method, and after transfer of this saturation detected indirectly through the water signal with enhanced sensitivity. [166]

The advantage of CEST over (super)paramagnetic contrast agents is the absence of potential toxic compounds like gadolinium. [187] Both endogenous compounds like urea [188] and exogenous compounds can be visualized. [166, 189, 190] For example, Bulte and co-workers synthesized diamagnetic CEST agents with altering amino acid sequences (lysine, arginine, threonine, and serine) that could be distinguished in an MRI phantom based on their different chemical shifts. [191] Polymers have been used in paraCEST and for example Eu-containing polymers were successfully developed. [192] Furthermore, Zhang *et al.* demonstrated that ionisable polymeric micelles can be used as pH-responsive CEST probe. Their design is unique in that CEST is essentially “off” at normal physiological pH and only switched “on” in an acidic environment. [193]

## Hyperpolarised probes

This category of MRI contrast agents is the most sensitive one, as polarisation techniques dramatically increase (up to five orders of magnitude) the population difference between the spin energy levels. [194] A disadvantage is the decay of the signal that is generated by the hyperpolarised probes, requiring fast injection and rapid accumulation at the target site. [169] Hyperpolarized gases (e.g.,  $^3\text{He}$  and  $^{129}\text{Xe}$ ) are clinically used for imaging the respiratory system [194], and a  $^{13}\text{C}$  hyperpolarized compound ( $^{13}\text{C}$  pyruvate) has been investigated in a phase 1 clinical trial as a metabolic agent for prostate cancer diagnosis. [195] Furthermore, hyperpolarised  $^{129}\text{Xe}$  has also been conjugated to dendrimers using cryptophane-A-cages [196], potentially opening up avenues for polymers too.

### 1.2.2 X-ray computed tomography

X-ray-computed tomography (CT) is a non-invasive clinical diagnostic tool that allows for 3D visual reconstruction and segmentation of tissues of interest. [197] High-resolution CT systems can be employed to carry out non-destructive 3D imaging of a variety of tissue types and organ systems, such as the gastrointestinal tract, cardiovascular system, renal tract, liver, lungs, bone, cartilage, tumorous tissue, etc. [198] Due to its relatively low cost, fastness, and high hospital availability, it is one of the most prevalent diagnostic tools. [199]

The technique is based on the variable absorption of x-rays by different tissues (expressed in Hounsfield units). X-rays were discovered by W.C. Roentgen in 1895 and named such for the sake of brevity. [200] They are a form of electromagnetic radiation with wavelengths between 0.01 and 10 nm. Conventionally, X-rays are generated by a vacuum tube using high voltage to accelerate electrons from a cathode to a tungsten. A CT image is obtained by rotating an X-ray source around an object with a detector positioned directly opposite the radiation source, creating an image by tomographic reconstruction. [198] An in-depth description is beyond the scope of this chapter, but can be found in published work. [201, 202]

#### *CT contrast agents*

Most human tissues are easily visualised by CT. However, it can be challenging to identify the interface between two tissues (e.g. tumour and liver) due to small differences in attenuation. [198] Contrast agents are able to increase the differences in tissue attenuation and improve the quality of images (higher signal-to-noise), leading to a more accurate diagnosis. [203] Currently, barium sulphate suspensions and water-soluble aromatic iodinated compounds are used as CT contrast agents. [204] However, the use of barium sulphate is restricted only to the gastrointestinal tract due to the inherent toxicity of  $\text{Ba}^{2+}$  ions. [203]

#### *Iodine*

Iodine has been historically the atom of choice for CT imaging as materials with a high atomic number (iodine  $Z = 53$ ) better absorb X-rays. [205] It is usually incorporated in low molecular weight aromatics and several have been approved for medical application, for example iohexal (Omnipaque, GE Healthcare), iopromide (Ultravist, Bayer Healthcare), and iopamidol (Isovue, Bracco Imaging). [198]

However due to their relatively small size, they tend to undergo rapid renal clearance from the body and exhibit nonspecific biodistribution. [203] This resulted in the development of nanoparticulate

iodine-containing contrast agents including nanosuspensions, nanoemulsions, microspheres, liposomes, micelles, polymeric particles, nanospheres, and nanocapsules (see Figure 1.10). [198] For example, polymer-based (2-methacryloyl oxyethyl-2,3,5-triodobenzoate-glycidylmethacrylate) nanoparticles that were synthesized by emulsion polymerization showed prolonged blood-pool residence time, followed by significant uptake by macrophages and allow for enhanced liver, spleen, and lymph node imaging in rat and mice models. [205] Furthermore, polymeric micelles were synthesized using an aliphatic 2,3,5-triodobenzoyl-substituted poly-L-lysine/mPEG copolymer and were reported as an excellent stealth blood-pool CT agent. [206]

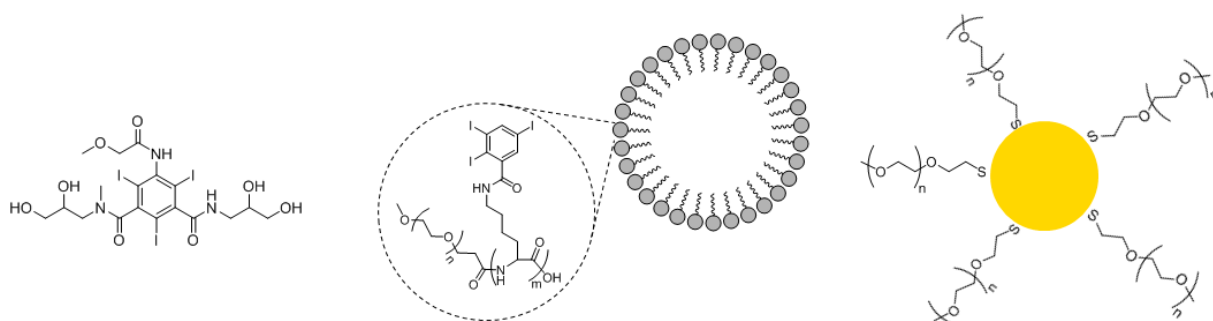


Figure 1.10: Examples of X-ray CT contrast agents. (A) Iopromide, a commercially available CT contrast agent; (B) an iodine containing polymeric nanoparticle (adapted with permission from Lusic *et al.* [198] Copyright 2013 American Chemical Society); and (C) polyethylene glycol coated gold nanoparticles (based on Kim *et al.* [207]).

## Lanthanides

Next to iodine, also lanthanide atoms such as gadolinium ( $Z = 64$ ), dysprosium ( $Z = 66$ ) and ytterbium ( $Z = 70$ ) have been investigated as CT contrast agent. These atoms have a higher atomic number and  $k$  absorption edge values leading to a higher X-ray attenuation and thus higher CT sensitivity on a per mole basis. [203] For example, clinically approved gadolinium-based MRI contrast agents have been successfully used for CT imaging of the cardiovascular system and for pulmonary/aortic angiography [208]. Nanoparticles have been explored too, for instance dyspropopium-DOTA-dextran [209] and rare-earth core nanoprobles (18 % ytterbium,  $\sim 25 - 28$  nm in size) with an amine-functionalized  $\text{SiO}_2$  shell and PEG coating. [210] However practically, a recent analysis comparing equal-attenuating doses of iodinated media vs gadolinium-containing media concluded that the cost of using gadolinium-based media could be up to 20-fold higher than when non-ionic iodinated media are used in a CT imaging procedure. [198]

## Gold nanoparticles

Finally, gold nanoparticles (AuNP) are of significant interest as X-ray imaging agents [211] as they have a high chemical stability, long circulation times, and a higher X-ray attenuation due to a high atom number ( $Z=79$ ) and absorption edge ( $k=81$ ). [212] PEGylated AuNPs have demonstrated to exhibit prolonged blood circulation times and were successfully used in rodents to image the cardiovascular system. [207] In addition, many targeted gold nanoparticles have also been investigated. [198] For example anti-Her2-antibody-labeled 15 nm AuNP demonstrated the potential of specifically targeting human breast cancer BT-474 cells. On the basis of CT attenuation, the anti-Her2-AuNPs showed 1.6 times higher accumulation in BT-474 than in MCF7 tumour types *in vivo*. [213]

### 1.2.3 Nuclear medicine: SPECT

Nuclear medicine is the branch of medicine that deals with the use of radioactive substances in research, diagnosis and treatment. [214] The most common imaging modalities in nuclear medicine are single-photon emission computed tomography (SPECT) and positron emission tomography (PET). [214] Nuclear medicine provides practically unlimited depth resolution and has a very high sensitivity. [215]

SPECT is similar to conventional nuclear medicine planar imaging using a gamma camera, but uses different angles that measure the gamma radiation using parallel-hole collimators and then transform it into a 3D data set using a tomographic reconstruction algorithm similar to X-ray CT. [215] However, where CT works with an external X-ray source, SPECT uses single-photon emitting radionuclides within the body. It has a high sensitivity, but provides no anatomical background and has a low resolution (8 - 12 mm). [214] Consequentially dual SPECT/CT scanners have emerged which have significantly improved scintigraphic localisation and characterisation of disease. [216]

#### *SPECT radiotracers*

SPECT imaging uses gamma-emitting radionuclides with energies in the range of 30 to 300 keV. [215] Technetium-99 m ( $^{99m}\text{Tc}$ ) is the most commonly used radionuclide thanks to its favourable physical properties (see Table 1.4) for diagnostic imaging. [217] Furthermore, it is widely available as a column eluate from commercially  $^{99}\text{Mo}/^{99m}\text{Tc}$  generators, which can be conveniently located in small hot laboratories in nuclear medicine clinics. [217] Next to  $^{99m}\text{Tc}$ , other commonly used gamma-emitting radionuclides are gallium-67 ( $^{67}\text{Ga}$ ), indium-111 ( $^{111}\text{In}$ ) and iodine-123 ( $^{123}\text{I}$ ) (see Table 1.4).  $^{123}\text{I}$  can be labelled covalently, however chelates are used for the labelling of  $^{99m}\text{Tc}$ ,  $^{67}\text{Ga}$  and  $^{111}\text{In}$ . [218] Since gamma-radiotracers have their own spectra, SPECT imaging has the unique capability of imaging multiple probes labelled with different isotopes allowing the simultaneous study of multiple cellular or molecular events. [217]

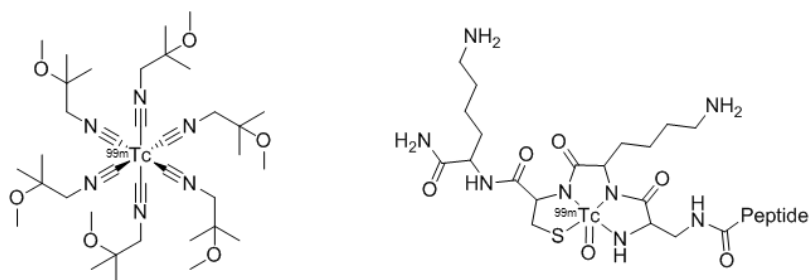
Table 1.4: Common gamma-emitting radionuclides for SPECT studies. [217]

Radio isotope	Half-life	$\gamma$ -energy (keV)
$^{99m}\text{Tc}$	6.02 h	141 (89 %)
$^{67}\text{Ga}$	78.2 h	93 (39 %), 185 (21%), 300 (17 %), 394 (5 %)
$^{111}\text{In}$	67.2 h	171 (91 %), 245 (94 %)
$^{123}\text{I}$	13.3 h	159 (83 %)

A broad array of SPECT isotope labelled molecules and tracers are available. [219, 220] Ranging from small molecules such as  $^{99\text{m}}\text{Tc}$  sestamibi to image the myocardium [221] or iobenguane to localise tumours such as pheochromocytomas and neuroblastomas [222]; to larger macromolecules such as radiolabelled peptides and antibodies. [220] For example, radio-labelled peptide  $^{99\text{m}}\text{Tc}$ -depreotide is used to detect somatostatin receptors-bearing pulmonary masses in patients proven or suspected to have pulmonary lesions by CT and/or chest X-ray (see Scheme 1.6). [223] Furthermore,  $^{111}\text{In}$ -satumomab pendetide contains the murine monoclonal antibody MAbB72.3 that is directed to tumour-associated glycoprotein. It is labelled with  $^{111}\text{InCl}_3$  using a chelating agent (DTPA) and is employed for the detection of colorectal and ovarian cancers. [224]

### Nanoparticles for SPECT

SPECT radionuclides have also been utilized to label nanoparticles. For example, superparamagnetic iron oxide nanoparticles with a polyethylene glycol coating were labelled with  $^{99\text{m}}\text{Tc}$  for *in vivo* sentinel node mapping. [225] Moreover, polyethylene glycol-coated, core-cross-linked polymeric micelles with an EphB4-binding peptide were dually labelled with  $^{111}\text{In}$  and a near-infrared fluorescence fluorophores (cyanine 7) and *in vivo* studies showed successful visualisation of prostate cancer xenografts. [226] A final example is the conjugation of  $^{99\text{m}}\text{Tc}$ -dipicolylamine-alendronate on superparamagnetic iron oxide nanoparticles to create a dual-modality imaging probe. [227]



Scheme 1.6: Examples of SPECT imaging agents; (A)  $^{99\text{m}}\text{Tc}$  sestamibi, and (B)  $^{99\text{m}}\text{Tc}$ -labelled depreotide.

#### 1.2.4 Nuclear medicine: PET

Positron emission tomography (PET) scanners are used to obtain *in vivo* images of the distribution and uptake of positron emitting radioisotopes [228] as compared to photon-emitting nuclides for SPECT. A PET scanner consists of many rings of scintillation detectors which surround the object. [229] A positron emitted by the radioisotope travels for a short distance in tissues before dissipating its kinetic energy in collision with electrons, and finally combines with an electron to form a positronium, a state that lasts for a very short time ( $10^{-10}$ s). [230] The subsequent positron-electron annihilation results in the emission of two 511 keV photons in opposite directions, which are sensed by the scintillation detectors. Next, an annihilation coincidence detection method is used to establish the trajectories or lines of response, and to obtain projection images of the nuclide distribution. [214]

The distance a positron travels limits the spatial resolution of PET and depends on the positron energy, e.g. the positron of fluorine-18 has a lower positron energy, resulting in a shorter path ( $\sim 2$  mm) compared to gallium-68 (9 mm). While SPECT is only limited by technology (e.g. collimator design) [214]. However, PET has still a higher resolution than SPECT (see Table 1.3) and has a very high sensitivity (order of 100 over SPECT). [231]

##### *PET radiotracers*

Positron-emitting radiotracers typically have shorter half-lives than SPECT nuclides (see Table 1.5). For example carbon-11 has a half-life of 20 minutes and fluorine-18 110 minutes. [218] Radiotracers with low atom numbers such as  $^{11}\text{C}$  and  $^{18}\text{F}$ , and  $^{124}\text{I}$  are covalently incorporated into molecules of interest, while chelates are used for radiometals, such as macrocyclic chelates as DOTA and 1,4,7-triazacyclononane-1,4,7-triacetic acid (NOTA). [232]

##### Fluorine-18

Fludeoxyglucose ( $^{18}\text{F}$ ) (FDG) is by far the most widely used PET tracer and is the most used molecular imaging agent in oncology (90 % of PET scans). [233] [ $^{18}\text{F}$ ]FDG is a marker of metabolism in tumour cells as the uptake in tumours is reflective of increased glycolysis, which is facilitated by overexpression of glucose transporters and glycolytic enzymes in malignant cells. [231] It plays a major role in the diagnosis, evaluation and follow-up of tumours, including lymphoma, lung cancer, brain cancer, head-and-neck tumours, melanoma and breast cancer. [230] Several other fluorine-18 containing radiotracers have been developed too, such as 3-deoxy-3-fluorothymidine (FLT) and  $^{18}\text{F}$ -Fluormisonidazole (FMISO). [233] FLT is used for imaging of tumour proliferation and FMISO is a well-established probe for hypoxia. [234]

Fluorine-18 labelling of nanoparticles or polymers has also been studied, however the short half-life complicates development. [235] For example  $^{18}\text{F}$ -labelled gold-peptide conjugates have been synthesized and studied by Guerrero *et al.* [236] using an *N*-succinimidyl-4- $^{18}\text{F}$ fluorobenzoate for conjugation. Herth and co-workers labelled an HPMA-polymer using 2- $^{18}\text{F}$ fluoroethyl-1-tosylate, which was coupled to the hydroxyl group of a tyramine moiety which was previously incorporated [237] and HPMA-*b*-(lauryl methacrylate) block-copolymers were employed in a later study to study the effect of different grades of PEGylation. [238]

Table 1.5: positron emitters used for radiolabelling of polymers and nanoparticles and their decay properties. [235]

Positron Emitter	Half-life	Decay properties (%)	$\beta^{+, \text{max-energy}}$ [MeV]
$^{11}\text{C}$	20.4 min	$\beta^+$ (99.8) / EC (0.2)	0.96
$^{13}\text{N}$	10.0 min	$\beta^+$ (100)	1.19
$^{18}\text{F}$	110 min	$\beta^+$ (97.0) / EC (3.0)	0.873
$^{64}\text{Cu}$	12.7 h	$\beta^+$ (19) / $\beta^-$ (40) / EC (41)	0.656
$^{66}\text{Ga}$	9.45 h	$\beta^+$ (57) / EC (43)	4.15
$^{68}\text{Ga}$	67.7 min	$\beta^+$ (90) / EC (10)	1.90
$^{72}\text{As}$	26.0 h	$\beta^+$ (88) / EC (22)	3.33
$^{76}\text{Br}$	16.2 h	$\beta^+$ (55) / EC (45) / $\gamma$	3.94
$^{86}\text{Y}$	14.7 h	$\beta^+$ (33) / EC (66) / $\gamma$	3.14
$^{89}\text{Zr}$	3.30 days	$\beta^+$ (23) / EC (77) / $\gamma$	1.81
$^{124}\text{I}$	4.18 days	$\beta^+$ (23) / EC (77) / $\gamma$	0.901

## Copper-64

Copper-64 radiopharmaceuticals have also attracted a lot of research over the last two decades. [235, 239] For example  $^{64}\text{Cu}$ -diacetyl-2,3-*bis*(*N*-methyl-3-thiosemicarbazone) for imaging hypoxia,  $^{64}\text{Cu}$ -labeled peptides for tumour-receptor targeting, and  $^{64}\text{Cu}$ -labeled monoclonal antibodies for targeting tumour antigens. [239] Extensive research has also been carried out for  $^{64}\text{Cu}$  labelled nanoparticles and polymers. [235, 239, 240] For example, mPEG core-shell star copolymers were synthesized and labelled with  $^{64}\text{Cu}$  and the biodistribution was studied. Linear arm polymers ( $D_H$  4.6 nm) were cleared rapidly and did not accumulate, while star polymers (25 to 70 nm) circulated for many hours, eventually captured by liver and spleen. [241]

## Other PET radioisotopes

Less studies have been published regarding  $^{68}\text{Ga}$ -labelled polymers and nanoparticles. [235] The advantage of  $^{68}\text{Ga}$  is that it is a generator-produced nuclide, meaning no on-site cyclotron is required and the costs for nuclide production are much lower. [231] Examples are poly-2,3-epoxy-propylmethacrylate latex nanoparticles (average 144 nm) labelled with  $^{68}\text{Ga}$  [242] or  $^{68}\text{Ga}$ -labelled superparamagnetic iron oxide nanoparticles. [243]

Even less studies have been published regarding other radio-isotopes, despite the opportunities present. For example, iodine-124 was conjugated to tyrosine on serum albumin coated manganese-doped iron oxides (see Figure 1.11). [244]

Finally, it has to be remarked that although PET radioisotope labeled nanoparticles have several advantages, such as higher tumor accumulation due to the EPR effect, this simultaneously also results in a higher background signal as the radioisotope labeled nanoparticles will reside longer in the vascular system and organs such as the liver and spleen.

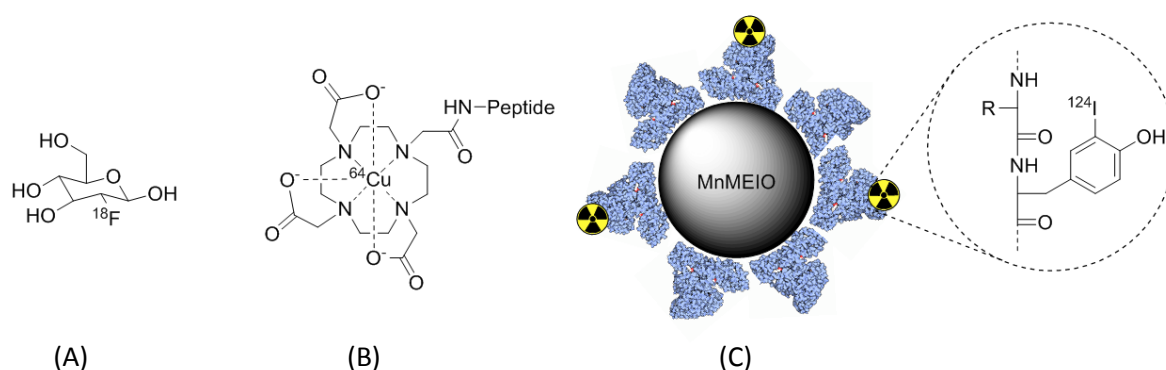


Figure 1.11: Examples of PET tracers: (A) fludeoxyglucose ( $^{18}\text{F}$ ), (B)  $^{64}\text{Cu}$ -DOTA labelled peptide and (C)  $^{124}\text{I}$ -labelled manganese-doped magnetism-engineered iron oxides (MnMEIO) [244].

### 1.2.5 Medical ultrasound

Medical ultrasound is the most widely used cross-sectional imaging modality worldwide, as it is safe, radiation free, portable, compact, real-time and cost effective. [245] Ultrasound is any acoustic energy with a frequency above human hearing ( $> 20$  kHz) and images are created by sending ultrasound pulses into tissue using a probe. Typical sonographic scanners operate in the frequency range of 2 to 18 MHz. [246] Ultrasound has many uses in medicine, such as in pregnancy, cardiovascular examination, or to visualise internal organs for potential pathologies or lesions. [247] Disadvantages of medical ultrasound include various limits on field of view, difficulty imaging structures behind bone and air, and its dependence on a skilled operator. [246]

#### *Ultrasound contrast agents*

Ultrasound contrast agents have been around since several decades [248] and several microbubble contrast agents have been clinically approved. [14] Although microbubbles are usually between 0.5 and 10  $\mu\text{m}$ , [249] they are still categorized as nanoparticles in literature. [14] Microbubbles consist of a gas core (e.g. air or perfluorocarbon) that comprises the majority of the total particle volume, and a shell that acts as a barrier between the encapsulated gas and the surrounding aqueous medium (see Figure 1.12). [248] Microbubbles oscillate and vibrate when a sonic energy field is applied and act as an echo-enhancer [250] and are used for general tissue delineation and perfusion. [251]

Sulphur hexafluoride microbubbles stabilised by phospholipids (Sonovue) are used to characterize liver lesions [142], and Optison, consisting of an albumin shell and octafluoropropane gas core is indicated for use in patients with suboptimal echocardiograms to opacify the left ventricle and to improve delineation of the left ventricular endocardial borders. Microbubbles with a polymer shell have also been developed. [249] For example, Cui *et al.* reported the preparation of poly(lactic-co-glycolic acid) microbubbles through a double-emulsion, solvent evaporation method with application in myocardial echocardiography [252]. Furthermore, Böhmer *et al.* described the fabrication of monodisperse microbubbles encapsulated with the copolymer poly(perfluorooctyl oxycaronyl)-poly(lactic acid), which were created by injecting an organic phase containing the polymer into an aqueous solution. [253]

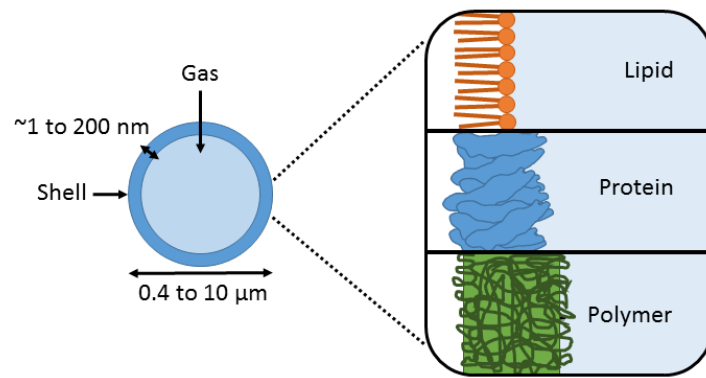


Figure 1.12: Principle of ultrasound microbubble contrast agents. The figure was inspired by Sirsi *et al.* [249] Microbubbles used for biomedical purposes are typically between 0.5 and 10  $\mu\text{m}$  diameter (the upper limit for passage through the lung capillaries). Different shell materials may be used, including lipid (~3 nm thick), protein (15–20 nm thick) and polymer (100–200 nm thick).

### 1.2.6 Fluorescence Imaging

Fluorescence imaging has been one of the most used imaging modalities in both biological sciences and medicine, and has led to the development of sophisticated microscopic, mesoscopic and macroscopic imaging systems, as well as miniaturized fibre-optic approaches, imaging probes and genetic reporter systems. [147] Fluorescence is the property of certain molecules to absorb light at one wavelength and to emit light at a longer wavelength. [144] Light in the near-infra range (NIR) range (wavelength: 650–900 nm) has multiple advantages over visible-range light, such as deeper tissue penetration due to less absorption by haemoglobin and water, and less autofluorescence from surrounding tissues (lower background). [254]

There are two types of NIR fluorescence imaging: fluorescence reflectance imaging (FRI) and tomographic fluorescence imaging (e.g., diffuse optical tomography and fluorescent molecular tomography). [144] FRI is a planar imaging method that captures emitted fluorescence through an appropriate filter after excitation, resulting in a high spatial resolution, real-time display, multichannel imaging, relatively low cost, and portability. [255] The main limitation of this method is its poor tissue penetration (< 1 cm). Therefore it is currently only used for superficial imaging or for surgical guidance, namely tumour detection (defining tumour margin and detecting tumour invisible to the naked eye), sentinel node mapping, and defining anatomy during surgical interventions. [144]

Tomographic fluorescence imaging is a three-dimensional imaging technique that requires reconstruction to create tomographic images similar to SPECT, CT and MRI. It has a higher depth sensitivity (< 10 cm) compared with FRI, however the temporal and spatial resolution is generally lower. [147] Diffuse optical tomography is currently under testing for the detection of breast cancer in clinical trials. [255]

#### *Fluorescent probes*

Several probes are being used in research for *in vivo* fluorescence-mediated cancer detection, both non-specific agents as well as targeted agents. [256] Non-specific agents accumulate in a tumour depending on its vascularity and/or impaired tumour capillary permeability. For example indocyanine green (ICG) has been approved by the FDA for the cardiac/hepatic function test and chorioretinal fluorescence angiography. [144] An example of a targeted agent is for example a fluorophore labelled monoclonal antibody that has been used to diagnose epidermal growth factor receptor expression in different tumour xenografts. [257] Nanoparticles, such as PEG-coated quantum dots, carbon nanotubes, dye-loaded nanoparticles and gold nanoparticles are also widely used. [256] For example, NIR fluorescent type II quantum dots have been investigated for sentinel lymph node mapping. [258]

### 1.2.7 Multimodal imaging

As aforementioned, each imaging modality has its advantages and disadvantages (see Table 1.6). Therefore the combined use of different modalities is becoming more common, especially to exploit the synergy between instrumentation for tomographic imaging of function (SPECT, PET) and anatomical imaging devices (CT and MRI) (see Figure 1.13). [259] Two approaches are used, either acquiring images at different times and then merging through digital image manipulation techniques or simultaneously acquiring images that are merged automatically. The asynchronous post-processing solution has several limitations, predominantly due to the different positioning of the patient in the two scans acquired at different times in separated instruments. [259, 260] Therefore the best solution to achieve consistency in time and space is carried out by synchronous acquisition of images. [260]

Table 1.6: Summary of advantages and disadvantages of the different imaging modalities. [148, 149]

Technique	Advantages	Disadvantages
MRI	High resolution Excellent soft tissue contrast Provide physiological and anatomical details No tissue penetration limit Minimal exposure to ionisable radiation	High cost Long imaging time Not quantitative Cannot be used in patients with metallic devices
CT	Fast High spatial resolution No tissue penetration limit	Poor resolution of soft tissues Radiation risk Not quantitative
PET	High sensitivity Quantitative Image biochemical processes No tissue penetration limit	High cost Radiation risk Can detect only one radionuclide Low spatial resolution
SPECT	High sensitivity No tissue penetration limit Can distinguish between radionuclides	Low spatial resolution Radiation risk
Ultrasound	Real-time imaging Low cost No radiation exposure	Poor image contrast Poor working in air-containing organs Operator dependent analysis
Fluorescence reflectance imaging	High sensitivity Multicolour imaging Provide functional information No radiation exposure	Low spatial resolution Poor depth penetration

Hasegawa *et al.* built in 1990 the first device that simultaneously detected photons (SPECT) and X-rays (CT), and paved the way for hybridization. [261] The first SPECT/CT and PET/CT were commercially introduced in 1998 and the use of the instruments has grown exponentially. [259] For example, in 2006 there were virtually no sales anymore of standalone PET instruments. [262] Compared to CT, MRI has several advantages, such as providing excellent tissue contrast and multidimensional functional, structural and morphological information (e.g. spectroscopy and blood-oxygen-level

dependent (BOLD) imaging). [263] Furthermore, the radiation dose for PET/MRI is lower than that for PET/CT. This is of particular importance for repeated studies for therapy monitoring and paediatric imaging [259], as there is an increasing risk for radiation-induced carcinogenesis. [264] However, the development of PET/MRI-fused systems was slower due to the economic and engineering challenges of merging the two modalities, and the first commercial PET/MRI prototype for a human scale hybrid scanner was only introduced in 2007. [265]

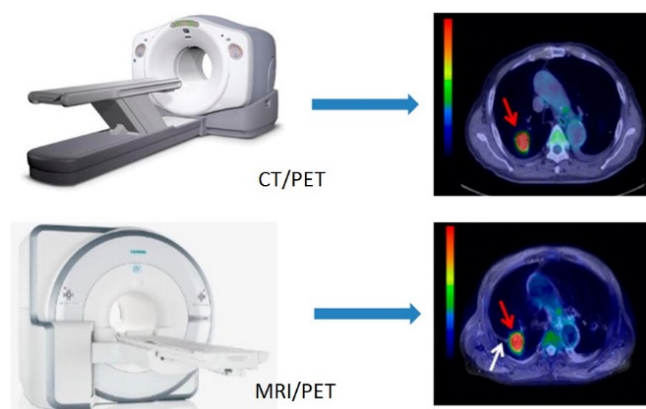


Figure 1.13: CT/PET and MRI/PET multimodal systems. Reprinted with permission from Hu *et al.* [263]

Copyright 2014 American Chemical Society.

## Multimodal Probes

The surge of multimodal scanning systems has resulted in the development of multimodal probes. [266] Ultimately the combined imaging methods and probes can work synergistically to enable high-resolution, high-sensitivity investigation of biological activity. [266] For example, for PET/MRI bimodal probes, the high sensitivity of PET can be used as a whole body screen to identify regions of interest, thereby reducing the volume of tissue that needs to be scanned, which reduces scan time required for high-resolution imaging by MRI. [265] Nanomedicine plays a vital role in the development of multimodal imaging agents as nanoparticles enable the combination of multiple imaging moieties on a single particle. A variety of multimodal nanoparticles have been developed, such as liposomes, inorganic nanoparticles (e.g. iron oxides, quantum dots, silica nanoparticles and doped nanoparticles), nanocomposites, dendrimers, polymers, and other macromolecules. [148, 266, 267]

Liposomes (or for example polymeric vesicles) have the advantage that imaging moieties can be included both in the aqueous core as well as conjugated to lipids in the bilayer. [268] For example, the CT contrast agent iohexol and MRI contrast agent gadoteridol were encapsulated into unilamellar

bilayer liposomes using an extrusion process, where CT is used to perform radiation dose mapping and MRI provides soft tissue contrast to identify target tissues. [269]

Superparamagnetic iron oxides are also often used as a platform for multimodal probes as the iron oxide itself is an MRI contrast agent and its surface enables functionalisation with polymers and secondary imaging moieties, such as optical probes (e.g. cyanine 5,5) [270] or PET radiotracers (e.g.  $^{64}\text{Cu}$  and  $^{18}\text{F}$ ). [232, 271, 272]. Furthermore, other inorganic nanoparticles are also very promising, for example doped nanoparticles can combine multiple moieties: core-shell  $\text{Fe}_3\text{O}_4@\text{NaLuF}_4:\text{Yb,Er/Tm}$  nanostructures combine MRI contrast from the iron oxide core with excellent X-ray attenuation of the  $\text{NaLuF}_4$ -based nanoparticles and up-conversion luminescence emission under excitation at 980 nm. [273] Another interesting example are Eu-doped  $\text{NaGdF}_4$  nanoparticles that combine MRI, CT and optical imaging applications in one particle. [274]

Polymer-based nanoparticles also have a great potential in multimodal imaging due to their versatility in size and shape, and the opportunity to incorporate multiple functional groups. For example, hyperbranched polymers were synthesized by RAFT polymerization combining  $^{19}\text{F}$  MRI imaging (using trifluoroethyl acrylate) and optical imaging (rhodamine or NIR797). It was possible to carry out confocal fluorescence imaging of individual cells *in vitro* and use  $^{19}\text{F}$  MRI (together with standard  $^1\text{H}$  MRI) and fluorescence imaging to detect the materials *in vivo*. [275] Another example are polymeric dextran nanoparticles that were labelled with the PET isotope zirconium-89 using desferoxamine and incorporate a near-infrared fluorochrome (VT680) for microscopic and cellular validation, creating a bimodal PET/optical probe. [276]

## 1.3 Nanoparticles for theranostics

### 1.3.1 Theranostics

At the intersection between treatment and diagnosis, interest has grown in uniting both paradigms into clinically effective nanomedicines. [149] Drug delivery and imaging both rely on the same target, therefore multifunctional nanoparticles have been developed in the last decade, resulting in the new field of theranostics, combining therapeutics and diagnosis. [277] Theranostic nanomedicines are very promising for the monitoring of drug delivery, drug release and drug efficacy. [278, 279] Firstly, theranostics agents can be used for validating and optimizing the properties of drug delivery vehicles as the combination of therapeutic and diagnostic agents in a single particle provides real-time feedback on pharmacokinetics, targeting of the disease site and any (off-target) accumulation of nanoparticles in healthy tissue. [278] Secondly, targeted theranostic nanoparticles can also be used for pre-screening patients and enabling personalized medicine. [280] For example, only when patients show high level of target site accumulation and respond well to the first treatment cycles, targeted therapy will be continued. Otherwise, other therapeutics could be attempted at an earlier stage. This will lead to more efficient treatments and a reduction of healthcare costs. [278]

### 1.3.2 Theranostic nanoparticles

A plethora of nanoparticles have been published with theranostic applications [149, 278, 281, 282], both inorganic and organic, and the journal *theranostics* was successfully introduced in 2011. Several interesting concepts will be shown here, but the reader is referred to above reviews for an extensive overview of the breadth of developed theranostic agents.

Antibodies developed to carry radioactivity for therapeutic purposes (e.g. Zevalin and Bexxar) can be viewed as the first theranostics on the market as the antibody triggers cell death and the radioisotope indium-111 can be used for imaging. [10] Nasongkla *et al.* developed an early example of a MR theranostic agent by incorporating iron oxide nanoparticles and a therapeutic agent inside a polymeric micelle with cancer-targeting capability via  $\alpha_v\beta_3$  integrins, showing controlled drug delivery, and efficient magnetic resonance imaging contrast characteristics. [283] A good example of a theranostic polymeric nanoparticle synthesized by RAFT polymerization was published by Li *et al.* [284] Core-cross-linked star polymers were prepared containing both an MRI moiety (Gd-DOTA) and a drug (doxorubicin) via a pH-sensitive imine bond. Fluorescence lifetime imaging microscopy confirmed intracellular drug release and the star polymer showed a high MRI relaxivity. Furthermore, Ardana *et al.* used RAFT polymerization to synthesize hyperbranched polymers suitable for  $^{19}\text{F}$  MRI and delivery of siRNA via disulfide-cleavable linkers for gene therapy. [285]

Another interesting study was recently carried out by Liu *et al.* in which a polymeric nanoparticle was developed containing a conjugated near-infrared fluorescent polymer as building block for NIR imaging and siRNA delivery. They were able to successfully treat mouse models of anaplastic thyroid cancer, a devastating disease with no effective therapy and an approximate 100 % mortality rate. The bright fluorescence enabled nanoparticle mapping of the biodistribution, in particular in both implanted tumours and their metastases within the lungs and lymph nodes. [286]

Several studies also reported smart theranostic nanoparticles that enable drug release monitoring by an increase of signal upon drug release. For example, the Hyeon group published a study regarding so-called tumour pH-sensitive magnetic nanogrenades composed of self-assembled iron oxide nanoparticles and pH-responsive ligands. Upon delivery to the tumour environment, the low acidity triggers a surface-charge switch and the nanoparticles are further disassembled into a highly active state in acidic subcellular compartments that “turns on” MR contrast, fluorescence and photodynamic therapeutic activity. [287] Basuki *et al.* also showed an MR contrast enhancement upon release of doxorubicin from the inner shell of polymeric-coated iron oxide nanoparticles, resulting in an increased water accessibility and hence relaxation. [288]

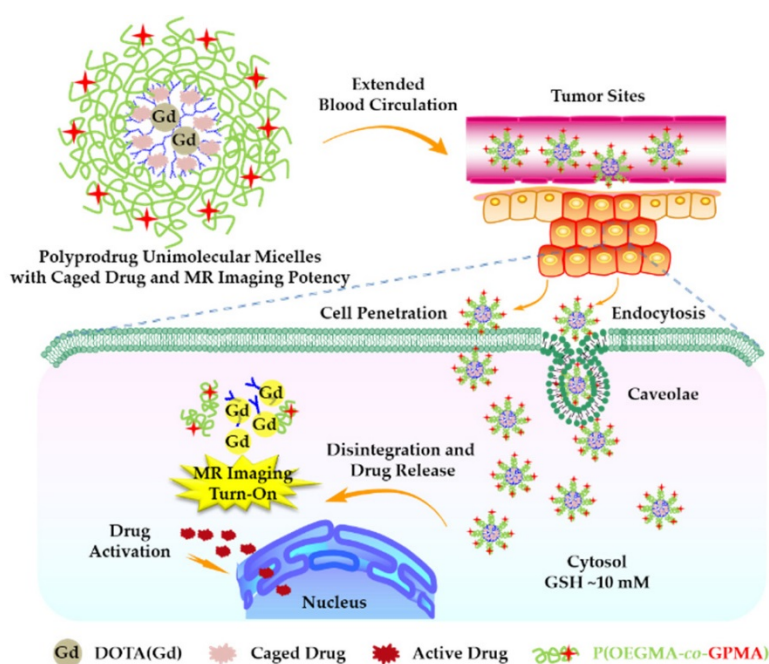


Figure 1.14: Example of a smart responsive theranostic nanoparticle. Reprinted with permission from Hu *et al.* Copyright 2014 American Chemical Society. [289]

Furthermore, Liu and co-workers developed nanocarriers based on hyperbranched polyprodrug amphiphiles conjugated with a gadolinium chelate for MR contrast using RAFT polymerization (see Figure 1.14). Upon cellular internalization, the reductive environment-actuated release of anticancer drug in the active form, activation of therapeutic efficacy (> 70-fold enhancement in cytotoxicity), and turn-on of MR imaging (~9.6-fold increase in  $T_1$  relaxivity) were simultaneously realized. [289] Another interesting study into monitoring drug release was published by the Kataoka group, who developed a platinum drug-loaded micelle with a fluorescent dye on the surface (boron-dipyrromethene green) and in the core (boron-dipyrromethene red). The core conjugated dye is normally quenched, however upon change of pH disassembly occurs resulting in drug release and dequenching of the dye. [290]

## 1.4 Aims

In summary, nanomedicine has emerged as a promising field in medicine integrating nanoscale technologies with materials sciences, chemistry and biology, resulting in nano-sized particles that are able to deliver otherwise insoluble drugs and simultaneously improve the kinetics of drug delivery. Moreover, nanoparticles have led to improved disease detection by the incorporation of imaging moieties such as MRI contrast agents, fluorescent dyes and/or radioisotopes.

However, further optimization of nanoparticles in regards to their overall architecture (morphology, surface, and size) is required to optimally exploit the benefits of nano-sized particles for both drug delivery and imaging. Furthermore, the introduction of hybrid imaging systems such as MRI/PET with potentially improved diagnostics, requires the development of multimodal nanoparticles that can take full advantage of these new imaging technologies.

The overall objective of this dissertation was therefore to develop novel methods to synthesize polymer-based nanoparticles with control over size, morphology and surface for application in both drug delivery and diagnostics. Furthermore, a dual-modality PET/MRI imaging agent was developed to exploit the benefits of multimodal PET/MRI imaging and to enable high-resolution, high-sensitivity investigation of biological activity.

First in **chapter 2**, polymerisation-induced self-assembly was exploited to create a library of polymer-based nanoparticles with different sizes and shapes, and their efficacy as drug delivery vehicle was assessed to determine the optimal morphology.

In **chapter 3**, a method was developed to synthesize novel epoxide surface-functional nanoparticles by polymerization-induced self-assembly, and the versatility of the functional group was investigated. In the second part of the chapter, the use of the different shaped nanoparticles as positive MRI contrast was investigated by conjugating a gadolinium chelate onto the self-assembled nanoparticles.

Finally, in **chapter 4**, a novel bimodal MRI/PET imaging probe was designed containing both gadolinium (for MRI) and radioiodine (for PET) by combining novel multicomponent chemistry with a core-cross-linked functional star polymer to optimally exploit the synergy between MRI and PET.

## 1.4 References

1. Lipinski, C.A., *Drug-like properties and the causes of poor solubility and poor permeability*. Journal of pharmacological and toxicological methods, 2000. **44**(1): p. 235-249.
2. Tibbitt, M.W., J.E. Dahlman, and R. Langer, *Emerging Frontiers in Drug Delivery*. Journal of the American Chemical Society, 2016. **138**(3): p. 704-717.
3. Cohen, Y. and S.Y. Shoushan, *Magnetic nanoparticles-based diagnostics and theranostics*. Curr Opin Biotechnol, 2013. **24**(4): p. 672-81.
4. Cho, K., et al., *Therapeutic nanoparticles for drug delivery in cancer*. Clinical cancer research, 2008. **14**(5): p. 1310-1316.
5. Slowing, I.I., et al., *Mesoporous silica nanoparticles for drug delivery and biosensing applications*. Advanced Functional Materials, 2007. **17**(8): p. 1225-1236.
6. Couvreur, P., *Nanoparticles in drug delivery: Past, present and future*. Advanced Drug Delivery Reviews, 2013. **65**(1): p. 21-23.
7. Barenholz, Y., *Doxil(R)--the first FDA-approved nano-drug: lessons learned*. J Control Release, 2012. **160**(2): p. 117-34.
8. Etheridge, M.L., et al., *The big picture on nanomedicine: the state of investigational and approved nanomedicine products*. Nanomedicine, 2013. **9**(1): p. 1-14.
9. Chauhan, V.P. and R.K. Jain, *Strategies for advancing cancer nanomedicine*. Nat Mater, 2013. **12**(11): p. 958-962.
10. Duncan, R. and R. Gaspar, *Nanomedicine(s) under the microscope*. Mol Pharm, 2011. **8**(6): p. 2101-41.
11. Albanese, A., P.S. Tang, and W.C. Chan, *The effect of nanoparticle size, shape, and surface chemistry on biological systems*. Annu Rev Biomed Eng, 2012. **14**: p. 1-16.
12. Truong, N.P., et al., *The importance of nanoparticle shape in cancer drug delivery*. Expert Opin Drug Deliv, 2015. **12**(1): p. 129-42.
13. Weissig, V., T.K. Pettinger, and N. Murdock, *Nanopharmaceuticals (part 1): products on the market*. International Journal of Nanomedicine, 2014. **9**: p. 4357-4373.
14. Anselmo, A.C. and S. Mitragotri, *Nanoparticles in the clinic*. Bioengineering & Translational Medicine, 2016. **1**(1): p. 10-29.
15. Jia, F., et al., *Multifunctional nanoparticles for targeted delivery of immune activating and cancer therapeutic agents*. J Control Release, 2013. **172**(3): p. 1020-34.
16. Duncan, R. and R. Gaspar, *Nanomedicine(s) under the Microscope*. Molecular Pharmaceutics, 2011. **8**(6): p. 2101-2141.
17. Schutz, C.A., et al., *Therapeutic nanoparticles in clinics and under clinical evaluation*. Nanomedicine (Lond), 2013. **8**(3): p. 449-67.
18. Lynch, I., I.L. Feitshans, and M. Kendall, *'Bio-nano interactions: new tools, insights and impacts': summary of the Royal Society discussion meeting*. Philosophical Transactions of the Royal Society of London B: Biological Sciences, 2015. **370**(1661).
19. Nel, A.E., et al., *Understanding biophysicochemical interactions at the nano-bio interface*. Nat Mater, 2009. **8**(7): p. 543-557.
20. Knop, K., et al., *Poly(ethylene glycol) in Drug Delivery: Pros and Cons as Well as Potential Alternatives*. Angewandte Chemie International Edition, 2010. **49**(36): p. 6288-6308.
21. Schöttler, S., et al., *Protein adsorption is required for stealth effect of poly(ethylene glycol)- and poly(phosphoester)-coated nanocarriers*. Nat Nano, 2016. **11**(4): p. 372-377.
22. Singh, R. and J.W. Lillard, *Nanoparticle-based targeted drug delivery*. Experimental and molecular pathology, 2009. **86**(3): p. 215-223.
23. Basuki, J.S., et al., *Magnetic nanoparticles with diblock glycopolymer shells give lectin concentration-dependent MRI signals and selective cell uptake*. Chemical Science, 2014. **5**(2): p. 715-726.
24. He, C., et al., *Effects of particle size and surface charge on cellular uptake and biodistribution of polymeric nanoparticles*. Biomaterials, 2010. **31**(13): p. 3657-3666.
25. Bilensoy, E., *Cationic nanoparticles for cancer therapy*. Expert Opin Drug Deliv, 2010. **7**(7): p. 795-809.
26. Alexis, F., et al., *Factors Affecting the Clearance and Biodistribution of Polymeric Nanoparticles*. Molecular Pharmaceutics, 2008. **5**(4): p. 505-515.
27. Blanco, E., H. Shen, and M. Ferrari, *Principles of nanoparticle design for overcoming biological barriers to drug delivery*. Nat Biotech, 2015. **33**(9): p. 941-951.

28. Choi, H.S., et al., *Design considerations for tumour-targeted nanoparticles*. Nat Nano, 2010. **5**(1): p. 42-47.
29. Yuan, F., et al., *Vascular permeability in a human tumor xenograft: molecular size dependence and cutoff size*. Cancer Res, 1995. **55**(17): p. 3752-6.
30. Bae, Y.H. and K. Park, *Targeted drug delivery to tumors: Myths, reality and possibility*. Journal of Controlled Release, 2011. **153**(3): p. 198-205.
31. Matsumura, Y. and H. Maeda, *A new concept for macromolecular therapeutics in cancer chemotherapy: mechanism of tumoritropic accumulation of proteins and the antitumor agent smancs*. Cancer Res, 1986. **46**(12 Pt 1): p. 6387-92.
32. Maeda, H., et al., *Tumor vascular permeability and the EPR effect in macromolecular therapeutics: a review*. Journal of controlled release, 2000. **65**(1): p. 271-284.
33. Fang, J., H. Nakamura, and H. Maeda, *The EPR effect: Unique features of tumor blood vessels for drug delivery, factors involved, and limitations and augmentation of the effect*. Advanced Drug Delivery Reviews, 2011. **63**(3): p. 136-151.
34. Sarin, H., *Physiologic upper limits of pore size of different blood capillary types and another perspective on the dual pore theory of microvascular permeability*. J Angiogenes Res, 2010. **2**: p. 14.
35. Hobbs, S.K., et al., *Regulation of transport pathways in tumor vessels: Role of tumor type and microenvironment*. Proceedings of the National Academy of Sciences, 1998. **95**(8): p. 4607-4612.
36. Chauhan, V.P., et al., *Normalization of tumour blood vessels improves the delivery of nanomedicines in a size-dependent manner*. Nat Nano, 2012. **7**(6): p. 383-388.
37. Sagnella, S.M., J.A. McCarroll, and M. Kavallaris, *Drug delivery: beyond active tumour targeting*. Nanomedicine: Nanotechnology, Biology and Medicine, 2014. **10**(6): p. 1131-1137.
38. Cabral, H., et al., *Accumulation of sub-100 nm polymeric micelles in poorly permeable tumours depends on size*. Nat Nanotechnol, 2011. **6**(12): p. 815-23.
39. Popovic, Z., et al., *A nanoparticle size series for in vivo fluorescence imaging*. Angew Chem Int Ed Engl, 2010. **49**(46): p. 8649-52.
40. CabralH, et al., *Accumulation of sub-100 nm polymeric micelles in poorly permeable tumours depends on size*. Nat Nano, 2011. **6**(12): p. 815-823.
41. Kano, M.R., et al., *Improvement of cancer-targeting therapy, using nanocarriers for intractable solid tumors by inhibition of TGF- $\beta$  signaling*. Proceedings of the National Academy of Sciences, 2007. **104**(9): p. 3460-3465.
42. Geng, Y., et al., *Shape effects of filaments versus spherical particles in flow and drug delivery*. Nat Nano, 2007. **2**(4): p. 249-255.
43. Chauhan, V.P. and R.K. Jain, *Strategies for advancing cancer nanomedicine*. Nat Mater, 2013. **12**(11): p. 958-62.
44. Black, K.C.L., et al., *Radioactive <sup>198</sup>Au-Doped Nanostructures with Different Shapes for In Vivo Analyses of Their Biodistribution, Tumor Uptake, and Intratumoral Distribution*. ACS Nano, 2014.
45. Bogart, L.K., et al., *Nanoparticles for Imaging, Sensing, and Therapeutic Intervention*. ACS Nano, 2014. **8**(4): p. 3107-3122.
46. Braunecker, W.A. and K. Matyjaszewski, *Controlled/living radical polymerization: Features, developments, and perspectives*. Progress in Polymer Science, 2007. **32**(1): p. 93-146.
47. Matyjaszewski, K. and T.P. Davis, *Handbook of radical polymerization*. 2002, Wiley-Interscience New York.
48. Boyer, C. and T.P. Davis, *Themed issue: synthesis of polymeric nanomaterials for medicine*. Polymer Chemistry, 2014. **5**(5): p. 1501-1502.
49. Matyjaszewski, K., *Atom Transfer Radical Polymerization (ATRP): Current Status and Future Perspectives*. Macromolecules, 2012. **45**(10): p. 4015-4039.
50. Boyer, C., et al., *Copper-Mediated Living Radical Polymerization (Atom Transfer Radical Polymerization and Copper(0) Mediated Polymerization): From Fundamentals to Bioapplications*. Chemical Reviews, 2016. **116**(4): p. 1803-1949.
51. Wang, J.-S. and K. Matyjaszewski, *Controlled/" living" radical polymerization. Atom transfer radical polymerization in the presence of transition-metal complexes*. Journal of the American Chemical Society, 1995. **117**(20): p. 5614-5615.
52. Matyjaszewski, K. and N.V. Tsarevsky, *Macromolecular Engineering by Atom Transfer Radical Polymerization*. Journal of the American Chemical Society, 2014. **136**(18): p. 6513-6533.
53. Matyjaszewski, K. and J. Xia, *Atom Transfer Radical Polymerization*. Chemical Reviews, 2001. **101**(9): p. 2921-2990.

54. Tang, W. and K. Matyjaszewski, *Effects of Initiator Structure on Activation Rate Constants in ATRP*. *Macromolecules*, 2007. **40**(6): p. 1858-1863.
55. Min, K., H. Gao, and K. Matyjaszewski, *Preparation of Homopolymers and Block Copolymers in Miniemulsion by ATRP Using Activators Generated by Electron Transfer (AGET)*. *Journal of the American Chemical Society*, 2005. **127**(11): p. 3825-3830.
56. Matyjaszewski, K., et al., *Diminishing catalyst concentration in atom transfer radical polymerization with reducing agents*. *Proceedings of the National Academy of Sciences*, 2006. **103**(42): p. 15309-15314.
57. Magenau, A.J., et al., *Electrochemically mediated atom transfer radical polymerization*. *Science*, 2011. **332**(6025): p. 81-4.
58. Ohtsuki, A., et al., *Photocontrolled Organocatalyzed Living Radical Polymerization Feasible over a Wide Range of Wavelengths*. *Journal of the American Chemical Society*, 2015. **137**(16): p. 5610-5617.
59. Rosen, B.M. and V. Percec, *Single-Electron Transfer and Single-Electron Transfer Degenerative Chain Transfer Living Radical Polymerization*. *Chemical Reviews*, 2009. **109**(11): p. 5069-5119.
60. Percec, V., et al., *Ultrafast Synthesis of Ultrahigh Molar Mass Polymers by Metal-Catalyzed Living Radical Polymerization of Acrylates, Methacrylates, and Vinyl Chloride Mediated by SET at 25 °C*. *Journal of the American Chemical Society*, 2006. **128**(43): p. 14156-14165.
61. Anastasaki, A., et al., *Cu(0)-Mediated Living Radical Polymerization: A Versatile Tool for Materials Synthesis*. *Chemical Reviews*, 2016. **116**(3): p. 835-877.
62. Konkolewicz, D., et al., *SARA ATRP or SET-LRP. End of controversy?* *Polymer Chemistry*, 2014. **5**(15): p. 4396-4417.
63. Konkolewicz, D., et al., *Reversible-Deactivation Radical Polymerization in the Presence of Metallic Copper. A Critical Assessment of the SARA ATRP and SET-LRP Mechanisms*. *Macromolecules*, 2013. **46**(22): p. 8749-8772.
64. Nicolas, J., et al., *Nitroxide-mediated polymerization*. *Progress in Polymer Science*, 2013. **38**(1): p. 63-235.
65. Hawker, C.J., A.W. Bosman, and E. Harth, *New polymer synthesis by nitroxide mediated living radical polymerizations*. *Chemical Reviews*, 2001. **101**(12): p. 3661-3688.
66. Fischer, H., *The Persistent Radical Effect: A Principle for Selective Radical Reactions and Living Radical Polymerizations*. *Chemical Reviews*, 2001. **101**(12): p. 3581-3610.
67. Chiefari, J., et al., *Living Free-Radical Polymerization by Reversible Addition-Fragmentation Chain Transfer: The RAFT Process*. *Macromolecules*, 1998. **31**(16): p. 5559-5562.
68. Boyer, C., et al., *Bioapplications of RAFT Polymerization*. *Chemical Reviews*, 2009. **109**(11): p. 5402-5436.
69. Semsarilar, M. and S. Perrier, *'Green' reversible addition-fragmentation chain-transfer (RAFT) polymerization*. *Nat Chem*, 2010. **2**(10): p. 811-820.
70. Boyer, C., M.H. Stenzel, and T.P. Davis, *Building nanostructures using RAFT polymerization*. *Journal of Polymer Science Part A: Polymer Chemistry*, 2011. **49**(3): p. 551-595.
71. Quinn, J.F., E. Rizzardo, and T.P. Davis, *Ambient temperature reversible addition-fragmentation chain transfer polymerisation*. *Chemical Communications*, 2001(11): p. 1044-1045.
72. Lowe, A.B., et al., *RAFT Polymerization in Homogeneous Aqueous Media*, in *Advances in Controlled/Living Radical Polymerization*. 2003, American Chemical Society. p. 586-602.
73. Moad, G., E. Rizzardo, and S.H. Thang, *Living Radical Polymerization by the RAFT Process*. *Australian Journal of Chemistry*, 2005. **58**(6): p. 379-410.
74. Boyer, C., et al., *RAFT Polymer End-Group Modification and Chain Coupling/Conjugation Via Disulfide Bonds*. *Australian Journal of Chemistry*, 2009. **62**(8): p. 830-847.
75. Yu, S.H., et al., *Transformation of RAFT Polymer End Groups into Nitric Oxide Donor Moieties: En Route to Biochemically Active Nanostructures*. *ACS Macro Letters*, 2015. **4**(11): p. 1278-1282.
76. Discher, D.E. and A. Eisenberg, *Polymer vesicles*. *Science*, 2002. **297**(5583): p. 967-73.
77. Blanz, A., S.P. Armes, and A.J. Ryan, *Self-Assembled Block Copolymer Aggregates: From Micelles to Vesicles and their Biological Applications*. *Macromol Rapid Commun*, 2009. **30**(4-5): p. 267-77.
78. Yokoyama, M., et al., *Preparation of micelle-forming polymer-drug conjugates*. *Bioconjugate Chemistry*, 1992. **3**(4): p. 295-301.
79. Kedar, U., et al., *Advances in polymeric micelles for drug delivery and tumor targeting*. *Nanomedicine*, 2010. **6**(6): p. 714-29.
80. Gref, R., et al., *Biodegradable long-circulating polymeric nanospheres*. *Science*, 1994. **263**(5153): p. 1600-3.

81. Kataoka, K., A. Harada, and Y. Nagasaki, *Block copolymer micelles for drug delivery: design, characterization and biological significance*. Advanced Drug Delivery Reviews, 2001. **47**(1): p. 113-131.
82. Rösler, A., G.W.M. Vandermeulen, and H.-A. Klok, *Advanced drug delivery devices via self-assembly of amphiphilic block copolymers*. Advanced Drug Delivery Reviews, 2012. **64**, **Supplement**: p. 270-279.
83. Jones, M.-C. and J.-C. Leroux, *Polymeric micelles – a new generation of colloidal drug carriers*. European Journal of Pharmaceutics and Biopharmaceutics, 1999. **48**(2): p. 101-111.
84. Lavasanifar, A., J. Samuel, and G.S. Kwon, *Micelles self-assembled from poly(ethylene oxide)-block-poly(N-hexyl stearate l-aspartamide) by a solvent evaporation method: effect on the solubilization and haemolytic activity of amphotericin B*. Journal of Controlled Release, 2001. **77**(1–2): p. 155-160.
85. van Sluis, R., et al., *In vivo imaging of extracellular pH using <sup>1</sup>H MRSI*. Magnetic Resonance in Medicine, 1999. **41**(4): p. 743-750.
86. Gao, G.H., Y. Li, and D.S. Lee, *Environmental pH-sensitive polymeric micelles for cancer diagnosis and targeted therapy*. J Control Release, 2013. **169**(3): p. 180-4.
87. Zhou, K., et al., *Tunable, Ultrasensitive pH-Responsive Nanoparticles Targeting Specific Endocytic Organelles in Living Cells*. Angewandte Chemie International Edition, 2011. **50**(27): p. 6109-6114.
88. Torchilin, V.P., *Multifunctional, stimuli-sensitive nanoparticulate systems for drug delivery*. Nature reviews Drug discovery, 2014. **13**(11): p. 813-827.
89. Wang, Y., et al., *A nanoparticle-based strategy for the imaging of a broad range of tumours by nonlinear amplification of microenvironment signals*. Nat Mater, 2014. **13**(2): p. 204-212.
90. Discher, B.M., et al., *Polymersomes: tough vesicles made from diblock copolymers*. Science, 1999. **284**(5417): p. 1143-6.
91. Lee, J.S. and J. Feijen, *Polymersomes for drug delivery: design, formation and characterization*. J Control Release, 2012. **161**(2): p. 473-83.
92. Brinkhuis, R.P., F.P.J.T. Rutjes, and J.C.M. van Hest, *Polymeric vesicles in biomedical applications*. Polymer Chemistry, 2011. **2**(7): p. 1449-1462.
93. Truong, N.P., et al., *Polymeric filomicelles and nanoworms: two decades of synthesis and application*. Polymer Chemistry, 2016. **7**(26): p. 4295-4312.
94. Oltra, N.S., P. Nair, and D.E. Discher, *From Stealthy Polymersomes and Filomicelles to “Self” Peptide-Nanoparticles for Cancer Therapy*. Annual review of chemical and biomolecular engineering, 2014. **5**: p. 281-299.
95. Geng, Y., et al., *Shape effects of filaments versus spherical particles in flow and drug delivery*. Nat Nanotechnol, 2007. **2**(4): p. 249-55.
96. Younghoon, K., et al., *Polymeric worm micelles as nano-carriers for drug delivery*. Nanotechnology, 2005. **16**(7): p. S484.
97. Christian, D.A., et al., *Flexible Filaments for in Vivo Imaging and Delivery: Persistent Circulation of Filomicelles Opens the Dosage Window for Sustained Tumor Shrinkage*. Molecular Pharmaceutics, 2009. **6**(5): p. 1343-1352.
98. Desimone\*, J.M., J.-Y. Wang, and Y. Wang, *Chapter 5 Particle Replication in Non-wetting Templates: a Platform for Engineering Shape- and Size-specific Janus Particles*, in *Janus Particle Synthesis, Self-Assembly and Applications*. 2012, The Royal Society of Chemistry. p. 90-107.
99. Hsiao, M.-S., et al., *Crystallization-Driven Self-Assembly of Block Copolymers with a Short Crystallizable Core-Forming Segment: Controlling Micelle Morphology through the Influence of Molar Mass and Solvent Selectivity*. Macromolecules, 2014. **47**(7): p. 2361-2372.
100. LaRue, I., et al., *Reversible Morphological Transitions of Polystyrene-b-polyisoprene Micelles*. Macromolecules, 2006. **39**(1): p. 309-314.
101. Truong, N.P., et al., *Facile access to thermoresponsive filomicelles with tuneable cores*. Chemical Communications, 2016. **52**(24): p. 4497-4500.
102. Canning, S.L., G.N. Smith, and S.P. Armes, *A Critical Appraisal of RAFT-Mediated Polymerization-Induced Self-Assembly*. Macromolecules, 2016. **49**(6): p. 1985-2001.
103. Charleux, B., et al., *Polymerization-Induced Self-Assembly: From Soluble Macromolecules to Block Copolymer Nano-Objects in One Step*. Macromolecules, 2012. **45**(17): p. 6753-6765.
104. Warren, N.J. and S.P. Armes, *Polymerization-Induced Self-Assembly of Block Copolymer Nano-objects via RAFT Aqueous Dispersion Polymerization*. Journal of the American Chemical Society, 2014. **136**(29): p. 10174-10185.
105. Yang, P., L.P.D. Ratcliffe, and S.P. Armes, *Efficient Synthesis of Poly(methacrylic acid)-block-Poly(styrene-alt-N-phenylmaleimide) Diblock Copolymer Lamellae Using RAFT Dispersion Polymerization*. Macromolecules, 2013. **46**(21): p. 8545-8556.

106. Blanz, A., et al., *Mechanistic Insights for Block Copolymer Morphologies: How Do Worms Form Vesicles?* Journal of the American Chemical Society, 2011. **133**(41): p. 16581-16587.
107. Wan, W.-M. and C.-Y. Pan, *One-pot synthesis of polymeric nanomaterials via RAFT dispersion polymerization induced self-assembly and re-organization*. Polymer Chemistry, 2010. **1**(9): p. 1475-1484.
108. Karagoz, B., et al., *Polymerization-Induced Self-Assembly (PISA) – control over the morphology of nanoparticles for drug delivery applications*. Polym. Chem., 2014. **5**(2): p. 350-355.
109. Caminade, A.-M., D. Yan, and D.K. Smith, *Dendrimers and hyperbranched polymers*. Chemical Society Reviews, 2015. **44**(12): p. 3870-3873.
110. Mintzer, M.A. and M.W. Grinstaff, *Biomedical applications of dendrimers: a tutorial*. Chemical Society Reviews, 2011. **40**(1): p. 173-190.
111. Inoue, K., *Functional dendrimers, hyperbranched and star polymers*. Progress in Polymer Science, 2000. **25**(4): p. 453-571.
112. Ren, J.M., et al., *Star Polymers*. Chem Rev, 2016. **116**(12): p. 6743-836.
113. Zheng, Y., et al., *Hyperbranched polymers: advances from synthesis to applications*. Chemical Society Reviews, 2015. **44**(12): p. 4091-4130.
114. Wang, D., et al., *Bioapplications of hyperbranched polymers*. Chemical Society Reviews, 2015. **44**(12): p. 4023-4071.
115. Tan, J.H., et al., *Hyperbranched polymers as delivery vectors for oligonucleotides*. Journal of Polymer Science Part A: Polymer Chemistry, 2012. **50**(13): p. 2585-2595.
116. Blencowe, A., et al., *Core cross-linked star polymers via controlled radical polymerisation*. Polymer, 2009. **50**(1): p. 5-32.
117. Gao, H. and K. Matyjaszewski, *Synthesis of functional polymers with controlled architecture by CRP of monomers in the presence of cross-linkers: from stars to gels*. Progress in Polymer Science, 2009. **34**(4): p. 317-350.
118. Aloorkar, N., et al., *Star polymers: an overview*. Int J Pharm Sci Nanotech, 2012. **5**: p. 1675-1684.
119. Gao, H. and K. Matyjaszewski, *Synthesis of Star Polymers by A New "Core-First" Method: Sequential Polymerization of Cross-Linker and Monomer*. Macromolecules, 2008. **41**(4): p. 1118-1125.
120. Jesberger, M., et al., *Hyperbranched polymers as scaffolds for multifunctional reversible addition–fragmentation chain-transfer agents: A route to polystyrene-core-polyesters and polystyrene-block-poly (butyl acrylate)-core-polyesters*. Journal of Polymer Science Part A: Polymer Chemistry, 2003. **41**(23): p. 3847-3861.
121. Hao, X., et al., *Dendrimers as scaffolds for multifunctional reversible addition–fragmentation chain transfer agents: Syntheses and polymerization*. Journal of Polymer Science Part A: Polymer Chemistry, 2004. **42**(23): p. 5877-5890.
122. Li, W. and K. Matyjaszewski, *Star Polymers via Cross-Linking Amphiphilic Macroinitiators by AGET ATRP in Aqueous Media*. Journal of the American Chemical Society, 2009. **131**(30): p. 10378-10379.
123. Syrett, J.A., et al., *Functional, star polymeric molecular carriers, built from biodegradable microgel/nanogel cores*. Chemical Communications, 2011. **47**(5): p. 1449-1451.
124. Wei, X., et al., *An arm-first approach to cleavable mikto-arm star polymers by RAFT polymerization*. Macromol Rapid Commun, 2014. **35**(8): p. 840-5.
125. Wong, E.H., A. Blencowe, and G.G. Qiao, *Quantitative formation of core cross-linked star polymers via a one-pot two-step single electron transfer-living radical polymerization*. Polymer Chemistry, 2013. **4**(17): p. 4562-4565.
126. Gao, H. and K. Matyjaszewski, *Synthesis of star polymers by a combination of ATRP and the "click" coupling method*. Macromolecules, 2006. **39**(15): p. 4960-4965.
127. Altintas, O., et al., *Constructing star polymers via modular ligation strategies*. Polymer Chemistry, 2012. **3**(1): p. 34-45.
128. Schmidt, B.V., et al., *Supramolecular three-armed star polymers via cyclodextrin host–guest self-assembly*. Polymer Chemistry, 2012. **3**(11): p. 3139-3145.
129. Han, S.-o., et al., *Development of Biomaterials for Gene Therapy*. Mol Ther, 2000. **2**(4): p. 302-317.
130. Brannon-Peppas, L. and J.O. Blanchette, *Nanoparticle and targeted systems for cancer therapy*. Advanced drug delivery reviews, 2004. **56**(11): p. 1649-1659.
131. Boyer, C., et al., *Effective delivery of siRNA into cancer cells and tumors using well-defined biodegradable cationic star polymers*. Molecular pharmaceutics, 2013. **10**(6): p. 2435-2444.
132. Teo, J., et al., *A Rationally Optimized Nanoparticle System for the Delivery of RNA Interference Therapeutics into Pancreatic Tumors in Vivo*. Biomacromolecules, 2016. **17**(7): p. 2337-51.

133. Xu, F., et al., *Star-shaped cationic polymers by atom transfer radical polymerization from  $\beta$ -cyclodextrin cores for nonviral gene delivery*. *Biomacromolecules*, 2009. **10**(2): p. 285-293.
134. Xu, Z., et al., *Unimolecular micelles of amphiphilic cyclodextrin-core star-like block copolymers for anticancer drug delivery*. *Chemical Communications*, 2015. **51**(87): p. 15768-15771.
135. Gu, D., et al., *Amphiphilic core cross-linked star polymers as water-soluble, biocompatible and biodegradable unimolecular carriers for hydrophobic drugs*. *Polymer Chemistry*, 2015. **6**(36): p. 6475-6487.
136. Liu, J., et al., *Synthesis of functional core, star polymers via RAFT polymerization for drug delivery applications*. *Macromolecular rapid communications*, 2012. **33**(9): p. 760-766.
137. Tucker, B.S., et al., *Facile synthesis of drug-conjugated PHPMA core-crosslinked star polymers*. *Polymer Chemistry*, 2015. **6**(23): p. 4258-4263.
138. Saleh-Ghadimi, L., M. Fathi, and A.A. Entezami, *Heteroarm star-shaped poly (N-isopropylacryamide-co-itaconic acid) copolymer prepared by glucose core as ATRP initiator*. *International Journal of Polymeric Materials and Polymeric Biomaterials*, 2014. **63**(5): p. 246-255.
139. Gindy, M.E. and R.K. Prud'homme, *Multifunctional nanoparticles for imaging, delivery and targeting in cancer therapy*. *Expert opinion on drug delivery*, 2009. **6**(8): p. 865-878.
140. Cheon, J. and J.H. Lee, *Synergistically integrated nanoparticles as multimodal probes for nanobiotechnology*. *Acc Chem Res*, 2008. **41**(12): p. 1630-40.
141. Shin, S.J., J.R. Beech, and K.A. Kelly, *Targeted nanoparticles in imaging: paving the way for personalized medicine in the battle against cancer*. *Integrative Biology*, 2013. **5**(1): p. 29-42.
142. Schneider, M., *Characteristics of SonoVue™*. *Echocardiography*, 1999. **16**: p. 743-746.
143. Phillips, E., et al., *Clinical translation of an ultrasmall inorganic optical-PET imaging nanoparticle probe*. *Science Translational Medicine*, 2014. **6**(260): p. 260ra149-260ra149.
144. Kosaka, N., et al., *Clinical implications of near-infrared fluorescence imaging in cancer*. *Future oncology (London, England)*, 2009. **5**(9): p. 1501-1511.
145. Choi, H.S. and J.V. Frangioni, *Nanoparticles for biomedical imaging: fundamentals of clinical translation*. *Molecular imaging*, 2010. **9**(6): p. 291.
146. Liong, M., et al., *Multifunctional inorganic nanoparticles for imaging, targeting, and drug delivery*. *ACS nano*, 2008. **2**(5): p. 889-896.
147. Weissleder, R. and M.J. Pittet, *Imaging in the era of molecular oncology*. *Nature*, 2008. **452**(7187): p. 580-589.
148. Lee, S.Y., et al., *Targeted multimodal imaging modalities*. *Advanced Drug Delivery Reviews*, 2014. **76**: p. 60-78.
149. Janib, S.M., A.S. Moses, and J.A. MacKay, *Imaging and drug delivery using theranostic nanoparticles*. *Adv Drug Deliv Rev*, 2010. **62**(11): p. 1052-63.
150. Brown, M.A. and R.C. Semelka, *MRI: Basic Principles and Applications*. 3 ed. 2003, Hoboken, USA: Wiley-Liss.
151. Hornak, J.P., *The Basics of MRI*. 2014, Interactive Learning Software: Henietta, USA.
152. Haacke, E.M., et al., *Magnetic Resonance Imaging: Physical Principles and Sequence Design*. 1 ed. 1999, Hoboken, USA: Wiley-Liss.
153. Bryson, J., J.W. Reineke, and T.M. Reineke, *Macromolecular Imaging Agents Containing Lanthanides: Can Conceptual Promise Lead to Clinical Potential?* *Macromolecules*, 2012. **45**(22): p. 8939-8952.
154. Langereis, S., et al., *Paramagnetic liposomes for molecular MRI and MRI-guided drug delivery*. *NMR in Biomedicine*, 2013. **26**(7): p. 728-744.
155. Caravan, P., et al., *Gadolinium(III) Chelates as MRI Contrast Agents: Structure, Dynamics, and Applications*. *Chem Rev*, 1999. **99**(9): p. 2293-352.
156. Lin, S.P. and J.J. Brown, *MR contrast agents: physical and pharmacologic basics*. *J Magn Reson Imaging*, 2007. **25**(5): p. 884-99.
157. Levitt, M.H., *Spin Dynamics: Basics of Nuclear Magnetic Resonance*. 1 ed. 2001, Chichester, UK: Wiley.
158. Wood, R., et al., *1.5 Tesla Magnetic Resonance Imaging Scanners Compared with 3.0 Tesla Magnetic Resonance Imaging Scanners: Systematic Review of Clinical Effectiveness*. *CADTH Technology Overviews*, 2012. **2**(2): p. e2201.
159. Brown, M.A. and R.C. Semelka, *MRI: basic principles and applications*. 2011: John Wiley & Sons.
160. Bottomley, P.A., et al., *A review of normal tissue hydrogen NMR relaxation times and relaxation mechanisms from 1-100 MHz: dependence on tissue type, NMR frequency, temperature, species, excision, and age*. *Med Phys*, 1984. **11**(4): p. 425-48.

161. Bernstein, M.A., K.F. King, and X.J. Zhou, eds. *Handbook of MRI Pulse Sequences*. 1 ed. 2004, Elsevier Academic Press: Burlington, USA.
162. Caravan, P., *Strategies for increasing the sensitivity of gadolinium based MRI contrast agents*. Chem Soc Rev, 2006. **35**(6): p. 512-23.
163. Caravan, P., et al., *Influence of molecular parameters and increasing magnetic field strength on relaxivity of gadolinium- and manganese-based T1 contrast agents*. Contrast Media Mol Imaging, 2009. **4**(2): p. 89-100.
164. Terreno, E., et al., *Challenges for molecular magnetic resonance imaging*. Chem Rev, 2010. **110**(5): p. 3019-42.
165. Tang, J., et al., *Macromolecular MRI contrast agents: Structures, properties and applications*. Progress in Polymer Science, 2013. **38**(3-4): p. 462-502.
166. van Zijl, P.C.M. and N.N. Yadav, *Chemical exchange saturation transfer (CEST): What is in a name and what isn't?* Magnetic Resonance in Medicine, 2011. **65**(4): p. 927-948.
167. Bye, N., et al., *Nitroxide-loaded hexosomes provide MRI contrast in vivo*. Langmuir, 2014. **30**(29): p. 8898-8906.
168. Thurecht, K.J., et al., *Functional hyperbranched polymers: toward targeted in vivo <sup>19</sup>F magnetic resonance imaging using designed macromolecules*. J Am Chem Soc, 2010. **132**(15): p. 5336-7.
169. Terreno, E. and S. Aime, *MRI Contrast Agents for Pharmacological Research*. Frontiers in Pharmacology, 2015. **6**: p. 290.
170. Aime, S., et al., *Lanthanide(III) chelates for NMR biomedical applications*. Chemical Society Reviews, 1998. **27**(1): p. 19-29.
171. Caravan, P., *Strategies for increasing the sensitivity of gadolinium based MRI contrast agents*. Chemical Society Reviews, 2006. **35**(6): p. 512-523.
172. Rohrer, M., et al., *Comparison of magnetic properties of MRI contrast media solutions at different magnetic field strengths*. Invest Radiol, 2005. **40**(11): p. 715-24.
173. Beija, M., et al., *Polymer-gold nanohybrids with potential use in bimodal MRI/CT: enhancing the relaxometric properties of Gd(III) complexes*. Journal of Materials Chemistry, 2012. **22**(40): p. 21382-21386.
174. Bridot, J.-L., et al., *Hybrid Gadolinium Oxide Nanoparticles: Multimodal Contrast Agents for in Vivo Imaging*. Journal of the American Chemical Society, 2007. **129**(16): p. 5076-5084.
175. Hou, Y., et al., *NaGdF<sub>4</sub> Nanoparticle-Based Molecular Probes for Magnetic Resonance Imaging of Intraperitoneal Tumor Xenografts in Vivo*. ACS Nano, 2013. **7**(1): p. 330-338.
176. Li, Y., et al., *Macromolecular Ligands for Gadolinium MRI Contrast Agents*. Macromolecules, 2012. **45**(10): p. 4196-4204.
177. Li, Y., et al., *The precise molecular location of gadolinium atoms has a significant influence on the efficacy of nanoparticulate MRI positive contrast agents*. Polymer Chemistry, 2014. **5**(7): p. 2592-2601.
178. Gupta, A.K. and M. Gupta, *Synthesis and surface engineering of iron oxide nanoparticles for biomedical applications*. Biomaterials, 2005. **26**(18): p. 3995-4021.
179. Arami, H., et al., *In vivo delivery, pharmacokinetics, biodistribution and toxicity of iron oxide nanoparticles*. Chemical Society Reviews, 2015. **44**(23): p. 8576-8607.
180. Reimer, P. and T. Balzer, *Ferucarbotran (Resovist): a new clinically approved RES-specific contrast agent for contrast-enhanced MRI of the liver: properties, clinical development, and applications*. European Radiology, 2003. **13**(6): p. 1266-1276.
181. Barrow, M., et al., *Design considerations for the synthesis of polymer coated iron oxide nanoparticles for stem cell labelling and tracking using MRI*. Chemical Society Reviews, 2015. **44**(19): p. 6733-6748.
182. Basuki, J.S., et al., *Grafting of P(OEGA) Onto Magnetic Nanoparticles Using Cu(0) Mediated Polymerization: Comparing Grafting "from" and "to" Approaches in the Search for the Optimal Material Design of Nanoparticle MRI Contrast Agents*. Macromolecules, 2013. **46**(15): p. 6038-6047.
183. Basuki, J.S., et al., *Magnetic nanoparticles with diblock glycopolymer shells give lectin concentration-dependent MRI signals and selective cell uptake*. Chemical Science, 2014. **5**(2): p. 715-726.
184. Ruiz-Cabello, J., et al., *Fluorine (<sup>19</sup>F) MRS and MRI in biomedicine*. NMR in biomedicine, 2011. **24**(2): p. 114-129.
185. Tirotta, I., et al., *<sup>19</sup>F Magnetic Resonance Imaging (MRI): From Design of Materials to Clinical Applications*. Chemical Reviews, 2015. **115**(2): p. 1106-1129.
186. Wang, K., *Multifunctional Nanostructured Polymers for Improved <sup>19</sup>F MRI in Australian Institute for Bioengineering and Nanotechnology*. 2014, The University of Queensland Brisbane, Australia. p. 223.

187. Perazella, M.A., *Gadolinium-contrast toxicity in patients with kidney disease: nephrotoxicity and nephrogenic systemic fibrosis*. *Curr Drug Saf*, 2008. **3**(1): p. 67-75.
188. Dagher, A.P., et al., *Imaging of urea using chemical exchange-dependent saturation transfer at 1.5T*. *J Magn Reson Imaging*, 2000. **12**(5): p. 745-8.
189. Sherry, A.D. and M. Woods, *Chemical Exchange Saturation Transfer Contrast Agents for Magnetic Resonance Imaging*. Annual review of biomedical engineering, 2008. **10**: p. 391-411.
190. Ward, K.M., A.H. Aletras, and R.S. Balaban, *A New Class of Contrast Agents for MRI Based on Proton Chemical Exchange Dependent Saturation Transfer (CEST)*. *Journal of Magnetic Resonance*, 2000. **143**(1): p. 79-87.
191. McMahon, M.T., et al., *New "multicolor" polypeptide diamagnetic chemical exchange saturation transfer (DIACEST) contrast agents for MRI*. *Magnetic Resonance in Medicine*, 2008. **60**(4): p. 803-812.
192. Wu, Y., et al., *Polymeric PARACEST Agents for Enhancing MRI Contrast Sensitivity*. *Journal of the American Chemical Society*, 2008. **130**(42): p. 13854-13855.
193. Zhang, S., et al., *A Novel Class of Polymeric pH-Responsive MRI CEST Agents*. *Chemical communications (Cambridge, England)*, 2013. **49**(57): p. 6418-6420.
194. Liu, Z., et al., *Pulmonary hyperpolarized noble gas MRI: recent advances and perspectives in clinical application*. *European journal of radiology*, 2014. **83**(7): p. 1282-1291.
195. Park, I., et al., *Changes in Pyruvate Metabolism Detected by Magnetic Resonance Imaging Are Linked to DNA Damage and Serve as a Sensor of Temozolomide Response in Glioblastoma Cells*. *Cancer Research*, 2014. **74**(23): p. 7115-7124.
196. Mynar, J.L., et al., *Xenon biosensor amplification via dendrimer-cage supramolecular constructs*. *J Am Chem Soc*, 2006. **128**(19): p. 6334-5.
197. Webb, W.R., W. Brant, and N. Major, *Fundamentals of body CT*. 3 ed. 2005, Philadelphia, USA: Saunders Elsevier.
198. Lusic, H. and M.W. Grinstaff, *X-ray-Computed Tomography Contrast Agents*. *Chemical Reviews*, 2013. **113**(3): p. 1641-1666.
199. Smith-Bindman, R., et al., *Radiation dose associated with common computed tomography examinations and the associated lifetime attributable risk of cancer*. *Arch Intern Med*, 2009. **169**(22): p. 2078-86.
200. Röntgen, W.C., *On a New Kind of Rays*. *Science*, 1896. **3**(59): p. 227-231.
201. Kalender, W.A., *Computed Tomography: Fundamentals, System Technology, Image Quality, Applications*. 3 ed. 2011, Munich, Germany: Publicis.
202. Romans, L.E., *Computed Tomography for Technologists: A Comprehensive Text*. 1 ed. 2010, Baltimore, United States: Lippincott Williams & Wilkins.
203. Lee, N., S.H. Choi, and T. Hyeon, *Nano-Sized CT Contrast Agents*. *Advanced Materials*, 2013. **25**(19): p. 2641-2660.
204. Yu, S.B. and A.D. Watson, *Metal-based X-ray contrast media*. *Chemical Reviews*, 1999. **99**(9): p. 2353-2377.
205. Aviv, H., et al., *Radiopaque iodinated copolymeric nanoparticles for X-ray imaging applications*. *Biomaterials*, 2009. **30**(29): p. 5610-6.
206. Torchilin, V.P., M.D. Frank-Kamenetsky, and G.L. Wolf, *CT visualization of blood pool in rats by using long-circulating, iodine-containing micelles*. *Acad Radiol*, 1999. **6**(1): p. 61-5.
207. Kim, D., et al., *Antibiofouling Polymer-Coated Gold Nanoparticles as a Contrast Agent for in Vivo X-ray Computed Tomography Imaging*. *Journal of the American Chemical Society*, 2007. **129**(24): p. 7661-7665.
208. Coche, E.E., F.D. Hammer, and P.P. Goffette, *Demonstration of pulmonary embolism with gadolinium-enhanced spiral CT*. *Eur Radiol*, 2001. **11**(11): p. 2306-9.
209. Vera, D.R. and R.F. Mattrey, *A molecular CT blood pool contrast agent*. *Acad Radiol*, 2002. **9**(7): p. 784-92.
210. Zhang, G., et al., *Dual modal in vivo imaging using upconversion luminescence and enhanced computed tomography properties*. *Nanoscale*, 2011. **3**(10): p. 4365-4371.
211. Hahn, M.A., et al., *Nanoparticles as contrast agents for in-vivo bioimaging: current status and future perspectives*. *Anal Bioanal Chem*, 2011. **399**(1): p. 3-27.
212. Xi, D., et al., *Gold nanoparticles as computerized tomography (CT) contrast agents*. *RSC Advances*, 2012. **2**(33): p. 12515-12524.
213. Hainfeld, J.F., et al., *Micro-CT enables microlocalisation and quantification of Her2-targeted gold nanoparticles within tumour regions*. *Br J Radiol*, 2011. **84**(1002): p. 526-33.

214. Rahmim, A. and H. Zaidi, *PET versus SPECT: strengths, limitations and challenges*. Nucl Med Commun, 2008. **29**(3): p. 193-207.
215. Celler, A., *Nuclear Medicine: SPECT and PET Imaging Principles*, in *Medical Imaging*. 2009, John Wiley & Sons, Inc. p. 101-126.
216. Roarke, M.C., B.D. Nguyen, and B.A. Pockaj, *Applications of SPECT/CT in Nuclear Radiology*. American Journal of Roentgenology, 2008. **191**(3): p. W135-W150.
217. Gomes, C.M., et al., *Molecular imaging with SPECT as a tool for drug development*. Advanced Drug Delivery Reviews, 2011. **63**(7): p. 547-554.
218. Vallabhajosula, S., *Molecular Imaging: Radiopharmaceuticals for PET and SPECT*. 1 ed. 2009, Berlin Heidelberg: Springer-Verlag.
219. Agdeppa, E.D. and M.E. Spilker, *A Review of Imaging Agent Development*. The AAPS Journal, 2009. **11**(2): p. 286-299.
220. Khalil, M.M., et al., *Molecular SPECT Imaging: An Overview*. International Journal of Molecular Imaging, 2011. **2011**.
221. Crane, P., et al., *Effect of mitochondrial viability and metabolism on technetium-99m-sestamibi myocardial retention*. European Journal of Nuclear Medicine, 1993. **20**(1): p. 20-25.
222. Scarsbrook, A.F., et al., *Anatomic and Functional Imaging of Metastatic Carcinoid Tumors*. RadioGraphics, 2007. **27**(2): p. 455-477.
223. Kahn, D., et al., *The Utility of 99mTc Depreotide Compared With F-18 Fluorodeoxyglucose Positron Emission Tomography and Surgical Staging in Patients With Suspected Non-small Cell Lung Cancer*. Chest, 2004. **125**(2): p. 494-501.
224. Maguire, R.T., et al., *Immunoscintigraphy in patients with colorectal, ovarian, and prostate cancer. Results with site-specific immunoconjugates*. Cancer, 1993. **72**(11 Suppl): p. 3453-62.
225. Madru, R., et al., *99mTc-Labeled Superparamagnetic Iron Oxide Nanoparticles for Multimodality SPECT/MRI of Sentinel Lymph Nodes*. Journal of Nuclear Medicine, 2012. **53**(3): p. 459-463.
226. Zhang, R., et al., *Peptide-conjugated polymeric micellar nanoparticles for Dual SPECT and optical imaging of EphB4 receptors in prostate cancer xenografts*. Biomaterials, 2011. **32**(25): p. 5872-9.
227. Torres Martin de Rosales, R., et al., *99mTc-Bisphosphonate-Iron Oxide Nanoparticle Conjugates for Dual-Modality Biomedical Imaging*. Bioconjugate Chemistry, 2011. **22**(3): p. 455-465.
228. Carlton, R.R. and A. McKenna-Adler, *Principles of Radiographic Imaging: An Art and A Science*. 5 ed. Vol. 1. 2012: Cengage Learning. 864.
229. Wernick, M.N. and J.N. Aarsvold, *Emission Tomography: The Fundamentals of PET and SPECT*. Revised ed. 2004: Academic Press.
230. Singh, H., A. Sasane, and R. Lodha, *Textbook of Radiology Physics*. 1 ed. 2016, New Delhi, India: Jaypee Brothers Medical Publishers.
231. Ametamey, S.M., M. Honer, and P.A. Schubiger, *Molecular Imaging with PET*. Chemical Reviews, 2008. **108**(5): p. 1501-1516.
232. Nedrow, J.R., et al., *Positron Emission Tomographic Imaging of Copper 64- and Gallium 68-Labeled Chelator Conjugates of the Somatostatin Agonist Tyr(3)-Octreotate*. Molecular imaging, 2014. **13**: p. DOI 10.2310/7290.2014.00020.
233. Alauddin, M.M., *Positron emission tomography (PET) imaging with (18)F-based radiotracers*. American Journal of Nuclear Medicine and Molecular Imaging, 2012. **2**(1): p. 55-76.
234. Liu, R.S., et al., *Biodistribution, pharmacokinetics and PET imaging of [(18)F]FMISO, [(18)F]FDG and [(18)F]FAC in a sarcoma- and inflammation-bearing mouse model*. Nucl Med Biol, 2009. **36**(3): p. 305-12.
235. Stockhofe, K., et al., *Radiolabeling of Nanoparticles and Polymers for PET Imaging*. Pharmaceuticals (Basel), 2014. **7**(4): p. 392-418.
236. Guerrero, S., et al., *Synthesis and in vivo evaluation of the biodistribution of a 18F-labeled conjugate gold-nanoparticle-peptide with potential biomedical application*. Bioconjug Chem, 2012. **23**(3): p. 399-408.
237. Herth, M.M., et al., *Radioactive Labeling of Defined HPMA-Based Polymeric Structures Using [18F]FETos for In Vivo Imaging by Positron Emission Tomography*. Biomacromolecules, 2009. **10**(7): p. 1697-1703.
238. Allmeroth, M., et al., *Modifying the body distribution of HPMA-based copolymers by molecular weight and aggregate formation*. Biomacromolecules, 2011. **12**(7): p. 2841-9.

239. Anderson, C.J. and R. Ferdani, *Copper-64 Radiopharmaceuticals for PET Imaging of Cancer: Advances in Preclinical and Clinical Research*. Cancer Biotherapy & Radiopharmaceuticals, 2009. **24**(4): p. 379-393.
240. Welch, M.J., C.J. Hawker, and K.L. Wooley, *The advantages of nanoparticles for PET*. J Nucl Med, 2009. **50**(11): p. 1743-6.
241. Fukukawa, K.-i., et al., *Synthesis and Characterization of Core–Shell Star Copolymers for In Vivo PET Imaging Applications*. Biomacromolecules, 2008. **9**(4): p. 1329-1339.
242. Cartier, R., et al., *Latex nanoparticles for multimodal imaging and detection in vivo*. Nanotechnology, 2007. **18**(19): p. 195102.
243. Stelter, L., et al., *Modification of aminosilanized superparamagnetic nanoparticles: feasibility of multimodal detection using 3T MRI, small animal PET, and fluorescence imaging*. Mol Imaging Biol, 2010. **12**(1): p. 25-34.
244. Choi, J.S., et al., *A hybrid nanoparticle probe for dual-modality positron emission tomography and magnetic resonance imaging*. Angew Chem Int Ed Engl, 2008. **47**(33): p. 6259-62.
245. Wells, P.N.T., *Physics and engineering: milestones in medicine*. Medical Engineering and Physics. **23**(3): p. 147-153.
246. Azhari, H., *Ultrasound: Medical Imaging And Beyond (An Invited Review)*. Current Pharmaceutical Biotechnology, 2012. **13**(11): p. 2104-2116.
247. Carovac, A., F. Smajlovic, and D. Junuzovic, *Application of Ultrasound in Medicine*. Acta Informatica Medica, 2011. **19**(3): p. 168-171.
248. Goldberg, B.B., J.-B. Liu, and F. Forsberg, *Ultrasound contrast agents: A review*. Ultrasound in Medicine and Biology, 1994. **20**(4): p. 319-333.
249. Sirsi, S. and M. Borden, *Microbubble Compositions, Properties and Biomedical Applications*. Bubble science engineering and technology, 2009. **1**(1-2): p. 3-17.
250. Calliada, F., et al., *Ultrasound contrast agents: basic principles*. Eur J Radiol, 1998. **27 Suppl 2**: p. S157-60.
251. Klibanov, A.L., *Microbubble Contrast Agents: Targeted Ultrasound Imaging and Ultrasound-Assisted Drug-Delivery Applications*. Investigative Radiology, 2006. **41**(3): p. 354-362.
252. Cui, W., et al., *Preparation and evaluation of poly(L-lactide-co-glycolide) (PLGA) microbubbles as a contrast agent for myocardial contrast echocardiography*. Journal of Biomedical Materials Research Part B: Applied Biomaterials, 2005. **73B**(1): p. 171-178.
253. Böhmer, M.R., et al., *Preparation of monodisperse polymer particles and capsules by ink-jet printing*. Colloids and Surfaces A: Physicochemical and Engineering Aspects, 2006. **289**(1–3): p. 96-104.
254. Frangioni, J.V., *In vivo near-infrared fluorescence imaging*. Current Opinion in Chemical Biology, 2003. **7**(5): p. 626-634.
255. Ntziachristos, V., C. Bremer, and R. Weissleder, *Fluorescence imaging with near-infrared light: new technological advances that enable in vivo molecular imaging*. European Radiology, 2003. **13**(1): p. 195-208.
256. Zhang, X., et al., *Near-infrared Molecular Probes for In Vivo Imaging*. Current Protocols in Cytometry, 2012. Chapter 12: Unit 12.27.
257. Barrett, T., et al., *In vivo diagnosis of epidermal growth factor receptor expression using molecular imaging with a cocktail of optically labeled monoclonal antibodies*. Clin Cancer Res, 2007. **13**(22 Pt 1): p. 6639-48.
258. Kim, S., et al., *Near-infrared fluorescent type II quantum dots for sentinel lymph node mapping*. Nat Biotech, 2004. **22**(1): p. 93-97.
259. Martí-Bonmatí, L., et al., *Multimodality imaging techniques*. Contrast Media & Molecular Imaging, 2010. **5**(4): p. 180-189.
260. Townsend, D.W., *Multimodality imaging of structure and function*. Physics in Medicine and Biology, 2008. **53**(4): p. R1.
261. Hasegawa, B.H., et al. *Description of a simultaneous emission-transmission CT system*. 1990.
262. Ell, P.J., *The contribution of PET/CT to improved patient management*. Br J Radiol, 2006. **79**(937): p. 32-6.
263. Hu, Z., et al., *From PET/CT to PET/MRI: advances in instrumentation and clinical applications*. Mol Pharm, 2014. **11**(11): p. 3798-809.
264. Brenner, D.J. and E.J. Hall *Computed Tomography — An Increasing Source of Radiation Exposure*. New England Journal of Medicine, 2007. **357**(22): p. 2277-2284.

265. Cherry, S.R., A.Y. Louie, and R.E. Jacobs, *The Integration of Positron Emission Tomography With Magnetic Resonance Imaging*. Proceedings of the IEEE, 2008. **96**(3): p. 416-438.
266. Louie, A., *Multimodality Imaging Probes: Design and Challenges*. Chemical Reviews, 2010. **110**(5): p. 3146-3195.
267. Garcia, J., T. Tang, and A.Y. Louie, *Nanoparticle-based multimodal PET/MRI probes*. Nanomedicine (Lond), 2015. **10**(8): p. 1343-59.
268. Langereis, S., et al., *Paramagnetic liposomes for molecular MRI and MRI-guided drug delivery*. NMR Biomed, 2013. **26**(7): p. 728-44.
269. Zheng, J., et al., *Multimodal contrast agent for combined computed tomography and magnetic resonance imaging applications*. Invest Radiol, 2006. **41**(3): p. 339-48.
270. Kircher, M.F., et al., *A multimodal nanoparticle for preoperative magnetic resonance imaging and intraoperative optical brain tumor delineation*. Cancer Res, 2003. **63**(23): p. 8122-5.
271. Lee, H.Y., et al., *PET/MRI dual-modality tumor imaging using arginine-glycine-aspartic (RGD)-conjugated radiolabeled iron oxide nanoparticles*. J Nucl Med, 2008. **49**(8): p. 1371-9.
272. Devaraj, N.K., et al., *<sup>18</sup>F Labeled Nanoparticles for in Vivo PET-CT Imaging*. Bioconjugate Chemistry, 2009. **20**(2): p. 397-401.
273. Zhu, X., et al., *Core-shell Fe<sub>3</sub>O<sub>4</sub>@NaLuF<sub>4</sub>:Yb,Er/Tm nanostructure for MRI, CT and upconversion luminescence tri-modality imaging*. Biomaterials, 2012. **33**(18): p. 4618-4627.
274. Sudheendra, L., et al., *NaGdF<sub>4</sub>:Eu<sup>3+</sup> Nanoparticles for Enhanced X-ray Excited Optical Imaging*. Chemistry of Materials, 2014. **26**(5): p. 1881-1888.
275. Rolfe, B.E., et al., *Multimodal Polymer Nanoparticles with Combined <sup>19</sup>F Magnetic Resonance and Optical Detection for Tunable, Targeted, Multimodal Imaging in Vivo*. Journal of the American Chemical Society, 2014. **136**(6): p. 2413-2419.
276. Majmudar, M.D., et al., *Polymeric Nanoparticle PET/MR Imaging Allows Macrophage Detection in Atherosclerotic Plaques*. Circulation Research, 2013. **112**(5): p. 755-761.
277. Cole, A.J., V.C. Yang, and A.E. David, *Cancer theranostics: the rise of targeted magnetic nanoparticles*. Trends Biotechnol, 2011. **29**(7): p. 323-32.
278. Lammers, T., et al., *Theranostic nanomedicine*. Acc Chem Res, 2011. **44**(10): p. 1029-38.
279. Evans, C., *Theranostic nanoparticles give the best of both worlds*. Science Translational Medicine, 2016. **8**(348): p. 348ec114-348ec114.
280. Kim, T.H., S. Lee, and X. Chen, *Nanotheranostics for personalized medicine*. Expert Rev Mol Diagn, 2013. **13**(3): p. 257-69.
281. Sharma, H., et al., *Metal nanoparticles: a theranostic nanotool against cancer*. Drug Discovery Today, 2015. **20**(9): p. 1143-1151.
282. Ryu, J.H., et al., *Theranostic nanoparticles for future personalized medicine*. Journal of Controlled Release, 2014. **190**: p. 477-484.
283. Nasongkla, N., et al., *Multifunctional Polymeric Micelles as Cancer-Targeted, MRI-Ultrasensitive Drug Delivery Systems*. Nano Letters, 2006. **6**(11): p. 2427-2430.
284. Li, Y., et al., *Nanoparticles Based on Star Polymers as Theranostic Vectors: Endosomal-Triggered Drug Release Combined with MRI Sensitivity*. Advanced Healthcare Materials, 2015. **4**(1): p. 148-156.
285. Ardana, A., A.K. Whittaker, and K.J. Thurecht, *PEG-Based Hyperbranched Polymer Theranostics: Optimizing Chemistries for Improved Bioconjugation*. Macromolecules, 2014. **47**(15): p. 5211-5219.
286. Liu, Y., et al., *Theranostic near-infrared fluorescent nanoplatform for imaging and systemic siRNA delivery to metastatic anaplastic thyroid cancer*. Proceedings of the National Academy of Sciences, 2016. **113**(28): p. 7750-7755.
287. Ling, D., et al., *Multifunctional Tumor pH-Sensitive Self-Assembled Nanoparticles for Bimodal Imaging and Treatment of Resistant Heterogeneous Tumors*. J Am Chem Soc, 2014.
288. Basuki, J.S., et al., *Using Fluorescence Lifetime Imaging Microscopy to Monitor Theranostic Nanoparticle Uptake and Intracellular Doxorubicin Release*. ACS Nano, 2013. **7**(11): p. 10175-10189.
289. Hu, X., et al., *Cell-penetrating hyperbranched polyprodrug amphiphiles for synergistic reductive milieu-triggered drug release and enhanced magnetic resonance signals*. J Am Chem Soc, 2015. **137**(1): p. 362-8.
290. Murakami, M., et al., *Improving drug potency and efficacy by nanocarrier-mediated subcellular targeting*. Sci Transl Med, 2011. **3**(64): p. 64ra2.

## Chapter 2: Polymerization-Induced Self-Assembly - Control over Morphology for Drug Delivery

## 2.1 Introduction

As described in the introduction, drug delivery carriers, such as polymeric nanoparticles, organic/inorganic nanoparticles, and dendrimers, have been widely used for therapeutic treatments in oncology and cardiovascular disease, as they can increase therapeutic efficacy by changing biodistribution via passive or active targeting. [1, 2] A number of different polymeric drug delivery platforms have already been used in human trials with very promising results. [3] Most commonly, spherical nanoparticles have been used for drug delivery. In contrast, other morphologies have received little attention, despite evidence that not only size but also morphology can make a considerable difference to the efficacy of drug delivery [2, 4-13].

DeSimone and co-workers [14] prepared different polymeric nanoparticles using top-down lithography fabrication, and subsequently demonstrated that cylindrical sub-micrometric particles presented higher cell uptake than equivalent cubic particles. In a more recent study by Ruoslahti, Mitragotri and co-workers [15], a higher cell uptake of polystyrene (PST) rods (compared to PST nanospheres) was reported. The same authors also demonstrated a preferential cell uptake of nanorods in targeted tissues using C57Bl/6 male mice. [16, 17] Thus, the published evidence strongly indicates that the nanoparticle morphology can play a key role in governing biodistribution and bioactivity. In the current study, different morphologies of polymeric nanoparticles were prepared using self-assembly of asymmetric block copolymers. [18, 19]

The first studies highlighting self-assembly of asymmetric block copolymers in solution were reported by Eisenberg's group, [20] using self-assembly of polystyrene-*b*-polyacrylic acid diblock copolymers. Different nanoparticle morphologies (spherical micelles, [21-23] worm-like micelles [5, 24-26] and vesicles [27-31] were obtained by self-assembly using co-solvency manipulation. One of the main drawbacks of the Eisenberg approach is the low polymer concentrations required (around 1%, w/w), limiting scale-up. There have been a number of recent synthetic developments addressing the problem of low concentration, as described in papers by An, [32, 33] Charleux, [34-38] Armes [39-47] and Pan [48-52]. The common feature of the three new approaches is the exploitation of simultaneously inducing self-assembly during the actual polymerization process. Inspired by the initial work of Armes [39] and Pan [48], a new approach was developed to synthesize polymeric nanoparticles with morphological control, using polymerization-induced self-assembly (PISA).

The PISA concept is based on the chain extension of homopolymers with a co-monomer to yield asymmetric block copolymers. During the chain extension with the second block, self-assembly is induced by the insolubility of the second block in the polymerization solution. The PISA approach can

be used to prepare families of nanoparticles varying in morphology using a single initial homopolymer via a simple one-pot reaction.

In this chapter, a one-pot RAFT dispersion polymerization with simultaneous self-assembly into controlled structures is reported. Morphologies including spherical, worm-like and rod-like micelles and vesicles were formed from well-defined amphiphilic block copolymers, poly[oligo(ethyleneglycol) methyl ether methacrylate]-block-[poly(styrene)-co-poly(vinyl benzaldehyde)] (POEGMA-*b*-P(ST-co-VBA)), which were synthesized by chain extension of dithiobenzoate functional POEGMA using RAFT polymerization. POEGMA was incorporated as the first block as it is hydrophilic, biocompatible and has anti-immunogenic properties. [3] VBA was selected as functional group as the aldehyde can be used to conjugate doxorubicin via a pH-sensitive imine linker. [3] Finally, the extremely hydrophobic PST segment was selected for its high glass transition temperature ensuring stability of the polymeric nanoparticles and enabling PISA. [28, 39, 48]

Morphology control was achieved by manipulating the number-average degree of polymerization ( $DP_n$ ) of the P(ST-co-VBA) blocks in the methanol polymerization medium. As the  $DP_n$  of the core polymer increased (with conversion) the block copolymers assembled sequentially into spherical micelles, worm-like micelles, rod-like micelles and vesicles, as determined by transmission electron microscopy (TEM). The aldehyde groups positioned in the core of the micellar structures were subsequently reacted with various amino compounds to either conjugate chemotherapy drugs or to crosslink the nanostructures. Diamino compounds were employed to crosslink the core nanoparticles using pH-responsive bonds (imines). The aldehyde groups were also exploited to conjugate doxorubicin (DOX, a commonly employed chemotherapy drug) via pH labile bonds (Schiff base or imine), with a drug loading of 5 wt%. The drug-loaded, self-assembled nanoparticles were then used to deliver DOX to breast cancer cells (MCF-7). Flow cytometry and confocal microscopy revealed different cell uptake mediated by the different nanoparticle morphologies. Cell viability assays using MCF-7 breast cancer cells were also conducted showing a significant effect of morphology on cytotoxicity.

## 2.2 Experimental Section

### 2.2.1 Materials

Styrene (ST, Sigma-Aldrich,  $\geq 99\%$ ) and 3-vinylbenzaldehyde (97%) were disinhibited by passing through a column of basic alumina (Sigma-Aldrich). Oligo(ethylene glycol) methyl ether methacrylate (OEGMA, average  $M_n = 300 \text{ g mol}^{-1}$ ), 1,3-diaminopropane ( $\geq 99\%$ ), sodium borohydride ( $\geq 98\%$ ), and doxorubicin·HCl ( $\geq 98\%$ ), were used as received from Sigma-Aldrich. Azobis(isobutyronitrile) (AIBN, Fluka, 98%) was purified by recrystallization from methanol. 4-Cyanopentanoic acid dithiobenzoate (CPADB) was prepared according to a procedure described elsewhere.[53]

### 2.2.2 Physical and analytical methods

#### *$^1\text{H}$ NMR*

$^1\text{H}$  NMR spectra were recorded using a Bruker Avance 300 (300 MHz) spectrometer.  $\text{CDCl}_3$  was used as solvent. All chemical shifts are reported in ppm ( $\delta$ ) relative to tetramethylsilane, referenced to the chemical shifts of residual solvent resonance ( $\text{CDCl}_3 = 7.26 \text{ ppm}$ ).

#### *Size exclusion chromatography*

Size exclusion chromatography (SEC) was implemented using a Shimadzu modular system comprising a DGU-12A degasser, a LC-10AT pump, a SIL-10AD automatic 304 injector, a CTO-10A column oven, a RID-10A refractive index detector, and a SPD-10A Shimadzu UV/Vis detector. A  $50 \times 7.8 \text{ mm}$  guard column and four  $300 \times 7.8 \text{ mm}$  linear columns ( $500$ ,  $10^3$ ,  $10^4$ , and  $10^5 \text{ \AA}$  pore size,  $5 \text{ }\mu\text{m}$  particle size) were used for the analyses. *N,N'*-dimethylacetamide (DMAc, HPLC grade, 0.05% w/v 2,6-dibutyl-4-methylphenol, 0.03% w/v lithium bromide) with a flow rate of  $1 \text{ mL min}^{-1}$  and a constant temperature of  $50 \text{ }^\circ\text{C}$  was used as the mobile phase with an injection volume of  $50 \text{ }\mu\text{L}$ . The samples were filtered through  $0.45 \text{ }\mu\text{m}$  PTFE filters. The unit was calibrated using commercially available linear polystyrene standards ( $0.5\text{--}1000 \text{ kDa}$ , Polymer Laboratories). Chromatograms were processed using Cirrus 2.0 software (Polymer Laboratories).

### *Transmission electron microscopy*

The sizes and morphologies of the block copolymers were observed using a JEOL 1400 transmission electron microscope (TEM) at an accelerating voltage of 100 kV. The solution of the block copolymers in dispersion medium was directly taken and diluted with methanol (2 mg mL<sup>-1</sup>) and deposited onto copper grid (ProSciTech). Uranyl acetate staining was applied and the samples were dried.

### *Dynamic light scattering*

DLS measurements were performed using a Malvern Zetasizer Nano Series running DTS software and using a 4 mW He-Ne laser operating at a wavelength of 633 nm and an avalanche photodiode detector. The scattered light was detected at an angle of 173°.

### *Attenuated Total Reflection-Fourier Transform Infrared Spectroscopy*

ATR-FTIR measurements were performed using a Bruker IFS66\S Fourier transform spectrometer by averaging 128 scans with a resolution of 4 cm<sup>-1</sup>.

### *Ultraviolet-visible spectrophotometry*

UV-Vis spectra were recorded using a Varian CARY 300 spectrophotometer. The amount of incorporated doxorubicin was determined by measuring the absorbance at 495 nm using a quartz cuvette.

### *Cell culture*

MCF-7 cells were grown in Dulbecco's Modified Eagle's Medium: Nutrient Mix F-12 (DMEM) supplemented with 10 % (v/v) Fetal Calf Serum (FCS) in a ventilated tissue culture flask T-75. The cells were incubated at 37° C in a 5 % CO<sub>2</sub>-humidified atmosphere and passaged every 2 - 3 days when monolayers at around 80% confluence were formed. Cell density was determined by counting the number of viable cells using a trypan blue dye (Sigma-Aldrich) exclusion test. For passaging and plating, cells were detached using 0.05 % trypsin-EDTA (Invitrogen), stained using trypan blue dye, and loaded on the haemocytometer. All the experiments were done in triplicate.

### *Cell viability*

The cytotoxicity of free DOX, dextran nanoparticles, and DOX-loaded nanoparticles was tested *in-vitro* by a standard Alamar Blue Assay. The assay is based on the ability of living cells to convert blue redox

dye (resazurin) into bright red resorufin which can be read in a spectrophometric reader. Nonviable cells rapidly lose metabolic capacity and thus do not generate a colour signal. The intensity of the colour is proportional to the cell viability. The cells were seeded at 10,000 cells/well for MCF-7 in 96 well tissue culture plates and incubated for 24 h. The medium was then replaced with fresh medium containing free DOX, dextran nanoparticles, and DOX-loaded nanoparticles over an equivalent DOX concentration range of 0.001 – 50  $\mu$ M. At 72 h post drug/nanoparticle incubation, treatments were removed and fresh media was added (100  $\mu$ L) followed by the addition of Alamar Blue dye (20  $\mu$ L) to each well and the cells were incubated for 6 h. Cell viability was determined as a percentage of untreated control cells, and IC<sub>50</sub> values were calculated via regression analysis using Microsoft Excel.

#### *In-vitro cell uptake by flow cytometry and confocal microscopy*

To examine nanoparticle uptake, MCF7 cells were seeded at a density of  $2 \times 10^5$  cells/well in 6-well tissue culture plates. The cells were left to grow for 24 h in DMEM media containing 10 % FBS at 37 °C in 5 % CO<sub>2</sub> atmosphere. After 24 h, doxorubicin loaded micelles were added to the wells (concentration of 0.125 $\mu$ M based on DOX) and the cells were incubated for 30 min, 1 h, 6 h, or 24 h. Following particle incubation, cells were rinsed twice with PBS to remove any non-uptaken nanoparticles. Cells were harvested by trypsinization and resuspended in 500  $\mu$ L of PBS for flow cytometry analysis using the FACScanto flow cytometer (BD Biosciences). Data shown are the mean fluorescent signal for 10,000 cells. MCF-7 cells that were not treated with nanoparticle solution were used as a control.

### 2.2.3 Syntheses

#### *Synthesis of poly(oligo(ethylene glycol) methyl ether methacrylate) (POEGMA) macro-CTA via RAFT polymerization*

A polymerization kinetics study of OEGMA was performed using the following procedure: OEGMA (6.0 g,  $2.0 \times 10^{-2}$  mol), CPADB (112 mg,  $4.06 \times 10^{-4}$  mol) and azobis(isobutyronitrile) (AIBN, 8.2 mg,  $5 \times 10^{-5}$  mol) were dissolved in 25 mL acetonitrile. The clear reaction mixture was then equally (5 mL each) divided into 6 vials, sealed with rubber septum and put into an ice-bath under continuous nitrogen flow for 30 minutes. The polymerization reaction was started by immersing the flasks into a pre-heated oil bath at 70 °C. Then each reaction flask was taken over 2 h time intervals up to 12 h and rapidly cooled in an ice-bath to terminate the polymerization. The conversion of the monomer during the polymerization was followed by taking a  $^1\text{H}$  NMR spectrum of the reaction solutions. The resulting polymers were purified by precipitating three times in 50 mL diethyl ether and petroleum spirit mixture (1:1, v/v) and dried under vacuum at room temperature for 24 h. Obtained results are given in Table 2.1.

POEGMA for the PISA experiments was prepared by RAFT polymerization in the presence of 4-cyanopentanoic acid dithiobenzoate (CPADB) as RAFT agent. For this purpose, OEGMA (12.0 g,  $4.00 \times 10^{-2}$  mol), CPADB (224 mg,  $8.00 \times 10^{-4}$  mol), AIBN (16.4 mg,  $1.00 \times 10^{-4}$  mol) and 50 mL acetonitrile were mixed in a 100 mL round bottom flask and sealed with rubber septum. The reaction mixture was immersed into an ice-bath and saturated with nitrogen by continuous gas flow for 30 minutes. The polymerization reaction was carried out for 8 h at 70 °C. The polymerization reaction was then terminated by rapid cooling and the resulting polymer was recovered by three times precipitation in a 50 mL diethyl ether and petroleum spirit (boiling range of 40-60 °C) mixture (1:1, v/v). The molecular weight of the dried POEGMA macro-CTA was determined by size exclusion chromatography (SEC) with  $M_{n,\text{SEC}}$  of  $9,500 \text{ g mol}^{-1}$  and  $\text{PDI} = 1.09$  (DMAc as mobile solvent and PST standards). The theoretical number average molecular weight ( $M_{n,\text{th}}$ ) was close to  $11,100 \text{ g mol}^{-1}$  from the conversion that was calculated from  $^1\text{H}$  NMR by comparing the vinyl peaks (6.05 and 5.5 ppm) to the methylene protons adjacent to the ester linkage at 4.1 ppm. The number of repeating units was also calculated from  $^1\text{H}$  NMR of the purified polymer sample by comparing RAFT agent's aromatic protons (between 7.9-7.4 ppm) to that of methylene protons adjacent to ester linkage at 4.1 ppm and was found to be 36.

The resulting POEGMA was used as macro-CTA for further block copolymer synthesis with styrene-vinyl benzaldehyde.

*Preparation of core functional POEGMA-*b*-P(ST-co-VBA) amphiphilic block copolymer via RAFT polymerization*

Core-functional POEGMA-*b*-P(ST-co-VBA) block copolymers with various morphologies were synthesized in methanol by RAFT dispersion polymerization with a molar feed ratio of ST : VBA : POEGMA : AIBN = 4750 : 250 : 1 : 0.5. For this purpose, POEGMA as a macro-CTA (222 mg,  $2.00 \times 10^{-5}$  mol), styrene (9.89 g,  $9.50 \times 10^{-2}$  mol), VBA (661 mg,  $5.00 \times 10^{-3}$  mol) as a functional monomer and AIBN (1.6 mg,  $1.00 \times 10^{-5}$  mol) were dissolved in 13.6 mL methanol (total monomer weight = total methanol weight). The reaction mixture was divided equally into eight vials to study the kinetics of the reaction. Each vial was sealed carefully and gently purged with nitrogen for 20 minutes. The reaction vials were then immersed in an oil bath at 70 °C, and the vials were taken out at specific time points: 4, 8, 12, 18, 24 and 36 hours. The polymerization was terminated by placing the reaction mixture into an ice-bath for 5 minutes and exposure to air. The polymer was purified by dialysis in methanol using a dialysis tube with a molecular weight cut off of 12,000 – 14,000 and changing the solvent three times. Morphologies and number average diameter of the block copolymer were investigated directly from the block copolymerization dispersion solution using samples diluted with methanol (2 mg/mL).

*Preparation of core-cross-linked POEGMA-*b*-P(ST-co-VBA) amphiphilic block copolymer*

Core-cross-linking of the block copolymer was achieved by reaction of aldehyde groups in the core with 1,3-diaminopropane in methanol at room temperature. For this purpose, 1,3-diaminopropane (3.4 mg,  $4.6 \times 10^{-5}$  mol) was reacted to  $2.3 \times 10^{-5}$  mol of aldehyde group containing (36 h sample, 60 mg) amphiphilic polymer dispersion in methanol and the reaction mixture was stirred for 48 h at room temperature. Cross-linking was tested by dissolving a few droplets in THF; the resulting solution did not lose its cloudiness. Subsequently, the obtained cross-linked sample was characterized by ATR-FTIR, DLS and TEM.

*Preparation of permanently core cross-linked POEGMA-*b*-P(ST-co-VBA) amphiphilic block copolymer*

Sodium borohydride (10.9 mg,  $2.88 \times 10^{-4}$  mol) was added to cross-linked POEGMA-*b*-P(ST-co-VBA) (containing  $7.7 \times 10^{-5}$  mol cross-linker) in methanol while stirring. The reaction was continued overnight and the vial was covered with a tissue to allow for  $H_{2(g)}$  release. Subsequently the reaction mixture was purified by dialysis in water (MWCO 12,000 – 14,000 Da) with repeated solvent changes.

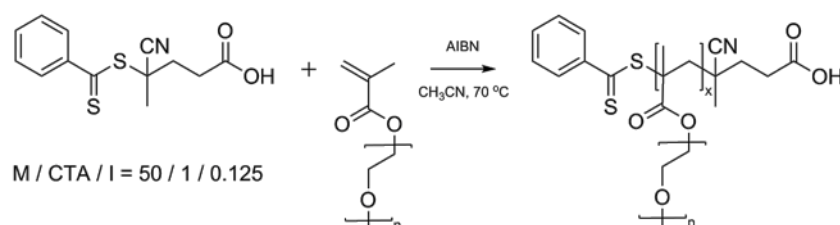
*Preparation of doxorubicin-loaded POEGMA-*b*-P(ST-co-VBA) amphiphilic block copolymer*

In the presence of triethylamine (50  $\mu\text{L}$ ,  $3.6 \times 10^{-4}$  mol), doxorubicin·HCl (2.0 mg,  $3.4 \times 10^{-6}$  mol) was dissolved in methanol containing POEGMA-*b*-P(ST-co-VBA) (5 mg) and the mixture was stirred at room temperature for 1 h. The mixture was first dialyzed (MWCO 3500 Da) against methanol for 24 h, and then against PBS buffer solution for 48 h to remove solvent, triethylamine, and free doxorubicin. The solution absorbance at 495 nm was measured on a CARY 300 spectrophotometer (Bruker) to determine the concentration. The amount of encapsulated DOX in the nanoparticles was quantified to be  $\sim 5.1$  wt% using a calibration curve of DOX·HCl in DMSO. The concentration of the polymers was determined by lyophilisation of a known volume.

## 2.3 Results and discussion

### Preparation of homopolymer macro-CTA

Initially, poly[oligo(ethyleneglycol) methyl ether methacrylate] (POEGMA) homopolymers were successfully synthesized using RAFT polymerization [54, 55] (Scheme 2.6) with 4-cyanopentanoic acid dithiobenzoate (CPADB) as a RAFT agent. The kinetics of the polymerization with a molar feed ratio of OEGMA : CPADB : AIBN = 10:500:1.25 in methanol at 70 °C were investigated by analysing the results at 2 h time intervals up to 12 h. The summary of molecular weights, polydispersities, and conversions for the polymerizations are given in Table 2.5 and Figure 2.15A. The data showed that the polymerization was well controlled with a low polydispersity index and high chain-end functionality.



Scheme 2.6: Synthesis of POEGMA homopolymer.

For the synthesis of the POEGMA macro-CTA, the same molar feed ratio was used, and the reaction was carried out for 12 h at 70 °C. The polymerization reaction was stopped at a conversion of around 60% to minimize the formation of dead polymers, yielding POEGMA with  $M_{n, \text{NMR}} = 11,100 \text{ g mol}^{-1}$  and PDI = 1.09 (Figure 2.15A).

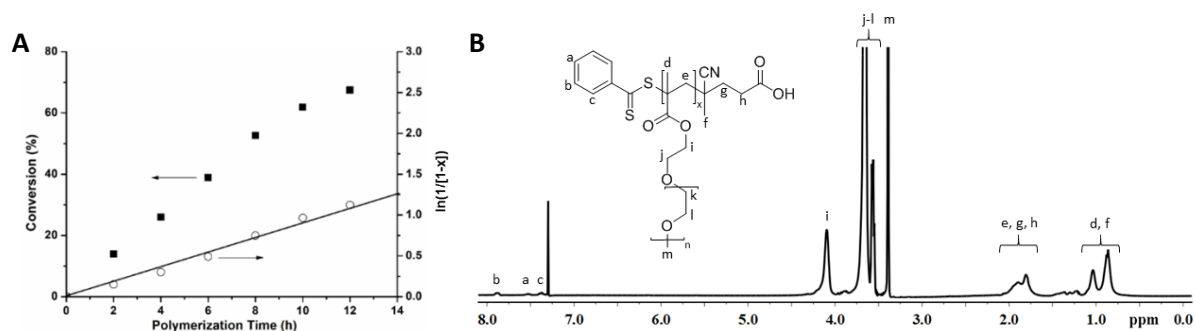


Figure 2.15: (A) Time-conversion and first-order kinetic plots for the polymerization of OEGMA in the presence of CPADB, and (B)  $^1\text{H}$  NMR spectra of POEGMA homopolymer recorded in  $\text{CDCl}_3$ .

Table 2.5: Conversion, molecular weight and polydispersity data for POEGMA homopolymers

Time (h)	Conversion (%) <sup>a</sup>	$M_{n,th}$ g mol <sup>-1</sup> <sup>b</sup>	$M_{n,SEC}$ g mol <sup>-1</sup> <sup>c</sup>	Yield (%) <sup>d</sup>	PDI
2	13.9	2400	4600	8.97	1.11
4	26.0	4200	6300	22.1	1.09
6	38.9	6100	8400	37.2	1.10
8	52.6	8200	10100	50.5	1.11
10	61.9	9600	11600	60.1	1.11
12	67.4	10400	12100	64.3	1.12

<sup>a</sup> OEGMA conversion was determined from <sup>1</sup>H NMR of the reaction mixture by comparing the vinyl peaks (6.05 and 5.50 ppm) to the methylene protons adjacent to the ester linkage at 4.1 ppm.

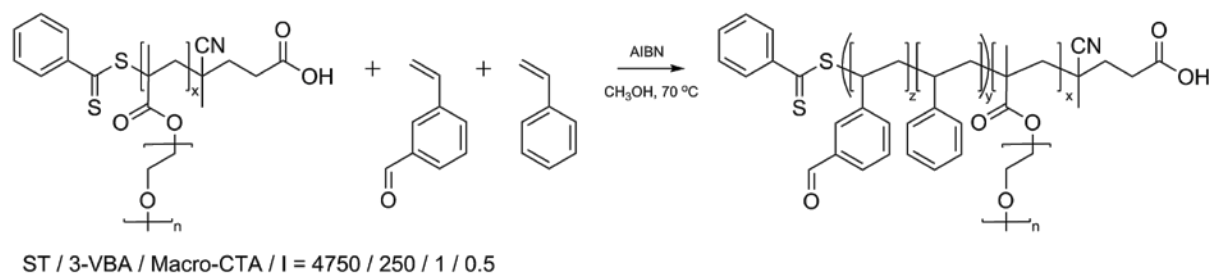
<sup>b</sup> NMR average molecular weight was calculated according to  $M_n = ([M]_0 / [RAFT]_0) \cdot \alpha \cdot M_{w,monomer} + M_{w,RAFT}$ , where  $[M]_0$ ,  $[RAFT]_0$ ,  $\alpha$ ,  $M_{w,monomer}$ ,  $M_{w,RAFT}$  are monomer RAFT agent concentration, monomer conversion molecular weights of monomer and RAFT agent, respectively.

<sup>c</sup> The experimental  $M_n$  and PDI were determined by SEC using dimethylacetamide as eluent solvent with polystyrene standards.

<sup>d</sup> Polymerization yield was determined gravimetrically.

#### Preparation of core functional POEGMA-*b*-P(ST-co-VBA) amphiphilic block copolymer with various morphologies

The POEGMA macro-CTA was then chain extended using a mixture of styrene (ST) and 3-vinylbenzaldehyde (VBA, 95 - 5 mol %) in methanol. The solvent, methanol, was chosen as the P(ST-co-VBA) block is insoluble in methanol, while in contrast, the monomers ST and VBA are soluble. The dispersion polymerization reactions were carried out at 70 °C using different polymerization times to control conversion and hence molecular weight (Scheme 2.7).



Scheme 2.7: Synthesis of POEGMA-*b*-P(OEGA-co-VBC).

To maintain good control over polymerization, it is important to maintain high RAFT end group fidelity and a constant radical concentration even under phase separation conditions. This high-level of control was maintained using a high molar feed ratio of 1 : 5000 for POEGMA : ST-VBA in methanol ( $w_{\text{solvent}} : w_{\text{monomer}} = 1 : 1$ ). After chain extension, the amphiphilic block copolymer structure was characterized by comparing  $^1\text{H}$  NMR spectra of the polymer chains before and after chain extension (Figure 2.15B and Figure 2.16A). Characteristic aldehyde proton and aromatic proton signals of PVBA were clearly observed at 9.9 ppm (m) and at 7.5 ppm (n) respectively confirming successful chain extension.

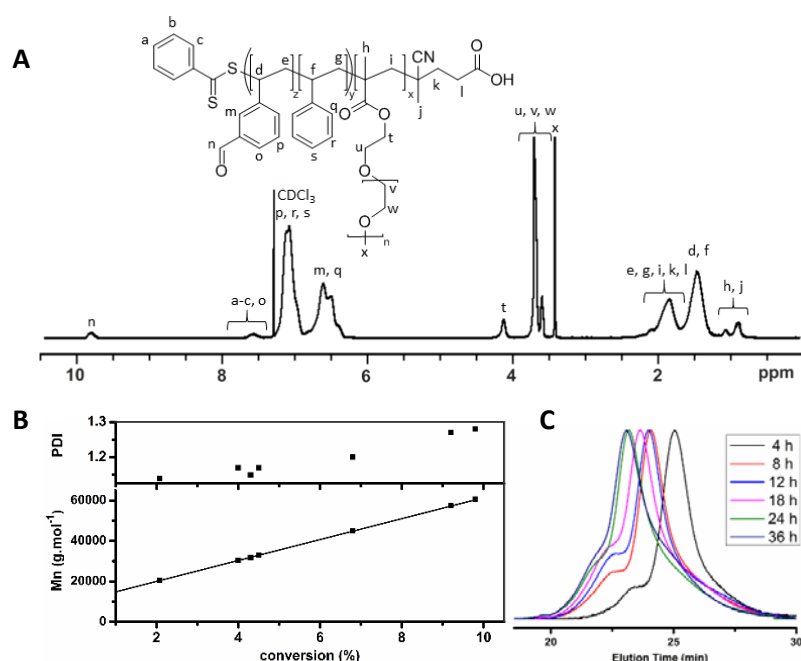


Figure 2.16: (A) POEGMA-*b*-P(OEGA-*co*-VBA) polymer recorded in  $\text{CDCl}_3$ , (B) evolution of molecular weight and PDI versus monomer conversion; (C) evolution of GPC traces versus polymerization time.

Table 2.6: Summary of the RAFT dispersion block copolymerization of styrene and 5% vinyl benzaldehyde using POEGMA as a macro-CTA.

Time (h)	VBA Conv. (%) <sup>a</sup>	ST Conv. (%) <sup>b</sup>	Total Conv. (%) <sup>c</sup>	$M_{n,\text{th}}$ ( $\text{g mol}^{-1}$ ) <sup>d</sup>	$M_{n,\text{SEC}}$ ( $\text{g mol}^{-1}$ ) <sup>e</sup>	PDI
4	7.2	3.0	3.2	28300	26300	1.16
8	8.6	5.6	5.8	41700	33600	1.20
12	10	6.6	6.8	47200	37600	1.21
18	18	9.0	9.4	61500	40300	1.20
24	22	9.2	9.8	63800	43300	1.20
36	24	9.4	10	65600	44000	1.20

<sup>a</sup> VBA conversion was calculated from the <sup>1</sup>H NMR spectrum of the reaction mixture by dividing the aldehyde protons of the poly(vinylbenzaldehyde) peak (9.75 ppm) integral by the sum of the aldehyde protons of both the vinyl benzaldehyde (10.03 ppm) and PVBA peak integrals.

<sup>b</sup> ST conversion was calculated from the <sup>1</sup>H NMR spectrum of the reaction mixture by dividing the sum of the polystyrene and poly(vinyl benzaldehyde) aromatic protons integrals between 7.2 ppm to 6.3 ppm (divided by 5 and excluding the NMR signal of one vinyl proton of both monomer peaks between 6.83 and 6.68 ppm) with the sum of ST and VBA vinyl peaks (5.8 and 5.3 ppm, divided by 2) and a aforementioned.

<sup>c</sup> Total conversion was calculated using  $\text{Conv}_T = 0.95 \times \text{Conv}_{\text{ST}} + 0.05 \times \text{Conv}_{\text{VBA}}$

<sup>d</sup> NMR molecular weight was calculated according to  $M_{n,th} = ([M_{\text{ST}}]_0 / [\text{RAFT}]_0) \cdot X_{\text{ST}} \cdot \text{Mw}_{\text{ST}} + ([M_{\text{VBA}}]_0 / [\text{RAFT}]_0) \cdot X_{\text{VBA}} \cdot \text{Mw}_{\text{VBA}} + \text{Mw}_{\text{RAFT}}$ , where  $[M_{\text{ST}}]_0$ ,  $[M_{\text{VBA}}]_0$ ,  $[\text{RAFT}]_0$ ,  $X_{\text{ST}}$ ,  $X_{\text{VBA}}$ ,  $\text{Mw}_{\text{ST}}$ ,  $\text{Mw}_{\text{VBA}}$  and  $\text{Mw}_{\text{RAFT}}$  are monomers and RAFT agent concentration, monomers conversion, molecular weight of monomer and RAFT agent, respectively.

<sup>e</sup> The experimental  $M_n$  and PDI were determined by SEC using dimethylacetamide as eluent solvent with polystyrene standards.

During the chain extension of POEGMA, molecular weight values and polydispersity indices of sample block copolymers were determined by <sup>1</sup>H NMR spectroscopy and SEC measurements taken at different polymerization times (Table 2.6). VBA was observed to be incorporated preferentially over ST. The molecular weight values determined by NMR and SEC were in accord with theoretical values showing a linear increase with conversion (Figure 2.16B) and low PDIs, consistent with the known traits of living polymerization.[56] SEC traces of the block copolymers taken at increasing polymerization times (Figure 2.16C) indicate unimodal molecular weight distributions and incremental shifts to lower retention times. The presence of molecular weight shoulders at lower retention times is consistent with the formation of dead polymers by coupling reactions, in accordance with a slight increase in PDI (1.16 to 1.21) (Table 2.6).

During the polymerization, the polymerization solution became cloudy-milky, indicating the formation of nanoparticles. This result motivated the determination of the size of the nanoparticles by DLS. The diameters of the nanoparticles obtained from the dispersion block copolymerization/self-organization were measured at different polymerization times using DLS (Figure 2.17A). The measurements were done following dilution in methanol of the polymerization solutions. The nanoparticle sizes were found to steadily increase with polymerization time; the number average sizes of the block copolymers increased from 25 nm to finally attain 144 nm, with relatively low dispersities (< 0.2). It must be noted that DLS is based on the assumption of spherical nanoparticles and is therefore only reliable for the spherical micelles and vesicles. An anomaly was observed in the DLS results, in which the sample taken at 36 h gave smaller diameter nanoparticles than the previous sample taken at 24 h reaction time. It is believed that this anomaly can be attributed to a morphology switch from rod-like to vesicle structures as non-spherical nanoparticles affect the scattering and thus intensity.

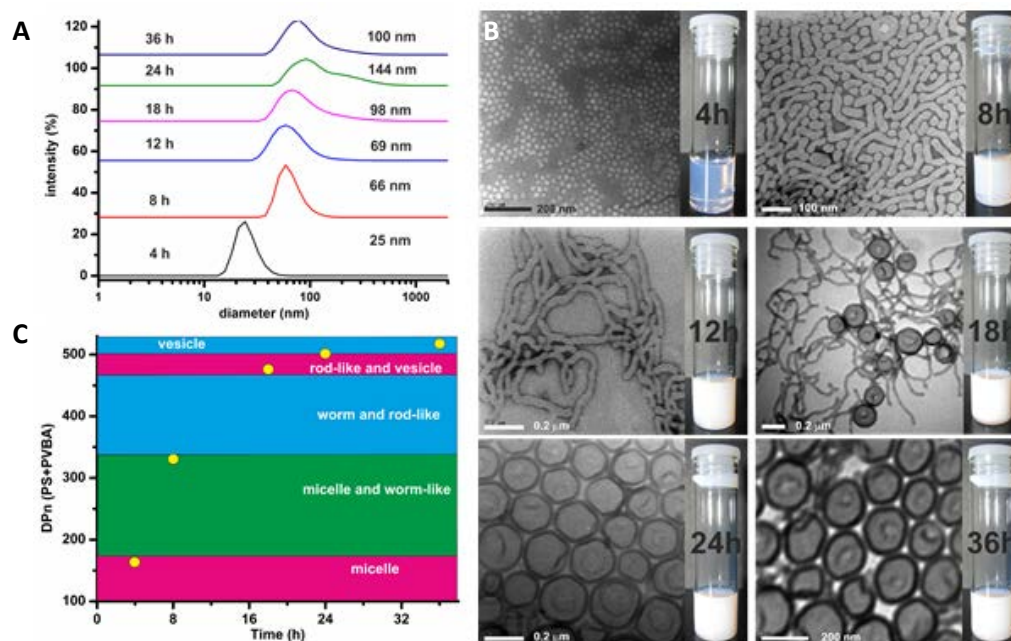


Figure 2.17: (A) Dynamic light scattering (DLS) of the solutions after different polymerization times showing intensity versus hydrodynamic diameter; (B) transmission electron microscopy (TEM) images of the different polymerization solutions after purification by dialysis against methanol; (C) a phase diagram summary showing structural changes at different polymerization times.

Nanoparticle morphologies were investigated using transmission electron microscopy (TEM) before and after purification by dialysis against methanol. The images (Figure 2.17B) showed that core functional asymmetric block copolymer aggregates first formed spherical micelles after 4 h, and subsequently, worm-like and rod-like vesicles with increasing polymerization times. Transmission electron micrographs confirmed the existence of four different morphologies, ranging from micelle to vesicles, from a single polymerizing system, with the spherical micelle and vesicle sizes in accordance with DLS data (Figure 2.17). SEM also confirmed the formation of the different morphologies observed by TEM (data not shown). The morphology changes were governed by the P(ST-co-VBA) chain lengths during the polymerization reaction. Spherical micelles formed from the block copolymer aggregates when DP<sub>n</sub> of the P(ST-co-VBA) block reached 175 units (Figure 2.17C). A morphology transition from micelles to worm and rod-like structures was observed for P(ST-co-VBA) blocks greater than 340 repeating units. Finally vesicles were formed when DP<sub>n</sub> of the second block reached over 500.

To further establish the versatility of PISA for the preparation of core functional POEGMA-*b*-P(ST-co-VBA) amphiphilic block copolymers, a second series was investigated in which the number of functional groups per block copolymer was increased. Specifically, the molar feed ratio of VBA was doubled from 5 to 10%, resulting in a molar feed ratio of POEGMA : ST-VBA : AIBN = 1 : 4500–500 : 0.5. Samples were taken at different polymerization times and analysed by <sup>1</sup>H NMR, SEC, DLS, and

TEM (see Table 2.7 and Figure 2.18). NMR showed a relatively similar conversion rate to the first series which is supported by SEC. The block copolymers have a PDI < 1.25 and the morphology transitions from micelle, worm-like and rod-like micelle to vesicle can be observed in DLS and TEM (see Figure 2.18). These results indicate that the number of functional groups per nanoparticle can be doubled without impeding the polymerization-induced assembly process.

Table 2.7: Summary of the RAFT dispersion block copolymerization of styrene and 10 % vinyl benzaldehyde in the presence of POEGMA as a macro-CTA.

Time (h)	VBA Conv. (%) <sup>a</sup>	ST Conv. (%) <sup>b</sup>	Total Conv. (%) <sup>c</sup>	$M_{n,th}$ g mol <sup>-1</sup> <sup>d</sup>	$M_{n,SEC}$ g mol <sup>-1</sup> <sup>e</sup>	PDI
4	6.5	4.3	4.4	26300	22800	1.15
8	12	5.9	6.2	38900	28800	1.16
12	15	7.7	8.0	45200	33300	1.18
18 <sup>f</sup>	12	6.4	6.8	40500	28900	1.22
24	20	9.9	10	80800	37600	1.24
36	21	11	12	82600	41000	1.22

<sup>a</sup> VBA conversion was calculated from <sup>1</sup>H NMR spectrum of the reaction mixture by dividing of aldehyde protons of the poly(vinylbenzaldehyde) peak (9.75 ppm) integral with the sum of aldehyde protons of vinyl benzaldehyde (10.03 ppm) and PVBA peak integrals.

<sup>b</sup> ST conversion was calculated from the <sup>1</sup>H NMR spectrum of the reaction mixture by dividing the sum of the polystyrene and poly(vinyl benzaldehyde) aromatic protons integrals between 7.2 ppm to 6.3 ppm (divided by 5 and excluding the NMR signal of one vinyl proton of both monomer peaks between 6.83 and 6.68 ppm) with the sum of ST and VBA vinyl peaks (5.8 and 5.3 ppm, divided by 2) and a aforementioned.

<sup>c</sup> Total conversion was calculated using  $Conv_T = 0.95 \times Conv_{(ST)} + 0.05 \times Conv_{(VBA)}$

<sup>d</sup> NMR molecular weight was calculated according to  $M_{n,th} = ([M_{ST}]_0 / [RAFT]_0) \cdot x_{ST} \cdot Mw_{ST} + ([M_{VBA}]_0 / [RAFT]_0) \cdot x_{VBA} \cdot Mw_{VBA} + Mw_{RAFT}$ , where  $[M_{ST}]_0$ ,  $[M_{VBA}]_0$ ,  $[RAFT]_0$ ,  $x_{ST}$ ,  $x_{VBA}$ ,  $Mw_{ST}$ ,  $Mw_{VBA}$  and  $Mw_{RAFT}$  are monomers and RAFT agent concentration, monomers conversion, molecular weight of monomer and RAFT agent, respectively.

<sup>e</sup> The experimental  $M_n$  and PDI were determined by SEC using dimethylacetamide as eluent solvent with polystyrene standards.

<sup>f</sup> The 18 h reaction had a slower reaction rate than expected, this is most likely caused by inadequate deoxygenation.

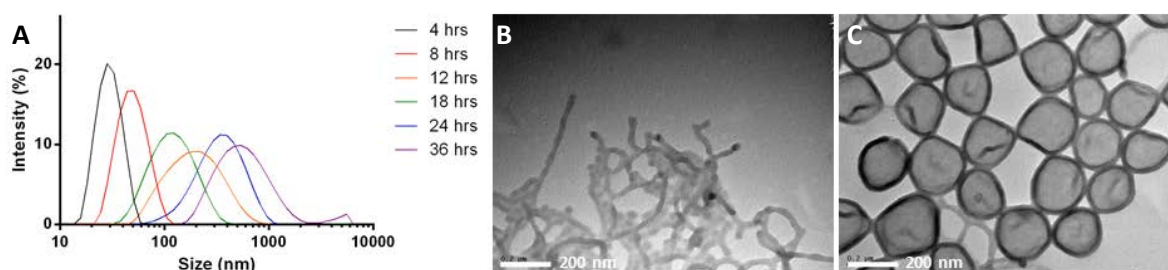
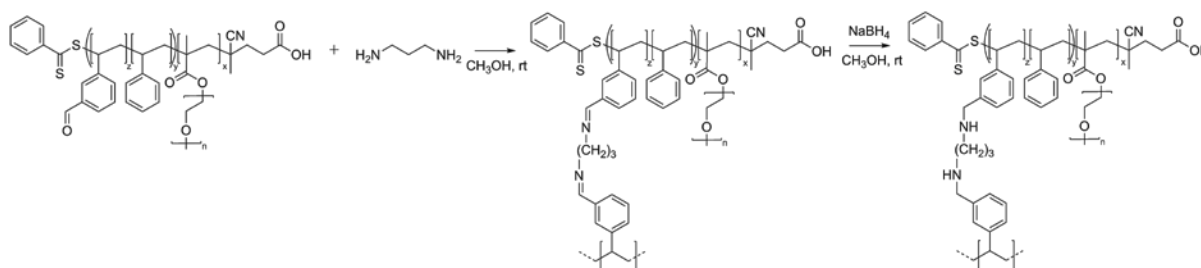


Figure 2.18: (A) Dynamic light scattering (DLS) of the solutions after different polymerization times (10% VBA) showing intensity versus hydrodynamic diameter; (B-C) transmission electron microscopy (TEM) images of polymerization solutions at 12 h (B) and 24 h (C) after purification by dialysis against methanol.

### Preparation of permanent core-cross-linked polymeric nanoparticles



Scheme 2.8: Core-cross-linking of self-assembled polymeric nanoparticles using 1,3-diaminopropane, followed by reduction of imine bonds in the presence of sodium borohydride.

Core-cross-linking of the POEGMA-*b*-P(ST-*co*-VBA) asymmetric block copolymer was achieved by reacting the aldehyde groups with 1,3-diaminopropane in methanol at room temperature, followed by reduction in the presence of sodium borohydride to yield secondary amines (Scheme 2.9). In this way, self-assembled block copolymer nanoparticles were stabilized via highly stable unbreakable bonds.

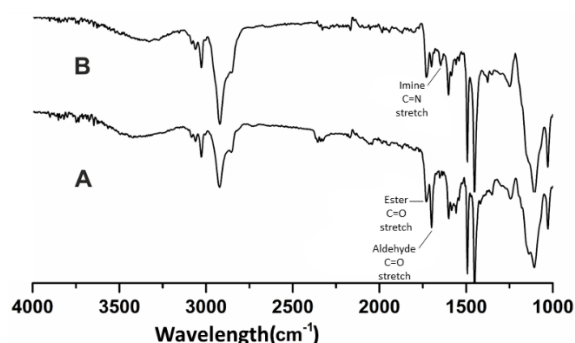


Figure 2.19: ATR-FTIR spectra before (A) and after cross-linking (B) of the POEGMA-*b*-PS-*co*-PVBA block copolymer (36 h sample).

The structural changes after core-cross-linking of the block copolymer were studied using ATR-FTIR spectroscopy (Figure 2.19). Spectra A is taken from the block copolymer solution before cross-linking: characteristic aldehyde and methacrylate ester carbonyl peaks can be observed at 1700 and 1740  $\text{cm}^{-1}$ , respectively. After cross-linking (spectra B) a new absorption peak appears at 1650  $\text{cm}^{-1}$ , corresponding to imine ( $\text{C}=\text{N}$ ) stretching vibrations. Furthermore, a decrease of the aldehyde carbonyl absorption at 1700  $\text{cm}^{-1}$  is consistent with successful cross-linking of the block copolymers due to reaction of the aldehyde group. The imine bond was successively converted to secondary amine by reduction in the presence of sodium borohydride. In addition, TEM was performed on the vesicles after core-cross-linking using THF as solvent. THF was chosen because it can solubilize both blocks. TEM confirmed the integrity of the vesicles in THF after cross-linking (Figure 2.20).

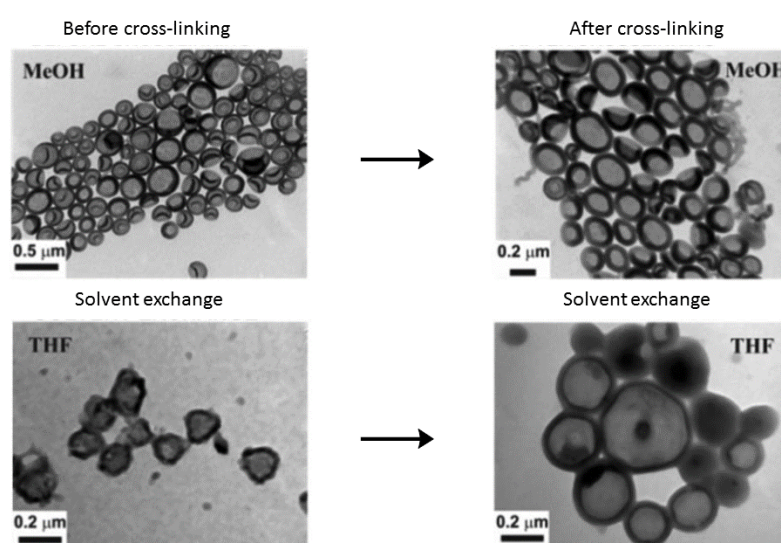


Figure 2.20: TEM images show the effect on stability of core-cross-linking of the self-assembled polymeric vesicles after challenging with a good solvent (THF).

#### *Preparation of doxorubicin-loaded polymeric nanoparticles*

The presence of aldehyde groups in the core of the nanoparticles was exploited to conjugate a widely used chemotherapy drug, doxorubicin (DOX), via pH-responsive bonds. The amino groups intrinsic to DOX·HCl (commercial form) were reacted overnight with the aldehyde groups (in methanol) in the presence of triethylamine to neutralize the acid. This synthetic strategy was previously reported by Davis and co-workers to successfully conjugate DOX to star polymers and other nanoparticles without any loss in DOX cytotoxicity. [57, 58] After DOX was loaded into the nanoparticles and subsequent careful purification, the amount of DOX conjugated was determined by UV-visible spectroscopy using the strong absorption at 495 nm together with a calibration curve (Figure 2.22). The drug loading efficiency was determined to be ~67% for all morphologies.  $^1\text{H}$  NMR spectroscopy confirmed the

decrease in the aldehyde signal at 9.9 ppm, and the drug loading using both NMR and UV-visible spectroscopy methods were in good agreement. A new signal in the NMR spectra (at 8.7 ppm) was attributed to imine formation. TEM analysis on the nanoparticles after drug conjugation indicated no significant size or morphological changes in water and in methanol (Figure 2.23).

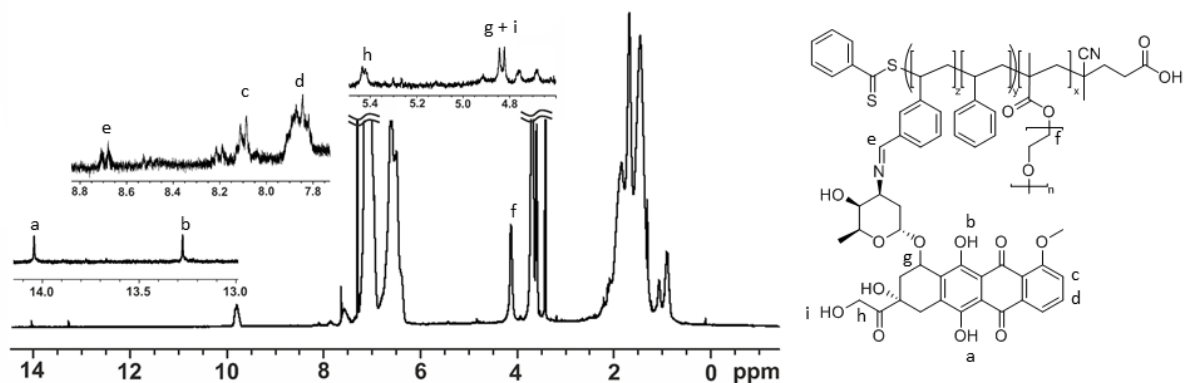


Figure 2.21:  $^1\text{H}$  NMR spectra taken after doxorubicin conjugation to the nanoparticles and extensive purification.

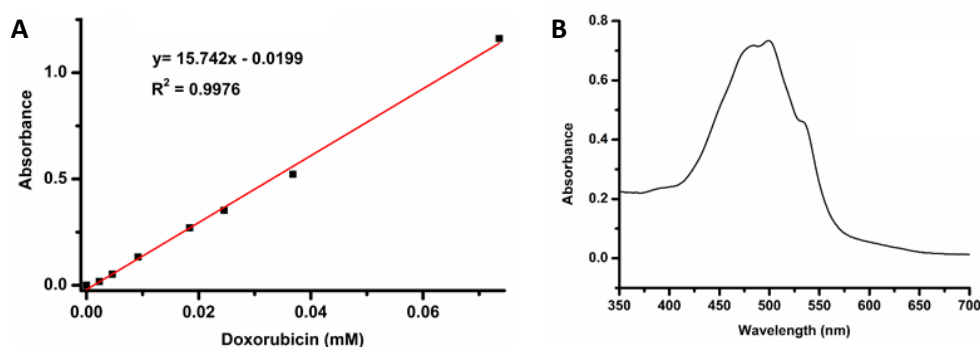


Figure 2.22: (A) Calibration curve of doxorubicin using UV-Vis (absorbance determined at 495 nm); (B) example of UV-visible absorbance of doxorubicin-conjugated polymeric vesicle.

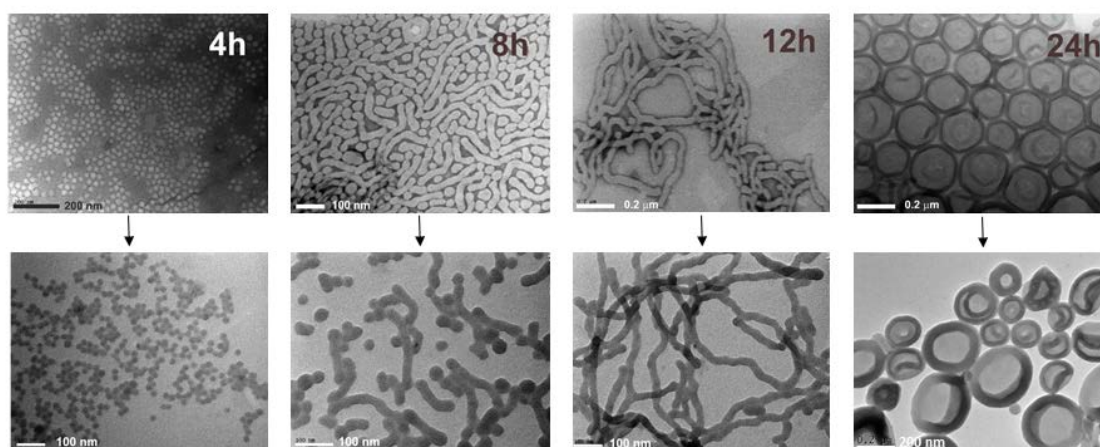


Figure 2.23: Transmission electron microscopy (TEM) micrographs of unloaded nanoparticles (top) and doxorubicin-loaded nanoparticles (bottom). Note: uranyl acetate staining was applied for the unloaded nanoparticles to increase contrast on the images.

### *Effect of morphology on drug delivery*

The drug delivery potential of the four different nanoparticle morphologies, i.e. micelle, worm-like, rod-like and vesicle was investigated. The drug loading was fixed at 5 % w/w. Firstly, the release of DOX was investigated under physiological conditions at pH 7.4 and pH 5.0 (see Figure 2.24). Over ~80 % of DOX was released from the nanoparticles at pH 5.0 after 72 h, while very slow release was observed at pH 7.4 (~10 %) demonstrating that DOX was released in a controlled manner. Interestingly, no significant difference in DOX released was observed between the different morphologies at pH 5.0 and at pH 7.4

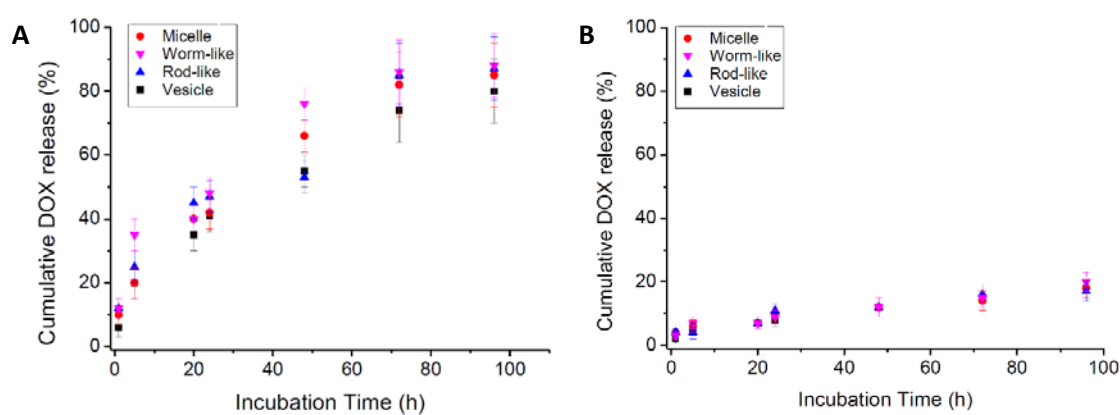


Figure 2.24: Doxorubicin released from different nanoparticles at (A) pH 5 and (B) pH 7.4.

The nanoparticle cell-uptake in breast cancer cells (MCF-7) was investigated using both flow cytometry and confocal microscopy (Figure 2.25 and Figure 2.26). The accumulation of DOX is easy to monitor as it has fluorescence emissions at 565 and 630 nm permitting direct tracking in cells. The four different DOX-loaded nanoparticles were incubated with MCF-7 cells for 24 h (concentration of 0.125 mM based on DOX). At different time points (1 h, 5 h and 24 h), the cells were analysed by flow cytometry to monitor the uptake of DOX (Figure 2.25). After 1 h, different nanoparticle cell associations were observed (higher association to less): rodlike = worm-like > vesicle = micelle. As the incubation time increased (24 h), the results indicated that nanoparticle cell association was enhanced for worm and rod-like structures (in comparison to micelles and vesicles).

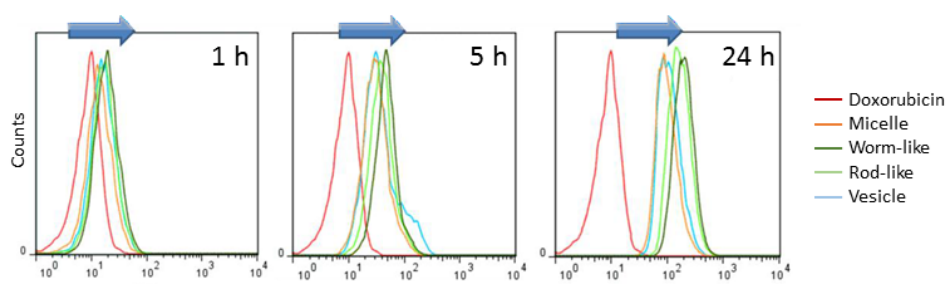


Figure 2.25: Cell association of different nanoparticle morphologies using MCF-7 breast cancer cells using flow cytometry at different time points (1 h, 5 h, and 24 h).

Prior observations made on inorganic nanoparticles (such as gold nanorods) and soft-nanoparticles (PST nanoparticles) seem consistent with our findings. [59-67] For example, Tang and co-workers investigated the influence of the silica nanoparticle shape on the cell uptake using human melanoma cells (A375). [68] The authors demonstrated that worm and rod-like (cylindrical) shapes, showed a greater adhesion of nanoparticles to the cell membrane due to their high surface of contact. This high adhesion of these cylindrical nanoparticles stimulated the cell uptake. Dawson, Aberg and co-workers obtained a similar result using PST nanoparticles. [69] The authors correlated the adhesion of these nano-objects with the cell membranes with their cell uptake. In summary, the higher aspect ratio of cylindrical nanoparticles (worm or rod-like) compared to spherical nanoparticles results in a higher surface of contact with the cell membranes, promoting cell uptake.

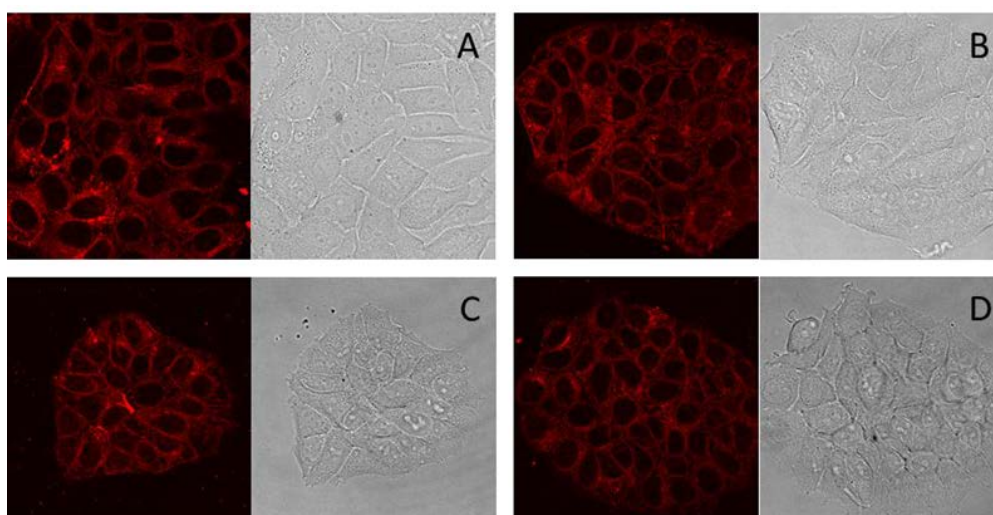


Figure 2.26: Confocal laser scanning microscopy showing cell uptake of different morphological nanostructures (A) micelles, (B) worm-like micelles, (C) rod-like micelles and (D) vesicles using MCF-7 cells after three hours of incubation. The images were acquired at  $\lambda_{ex} = 485$  nm and  $\lambda_{em}$  between 565 and 630 nm. Doxorubicin is located in the cytoplasm.

Confocal microscopy confirmed the intracellular accumulation of DOX for all the different nanoparticles. The punctate staining potentially indicates uptake via the endolysosomal pathway (Figure 2.26).<sup>7,9</sup>

Cytotoxicity studies were also performed for the four different nanostructures loaded with DOX using the MCF-7 cell-line. Firstly, the four polymeric nanoparticles without DOX were all non-toxic at the concentrations employed in this study (up to 10 mg mL<sup>-1</sup>) which is in good agreement with previous studies using similar polymers (data not shown). [70-72] After DOX conjugation, differences in cytotoxicity were observed dependent on the nanoparticle morphology, with the lowest IC<sub>50</sub> values obtained for worm and rod-like structures (7 times lower than spherical micelles), while the highest IC<sub>50</sub> was observed for micelles and vesicles. The enhancement in toxicity for the worm and rod-like nanoparticles might be related to higher cell uptake. As a comparison, the IC<sub>50</sub> of DOX for MCF-7 was also determined. The IC<sub>50</sub> value of DOX is in good agreement with published values (Table 2.4). [73, 74]

Table 2.8: Variations in IC<sub>50</sub> (μM) with nanoparticle morphology (MCF-7 cell line).

Morphology	IC <sub>50</sub> (mM)
DOX	0.093 (± 0.008)
Micelle(DOX)	1.928 (± 0.2)
Worm-like(DOX)	0.302 (± 0.02)
Rod-like(DOX)	0.796 (± 0.1)
Vesicle(DOX)	2.193 (± 0.1)

## 2.4 Conclusion

In this chapter, four different functional POEGMA-*b*-P(ST-co-VBA) block copolymer nanoparticles were prepared using one-pot polymerization induced self-assembly. Aldehyde groups in the nanoparticle cores were exploited to cross-link the particles (imparting stability), and to conjugate doxorubicin. Using MCF-7 cells, a significant effect of morphology on nanoparticle cell uptake was demonstrated, with the highest cell uptake observed for worm-like and rod-like structures. The changes in cell uptake were reflected in changes to the cytotoxicity of DOX-loaded nanoparticles.

## 2.5 References

1. Bamrungsap, S., et al., *Nanotechnology in therapeutics: a focus on nanoparticles as a drug delivery system*. Nanomedicine, 2012. **7**(8): p. 1253-1271.
2. Cho, E.J., et al., *Nanoparticle Characterization: State of the Art, Challenges, and Emerging Technologies*. Molecular Pharmaceutics, 2013. **10**(6): p. 2093-2110.
3. Duncan, R. and R. Gaspar, *Nanomedicine(s) under the Microscope*. Molecular Pharmaceutics, 2011. **8**(6): p. 2101-2141.
4. Albanese, A., P.S. Tang, and W.C. Chan, *The effect of nanoparticle size, shape, and surface chemistry on biological systems*. Annu Rev Biomed Eng, 2012. **14**: p. 1-16.
5. Geng, Y., et al., *Shape effects of filaments versus spherical particles in flow and drug delivery*. Nat Nano, 2007. **2**(4): p. 249-255.
6. Kunzmann, A., et al., *Efficient internalization of silica-coated iron oxide nanoparticles of different sizes by primary human macrophages and dendritic cells*. Toxicol Appl Pharmacol, 2011. **253**(2): p. 81-93.
7. Avila-Olias, M., et al., *Inspired by nature: fundamentals in nanotechnology design to overcome biological barriers*. Ther Deliv, 2013. **4**(1): p. 27-43.
8. Park, S., et al., *Therapeutic nanorods with metallic multi-segments: Thermally inducible encapsulation of doxorubicin for anti-cancer therapy*. Nano Today, 2012. **7**(2): p. 76-84.
9. Tang, L., et al., *Size-Dependent Tumor Penetration and in Vivo Efficacy of Monodisperse Drug-Silica Nanoconjugates*. Molecular Pharmaceutics, 2013. **10**(3): p. 883-892.
10. Venkataraman, S., et al., *The effects of polymeric nanostructure shape on drug delivery*. Adv Drug Deliv Rev, 2011. **63**(14-15): p. 1228-46.
11. Oh, W.-K., et al., *Shape-Dependent Cytotoxicity and Proinflammatory Response of Poly(3,4-ethylenedioxythiophene) Nanomaterials*. Small, 2010. **6**(7): p. 872-879.
12. Pegoraro, C., et al., *Enhanced drug delivery to melanoma cells using PMPC-PDPA polymersomes*. Cancer Lett, 2013. **334**(2): p. 328-37.
13. LoPresti, C., et al., *Controlling Polymersome Surface Topology at the Nanoscale by Membrane Confined Polymer/Polymer Phase Separation*. ACS Nano, 2011. **5**(3): p. 1775-1784.
14. Gratton, S.E., et al., *The effect of particle design on cellular internalization pathways*. Proc Natl Acad Sci U S A, 2008. **105**(33): p. 11613-8.
15. Kolhar, P., et al., *Using shape effects to target antibody-coated nanoparticles to lung and brain endothelium*. Proc Natl Acad Sci U S A, 2013. **110**(26): p. 10753-8.
16. Champion, J.A., Y.K. Katare, and S. Mitragotri, *Particle shape: a new design parameter for micro- and nanoscale drug delivery carriers*. J Control Release, 2007. **121**(1-2): p. 3-9.
17. Muro, S., et al., *Control of endothelial targeting and intracellular delivery of therapeutic enzymes by modulating the size and shape of ICAM-1-targeted carriers*. Mol Ther, 2008. **16**(8): p. 1450-8.
18. Schacher, F.H., P.A. Rupar, and I. Manners, *Functional Block Copolymers: Nanostructured Materials with Emerging Applications*. Angewandte Chemie International Edition, 2012. **51**(32): p. 7898-7921.
19. Sanchez-Gaytan, B.L., et al., *Interfacial assembly of nanoparticles in discrete block-copolymer aggregates*. Angew Chem Int Ed Engl, 2007. **46**(48): p. 9235-8.
20. Zhang, L. and A. Eisenberg, *Morphogenic Effect of Added Ions on Crew-Cut Aggregates of Polystyrene-b-poly(acrylic acid) Block Copolymers in Solutions*. Macromolecules, 1996. **29**(27): p. 8805-8815.
21. Zhang, L. and A. Eisenberg, *Multiple Morphologies of "Crew-Cut" Aggregates of Polystyrene-b-poly(acrylic acid) Block Copolymers*. Science, 1995. **268**(5218): p. 1728-31.
22. Savic, R., et al., *Micellar nanocontainers distribute to defined cytoplasmic organelles*. Science, 2003. **300**(5619): p. 615-8.
23. Li, Z., et al., *Multicompartment micelles from ABC miktoarm stars in water*. Science, 2004. **306**(5693): p. 98-101.
24. Won, Y.-Y., H.T. Davis, and F.S. Bates, *Giant Wormlike Rubber Micelles*. Science, 1999. **283**(5404): p. 960-963.
25. Klok, H.A. and S. Lecommandoux, *Supramolecular Materials via Block Copolymer Self-Assembly*. Advanced Materials, 2001. **13**(16): p. 1217-1229.
26. Rodríguez-Hernández, J., et al., *Toward 'smart' nano-objects by self-assembly of block copolymers in solution*. Progress in Polymer Science, 2005. **30**(7): p. 691-724.
27. Discher, B.M., et al., *Polymersomes: tough vesicles made from diblock copolymers*. Science, 1999. **284**(5417): p. 1143-6.

28. Discher, D.E. and A. Eisenberg, *Polymer vesicles*. Science, 2002. **297**(5583): p. 967-73.
29. Marguet, M., L. Edembe, and S. Lecommandoux, *Polymersomes in Polymersomes: Multiple Loading and Permeability Control*. Angewandte Chemie, 2012. **124**(5): p. 1199-1202.
30. Rodríguez-Hernández, J. and S. Lecommandoux, *Reversible Inside-Out Micellization of pH-responsive and Water-Soluble Vesicles Based on Polypeptide Diblock Copolymers*. Journal of the American Chemical Society, 2005. **127**(7): p. 2026-2027.
31. Chécot, F., et al., *Water-Soluble Stimuli-Responsive Vesicles from Peptide-Based Diblock Copolymers*. Angewandte Chemie International Edition, 2002. **41**(8): p. 1339-1343.
32. Liu, G., et al., *Aqueous Dispersion Polymerization of 2-Methoxyethyl Acrylate for the Synthesis of Biocompatible Nanoparticles Using a Hydrophilic RAFT Polymer and a Redox Initiator*. Macromolecules, 2011. **44**(13): p. 5237-5245.
33. Liu, G., Q. Qiu, and Z. An, *Development of thermosensitive copolymers of poly(2-methoxyethyl acrylate-co-poly(ethylene glycol) methyl ether acrylate) and their nanogels synthesized by RAFT dispersion polymerization in water*. Polymer Chemistry, 2012. **3**(2): p. 504-513.
34. Delaittre, G., et al., *Formation of polymer vesicles by simultaneous chain growth and self-assembly of amphiphilic block copolymers*. Chemical Communications, 2009(20): p. 2887-2889.
35. Boisse, S., et al., *Amphiphilic block copolymer nano-fibers via RAFT-mediated polymerization in aqueous dispersed system*. Chemical Communications, 2010. **46**(11): p. 1950-1952.
36. Charleux, B., et al., *Polymerization-Induced Self-Assembly: From Soluble Macromolecules to Block Copolymer Nano-Objects in One Step*. Macromolecules, 2012. **45**(17): p. 6753-6765.
37. Delaittre, G., et al., *Synthesis by nitroxide-mediated aqueous dispersion polymerization, characterization, and physical core-crosslinking of pH- and thermoresponsive dynamic diblock copolymer micelles*. Polymer Chemistry, 2012. **3**(6): p. 1526-1538.
38. Zhang, X., J. Rieger, and B. Charleux, *Effect of the solvent composition on the morphology of nano-objects synthesized via RAFT polymerization of benzyl methacrylate in dispersed systems*. Polymer Chemistry, 2012. **3**(6): p. 1502-1509.
39. Blanazs, A., et al., *Mechanistic Insights for Block Copolymer Morphologies: How Do Worms Form Vesicles?* Journal of the American Chemical Society, 2011. **133**(41): p. 16581-16587.
40. Blanazs, A., et al., *Sterilizable Gels from Thermoresponsive Block Copolymer Worms*. Journal of the American Chemical Society, 2012. **134**(23): p. 9741-9748.
41. Blanazs, A., A.J. Ryan, and S.P. Armes, *Predictive Phase Diagrams for RAFT Aqueous Dispersion Polymerization: Effect of Block Copolymer Composition, Molecular Weight, and Copolymer Concentration*. Macromolecules, 2012. **45**(12): p. 5099-5107.
42. Fielding, L.A., et al., *RAFT dispersion polymerization in non-polar solvents: facile production of block copolymer spheres, worms and vesicles in n-alkanes*. Chemical Science, 2013. **4**(5): p. 2081-2087.
43. Li, Y. and S.P. Armes, *RAFT Synthesis of Sterically Stabilized Methacrylic Nanolatexes and Vesicles by Aqueous Dispersion Polymerization*. Angewandte Chemie International Edition, 2010. **49**(24): p. 4042-4046.
44. Ladmiral, V., et al., *Polymerization-Induced Self-Assembly of Galactose-Functionalized Biocompatible Diblock Copolymers for Intracellular Delivery*. Journal of the American Chemical Society, 2013. **135**(36): p. 13574-13581.
45. Lomas, H., et al., *Non-cytotoxic polymer vesicles for rapid and efficient intracellular delivery*. Faraday Discussions, 2008. **139**(0): p. 143-159.
46. Sugihara, S., et al., *Non-spherical morphologies from cross-linked biomimetic diblock copolymers using RAFT aqueous dispersion polymerization*. Soft Matter, 2011. **7**(22): p. 10787-10793.
47. Sugihara, S., et al., *Aqueous Dispersion Polymerization: A New Paradigm for in Situ Block Copolymer Self-Assembly in Concentrated Solution*. Journal of the American Chemical Society, 2011. **133**(39): p. 15707-15713.
48. Wan, W.-M., C.-Y. Hong, and C.-Y. Pan, *One-pot synthesis of nanomaterials via RAFT polymerization induced self-assembly and morphology transition*. Chemical Communications, 2009(39): p. 5883-5885.
49. Wan, W.-M., X.-L. Sun, and C.-Y. Pan, *Morphology Transition in RAFT Polymerization for Formation of Vesicular Morphologies in One Pot*. Macromolecules, 2009. **42**(14): p. 4950-4952.
50. Wan, W.M., X.L. Sun, and C.Y. Pan, *Formation of Vesicular Morphologies via Polymerization Induced Self-Assembly and Re-Organization*. Macromol Rapid Commun, 2010. **31**(4): p. 399-404.
51. Sun, J.-T., C.-Y. Hong, and C.-Y. Pan, *Recent advances in RAFT dispersion polymerization for preparation of block copolymer aggregates*. Polymer Chemistry, 2013. **4**(4): p. 873-881.

52. Sun, J.-T., C.-Y. Hong, and C.-Y. Pan, *Formation of the block copolymer aggregates via polymerization-induced self-assembly and reorganization*. *Soft Matter*, 2012. **8**(30): p. 7753-7767.
53. Mitsukami, Y., et al., *Water-Soluble Polymers. 81. Direct Synthesis of Hydrophilic Styrenic-Based Homopolymers and Block Copolymers in Aqueous Solution via RAFT*. *Macromolecules*, 2001. **34**(7): p. 2248-2256.
54. Boyer, C., et al., *Bioapplications of RAFT Polymerization*. *Chemical Reviews*, 2009. **109**(11): p. 5402-5436.
55. Boyer, C., M.H. Stenzel, and T.P. Davis, *Building nanostructures using RAFT polymerization*. *Journal of Polymer Science Part A: Polymer Chemistry*, 2011. **49**(3): p. 551-595.
56. Goto, A. and T. Fukuda, *Kinetics of living radical polymerization*. *Progress in Polymer Science*, 2004. **29**(4): p. 329-385.
57. Liu, J., et al., *Synthesis of Functional Core, Star Polymers via RAFT Polymerization for Drug Delivery Applications*. *Macromolecular Rapid Communications*, 2012. **33**(9): p. 760-766.
58. Duong, H.T.T., et al., *Functionalizing Biodegradable Dextran Scaffolds Using Living Radical Polymerization: New Versatile Nanoparticles for the Delivery of Therapeutic Molecules*. *Molecular Pharmaceutics*, 2012. **9**(11): p. 3046-3061.
59. Zhou, W., X. Liu, and J. Ji, *Fast and selective cancer cell uptake of therapeutic gold nanorods by surface modifications with phosphorylcholine and Tat*. *Journal of Materials Chemistry*, 2012. **22**(28): p. 13969-13976.
60. Arnida, A. Malugin, and H. Ghandehari, *Cellular uptake and toxicity of gold nanoparticles in prostate cancer cells: a comparative study of rods and spheres*. *Journal of Applied Toxicology*, 2010. **30**(3): p. 212-217.
61. Oh, E., et al., *Cellular Uptake and Fate of PEGylated Gold Nanoparticles Is Dependent on Both Cell-Penetration Peptides and Particle Size*. *ACS Nano*, 2011. **5**(8): p. 6434-6448.
62. Albanese, A. and W.C.W. Chan, *Effect of Gold Nanoparticle Aggregation on Cell Uptake and Toxicity*. *ACS Nano*, 2011. **5**(7): p. 5478-5489.
63. Chithrani, B.D., A.A. Ghazani, and W.C.W. Chan, *Determining the Size and Shape Dependence of Gold Nanoparticle Uptake into Mammalian Cells*. *Nano Letters*, 2006. **6**(4): p. 662-668.
64. Duncan, B., C. Kim, and V.M. Rotello, *Gold nanoparticle platforms as drug and biomacromolecule delivery systems*. *Journal of controlled release : official journal of the Controlled Release Society*, 2010. **148**(1): p. 122-127.
65. Wang, T., et al., *Cellular uptake of nanoparticles by membrane penetration: a study combining confocal microscopy with FTIR spectroelectrochemistry*. *ACS Nano*, 2012. **6**(2): p. 1251-9.
66. Elsabahy, M. and K.L. Wooley, *Design of polymeric nanoparticles for biomedical delivery applications*. *Chemical Society Reviews*, 2012. **41**(7): p. 2545-2561.
67. Zhu, J., et al., *Disk-cylinder and disk-sphere nanoparticles via a block copolymer blend solution construction*. *Nat Commun*, 2013. **4**: p. 2297.
68. Huang, X., et al., *The effect of the shape of mesoporous silica nanoparticles on cellular uptake and cell function*. *Biomaterials*, 2010. **31**(3): p. 438-48.
69. Lesniak, A., et al., *Nanoparticle Adhesion to the Cell Membrane and Its Effect on Nanoparticle Uptake Efficiency*. *Journal of the American Chemical Society*, 2013. **135**(4): p. 1438-1444.
70. Pissuwan, D., et al., *In Vitro Cytotoxicity of RAFT Polymers*. *Biomacromolecules*, 2010. **11**(2): p. 412-420.
71. Duong, H.T.T., et al., *Acid Degradable and Biocompatible Polymeric Nanoparticles for the Potential Codelivery of Therapeutic Agents*. *Macromolecules*, 2011. **44**(20): p. 8008-8019.
72. Duong, H.T.T., et al., *Intracellular nitric oxide delivery from stable NO-polymeric nanoparticle carriers*. *Chemical Communications*, 2013. **49**(39): p. 4190-4192.
73. Soule, H.D., et al., *Isolation and characterization of a spontaneously immortalized human breast epithelial cell line, MCF-10*. *Cancer Res*, 1990. **50**(18): p. 6075-86.
74. Fornari, F.A., et al., *Interference by doxorubicin with DNA unwinding in MCF-7 breast tumor cells*. *Molecular Pharmacology*, 1994. **45**(4): p. 649-656.

## Chapter 3: Polymerization-Induced Self-Assembly - Control over Surface and Morphology for $T_1$ -weighted MR imaging

### 3.1 Introduction

Magnetic resonance imaging (MRI) is a very powerful tool for non-invasive clinical diagnosis [1] and the number of MRI scanners in hospitals is continuously increasing. [2] Due to the relatively low sensitivity of MRI, contrast agents are routinely employed to increase signal in MR images and herewith improve diagnosis. [3] Currently, only small molecule  $Gd^{3+}$ -chelates are being used in the clinical setting, although extensive research has been carried out towards more efficient contrast agents by optimizing the construct (e.g. conjugation to macromolecules such as dendrimers, polymers or proteins) [4-6] and the introduction of active targeting. [7] Furthermore, research has also been directed to other methods of signal enhancement, such as  $T_2$ -weighted contrast agents [8, 9] (superparamagnetic iron oxides, e.g. Magnevist and Endorem), chemical-exchange saturation transfer (CEST) agents [10] and fluorine ( $^{19}F$ ) imaging. [11, 12] This research was further driven by the discovery of nephrogenic systemic fibrosis (NSF) in 2000 [13] which is likely caused by free  $Gd^{3+}$ . [14] This led to discussions in regards to the safety of gadolinium chelates, resulting to a transition to superior cyclic chelates [15] and restrictions for patients with limited kidney function (estimated glomerular filtration rate test < 25) [16]. However, new gadolinium-based contrast agents are still advantageous due to their familiarity and track record in the clinical practice.

An important factor in the pharmacokinetics and biodistribution of MRI contrast agents and nanoparticles in general is their size. [17] Very small particles (< 11 nm) are eliminated quickly by renal and hepatobiliary clearance, whereas larger particles(> 200 nm) are efficiently cleared by the mononuclear phagocytic system. [18] Size is also a key feature in the passive targeting of cancer by exploiting the enhanced permeability and retention (EPR) effect. [18, 19] Furthermore studies also showed that the conjugation of gadolinium-chelates to macromolecules such as albumin, dendrimers and polymeric stars resulted in a higher contrast efficacy (viz. relaxivity). [7, 20, 21]

Recent studies demonstrated that the nanoparticle shape also has important implications on biodistribution, cellular uptake and clearance. [22] For example, spherical micelles are taken up by phagocytes more readily than micelles that have been extended into filaments by shear flow such as would be experienced in the blood stream. [23] The longer circulation time and higher surface interactions have been exploited for improved drug delivery [22] and several studies for applications in MRI have also been published, although these have mainly focused on iron oxides. [24-29]

For example, in an influential study Park *et al.* studied dextran-coated magnetic iron oxide nanoworms and reported that nanoworms improved the magnetic relaxivity, increased the ability to attach to tumour cells *in vitro* owing to enhanced multivalent interactions and amplified their passive

accumulation *in vivo* over spherical nanoparticle controls. [24] Several studies also reported the synthesis of solid gadolinium containing rod-like nanoparticles, such as gadolinium-modified NaDyF<sub>4</sub> nanorods, [30] gadolinium-functionalized gold nanorods [31] and dextran-coated gadolinium phosphate nanoparticles. [32] However, there have been only limited reports of flexible gadolinium-labelled filomicelles [33, 34] despite of potential applications in drug delivery and diagnostics. These include a study of Bruckman *et al.* who loaded tobacco mosaic virus rods (300 x 18 nm) with gadolinium and showed an increase in  $r_1$  relaxivity, [33] and a 2007 study by Tesauro *et al.* in which rod-like phospholipid micelles were reported containing the bioactive peptide CCK8. [34] However, to our knowledge, no studies of soft polymeric filomicelles have been reported in literature.

Polymerization-induced self-assembly (PISA) enables a facile pathway towards the synthesis of soft nanoparticles with different sizes and shape, including non-spherical, and the applications of polymerization-induced self-assembly have grown rapidly over the recent years due to the beneficial elements of this method. [35, 36] Starting with Eisenberg's work [37], several improvements have allowed access to an increased range of solvents, shapes, surfaces and post modification reactions. [38]

In this chapter, PISA was utilized to synthesize a library of surface-functional nanoparticles with different shapes (spherical and filomicelles) and sizes containing an epoxide functionality on the surface which allowed the conjugation of a suitably functional gadolinium chelates. First, the versatility of the epoxides for further post synthetic functionalisation of the pre-assembled nanoparticles was fully explored using primary amines, thiols and ring-opening by sodium azide followed by copper(I)-catalysed alkyne-azide cycloaddition (CuAAC). Subsequently, pre-synthesized cyclic Gd<sup>3+</sup>-chelates were conjugated using primary amines and the efficiency of the different morphologies on MR contrast was investigated with potential applications as blood pool agent in magnetic resonance angiography (MRA) and in cancer theranostics.

## 3.2 Experimental Section

### 3.2.1 Materials

Styrene (ST, Sigma-Aldrich,  $\geq 99\%$ ) and glycidyl methacrylate (97 %) were disinhibited by passing through a column of basic alumina (Sigma-Aldrich). Agarose (type 1, low EEO,  $\leq 10\%$  water), 5(6)-aminofluorescein ( $\geq 75\%$ ), 3-butyne-1-ol (97 %), copper(I) bromide (99.999 %), furfuryl mercaptan ( $\geq 97\%$ ), gadolinium(III) chloride hexahydrate (99 %), oligo(ethylene glycol) methyl ether methacrylate (OEGMA, average  $M_n = 300\text{ g mol}^{-1}$ ), N,N,N',N'',N''-pentamethyl-diethylenetriamine (99 %), propargylamine (98 %), sodium azide ( $\geq 99.5\%$ ), triethylamine ( $\geq 99\%$ ), and trifluoroacetic acid (99 %) were used as received from Sigma-Aldrich. Ammonium chloride (99.5 %) and potassium hydroxide pellets ( $\geq 85\%$ ) were purchased from Chem-Supply, 4-aminobutyl-DOTA-tris (t-butyl ester) from Macrocyclics and Chelex® 100 resin was supplied by Bio-Rad. Azobis(isobutyronitrile) (AIBN, Fluka, 98 %) was purified by recrystallization from methanol. 4-Cyanopentanoic acid dithiobenzoate (CPADB) was prepared according to a procedure described elsewhere [39] or used as received from Sigma Aldrich. Dialysis was performed using Cellu-Sep regenerated cellulose tubular membranes with nominal molecular cut-off weights of 3500, 6000, or 12,000 – 14,000 Da.

### 3.2.2 Physical and analytical methods

#### *<sup>1</sup>H NMR*

<sup>1</sup>H NMR spectra were recorded using a Bruker Avance 300 (300 MHz) spectrometer or Bruker UltraShield 400 (400.13 MHz) spectrometer running Bruker Topspin, version 1.3. Deuterated chloroform (CDCl<sub>3</sub>) or deuterium oxide (D<sub>2</sub>O) was used as solvent. All chemical shifts are reported in ppm ( $\delta$ ) relative to tetramethylsilane, referenced to the chemical shifts of residual solvent resonance (CDCl<sub>3</sub> = 7.26 ppm).

#### *Size exclusion chromatography*

DMAc size exclusion chromatography (SEC) was implemented using a Shimadzu modular system comprising a SIL20AD automatic injector, a DGU12A degasser, a CTO10A column oven, a LC10AT pump, a RID10A differential refractive-index detector, and a SPD10A Shimadzu UV/Vis detector. A 50  $\times$  7.8 mm guard column followed by three KF-805L columns in series (300  $\times$  8 mm linear columns, bead size: 10  $\mu$ m, pore size maximum: 5000 Å) were used for the analyses. N,N'-Dimethylacetamide (DMAc, HPLC grade, 0.03 % w/v LiBr) with a flow rate of 1 mL min<sup>-1</sup> and a constant temperature of 50 °C was used as the mobile phase. The samples were filtered through 0.45  $\mu$ m filters prior to injection. The

unit was calibrated using commercially available linear poly(styrene) standards (0.5–2000 kDa, Polymer Laboratories). Chromatograms were processed using Cirrus 2.0 software (Polymer Laboratories).

#### *Transmission electron microscopy*

The sizes and morphologies of the block copolymers were observed using a transmission electron microscopy JEOL 1400 TEM at an accelerating voltage of 100 kV. The solution of the block copolymers in dispersion medium was directly taken and diluted with methanol (2 mg mL<sup>-1</sup>) and deposited onto copper grid (ProSciTech). Uranyl acetate staining was applied and the samples were dried.

#### *Dynamic light scattering*

DLS measurements were performed using a Malvern Zetasizer Nano Series running DTS software and using a 4 mW He–Ne laser operating at a wavelength of 633 nm and an avalanche photodiode detector. The scattered light was detected at an angle of 173°.

#### *Attenuated Total Reflection-Fourier Transform Infrared Spectroscopy*

ATR-FTIR measurements were performed using a Bruker IFS66\S Fourier transform spectrometer by averaging 128 scans with a resolution of 4 cm<sup>-1</sup>. Or using a Shimadzu IRTracer 100 Fourier transform infrared spectrometer with a GladiATR 10 single reflection ATR accessory. Spectra were then obtained in the mid infrared region of 4000–600 cm<sup>-1</sup> at a resolution of 8 cm<sup>-1</sup> (512 scans) and analysed using LabSolution IR software.

#### *Ultraviolet-visible spectroscopy*

UV-Vis spectra were recorded using a Varian CARY 300 spectrophotometer. The amount of incorporated 5(6)-aminofluorescein was determined by measuring the absorbance at 489 nm using a quartz cuvette.

#### *Ultra-high performance liquid chromatography / mass spectroscopy (UHPLC/MS)*

The chromatographic analysis was performed using an Agilent 1260 Infinity system equipped with a binary pump (G1312C), autosampler (G1367E), DAD module (G4212A) and an 1100 MSD mass spectrometer. System control, data acquisition and interpretation were made using LC/MSD Chemstation Rev.B.04.03 coupled with Masshunter Easy Access Software.

For LC: reverse phase HPLC analysis was carried out using a Poroshell 120 EC-C18 column (3.0 x 50 mm, 2.7-micron) at 35°C and an injection volume of 1 µl. Starting with water containing 0.1 % formic acid), a gradient was introduced (5-100 % acetonitrile containing 0.1 % formic acid) over 3.8 minutes with a flow rate of 0.500 mL/min.

For MS: ionization was performed using a quadrupole API-ES source, a capillary voltage of 3000 V and a drying gas temperature of 350°C

#### *Inductively Coupled Plasma–Optical Emission Spectrometry (ICP-OES)*

The Gd<sup>3+</sup> content of the polymer-based nanoparticles was determined by inductively coupled plasma–optical emission spectrometry (ICP-OES) using a Perkin-Elmer OPTIMA 7300 spectrometer. Samples were prepared by dissolving 0.5 mg of polymer in 10 mL of ultrapure water.

#### *Magnetic Resonance Imaging*

MRI scans were taken from aqueous dilution series in a Costar 96-well assay block (3959, 1 ml well volume, round bottom). To limit artefacts, the backside of the assay block was filled with 3 % agarose using the following procedure: 200 ml TAE buffer (40 mM tris base, 40 mM acetic acid, and 1 mM EDTA) was rapidly stirred and 6.0 g agarose (type 1, low eeo) was added slowly to let it disperse well. Next, the dispersion was heated to 95 °C until all agarose was dissolved (15 minutes). Any bubbles were removed by gentle shaking. The solution was then allowed to cool down to 60 °C before carefully decanting it into the backside of the 96-well assay block. The agarose was cooled further for another hour and formed a semi-transparent white hydrogel.

Dilution series of DOTA(Gd) conjugated polymeric nanoparticles and amine-DOTA(Gd) were prepared (dilution factor 2, 1 ml each, highest concentration ~ 0.25 mM Gd, 5 dilutions), and remaining wells were filled with water as control. Finally, the wells were sealed with parafilm to prevent spillage and well-to-well contamination.

The MRI properties of the gadolinium-labelled polymeric nanoparticles were studied using a state-of-the-art 7-Tesla whole-body MRI scanner (MAGNETOM 7T, Siemens) using Nova single channel transmit with 32 receiver channels with an internal diameter of 18.5 cm and a 21 cm field of view along the z-direction). A dilution series of each nanoparticle in water was prepared in a 96 wells plate for high-throughput measurement. The space between the wells was filled with 3 % agarose to minimize susceptibility effects caused by water-air interfaces.

For the determination of the  $r_1$  relaxivity, inversion recovery sequences were utilized with different inversion times (22, 250, 500, 1000, 2000, 3000, and 4000 ms), TR = 5000 ms and TE 11.5 ms. All images were acquired with a 2 mm slice thickness, 150 x 112.5 mm FOV, 256 x 192 matrix size, and 1 average. To quantify the  $r_2$  relaxivity, a Carr-Purcell-Meiboom-Gill (CPMG) multi-echo spin echo sequence was used to acquire 32 images at echo times (TE) ranging from 11.5 to 368 ms with a repetition time (TR) of 5000 ms.

### 3.2.3 Syntheses

#### *Preparation of poly(glycidyl methacrylate) [PGMA]*

RAFT agent 4-cyanopentanoic acid dithiobenzoate (CPADB, 250 mg,  $8.95 \times 10^{-4}$  mol), glycidyl methacrylate (GMA, 2.44 mL,  $1.79 \times 10^{-2}$  mol), and azobis(2-methylpropionitrile) (AIBN, 14.7 mg,  $8.95 \times 10^{-5}$  mol) were dissolved in toluene (12.2 mL) in a septa-sealed vial. The vial was placed in an ice bath, and the solution was purged with nitrogen for 30 min. The ratio between the monomer, RAFT agent and AIBN in the polymerization medium was 20:1.0:0.1. After deoxygenation, the reaction mixture was then placed in an oil bath at 70 °C. After 1:30 h of reaction, it was quenched via rapid cooling and exposure to air. The reaction was directly analysed by  $^1\text{H}$  NMR to determine the monomer conversion. The polymer was concentrated by partial evaporation of solvent, and the polymer was precipitated four times in 9: 1 petroleum spirit (BR 40 - 60 °C) to diethyl ether to remove the non-reacted monomer and RAFT agent. The purified polymer was then carefully dried at 30 °C under vacuum overnight to give 505 mg of a pink crystalline solid and characterized by SEC and  $^1\text{H}$  NMR.

#### *Preparation of poly(glycidyl methacrylate)-block-poly(oligo(ethylene glycol) methyl ether methacrylate) [PGMA-b-POEGMA]*

The previously synthesized PGMA was used as a macro-CTA (100 mg,  $M_n \sim 990$  g/mol (based on  $^1\text{H}$  NMR), i.e.  $1.01 \times 10^{-4}$  mol of polymer), in the presence of oligo(ethylene glycol) methyl ether methacrylate] (OEGMA) 1.44 mL,  $M_n \sim 300$  g/mol,  $5.05 \times 10^{-3}$  mol), and AIBN (2.1 mg,  $1.2 \times 10^{-5}$  mol) as initiator. The compounds were dissolved in 7.2 mL acetonitrile in a septa-sealed vial, which was then placed in an ice bath and the solution was purged with nitrogen for 30 min. The ratio between the monomer, macro-RAFT agent and initiator in the polymerization mixture was 50 : 1 : 0.125. After deoxygenation, the reaction medium was placed in an oil bath at 70 °C. After 6 h of reaction, it was quenched via rapid cooling and exposure to air. The polymer was concentrated by partial evaporation of solvent and purified by precipitation four times with a 1:1 mixture of diethyl ether and petroleum spirit (BR 40 – 60 °C). The purified polymer was then dried at 30 °C in vacuo overnight to give 579 mg of a red gel-like solid.

#### *Preparation of poly(glycidyl methacrylate)-block-poly(oligo(ethylene glycol) methyl ether methacrylate)-block-poly(styrene) [PGMA-b-POEGMA-b-PST]*

PGMA-b-POEGMA was used as macro-CTA (177 mg,  $M_n \sim 9,240$  g/mol (based on  $^1\text{H}$  NMR), i.e.  $1.9 \times 10^{-5}$  mol of polymer). Styrene (ST, disinhibited using basic alumina, 11.0 mL,  $9.60 \times 10^{-2}$  mol), AIBN

(1.26 mg,  $7.66 \times 10^{-6}$  mol), and methanol (14.1 ml) were added, and the solution was shortly stirred. The ratio between the styrene, macro-CTA and initiator in the polymerization mixture was 5000 : 1.0 : 0.4; with styrene to methanol 1 : 1.1 (%w/w). The reaction mixture was equally distributed over 8 vials (3 ml each), which were then sealed with septa and parafilm. This was followed by mild purging with nitrogen for 30 minutes in an ice-bath to limit methanol evaporation. After deoxygenation, the reaction mediums were placed in an oil bath at 70 °C for different reaction times: 4, 8, 13, 16, 20, 24, 30 and 37 hrs. Each reaction was quenched by rapid cooling and exposure to air. The polymers were purified by dialysis against methanol (MWCO 12,000 – 14,000) and the solvent was changed four times to remove all monomer. The purified polymers were characterized by  $^1\text{H}$  NMR, SEC, DLS and TEM.

#### *Preparation of furfuryl mercaptan conjugated nanoparticles [PFHPMA-*b*-POEGMA-*b*-PST]*

Furfuryl mercaptan (1.4  $\mu\text{L}$ ,  $1.4 \times 10^{-5}$  mol), and triethylamine (1.2  $\mu\text{L}$ ,  $8.6 \times 10^{-6}$  mol) were added to PGMA-POEGMA-PST (7.2 mg in 1 ml methanol, depending on  $M_{n,\text{polymer}}$ ), resulting in a ratio of 10 : 6 : 1 per epoxide. The reaction solution is put on an orbital shaker (160 RPM, at RT) for 20 hrs, before increasing the temperature to 50 °C for two hours. The sample was purified by dialysis against methanol (MWCO 6,000), and the solvent was changed three times. The purified polymers were characterized by  $^1\text{H}$  NMR, SEC, DLS and TEM.

#### *Preparation of azide ring-opened nanoparticles [PAHPMA-*b*-POEGMA-*b*-PST]*

Sodium azide (2.8 mg,  $4.3 \times 10^{-5}$  mol) and ammonium chloride (2.3 mg,  $4.3 \times 10^{-5}$  mol) were added to PGMA-POEGMA-PST (17 mg,  $0.86 \times 10^{-7}$  mol in 2 mL methanol), resulting in a ratio of 10:10:1 per epoxide. The reaction solution is put on an orbital shaker (160 RPM, at 50 °C) for 24 hrs, before purification by dialysis against methanol (MWCO 12,000-14,000 Da), and the solvent was changed three times. Subsequently, completion of reaction was confirmed by ATR-FTIR and  $^1\text{H}$  NMR and the nanoparticles were characterized by DLS and TEM.

#### *Preparation of 3-butyn-1-ol conjugated nanoparticles [PHTHPMA-*b*-POEGMA-*b*-PST]*

Deoxygenated 3-butyn-1-ol (0.18  $\mu\text{L}$ ,  $2.3 \times 10^{-6}$  mol in methanol) was added to deoxygenated PAHPMA-*b*-POEGMA-*b*-PST (10 mg,  $3.7 \times 10^{-7}$   $\mu\text{mol}$ ) in methanol, followed by the addition of deoxygenated copper(I) bromide (0.13 mg,  $9.3 \times 10^{-7}$  mol) and N,N,N',N'',N''-pentamethyldiethylenetriamine (PMDTA, 0.19  $\mu\text{L}$ ,  $9.3 \times 10^{-7}$  mol) in methanol, resulting in a ratio of 1.25 : 0.5 : 0.5 : 1 (3-butyn-1-ol : Cu(I)Br : PMDTA : azide-group). All solutions were prepared as stock solution to facilitate the experimental work. The reaction mixture was then stirred at 50 °C for 24 hrs,

before purification by dialysis against methanol (MWCO 12,000 – 14,000 Da), and the solvent was changed three times. Subsequently, completion of reaction was confirmed by ATR-FTIR and  $^1\text{H}$  NMR, and the nanoparticles were characterized by DLS and TEM.

*Preparation of 5(6)-aminofluorescein conjugated nanoparticles [P(FAm-HPMA)-b-POEGMA-b-PST]*

5(6)-fluoresceinamine (75 % purity) (9.3 mg,  $2.7 \times 10^{-5}$  mol), and triethylamine (2.2  $\mu\text{L}$ ,  $1.6 \times 10^{-5}$  mol) were added to PGMA-POEGMA-PST (10.2 mg in 1 mL methanol, depending on  $M_{n,\text{polymer}}$ ), resulting in a ratio of 10 : 6 : 1 per epoxide. The reaction solution is put on an orbital shaker (160 RPM, at RT) for 20 hrs, before increasing the temperature to 50 °C for two hours. The sample was purified by dialysis in methanol (MWCO 6,000), and the solvent was changed three times. The purified polymers were characterized by  $^1\text{H}$  NMR, SEC, UV-Vis and TEM.

*Preparation of 4-aminobutyl-DOTA-tris (t-butyl ester) conjugated nanoparticles [P(DOTA(tBu)-HPMA)-b-POEGMA-b-PST]*

4-Aminobutyl-DOTA-tris (t-butyl ester) (11.3 mg,  $1.6 \times 10^{-5}$  mol), and triethylamine (1.4  $\mu\text{L}$ ,  $1.4 \times 10^{-5}$  mol) were added to PGMA-POEGMA-PST (7.2 mg in 1 mL methanol, depending on  $M_{n,\text{polymer}}$ ), resulting in a ratio of 10 : 6 : 1 per epoxide. The reaction solution is put on an orbital shaker (160 RPM, at RT) for 20 hrs, before increasing the temperature to 50 °C for two hours. The sample was purified by dialysis against methanol (MWCO 12,000 – 14,000 Da), and the solvent was changed three times. The purified polymers were characterized by  $^1\text{H}$  NMR, SEC, and DLS.

*Preparation of 4-aminobutyl-DOTA [DOTA-NH<sub>2</sub>]*

4-Aminobutyl-DOTA-tris (t-butyl ester) (250 mg,  $3.59 \times 10^{-4}$  mol) was dissolved in 5 ml trifluoroacetic acid (TFA) and stirred for 16 h at room temperature. Subsequently, the solvent was removed under reduced pressure at 40 °C and completion of reaction was confirmed by ATR-FTIR and LC-MS.

MS(ESI):  $m/z$ : 447.3 [M-H]<sup>+</sup>

*Preparation of 4-aminobutyl-DOTA(Gd) [Gd-DOTA-NH<sub>2</sub>]*

4-aminobutyl-DOTA (100 mg,  $2.11 \times 10^{-4}$  mol) was dissolved in 4 ml ultrapure water and gadolinium(III) chloride hexahydrate (GdCl<sub>3</sub>) (117 mg,  $3.16 \times 10^{-4}$  mol) was added, and the pH was increased to 6 by addition of a KOH (2 M) solution. Subsequently, the solution was stirred at 50 °C and the pH was readjusted to 6 after 2 hours. After that, the reaction was continued for a total reaction time of 24 h.

The excess of  $\text{GdCl}_3$  was removed by the addition of Chelex-100 resin. This was followed by filtration and lyophilisation of the filtrate, resulting in an off-white solid.

MS(ESI):  $m/z$ : 602.3  $[\text{M-H}]^+$

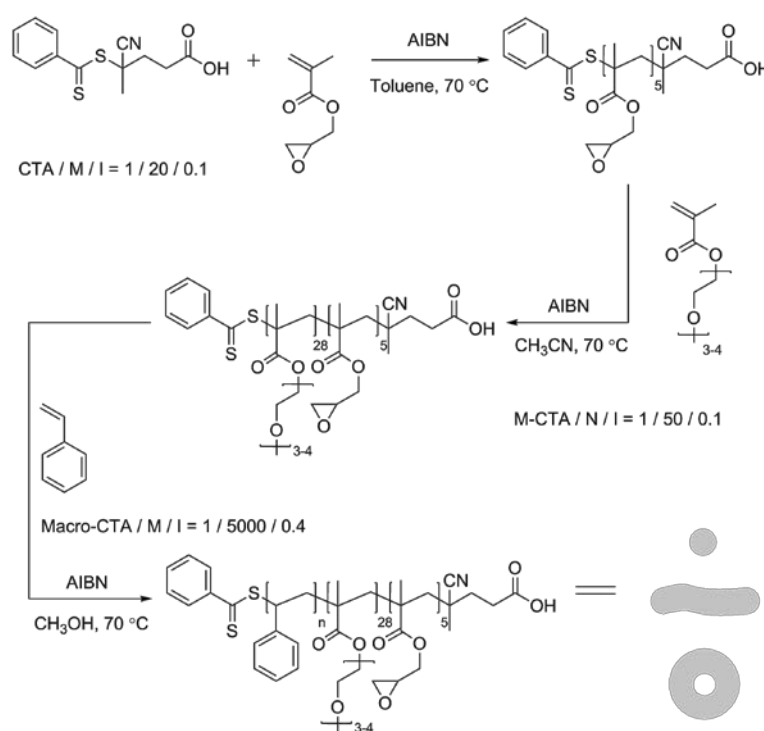
*Preparation of Gd-DOTA conjugated nanoparticles  $[P(\text{Gd-DOTA-HPMA})\text{-}b\text{-POEGMA}\text{-}b\text{-PST}]$*

4-aminobutyl-Gd-DOTA (20 mg,  $3.3 \times 10^{-5}$  mol), and triethylamine (2.8  $\mu\text{L}$ ,  $2.0 \times 10^{-5}$  mol) were added to PGMA-POEGMA-PST (20.9 mg in 1.45 mL methanol, depending on  $M_{n,\text{polymer}}$ ), resulting in a ratio of 10:6:1 per epoxide. The reaction solution is stirred overnight (16 h) at room temperature, before increasing the temperature to 50 °C and continuing the reaction for another 24 h. The sample was then purified by dialysis against methanol (MWCO 12,000 – 14,000), and the solvent was changed three times, followed by three solvent changes in ultrapure water. The reaction was analysed by ICP-AES and the particles were characterized by DLS, TEM and MRI.

### 3.3 Results and discussion

#### 3.3.1 Preparation of PGMA surface-functional block

First, poly(glycidyl methacrylate) (PGMA) was successfully prepared using reversible addition fragmentation chain transfer (RAFT) polymerization as surface-functional block (see Scheme 3.10). 4-Cyanopentanoic acid dithiobenzoate (CPADB) was chosen as a chain transfer agent for its good control over the polymerization of methacrylates and styrenes. [40] A very short functional block of around 5 units was synthesized (see Figure 3.27 and Table 3.9) to limit the effect of the relatively more hydrophobic PGMA on the self-assembly and generate well defined self-assembled nanostructures. The degree of polymerization was determined by comparing the  $^1\text{H}$  NMR signal of the aromatic protons of the RAFT agent to the proton signals of the monomeric epoxide ring. Furthermore the conversion rate was kept low to both minimize the formation of dead polymer which may interfere with the PISA process and maintain high chain end livingness.



Scheme 3.9: synthesis of the PGMA and diblock copolymer PGMA-*b*-POEGMA, followed by the one-pot synthesis of amphiphilic triblock polymeric nanoparticles by RAFT-mediated polymerization-induced self-assembly.

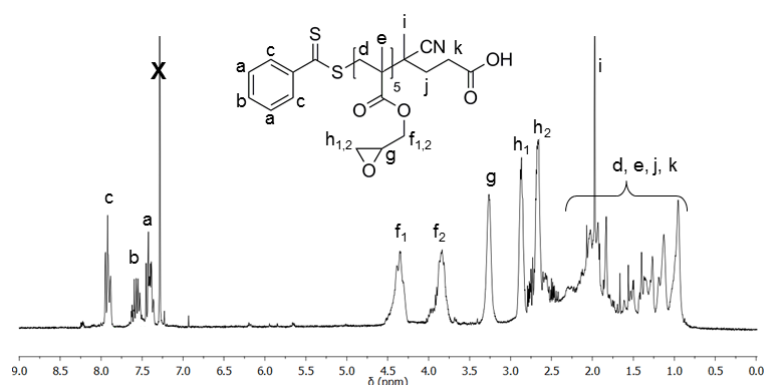


Figure 3.27:  $^1\text{H}$  NMR spectra of poly(glycidyl methacrylate) as recorded in  $\text{CDCl}_3$ .

### 3.3.2 Preparation of chain extended hydrophilic macro-CTA

The purified PGMA was then used as a macro-CTA for the chain extension with oligo(ethylene glycol) methyl ether methacrylate (OEGMA) to provide the hydrophilicity needed for an effective PISA process. The incorporation of POEGMA also limits clearance by the mononuclear phagocyte system, and leads to a better biocompatibility, longer circulation times, and decreased aggregation for future biological applications. [41] A number-average molecular weight of below 10,000 was targeted (see Figure 3.28 and Table 3.9) as this facilitated the polymerization-induced reorganisation. The molecular weight was determined by comparing the  $^1\text{H}$  NMR signals of the aromatic group of the chain transfer agent to the protons of the monomeric methylene protons adjacent to the ester linkage at  $\delta$  4.1 ppm.

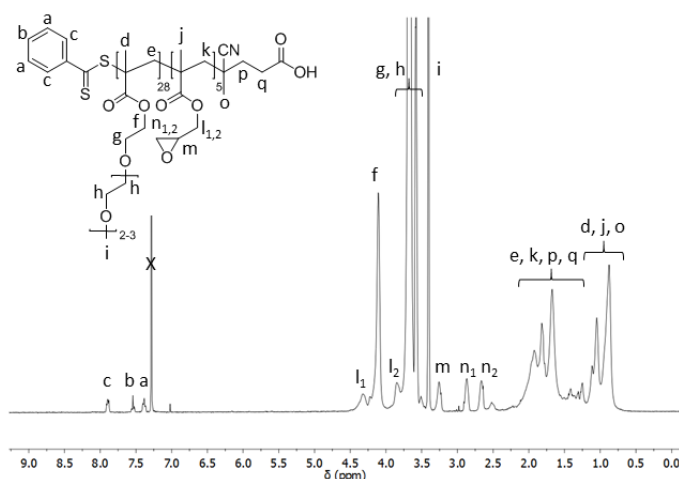


Figure 3.28:  $^1\text{H}$  NMR spectra of PGMA-b-POEGMA as recorded in  $\text{CDCl}_3$ .

### 3.3.3 Preparation of surface-functional block copolymer with various morphologies

Subsequently, PGMA-*b*-POEGMA was used as macro-CTA in the RAFT dispersion polymerization of styrene in methanol, i.e. PISA. As was shown in chapter 2, styrene (ST) is an excellent monomer to be employed in the PISA process in methanol as its homopolymer is insoluble in methanol while the monomer is soluble. The dispersion polymerization was successfully carried out at 70 °C using a high molar feed ratio 1:5000 of PGMA-*b*-POEGMA: ST and was stopped at different polymerization times to yield a range of polymeric nanoparticulate morphologies.

The stability of the functional epoxide group against solvolysis was monitored by  $^1\text{H}$  NMR during the polymerizations and subsequent purifications. The characteristic epoxide signals at  $\delta$  2.85 and 2.65 ppm can be clearly observed in each step (see Figure 3.29A) and the constant ratio compared to the dithiobenzoate signals of the RAFT agent at  $\delta$  7.35 – 7.9 ppm and/or methyl ether signal of POEGMA at  $\delta$  3.3 ppm confirmed the stability of the epoxide against solvolysis. Furthermore, the epoxide functionality was stable over two weeks of storage at -20 °C. The peaks of POEGMA at  $\delta$  4.1 - 3.6 ppm are clearly visible after chain extension with OEGMA, and were used in the third step to calculate the degree of polymerization of styrene using the characteristic styrene peak between  $\delta$  6.3 and 6.9 ppm representing two aromatic protons, indicating successful synthesis of the amphiphilic triblock copolymer.

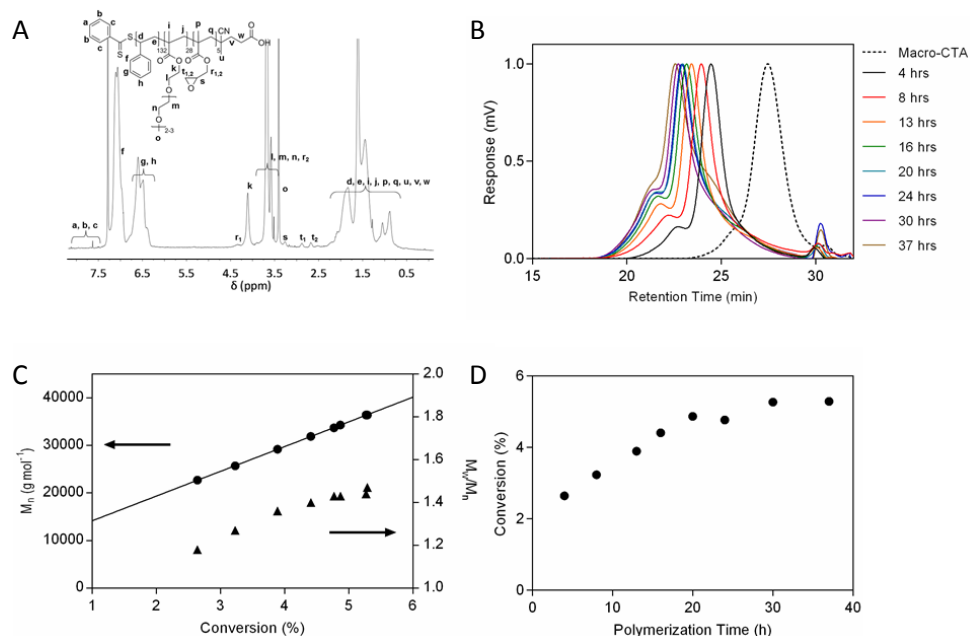


Figure 3.29: (A)  $^1\text{H}$  NMR spectrum of PGMA-*b*-POEGMA-*b*-PST polymers (recorded in  $\text{CDCl}_3$ ); (B) evolution of SEC traces versus polymerization times. (C) Evolution of molecular weight and PDI versus monomer conversion; and (D) conversion versus time plot for the dispersion polymerization of styrene in the presence of macro-CTA.

In polymerisation-induced self-assembly it is essential to maintain control over the growth rate of the polymer after phase separation as was previously shown in chapter 2. SEC traces of the dispersion polymerizations clearly showed that the molecular weight increased with polymerization time (see Figure 3.29B). The livingness of the system was confirmed by a linear increase of molecular weight with conversion, although an increase in PDI was observed (see Figure 3.29C). The presence of molecular weight shoulders at lower retention times is consistent with the formation of dead polymers by coupling reactions, even though conversion rates were kept below 60 %. Styrene conversion continuously increased and a conversion of 5.3 % was achieved after 37 h. Additional experiments showed a further increase in conversion to 7.5 % after 70 h, however  $^1\text{H}$  NMR indicated solvolysis of the epoxide (absence peaks at  $\delta$  2.85 and 2.65 ppm, data not shown). It is proposed that there is a trade-off between lower polymerization rate (i.e. lower initiator concentration) and therewith less dead polymer versus solvolysis of the epoxide functional group when performing the dispersion polymerization in methanol.

Table 3.9: monomer conversion, average number of monomer units (as per  $^1\text{H}$  NMR),  $^1\text{H}$  NMR-determined molecular weight, SEC measured  $M_n$  and polydispersity, number-average hydrodynamic particle diameters and DLS polydispersity and the predominant morphologies obtained by TEM for triblock polymeric nanoparticles with increasing styrene monomer conversion: spherical micelle (M), short wormlike micelle (SW), long wormlike micelle (LW), and vesicle (V).

Polymer	Reaction	Conv	<sup>1</sup> H NMR			SEC			DLS		TEM
	Time (h)	(%) <sup>a</sup>	GMA	OEGMA	ST	M <sub>n</sub> <sup>b</sup> (g mol <sup>-1</sup> )	M <sub>n</sub> <sup>c</sup> (g mol <sup>-1</sup> )	PDI	D <sub>h</sub> (nm) No. avg.	PDI	
PGMA	1.5	25	5	-	-	983	3016	1.10	-	-	-
POEGMA- <i>b</i> -POEGMA	6	56	5	28	-	9383	12967	1.11	-	-	-
PGMA- <i>b</i> -POEGMA- <i>b</i> -PSt	4	2.6	5	28	132	22683	17120	1.18	21.8	0.11	M
	8	3.2	5	28	161	25743	19515	1.27	30.0	0.11	M
	13	3.9	5	28	194	29175	21794	1.36	64.0	0.15	M , SW
	16	4.4	5	28	220	31864	22496	1.40	98.6	0.14	LW
	20	4.9	5	28	244	34295	22958	1.43	122.0	0.14	LW, V
	24	4.8	5	28	238	33734	23463	1.43	121.3	0.14	LW, V
	30	5.3	5	28	264	36382	24958	1.44	152.5	0.15	LW, V
	37	5.3	5	28	264	36440	23266	1.47	121.3	0.06	V

<sup>a</sup> The molecular weight of each polymer was determined using the following formulas:

$\overline{M}_{n, \text{PGMA, NMR}} = [([ \text{at } 2.7\text{ppm} + [ \text{at } 2.9\text{ppm} + [ \text{at } 3.3\text{ppm} + [ \text{at } 3.9\text{ppm} + [ \text{at } 4.1\text{ppm} ] / 5 ] / [([ \text{at } 7.9\text{ppm} ) / 2] \cdot M_{n, \text{PGMA}} + M_{n, \text{CPADB}}]$ . Where  $[ \text{at } 7.9\text{ppm}$  corresponds to the signal of two aromatic protons of the RAFT agent.

$\overline{M}_{n, \text{PGMA-}b\text{-POEGMA, NMR}} = [ [ \text{at } 4.1\text{ppm} / [ \text{at } 7.9\text{ppm} ] \cdot M_{n, \text{POEGMA}} + M_{n, \text{PGMA}} ]$ , with  $[ \text{at } 4.1\text{ppm}$  corresponding to the ester signal of OEGMA,

$\overline{M}_{n, \text{PGMA-}b\text{-POEGMA-}b\text{-PS, NMR}} = [ [ \text{at } 6.3\text{-}6.9\text{ppm} / [ \text{at } 4.1\text{ppm} ] \cdot 2/3 \cdot M_{n, \text{PS}} + M_{n, \text{PGMA-}b\text{-POEGMA}} ]$ , with  $[ \text{at } 4.1\text{ppm}$

<sup>b</sup> Assessed by SEC in DMAC (0.03 % w/v LiBr, 0.05 % BHT) using a conventional calibration curve with narrow molecular weight distribution polystyrene standards.

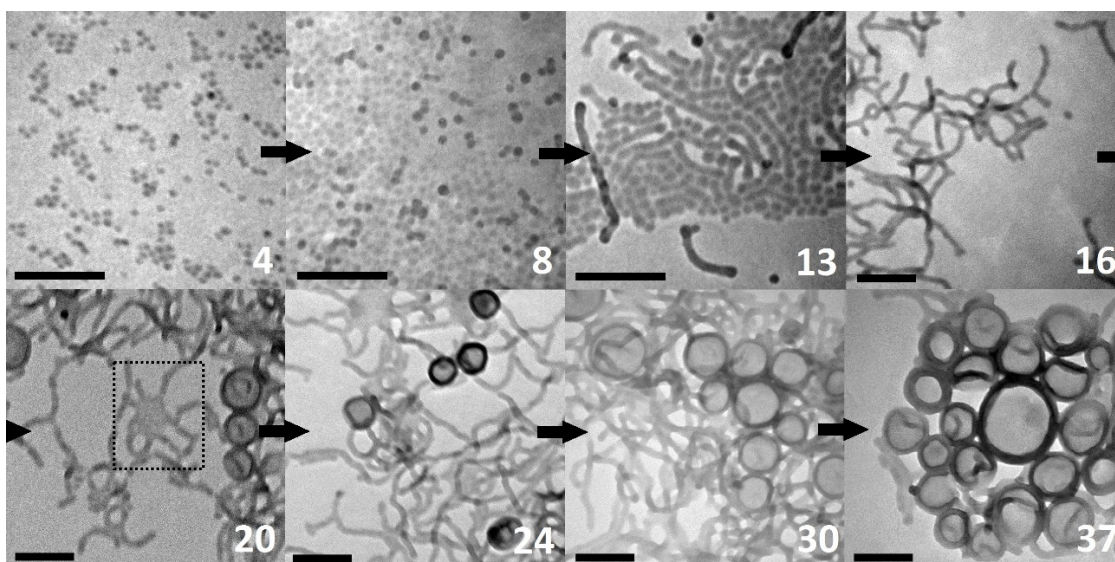


Figure 3.30: illustrative transmission electron micrographs showing the transition between the different morphologies over polymerization time (in hours): spherical micelle → short wormlike micelle → long wormlike micelle → branched worm → octopi → vesicle. The scalar bars represent 200 nm.

The structural evolution was assessed by  $^1\text{H}$  NMR, DLS and TEM. (Figure 3.30 and Table 3.9) The morphology is predominantly dependent on the degree of polymerization ( $\text{DP}_n$ ) of styrene as this affects the volume and length of the hydrophobic part and therewith packing diameter.[42, 43] The first sample was taken after 4 h, when a limited degree of cloudiness of the dispersion polymerization mixture was noted after cooling down. TEM and DLS confirmed the presence of spherical micelles with a  $\text{DP}_{\text{ST,avg}}$  of 132 and a number-average hydrodynamic diameter of 21.8 nm. Increasing the polymerization time to 8 h resulted in larger spherical micelles of 30 nm in size. After 13 h a mixture of short worm-like micelles and spherical micelles was formed with a diameter of 30 nm, transitioning into predominantly long worm-like micelles and branched worms at 16 hours.

The gradual transition from long worm-like micelles and branched worms to vesicles occurred slowly due to a reduced polymerization rate. ‘Octopi’ structures were also observed, which is an intermediate morphology between worm and vesicle as the branched worms undergo partial coalescence and develop nascent bilayers with protruding “tentacles”[42], however due to their transient nature, it was not possible to solely purify these structures. Finally after 37 hours, vesicle was the predominant morphology. All hydrodynamic diameters (assessed by DLS) of the nanoparticles were determined after purification by dialysis against methanol and are shown in Table 3.9. In summary, morphologies of micelles (4, 8 h), worms (16 h), and vesicles (37 h) were prepared by PISA containing active epoxide groups on the surface. Furthermore, transitional phases were observed in between the main morphologies.

### *3.3.4 Investigating versatility of surface functionality*

The versatility of the surface functionality of the main morphologies was demonstrated by conjugating a primary thiol (furfuryl mercaptan), primary amine (i.e. fluorescein amine), and introducing azide functionality by ring opening using sodium azide followed by a proof of concept copper(I)-catalysed azide–alkyne cycloaddition (CuAAC) click reaction with propargylamine. All reactions were carried out on self-assembled nanoparticles in solution. Afterwards, the products were assessed by  $^1\text{H}$  NMR, SEC, DLS and TEM.

#### *Conjugation of primary thiol compounds*

Firstly, the conjugation of a primary thiol, i.e. furfuryl mercaptan, was tested using the three main morphologies: micelle, worm-like micelle, and vesicle. This compound was selected as the aromatic furan group is easily identifiable in the  $^1\text{H}$  NMR spectra well resolved from the styrene signal, which facilitates assessing the conjugation efficacy. The reaction was carried out using a ten-fold excess of furfuryl mercaptan per epoxide in the presence of triethylamine as base. The reaction was continued for 20 h at room temperature, followed by two hours at 50°C. The mild conditions were chosen to limit solvolysis.

A shift of the furan aromatic signals was observed after conjugation, resulting in partial overlapping with the styrene signals, however successful conjugation was observed by monitoring the aromatic proton signal shift between  $\delta$  7.41 and 7.45 ppm (Figure 3.31A). Furthermore, disappearance of the signals at  $\delta$  2.85 and 2.65 ppm indicated complete ring-opening due to conjugation and partial solvolysis. (Figure 3.31B) The yield was estimated by  $^1\text{H}$  NMR to be 17 – 22 % by comparing the signal at  $\sim\delta$  7.43 ppm to the POEGMA signal at  $\delta$  4.1 ppm, see Table 10). This results in on average 1.2 to 1.4 furfuryl mercaptan molecules per polymer. TEM confirmed that the morphology remained unchanged (see Figure 3.31C).

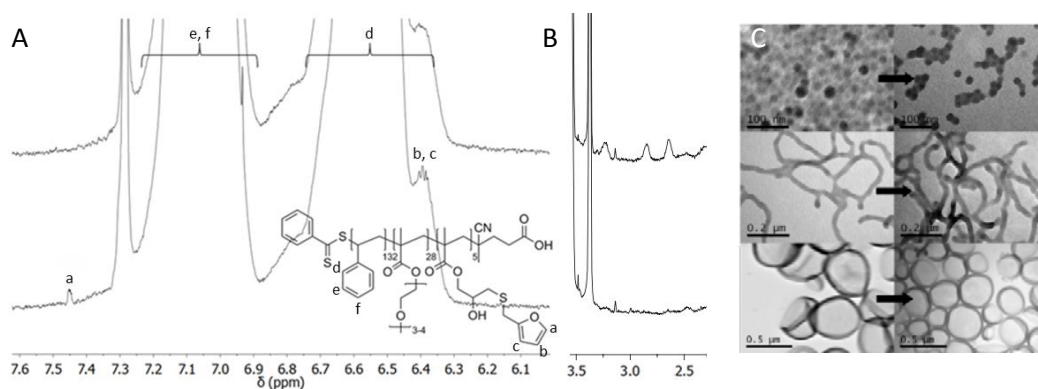


Figure 3.31: (A-B) amplifications of the  $^1\text{H}$  NMR spectra of the reaction of furfuryl mercaptan to worm-like micelles (PGMA-*b*-POEGMA-*b*-PS) in deuterated chloroform (top: before conjugation, bottom: after conjugation) (A) appearance of peak at 7.43 ppm after dialysis demonstrates successful furfuryl mercaptan conjugation, (B) the disappearance of NMR signals belonging to the epoxide groups indicate complete ring-opening. (C) TEM confirmed stability of each morphology after conjugation.

Table 10: conjugation of furfuryl mercaptan to epoxide surface-functional polymeric nanoparticles.

Polymer	DP ( $^1\text{H}$ NMR)			Furfuryl mercaptan Conjugation (%)	TEM shape	
	GMA	OEGMA	ST		Before conjugation	After conjugation
PGMA- <i>b</i> -POEGMA- <i>b</i> -PS	5	28	132	18	M	M
	5	28	220	22	LW	LW
	5	28	264	17	V	V

#### Preparation of azide surface-functional nanoparticles

The spring-loaded epoxide can be nucleophilically opened by sodium azide creating an azide group, which are widely used due to their efficiency in ‘clicking’ [44] to a terminal alkyne via the azide-alkyne Huisgen cycloaddition. An additional advantage of azides is their stability towards dimerizations and hydrolysis, [44] however caution should be exerted regarding their heat and shock-sensitivity and organic azides can be explosive with little input of external energy if the compound has a low carbon-to-nitrogen ratio ( $\text{C/N} < 3$ ).

The epoxide-groups of the self-assembled nanoparticles in methanol were ring-opened using an excess of sodium azide with ammonium chloride as coordinating salt. After purification, the nanoparticles were characterized by ATR-FTIR and  $^1\text{H}$  NMR. IR showed the appearance of a peak at  $2100\text{ cm}^{-1}$  that is attributed to azide bond stretching (see Figure 3.32A), confirming successful ring opening, while NMR indicated full conversion of the epoxide group by the disappearance of the signals at  $\delta\ 2.85\text{ ppm}$  and  $\delta\ 2.65\text{ ppm}$  (see

Figure 3.32B). As additional validation, the ring-opening by sodium azide was also performed in DMF (a good solvent), confirming similar results (see Figure 3.33). Finally, the morphologies were found to remain stable to ring-opening as assessed by DLS (Figure 3.33B).

In summary, azide surface-functional nanoparticles with different morphologies were successfully prepared when self-assembled, without the need for solvent switch.

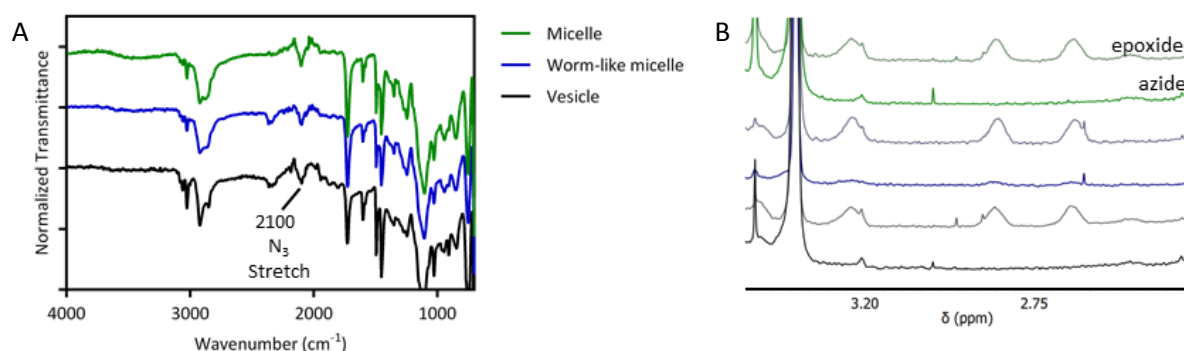


Figure 3.32: (A) ATR-FTIR spectra of the three main morphologies after ring-opening with sodium azide, showing the appearance of a peak at 2100 cm<sup>-1</sup> indicating azide bond stretching. (B) <sup>1</sup>H NMR spectra of each morphology before and after ring-opening, showing complete ring-opening of the epoxide groups.

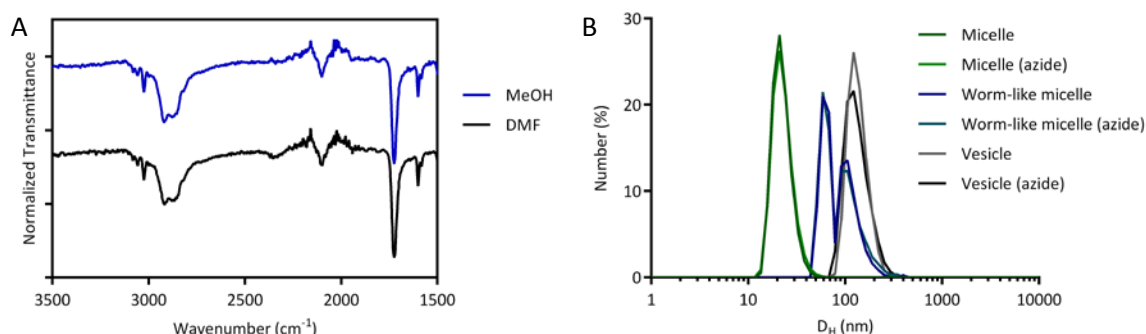


Figure 3.33: (A) ATR FTIR spectra of ring-opening with sodium azide in methanol (MeOH, self-assembled nanoparticles) versus in *N,N*-dimethylformamide (DMF, dissolved polymer) showing similar efficiency; (B) dynamic light scattering showing stability of self-assembled nanoparticles upon ring-opening.

### Testing CuAAC-click reaction to azide surface-functional nanoparticles

A proof-of-concept CuAAC click reaction was performed using propargylamine as model alkyne. Copper(I) bromide was used as source of copper(I), which was stabilized using *N,N,N',N'',N''*-pentamethyldiethylenetriamine (PMDTA) to prevent disproportionation. The click reaction was carried out using a ratio of 1.25 : 0.5 : 0.5 : 1 of 3-butyne-1-ol : Cu(I)Br : PMDTA : azide-group. The

reaction was carried out in both methanol and DMF as solvents to confirm and compare the efficacy of CuAAC click reactions. ATR FTIR revealed complete consumption of the azide peak (stretch) at  $2100\text{ cm}^{-1}$  in both solvents (see Figure 3.34A), indicating successful conjugation. Furthermore, DLS showed that polymeric micelles (used here as an example) remain unchanged to the introduced surface modifications (see Figure 3.34B).

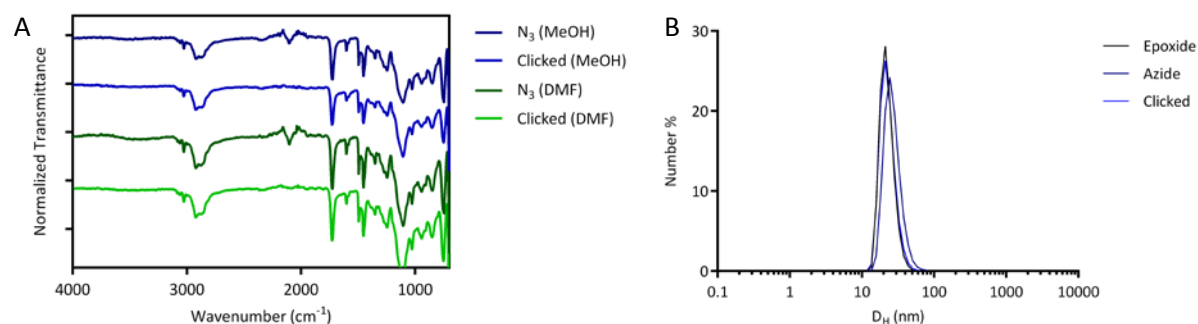


Figure 3.34: (A) ATR FTIR of azide-functional polymers in methanol (micelles) or DMF (dissolved), before and after CuAAC click reaction with propargylamine. (B) Number-average distribution in DLS of epoxide-functional, azide-functional and propargyl-clicked polymeric micelles.

In summary, both ring-opening using sodium azide, and the subsequent CuAAC click reaction using propargylamine as model compound could be carried out successfully using self-assembled polymers in methanol without the need of a solvent switch.

#### *Conjugation of primary amine compounds*

Initially a small library of primary amines which included furfuryl amine, propargyl amine, D-mannose amine, and 1-(3-aminopropyl)imidazole were investigated for their potential to react with the epoxide-functional nanoparticles both in methanol and water. Disappearance of the epoxide-signals in  $^1\text{H}$  NMR was observed in both solvents, and solvolysis could be excluded as the epoxide signals were unaffected when subjected to reaction conditions in absence of the primary amine (see Figure 3.35B). However, no new NMR signals were observed, which was attributed to the crowded NMR spectra originating from PST ( $\delta$  7.4 – 6.1 ppm), POEGMA ( $\delta$  4.4 – 3.3 ppm) and the polymer backbone ( $\delta$  2.3 – 0.6 ppm).

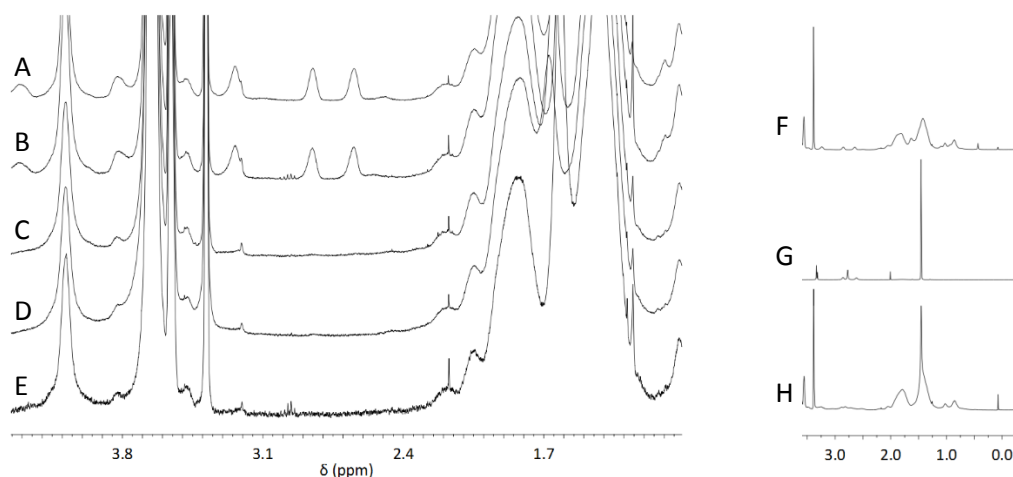


Figure 3.35: On the left <sup>1</sup>H NMR study of the conjugation of a primary amine, propargylamine, to the epoxide surface-functional polymeric nanoparticles. (A) epoxide surface-functional polymeric nanoparticles, showing oligoethylene glycol methyl ether NMR signals between  $\delta$  4.1 – 3.3 ppm, and epoxide NMR signals at  $\delta$  3.24, 2.85, and 2.65 ppm; (B) after reaction conditions of 50 °C overnight; (C) 10 eq. of propargylamine and 6 eq. of triethylamine (per epoxide); (D) 10 eq. of propargylamine; (E) 6 eq. of triethylamine. On the right <sup>1</sup>H NMR study of the conjugation of 4-aminobutyl-DOTA-tris (t-butyl ester) to the epoxide surface-functional polymeric nanoparticles: (F) epoxide surface-functional polymeric nanoparticles, showing the polymer backbone NMR signals; (G) 4-aminobutyl-DOTA-tris (t-butyl ester), showing the large proton NMR signal for the t-butyl groups; (H) conjugation of NH<sub>2</sub>-DOTA(tBu) to the polymeric nanoparticle.

Therefore, 4-aminobutyl-DOTA-tris (t-butyl ester) (NH<sub>2</sub>-DOTA(tBu)) was exploited as it was expected that successful conjugation could be confirmed due to the presence of a new <sup>1</sup>H NMR signal due to the strong t-butyl protons (arising from 27 protons per conjugated molecule, see Figure 3.35G). <sup>1</sup>H NMR spectra indeed showed the appearance of a NMR signal at  $\delta$  1.57 ppm indicating successful conjugation (see Figure 3.35H), however the determination of an accurate conjugation efficiency was complicated by the overlapping polymer background signal.

Hence 5(6)-fluoresceinamine (FAm) was selected to evaluate the conjugation of a primary amine, as the dye permits a more accurate quantification of the coupling efficiency by UV-Vis spectroscopy. All three main morphologies: micelle, worm-like micelle and vesicle were tested using the same conditions as for furfuryl mercaptan. Upon purification, the compounds were redissolved in THF for UV-Vis characterization (see Figure 3.36A) as the self-assembled nanoparticles displayed a high background absorbance in methanol. The FAM-conjugation efficiency was determined by comparing the absorbance of the FAM-labelled polymers at 489 nm to a calibration series of different concentrations of FAM in methanol (see Figure 3.36B). Methanol was used as solvent as FAM is not

soluble in THF. This already suggests that the absorbance signal of the polymer at 489 nm can only be attributed to conjugated dye as opposed to free dye.

Data analysis shows an average FAm coupling efficiency of 23 %, with the highest for the micelle (26 %) and the lowest for the vesicle morphology (19 %). This implies that each polymer has at least one FAm conjugated. The relatively low efficacy could be caused by steric hindrance (all epoxide groups are located next to each other).

The conjugation of FAm was also investigated using size-exclusion chromatography (SEC, in DMAc) equipped with both a refractive index and UV-Vis detector to further validate successful covalent conjugation as opposed noncovalent interactions such as hydrophobic interactions and  $\pi$ - $\pi$  stacking.

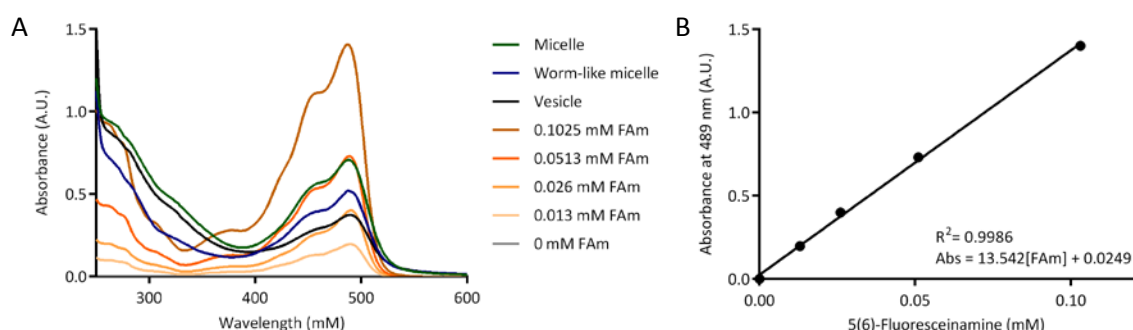


Figure 3.36: (A) UV-Vis absorbance of (5)6-fluoresceinamine (FAM)-labelled polymers in THF (1 mg / mL) and a calibration series of FAM (in methanol as FAM is not soluble in THF). (B) Calibration curve of FAM with  $R^2$  of 0.9986.

Table 3.11: conjugation of 5(6)-fluoresceinamine to epoxide surface-functional polymeric nanoparticles.

Polymer	DP ( $^1H$ NMR)			5(6)-Fluoresceinamine Conjugation (%)	TEM shape	
	GMA	OEGMA	ST		Before conjugation	After conjugation
PGMA- <i>b</i> -POEGMA- <i>b</i> -PS	5	28	132	26	M	M
	5	28	220	23	LW	LW
	5	28	264	19	V	V

DMAc SEC demonstrated that the retention time of the absorbance signal of FAM (489 nm) correlated to the retention time of the polymer (as detected by refractive index), confirming FAM was covalently bound to the polymer (see Figure 3.37A). The absence of an absorbance signal at higher retention times indicated the absence of any noncovalently bound FAM.

Finally, the FAM-labelled nanoparticles were also imaged by TEM, and the morphologies were shown to be stable to the labelling (see Figure 3.37B and Table 3.11)

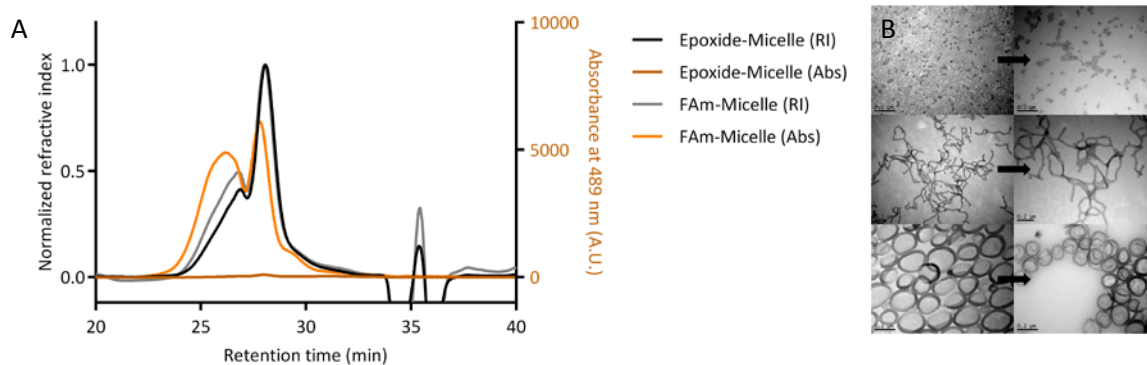
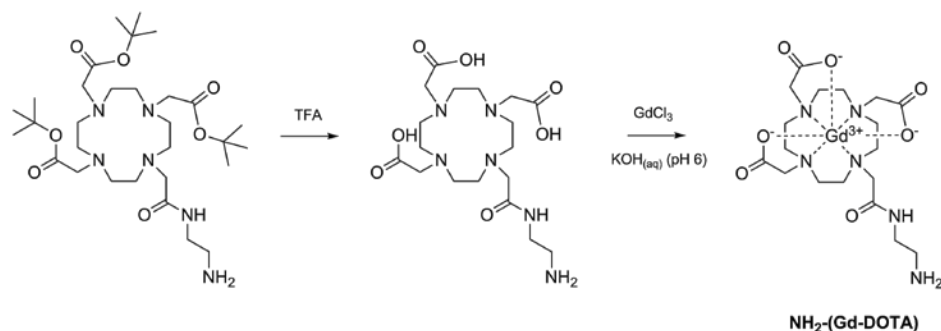


Figure 3.37: (A) size-exclusion chromatograms in DMAc of polymer before and after 5(6)-fluoresceinamine conjugation, on the left axis the refractive index is displayed and on the right axis absorbance at 489 nm. (B) Transmission electron micrographs showing the different morphologies before and after fluorophore conjugation.

### 3.3.5 Preparation of $T_1$ -weighted MR contrast agents with different morphologies

The three different morphologies were labelled with Gd-DOTA to investigate their potential as MRI contrast agent. Firstly, an amine-functional gadolinium chelate ( $\text{NH}_2$ -Gd-DOTA) was synthesized in a two-step reaction (see Scheme 3.11). 4-Aminobutyl-DOTA-tris (t-butyl ester) was deprotected overnight in trifluoroacetic acid (TFA) and completion of the reaction was assessed by  $^1\text{H}$  NMR and LC-MS. Proton NMR showed the complete disappearance of the *tert*-butyl ester signal at 1.41 ppm, and LC-MS revealed a  $m/z$  of 447.3 ( $\text{M}+\text{H}$ ) (see Figure 3.38).



Scheme 3.10: synthesis of amine-functional gadolinium-DOTA chelate.

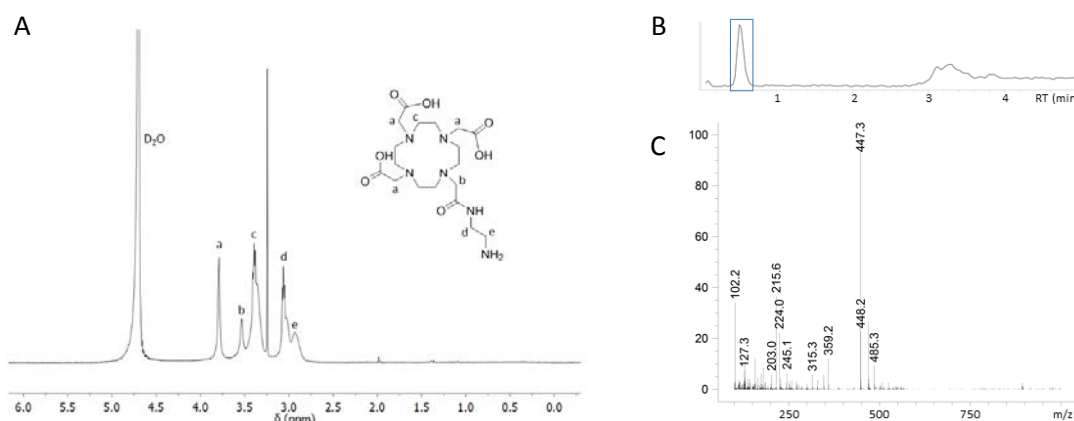


Figure 3.38: (A)  $^1\text{H}$  NMR spectra of 4-aminobutyl-DOTA recorded in deuterium oxide, demonstrating complete removal of the *tert*-butyl ester protection groups at  $\delta$  1.41 ppm. (B) API-ESI positive mode chromatogram with (C) mass spectrum of main signal ( $M + H$ , 447.3).

In the next step, the chelate was incubated in the presence of gadolinium under slightly acidic conditions (pH 6) at 50 °C for 24 hours to facilitate complexation. Finally free gadolinium was removed using a chelating material, Chelex 100, which has the ability to bind transition metal ions such as gadolinium, followed by filtration and lyophilisation to obtain a white solid. The final compound, 4-aminobutyl-DOTA(Gd), was successfully characterized by LC-MS with  $m/z$  602.3 ( $M + H$ ).

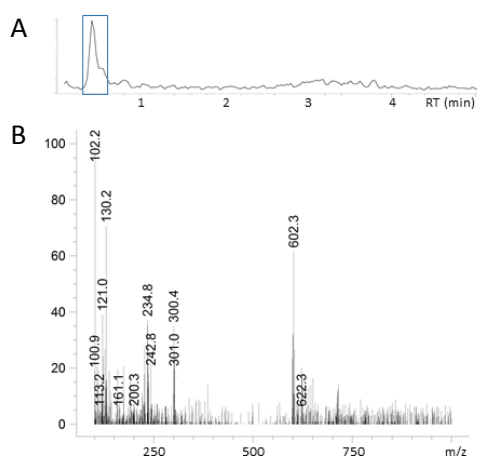
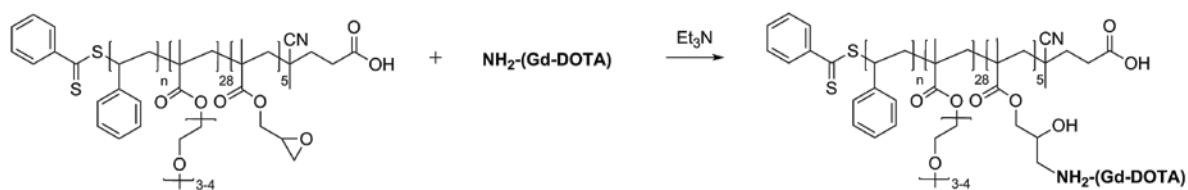


Figure 3.39: (A) API-ESI positive mode chromatogram with (B) mass spectrum of main signal ( $M + H$ , 602.3) representing 4-aminobutyl-DOTA(Gd).

Next, 4-aminobutyl-DOTA(Gd) was conjugated to the epoxide surface-functional nanoparticles (PGMA-*b*-POEGMA-*b*-PS) using the same reaction conditions as for the other primary amines (see Scheme 3.12). After purification by dialysis and solvent switch to water, the gadolinium content was determined by inductively coupled plasma optical emission spectroscopy (ICP-OES).



Scheme 3.11: synthesis of Gd-DOTA labelled nanoparticles

The coupling efficiency could be determined using the molecular weight of the used polymers (as determined by  $^1\text{H}$  NMR), the concentration of polymer and gadolinium content (ICP-OES) (see Table 3.12). The highest conjugation efficiency was achieved for the micellar nanoparticles, between 23 to 25 %. This translates to around 1.2 gadolinium chelates per polymer. The efficiency was lower for the vesicle morphology, i.e. approximately 15 %. It is proposed that the high polarity of the chelate limits penetration throughout the polymersome membrane, limiting conjugation to the epoxide groups presented on the inner membrane. The Gd-conjugated polymers could not be characterized by NMR due to the presence of gadolinium. TEM confirmed stability of each morphology upon conjugation (see Figure 3.40).

A potential solution for increasing the gadolinium-loading for vesicles is to couple the amino-chelate to the macro-RAFT (PGMA-*b*-POEGMA) before dispersion polymerization as this would result in a higher Gd-labelling for the inner membrane, and moreover also lead to a higher overall conjugation efficiency due to higher reactant concentrations and less steric hindrance than when carrying out the conjugation on dispersed nanoparticles. This pathway was explored in a pilot study, but partial hydrolysis of the RAFT end-group was observed that limited control over the subsequent dispersion polymerization, resulting in a high polymer polydispersity ( $\text{PDI}_{\text{SEC}} \sim 1.75$ ). Nevertheless DLS and TEM measurements showed the presence of narrowly dispersed spherical structures with a number-average hydrodynamic diameter of 180 nm and a  $\text{PDI}_{\text{DLS}}$  of 0.038.

Table 3.12: efficacy of Gd-chelate conjugation to the different morphologies when using an amine-functional gadolinium chelate ( $\text{NH}_2\text{-Gd-DOTA}$ )

Morphology	Coupling efficacy (%)	Gd per polymer	$M_{n,\text{SEC}}$	$M_{n,\text{SEC}}$	PDI
			before Gd-labelling ( $\text{g mol}^{-1}$ )	after Gd-labelling ( $\text{g mol}^{-1}$ )	
Micelle	23	1.17	17120	17510	1.31
Worm-like micelle	25	1.24	22496	22942	1.42
Vesicle	15	0.75	23266	23450	1.48

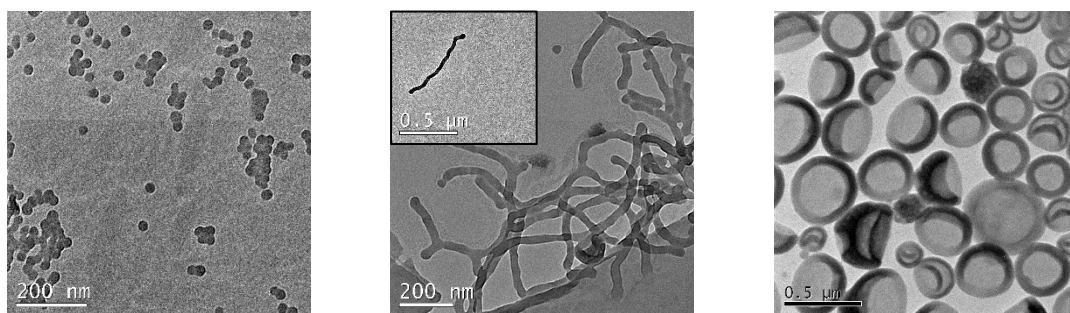


Figure 3.40: Representative TEM images of each DOTA(Gd)-labelled nanoparticle: micelle, filomicelle and vesicle.

### *Study of relaxivity of different morphologies by 7 T MRI*

The MRI properties of the gadolinium-labelled polymeric nanoparticles were studied using a state-of-the-art 7-Tesla whole-body MRI scanner (MAGNETOM 7T, Siemens) using Nova single channel transmit with 32 receiver channels with an internal diameter of 18.5 cm and a 21 cm field of view along the z-direction). A dilution series of each nanoparticle in water was prepared in a 96 wells plate for high-throughput measurement. The space between the wells was filled with 3 % agarose to minimize susceptibility effects caused by water-air interfaces.

For the determination of the  $r_1$  relaxivity, inversion recovery sequences were utilized with different inversion times, ranging from 22 to 4000 ms ( $TR/TE = 5000 / 11.5$  ms). All images were acquired with a 2 mm slice thickness, 150 x 112.5 mm FOV, 256 x 192 matrix size, and 1 average. To quantify the  $r_2$  relaxivity, a Carr-Purcell-Meiboom-Gill (CPMG) multi-echo spin echo sequence was used to acquire 32 images at echo times (TE) ranging from 11.5 to 368 ms with a repetition time (TR) of 5000 ms.

Region of interest (ROI) areas of 5 x 5 voxels (25 voxels) were manually placed over the central part of each well on the images. To calculate the  $R_1$  relaxation rate ( $R_1 = 1 / T_1$ ), the signals from each region of interest were averaged and plotted as a function of inversion time. The  $R_1$  values were then calculated (as the decay constants) by numerically fitting (using a nonlinear least-squares algorithm (Matlab) the data to the following equation.

$$S = S_0(1 - 2e^{-TI \cdot R_1}) \quad (3.1)$$

To calculate  $R_2$ , the signals from each region of interest were averaged and plotted as a function of TE. The  $R_2$  values were then calculated by numerically fitting (using a nonlinear least-squares algorithm (Matlab) the data to a monoexponential equation.

$$S = S_0 e^{-TE \cdot R_2} \quad (3.2)$$

The respective longitudinal and transverse relaxation rates,  $R_1$  and  $R_2$ , were then plotted as a function of the gadolinium concentration and linear least-squares analysis (GraphPad Prism) was used to determine the  $r_1$  and  $r_2$  relaxivities. These give an indication of the efficiency of contrast enhancement by MRI contrast agents as defined by the formula below. The higher the relaxivity, the more efficient the contrast agent is in shortening the relaxation times and thus enhancing contrast.

The efficiency depends on various factors including the external field strength, the number of coordinated water molecules, water exchange rate, rotational diffusion, first and second coordination sphere hydration, and the ion to water proton distance. [4] Critical parameters such as the residence time of the coordinated water ( $\tau_M$ ) and the rotational correlation time of the final molecule ( $\tau_R$ ) are most influential in determining contrast efficacy when attaching CAs to a nanoparticle structure.

$$r_{1,2} = \frac{R_{1,2} - R_{1,2(0)}}{[Gd]} \quad (3.3)$$

$R_{1,2(0)}$  is the relaxation rate in absence of the contrast agent (water only).

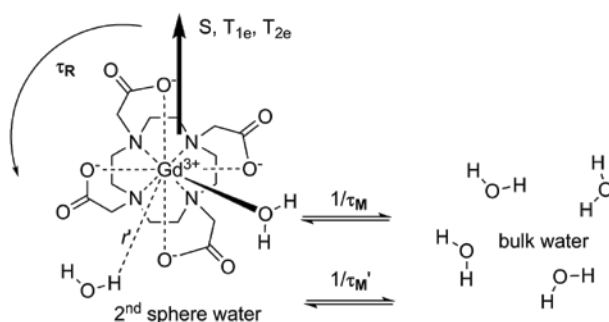


Figure 3.41: Factors influencing solvent water relaxation, adapted from Caravan *et al.* [4] The metal complex has an inner sphere of nitrogen and oxygen atoms from the DOTA ligand and a coordinated water molecule. There is a distinct second hydration sphere with Gd-H distance  $r$ , and water molecules from both spheres undergo exchange with bulk water at rates  $1/\tau_M$  and  $1/\tau_M'$  for first- and second-sphere exchange

The results of the MRI measurements are plotted in Figure 3.42 and the extracted relaxivity values are summarized in Table 13. The conjugation of the Gd-chelate onto the micelles resulted in a 53 % enhancement of  $r_1$  relaxivity relative to  $NH_2$ -Gd-DOTA ( $3.46 \text{ mM}^{-1}\text{s}^{-1}$ ). The worm-like micelles showed an even higher increase of 76 % (to  $6.10 \text{ mM}^{-1}\text{s}^{-1}$ ), while conjugation to the vesicles lead to an improvement of 72 %. The relaxivity enhancement can be attributed to the more optimal (slower) rotational correlation times when conjugated to nanoparticles. For example, Vasovist (MS-325) (an albumin-targeted intravascular contrast agent) displayed an increased relaxivity upon binding to

albumin caused by a slower tumbling rate. [20] In addition, a recent study by Li *et al.* showed an increase in  $r_1$  relaxivity upon conjugation to core-cross-linked star polymers at field strengths ranging from 0.47 to 9.4 T. [21]

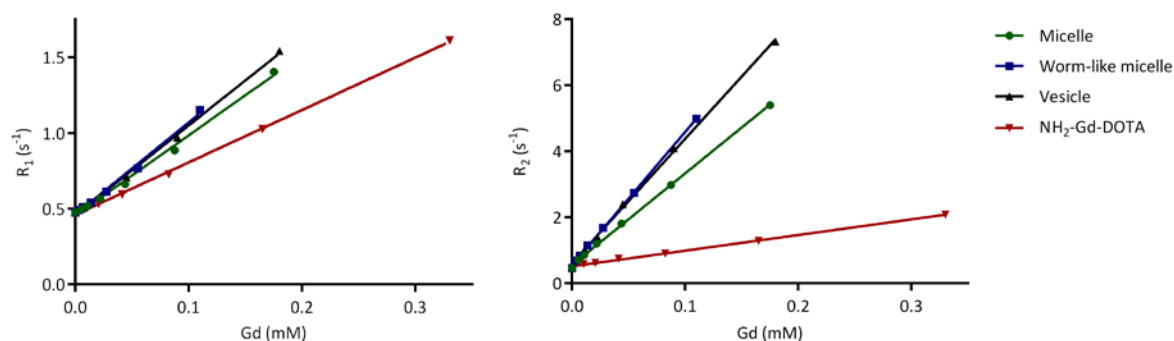


Figure 3.42: (A) Longitudinal relaxation rates ( $R_1$ ) plotted versus gadolinium concentration (by ICP-OES) for the different morphologies and amine-functional gadolinium chelate ( $R^2 \geq 0.9959$ ); and (B) transversal relaxation rates ( $R_2$ ) plotted versus gadolinium concentration ( $R^2 \geq 0.9975$ ).

Table 13:  $T_1$  and  $T_2$  relaxivity ( $r_1$  and  $r_2$ ) for the different morphologies and amine-functional gadolinium chelate as control.

	$r_1$ ( $\text{mM}^{-1}\text{s}^{-1}$ )	$r_1$ ( $\text{mM}^{-1}\text{s}^{-1}$ ) per polymer	$r_2$ ( $\text{mM}^{-1}\text{s}^{-1}$ )	$r_2$ ( $\text{mM}^{-1}\text{s}^{-1}$ ) per polymer	$r_2/r_1$
Micelle	5.29	6.28	27.78	32.50	5.3
Worm-like micelle	6.10	7.56	40.43	50.13	6.6
Vesicle	5.94	4.45	37.74	28.13	6.4
NH <sub>2</sub> -Gd-DOTA	3.46	-	4.74	-	1.4

The highest  $r_1$  relaxivity is observed for worm-like micelles and can be elucidated due to their larger size, resulting in slower rotational dynamics as compared to spherical micelles. The vesicles have a comparable  $r_1$  relaxivity, however they have a lower gadolinium loading resulting in a lower local gadolinium concentration resulting in a less efficient contrast agent (see Table 13). The observed  $r_1$  relaxivities are similar to published values in literature. For example, Mishra *et al.* reported a maximal  $r_1$  of  $4.82 \text{ mM}^{-1}\text{s}^{-1}$  for avidin-conjugated Gd chelates at 7 T [45] and Servant *et al.* described a  $r_1$  relaxivity of  $6.6 \text{ mM}^{-1}\text{s}^{-1}$  for gadolinium-functionalised multi-walled carbon nanotubes. [46]

The  $r_2/r_1$  ratio is much higher for the polymeric nanoparticles than for the chelate. This can be explained by the molecular parameters and field strength. At high-field strength (7 T), slow rotating nanoparticles are less effective in increasing  $r_1$  relaxivity as compared to lower-field (1.5 T), whereas the  $r_2$  relaxivity is relatively field independent. [4] For example, core-cross-linked star polymers had

an  $r_1$  relaxivity of  $15.6 \text{ mM}^{-1}\text{s}^{-1}$  at 1.4 T, compared to only  $4.7 \text{ mM}^{-1}\text{s}^{-1}$  at 9.4 T. [21] At the same time, the fast tumbling chelate exhibits a relatively field independent but low  $r_1$  and  $r_2$  relaxivities. Gadolinium-conjugated nanoparticles are still beneficial at high-field strengths, but they are even more efficient at the lower field strengths that are currently being used in the clinical practice (1.5 – 3 T). Therefore it would be recommended to also measure the  $T_1$  relaxivity at these field strengths to obtain additional information regarding the effect of morphology on the relaxation parameters (rotational correlation and water exchange rates).

### 3.4 Conclusion

Polymerization-induced self-assembly was exploited to prepare surface-functional polymer-based nanoparticles with different sizes and morphologies: micelles, worm-like micelles (filomicelles) and vesicles. The versatility of the epoxide functional groups and the stability of the shapes to surface modification was successfully demonstrated by conjugation to primary amines, thiols and ring-opening by azide followed by a CuAAC click reaction. Finally, the application of the diverse polymeric nanoparticles for  $T_1$ -weighted MRI was investigated, showing that the worm-like micelle is the most promising candidate as it coalesces a good gadolinium-labelling efficiency with a high  $r_1$  relaxivity. Due to the enhanced blood circulation times of filomicelles, the gadolinium-labelled worm-like micelles have potential applications as intravascular contrast agent for magnetic resonance angiography and in tumour targeting. The gadolinium loading could be further improved by increasing the number of glycidyl groups and using CuAAC click reactions for the conjugation of the gadolinium chelate.

### 3.5 References

1. Estelrich, J., M.J. Sánchez-Martín, and M.A. Busquets, *Nanoparticles in magnetic resonance imaging: from simple to dual contrast agents*. International Journal of Nanomedicine, 2015. **10**: p. 1727-1741.
2. P&S Market Research, *Global Magnetic Resonance Imaging (MRI) Market Size, Share, Development, Growth and Demand Forecast to 2022*. 2016.
3. Strijkers, G.J., et al., *MRI contrast agents: current status and future perspectives*. Anticancer Agents Med Chem, 2007. **7**(3): p. 291-305.
4. Caravan, P., *Strategies for increasing the sensitivity of gadolinium based MRI contrast agents*. Chemical Society Reviews, 2006. **35**(6): p. 512-523.
5. Bryson, J.M., J.W. Reineke, and T.M. Reineke, *Macromolecular Imaging Agents Containing Lanthanides: Can Conceptual Promise Lead to Clinical Potential?* Macromolecules, 2012. **45**(22): p. 8939-8952.
6. Yang, C.-T. and K.-H. Chuang, *Gd(iii) chelates for MRI contrast agents: from high relaxivity to "smart", from blood pool to blood-brain barrier permeable*. MedChemComm, 2012. **3**(5): p. 552-565.
7. Kobayashi, H. and M.W. Brechbiel, *Nano-sized MRI contrast agents with dendrimer cores*. Advanced Drug Delivery Reviews, 2005. **57**(15): p. 2271-2286.
8. Na, H.B., I.C. Song, and T. Hyeon, *Inorganic Nanoparticles for MRI Contrast Agents*. Advanced Materials, 2009. **21**(21): p. 2133-2148.
9. Arami, H., et al., *In vivo delivery, pharmacokinetics, biodistribution and toxicity of iron oxide nanoparticles*. Chemical Society Reviews, 2015. **44**(23): p. 8576-8607.
10. van Zijl, P.C.M. and N.N. Yadav, *Chemical exchange saturation transfer (CEST): What is in a name and what isn't?* Magnetic Resonance in Medicine, 2011. **65**(4): p. 927-948.
11. Ruiz-Cabello, J., et al., *Fluorine (<sup>19</sup>F) MRS and MRI in biomedicine*. NMR in biomedicine, 2011. **24**(2): p. 114-129.
12. Thurecht, K.J., et al., *Functional hyperbranched polymers: toward targeted in vivo <sup>19</sup>F magnetic resonance imaging using designed macromolecules*. J Am Chem Soc, 2010. **132**(15): p. 5336-7.
13. Cowper, S.E., et al., *Scleromyxoedema-like cutaneous diseases in renal-dialysis patients*. Lancet, 2000. **356**(9234): p. 1000-1.
14. Kuo, P.H., et al., *Gadolinium-based MR Contrast Agents and Nephrogenic Systemic Fibrosis*. Radiology, 2007. **242**(3): p. 647-649.
15. Reilly, R.F., *Risk for Nephrogenic Systemic Fibrosis with Gadoteridol (ProHance) in Patients Who Are on Long-Term Hemodialysis*. Clinical Journal of the American Society of Nephrology : CJASN, 2008. **3**(3): p. 747-751.
16. Perez-Rodriguez, J., et al., *Nephrogenic Systemic Fibrosis: Incidence, Associations, and Effect of Risk Factor Assessment—Report of 33 Cases*. Radiology, 2009. **250**(2): p. 371-377.
17. Albanese, A., P.S. Tang, and W.C. Chan, *The effect of nanoparticle size, shape, and surface chemistry on biological systems*. Annu Rev Biomed Eng, 2012. **14**: p. 1-16.
18. Chauhan, V.P. and R.K. Jain, *Strategies for advancing cancer nanomedicine*. Nat Mater, 2013. **12**(11): p. 958-962.
19. Matsumura, Y. and H. Maeda, *A new concept for macromolecular therapeutics in cancer chemotherapy: mechanism of tumoritropic accumulation of proteins and the antitumor agent smancs*. Cancer Res, 1986. **46**(12 Pt 1): p. 6387-92.
20. Caravan, P., et al., *Gadolinium(III) Chelates as MRI Contrast Agents: Structure, Dynamics, and Applications*. Chem Rev, 1999. **99**(9): p. 2293-352.
21. Li, Y., et al., *The precise molecular location of gadolinium atoms has a significant influence on the efficacy of nanoparticulate MRI positive contrast agents*. Polymer Chemistry, 2014. **5**(7): p. 2592-2601.
22. Truong, N.P., et al., *The importance of nanoparticle shape in cancer drug delivery*. Expert Opin Drug Deliv, 2015. **12**(1): p. 129-42.
23. Geng, Y., et al., *Shape effects of filaments versus spherical particles in flow and drug delivery*. Nat Nano, 2007. **2**(4): p. 249-255.
24. Park, J.-H., et al., *Magnetic Iron Oxide Nanoworms for Tumor Targeting and Imaging*. Advanced Materials, 2008. **20**(9): p. 1630-1635.
25. Park, S., et al., *Therapeutic nanorods with metallic multi-segments: Thermally inducible encapsulation of doxorubicin for anti-cancer therapy*. Nano Today, 2012. **7**(2): p. 76-84.

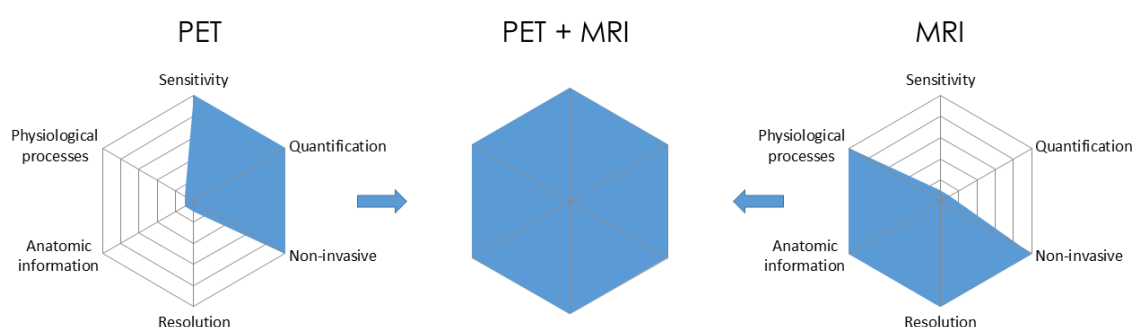
26. Karagoz, B., et al., *An efficient and highly versatile synthetic route to prepare iron oxide nanoparticles/nanocomposites with tunable morphologies*. *Langmuir*, 2014. **30**(34): p. 10493-502.
27. Mohapatra, J., et al., *Iron oxide nanorods as high-performance magnetic resonance imaging contrast agents*. *Nanoscale*, 2015. **7**(20): p. 9174-9184.
28. Wang, G., et al., *High-relaxivity superparamagnetic iron oxide nanoworms with decreased immune recognition and long-circulating properties*. *ACS Nano*, 2014. **8**(12): p. 12437-49.
29. Yang, X., et al., *Multifunctional SPIO/DOX-loaded wormlike polymer vesicles for cancer therapy and MR imaging*. *Biomaterials*, 2010. **31**(34): p. 9065-9073.
30. Zhou, J., et al., *Gadolinium complex and phosphorescent probe-modified NaDyF<sub>4</sub> nanorods for T1- and T2-weighted MRI/CT/phosphorescence multimodality imaging*. *Biomaterials*, 2014. **35**(1): p. 368-77.
31. Sun, H., et al., *GdIII functionalized gold nanorods for multimodal imaging applications*. *Nanoscale*, 2011. **3**(5): p. 1990-1996.
32. Hifumi, H., et al., *Dextran Coated Gadolinium Phosphate Nanoparticles for Magnetic Resonance Tumor Imaging*. *Journal of Materials Chemistry*, 2009. **19**(35): p. 6393-6399.
33. Bruckman, M.A., et al., *Tobacco mosaic virus rods and spheres as supramolecular high-relaxivity MRI contrast agents*. *Journal of Materials Chemistry B*, 2013. **1**(10): p. 1482-1490.
34. Tesauro, D., et al., *Peptide Derivatized Lamellar Aggregates as Target-Specific MRI Contrast Agents*. *ChemBioChem*, 2007. **8**(8): p. 950-955.
35. Canning, S.L., G.N. Smith, and S.P. Armes, *A Critical Appraisal of RAFT-Mediated Polymerization-Induced Self-Assembly*. *Macromolecules*, 2016. **49**(6): p. 1985-2001.
36. Warren, N.J. and S.P. Armes, *Polymerization-Induced Self-Assembly of Block Copolymer Nano-objects via RAFT Aqueous Dispersion Polymerization*. *Journal of the American Chemical Society*, 2014. **136**(29): p. 10174-10185.
37. Zhang, L. and A. Eisenberg, *Multiple Morphologies of "Crew-Cut" Aggregates of Polystyrene-*b*-poly(acrylic acid) Block Copolymers*. *Science*, 1995. **268**(5218): p. 1728-31.
38. Derry, M.J., L.A. Fielding, and S.P. Armes, *Polymerization-induced self-assembly of block copolymer nanoparticles via RAFT non-aqueous dispersion polymerization*. *Progress in Polymer Science*, 2016. **52**: p. 1-18.
39. Mitsukami, Y., et al., *Water-Soluble Polymers. 81. Direct Synthesis of Hydrophilic Styrenic-Based Homopolymers and Block Copolymers in Aqueous Solution via RAFT*. *Macromolecules*, 2001. **34**(7): p. 2248-2256.
40. Karagoz, B., et al., *Polymerization-Induced Self-Assembly (PISA) – control over the morphology of nanoparticles for drug delivery applications*. *Polym. Chem.*, 2014. **5**(2): p. 350-355.
41. Rabanel, J.M., P. Hildgen, and X. Banquy, *Assessment of PEG on polymeric particles surface, a key step in drug carrier translation*. *J Control Release*, 2014. **185**: p. 71-87.
42. Blanazs, A., et al., *Mechanistic Insights for Block Copolymer Morphologies: How Do Worms Form Vesicles?* *Journal of the American Chemical Society*, 2011. **133**(41): p. 16581-16587.
43. Blanazs, A., A.J. Ryan, and S.P. Armes, *Predictive Phase Diagrams for RAFT Aqueous Dispersion Polymerization: Effect of Block Copolymer Composition, Molecular Weight, and Copolymer Concentration*. *Macromolecules*, 2012. **45**(12): p. 5099-5107.
44. Kolb, H.C., M.G. Finn, and K.B. Sharpless, *Click Chemistry: Diverse Chemical Function from a Few Good Reactions*. *Angewandte Chemie International Edition*, 2001. **40**(11): p. 2004-2021.
45. Mishra, A., et al., *A new class of Gd-based DO3A-ethylamine-derived targeted contrast agents for MR and optical imaging*. *Bioconjug Chem*, 2006. **17**(3): p. 773-80.
46. Servant, A., et al., *Gadolinium-functionalised multi-walled carbon nanotubes as a T1 contrast agent for MRI cell labelling and tracking*. *Carbon*, 2016. **97**: p. 126-133.

## Chapter 4: Designed nanoparticles for dual-modality imaging and drug/radiopharmaceutical delivery: combining SPECT/PET and MRI

## 4.1 Introduction

There is a great need to develop efficient imaging agents for the enhanced early detection of cancer and cardiovascular diseases. An early diagnosis will increase the chance of successful treatment outcomes via earlier and individualized treatment protocols. Several imaging modalities are presently used for the diagnosis of diseases, however all have their advantages and disadvantages as was discussed in chapter 1. [1, 2] For example, positron emission tomography (PET) has a high signal sensitivity, but has low resolution and does not provide any information regarding anatomical structure, which thus necessitates the use of computerized tomography (CT) or magnetic resonance imaging (MRI). CT is useful for obtaining clear *in vivo* images of anatomical structures, and is economically favorable compared with other imaging modalities. However, it is not useful for soft tissue imaging as it yields poor-quality images of soft tissues. [3] While MRI provide can provide an excellent soft tissue contrast without exposure to ionizing radiation, has a high resolution, but low sensitivity and cannot be quantified. [4]

Consequently, the synergistic combination of PET and MRI has great potential to become the next generation of dual-modality scanners in medical imaging. [5] (see Scheme 4.13) This combination would overcome the inherent disadvantages of each single instrument by combining the high-resolution, anatomical imaging strengths of MRI, with the sensitivity and quantifiable signal of PET. [6] Furthermore, patients would receive a greatly reduced radiation dose relative to current dual-modality scanners (e.g. PET/CT), and the technique would also be helpful for improving our understanding of certain malignant and/or benign cancers in soft tissues. [1] The first commercially available integrated whole-body PET/MR scanner was released by Siemens in 2011 [7], and PET/MR scanners are being introduced to more and more medical clinics around the world. [8]



Scheme 4.12: A hybrid PET/MRI system synergistically compensates for the limitations of each modality.

The development of dual-modality PET-MRI agents will enhance the diagnostic capacity of multimodal imaging in the clinical setting as it would allow image co-registration, and mapping of biomarkers

across resolution scales, resulting in a more accurate diagnosis. [1] Nanomedicine, using nano-sized particles (1 to 1000 nm) offers the potential to achieve this as the large surface to volume ratio enables the introduction of multiple functional groups onto the surface for imaging, targeting, and therapeutic applications. [3] Moreover, modification of the size, shape and surface of nanoparticles results in enhanced blood circulation times, and increased tumour uptake via the enhanced permeability and retention effect (EPR). [9]

Only recently have PET/MRI dual-mode probes emerged in the literature. [10] However, these were mostly based on the combination of PET isotopes with superparamagnetic iron oxide (SPIO) nanoparticles, [4-6, 11-13] providing a hypointense MRI contrast that can be hard to interpret. [6] In contrast, only a few small-molecule probes were based on positive gadolinium MRI contrast agents. [14, 15] Previously, some studies have also been published regarding bimodal positive MRI/SPECT imaging probes, where the radio-isotope (such as technetium-99m [16], indium-111 [17], and iodine-125/127) [18] was utilized to increase sensitivity or employed to address the essential question of the fate of the nanoparticles and their degradation products [17, 19].

Functional polymeric nanoparticles comprised of star polymers have attracted a lot of research interest, since they have unique properties in terms of the relationship between arm number, arm molecular weight and solvent viscosity. [20, 21] The high molecular weight of these materials allows them to take advantage of the passive targeting of vascularized tumours with leaky vasculature. Together with the reduced lymphatic drainage, this enhanced permeability and retention (EPR) effect [9] leads to tumour accumulation of the nanoparticles. [22]

Davis and co-workers published work demonstrating the unique opportunities for the specific modification and controlled biodegradability of biocompatible polyethylene glycol (PEG) based star polymers synthesised via an arm-first RAFT process. [21, 23] PEG-based polymer materials are of particular interest in biomedical applications as they have been shown to prevent clearance by the mononuclear phagocyte system and lead to better biocompatibility, longer circulation times, and decreased aggregation. [24] The size of the stars can be varied between 10 and 40 nm by changing the molecular weight of the PEG-based arms, giving a facile approach for investigating the influence of size on passive targeting, biodistribution and clearance. The chemistry afforded by the use of the RAFT polymerisation process (via telechelic RAFT agents) facilitates star modification either through RAFT end group degradation by aminolysis to yield a thiol end group, [25, 26] or accessing the orthogonal chemistry of the RAFT R-group (for example an activated amine reactive ester. [27] Furthermore,

potential incorporation of a biodegradable linker in the polymer structure, such as disulfide, acetal or ketal also affords the opportunity to precisely control the biodegradation of the star polymer. [23]

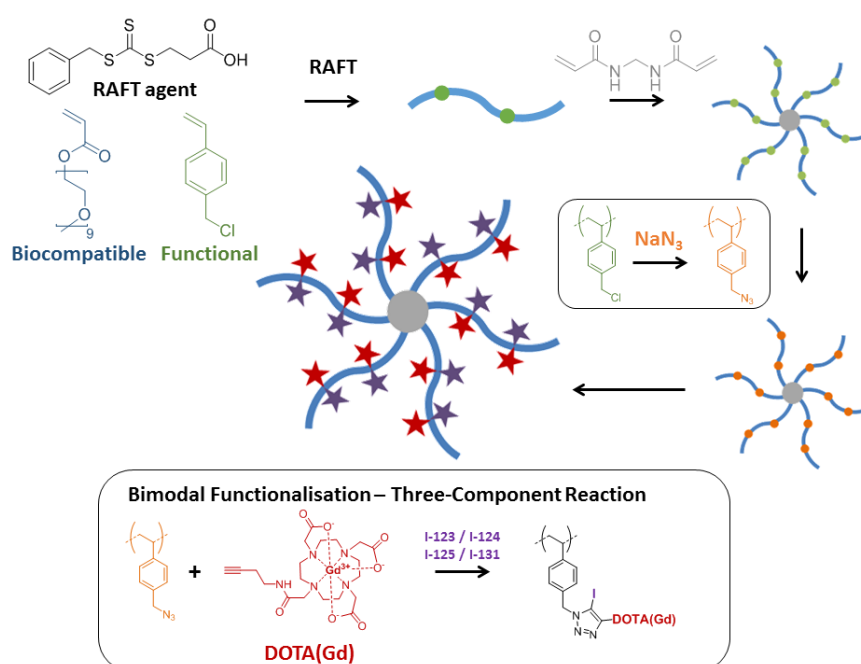
Recently, Li *et al.* published on the use of star polymers as MRI contrast agent, facilitated by conjugating Gd-DOTA to the core, arm or star-surface. [28-30] Gadolinium(III) complexes are often used in clinical MRI to increase contrast by selectively relaxing the water molecules near the complex, resulting in a shorter longitudinal ( $T_1$ ) relaxation and hence signal enhancement on  $T_1$ -weighted MRI scans. [31] Chelation is required due to its *in vivo* toxicity, and several low molecular weight  $Gd^{3+}$  chelates, such as Gd-diethylenetriaminepentaacetic acid (Gd-DTPA) or Gd-tetraazacyclododecane tetraacetic acid (Gd-DOTA), exist as commercial products and are routinely employed in clinical settings. [31] However, optimization of relaxation parameters such as rotational correlation time and water exchange is required to further increase the sensitivity of these agents for molecular imaging, and this can be achieved by conjugation to slow rotating nanoparticles while simultaneously increasing the local contrast agent concentration. [32]

Core and arm incorporation of Gd-DOTA was achieved by means of copolymerization of the activated ester monomer pentafluorophenyl acrylate (PFPA) in the polymeric arm, showing the potential of introducing metal-binding chelates and the possibility of varying its location inside the star structure. [29] MRI relaxivity, the efficiency of the contrast agent to change contrast, was the highest when localized on the surface due to maximum water accessibility and rotational dynamics. However, overall molecular relaxivity was highest when conjugated to the arms as this allowed a much higher number of contrast agents per molecule. [29] Other functional monomers have also been incorporated, such as 2-vinyl-4,4-dimethyl-5-oxazolone (VDM) and 4-vinylbenzaldehyde. [33]

As mentioned above, nuclear imaging (i.e. PET and SPECT) is widely used as a powerful diagnostic tool by clinicians and scientists [34] due to its high sensitivity (the level of detection approaches  $10^{-11}$  M of tracer for PET) and isotropism (i.e., ability to detect expression accurately, regardless of tissue depth), which provide reliability for quantitative imaging analyses of *in vivo* abnormalities. [35] Typically radionuclides are attached to a platform of interest (such as an antibody, nanoparticles or drug) by covalent binding (for example fluodeoxyglucose( $^{18}F$ ), the standard radiotracer used by PET neuroimaging and cancer patient management, [36] and radio-iodine [37]), or through specially designed high affinity binding groups, for example 1,4,7-triazacyclononane-1,4,7-trisacetic acid (NOTA) for copper-64 and gallium-68. [38] Iodine is attractive for multiscale imaging as its numerous radioisotopes enable a wide range of applications: the low-energy  $\gamma$ -emission of iodine-125 ( $t_{1/2}$  = 59.4 days) for autoradiography, the more energetic  $\gamma$ -rays of iodine-123 ( $t_{1/2}$  = 13.2 h) for single photon

emission computed tomography (SPECT),  $\beta$ -particles from iodine-131 ( $t_{1/2} = 8.0$  days) for radioimmunotherapy, and  $\beta^+$  from iodine-124 ( $t_{1/2} = 4.18$  days) for PET. [37, 39]

Dual-modality using the star polymers, combining gadolinium chelates and radio-iodine, can be achieved using a recently published one-pot three-component reaction, using a copper(II)-mediated reaction of azides, alkynes, and iodine-125 to yield 5-iodo-1,2,3-triazoles. [37, 40] The Arstad group synthesized a library of structurally diverse iodine-125-labelled triazoles functionalized with bioconjugation groups, fluorescent dyes, and biomolecules. [37]



Scheme 4.13: Synthesis pathway for the development of bimodal PET/MRI core-cross-lined star polymer. Different iodine radioisotopes can be incorporated: e.g. iodine-123 for SPECT, iodine-124 for PET and iodine-131 for radioimmunotherapy.

In this chapter, a bimodal core-cross-linked star polymer was developed that contains both an MRI contrast agent (Gd-DOTA) and a radio-isotope (iodine-125) using the three-component reaction (see Scheme 4.14), where iodine-125 can be replaced by iodine-124 for PET imaging, or potentially iodine-131 for radioimmunotherapy. First, an azide functional star polymer was synthesized using the arm-first method. Next the one-pot three-component (azide, alkyne, iodine) reaction was investigated for macromolecules using a model system comprising a linear azide functional polymer, a simple alkyne (3-butyn-1-ol) and cold sodium iodide, followed by applying the three-component reaction to the more complex star architecture. In the next step, both linear and star polymers were successfully labelled with iodine-125 using 3-butyn-1-ol or butyne-DOTA(Gd), and finally the MRI properties of the bimodal star polymer were studied.

## 4.2 Experimental Section

### 4.2.1 Materials

4-Vinylbenzyl chloride (90 %, Sigma-Aldrich) was passed through a column of basic alumina (Sigma-Aldrich) in order to remove the inhibitor before use. 3-butyn-1-ol (97 %), copper(II) chloride (> 99.999 %), gadolinium(III) chloride hexahydrate (99 %), *N,N'*-methylenebis(acrylamide) (DMAc, 99 %), oligo(ethylene glycol) methyl ether acrylate (average  $M_n$  480 g mol<sup>-1</sup>), propargylamine (98 %), sodium iodide ( $\geq$  99.5 %), triethyl amine ( $\geq$  99 %), and trifluoroacetic acid (99 %) were used as received from Sigma-Aldrich. *N,N*-dimethylformamide (DMF,  $\geq$  99.8 %) was supplied by Merck Millipore. Potassium hydroxide pellets ( $\geq$  85 %) were purchased from Chem-Supply. Butyne-DOTA-tris(*t*-butyl ester) was obtained from Macrocyclics and Chelex® 100 resin was supplied by Bio-Rad. Azobis(isobutyronitrile) (AIBN, Fluka, 98 %) was purified by recrystallization from methanol. Iodine-125 radionuclide (0.1 M sodium hydroxide) was obtained from Perkin Elmer and diluted to 100 MBq/mL in DMSO). Finally, 3-(benzyl sulfanyl thiocarbonyl sulfanyl)-propanoic acid (BSPA) was prepared according to a procedure described in literature. [41]

### 4.2.2 Physical and analytical methods

#### <sup>1</sup>H NMR

<sup>1</sup>H NMR spectra were recorded using a Bruker UltraShield 400 (400.13 MHz) spectrometer running Bruker Topspin, version 1.3. Deuterated chloroform (CDCl<sub>3</sub>), dimethyl sulfoxide-d<sub>6</sub> (DMSO-d<sub>6</sub>) or deuterium oxide (D<sub>2</sub>O) was used as solvent. All chemical shifts are reported in ppm ( $\delta$ ) relative to tetramethylsilane, referenced to the chemical shifts of the residual solvent resonances (CDCl<sub>3</sub> = 7.26 ppm, DMSO-d<sub>6</sub> = 2.50, D<sub>2</sub>O = 4.79). [42]

#### Size exclusion chromatography

DMAc size exclusion chromatography (SEC) was implemented using a Shimadzu modular system comprising a SIL20AD automatic injector, a DGU12A degasser, a CTO10A column oven, a LC10AT pump, a RID10A differential refractive-index detector, and a SPD10A Shimadzu UV/Vis detector. A 50  $\times$  7.8 mm guard column followed by three KF-805L columns in series (300  $\times$  8 mm linear columns, bead size: 10  $\mu$ m, pore size maximum: 5000 Å) were used for the analyses. *N,N'*-Dimethylacetamide (DMAc, HPLC grade, 0.03% w/v lithium bromide) with a flow rate of 1 mL min<sup>-1</sup> and a constant temperature of 50 °C was used as the mobile phase. The samples were filtered through 0.45  $\mu$ m filters prior to injection. The unit was calibrated using commercially available linear poly(styrene) standards (0.5–

2000 kDa, Polymer Laboratories). Chromatograms were processed using Cirrus 2.0 software (Polymer Laboratories).

For radio-iodine

Aqueous size exclusion chromatography (SEC) was implemented using a Waters system comprising a Waters 717 autosampler, a Waters In-line degasser, a Waters 515 HPLC pump, a Waters 2414 refractive index detector, a Waters 486 tuneable absorbance detector and an IN/US Systems  $\gamma$ -RAM model 4 radio-HPLC detector (15 mm loop and HV of 190). An Agilent PL aquagel-OH 50 column was used for analysis.

A phosphate buffer (0.10 mM, 0.1 M sodium nitrate, containing 20 % DMSO (HPLC grade) with a flow rate of 0.6 mL min<sup>-1</sup> and a constant temperature of 40 °C was used as the mobile phase. The samples were filtered through 0.45  $\mu$ m filters (Alltech 13 mm nylon syringe filter polypropylene housing) prior to injection. Chromatograms were then processed using Waters software.

#### *Dynamic light scattering*

DLS measurements were performed using a Malvern Zetasizer Nano Series running DTS software and using a 4 mW He-Ne laser operating at a wavelength of 633 nm and an avalanche photodiode detector. The scattered light was detected at an angle of 173°.

#### *Attenuated Total Reflectance-Fourier Transform Infrared Spectroscopy*

ATR-FTIR measurements were performed using a Shimadzu IRTracer 100 Fourier transform infrared spectrometer with a GladiATR 10 single reflection ATR accessory. Spectra were then obtained in the mid infrared region of 4000–600 cm<sup>-1</sup> at a resolution of 8 cm<sup>-1</sup> (512 scans) and analysed using LabSolution IR software.

#### *Ultra-high performance liquid chromatography / mass spectroscopy (UHPLC/MS)*

The chromatographic analysis was performed using an Agilent 1260 Infinity system equipped with a binary pump (G1312C), autosampler (G1367E), DAD module (G4212A) and an 1100 MSD mass spectrometer. System control, data acquisition and interpretation were made using LC/MSD Chemstation Rev.B.04.03 coupled with Masshunter Easy Access Software.

For LC: reverse phase HPLC analysis was carried out using a Poroshell 120 EC-C18 column (3.0 x 50 mm, 2.7-micron) at 35°C and an injection volume of 1  $\mu$ L. Starting with water containing 0.1% formic

acid), a gradient was introduced (5-100% acetonitrile containing 0.1% formic acid) over 3.8 minutes with a flow rate of 0.500 mL/min.

For MS: ionization was performed using a quadrupole API-ES source, a capillary voltage of 3000 V and a drying gas temperature of 350°C

#### *Inductively Coupled Plasma–Optical Emission Spectrometry (ICP-OES)*

The  $\text{Gd}^{3+}$  content of the polymer-based nanoparticles was determined by inductively coupled plasma–optical emission spectrometry (ICP-OES) using a Perkin-Elmer OPTIMA 7300 spectrometer. Samples were prepared by dissolving 0.5 mg of polymer in 10 mL of ultrapure water.

### 4.2.3 Syntheses

#### *Preparation of poly(4-vinylbenzyl chloride-co-oligo(ethylene glycol) methyl ether acrylate [P(VBC-co-OEGA)]*

RAFT agent 3-(benzyl sulfanyl thiocarbonyl sulfanyl)-propanoic acid (BSPA, 70.8 mg,  $2.6 \times 10^{-4}$  mol), 4-vinylbenzyl chloride (4-VBC, 189  $\mu$ L,  $1.34 \times 10^{-3}$  mol), oligo(ethylene glycol) methyl ether acrylate (OEGA, 7.0 mL,  $1.6 \times 10^{-2}$  mol) and azobis(2-methylpropionitrile) (AIBN, 4.3 mg,  $2.6 \times 10^{-5}$  mol) were dissolved in toluene (14.0 mL) in a septa-sealed vial. The vial was placed in an ice bath, and the solution was purged with nitrogen for 45 min. The ratio between the 4-VBC, OEGA, RAFT agent and AIBN in the polymerization medium was 5 : 60 : 1 : 0.1. After deoxygenation, the reaction mixture was then placed in an oil bath at 70 °C. After 10 h of reaction, the reaction was quenched via rapid cooling and exposure to oxygen. The reaction was directly analysed by  $^1\text{H}$  NMR to determine the monomer conversion. The polymer was concentrated by partial evaporation of solvent, and the polymer was precipitated five times in 2 : 1 diethyl ether to petroleum spirit (BR 40 - 60 °C) to remove the non-reacted monomer and RAFT-agent. The purified polymer was then dried at 30 °C under vacuum overnight to give 1.5 g of a yellow viscous solution.

#### *Preparation of core-cross-linked P(VBC-co-OEGA) stars [P[P(VBC-co-OEGA)-co-MBAA]]*

P(VBC-co-OEGA) linear arm (250 mg,  $2.91 \times 10^{-5}$  mol,  $M_n = 8600$  g mol $^{-1}$ , PDI = 1.16), N,N'-methylenebis(acrylamide) (27.7 mg,  $1.80 \times 10^{-4}$  mol) and AIBN (1.6 mg,  $9.8 \times 10^{-6}$  mol) were dissolved in 3 ml toluene in a septa-sealed vial. The ratio between arm polymer, cross-linker, and AIBN in the polymerization medium was 1 : 6 : 0.33. The vial was then purged for 30 minutes at 0 °C. The polymerization was carried at 70 °C for 24 h, before quenching the reaction via rapid cooling and exposure to oxygen. The conversion was determined by  $^1\text{H}$  NMR and the star polymer was purified by precipitation in diethyl ether/chloroform (12:1 v/v) and then dried under vacuum. Yield 175 mg. The product was analysed by  $^1\text{H}$  NMR, SEC, and ATR-FTIR.

#### *Preparation of azide-functional linear polymer P(VBAz-co-OEGA)*

P(VBC-co-OEGA) linear arm (500 mg,  $5.81 \times 10^{-5}$  mol,  $M_n = 8600$  g mol $^{-1}$ , PDI = 1.16) was dissolved in 15 ml N,N-dimethylformamide (DMF) and sodium azide was added (95.9 mg,  $1.45 \times 10^{-5}$  mol). The reaction was stirred for 48 h in darkness at room temperature. Afterwards, excess sodium azide was removed by dialysis in darkness (molecular weight cutoff 3,500 Da, three times DMF solvent change, followed by three times acetone solvent change). Finally, the purified polymer was dried under vacuum and analysed by  $^1\text{H}$  NMR, SEC, and ATR-FTIR.

#### *Preparation of azide-functional core-cross-linked star [P(P(VBAz-co-OEGA)-co-MBAA)]*

Core-cross-linked P(VBC-co-OEGA) star (250 mg,  $4.46 \times 10^{-6}$  mol,  $M_n = 56,000 \text{ g mol}^{-1}$ , PDI = 1.10) was dissolved in 7.2 ml DMF and sodium azide was added (95.9 mg,  $1.45 \times 10^{-5}$  mol). The reaction was stirred for 48 h in darkness at room temperature. Afterwards, excess sodium azide was removed by dialysis in darkness (molecular weight cutoff 12,000 – 14,000 Da, three times DMF solvent change, followed by three times acetone solvent change). Finally, the purified polymer was dried under vacuum and analysed by  $^1\text{H}$  NMR, SEC, and ATR-FTIR.

#### *Preparation of butyne-DOTA*

Butyne-DOTA-tris(t-butyl ester) (180 mg,  $2.34 \times 10^{-4}$  mol) was dissolved in 5 ml trifluoroacetic acid (TFA) and stirred for 16 h at room temperature. Subsequently, the solvent was removed under reduced pressure at 40 °C and completion of reaction was confirmed by  $^1\text{NMR}$  and UHPLC-MS.

MS(ESI): m/z: 456.2 [M+H]<sup>+</sup>

#### *Preparation of butyne-DOTA(Gd)*

Butyne-DOTA (100 mg,  $2.20 \times 10^{-4}$  mol) was dissolved in 4 ml ultrapure water, gadolinium(III) chloride hexahydrate ( $\text{GdCl}_3$ ) (117 mg,  $3.16 \times 10^{-4}$  mol) was added and the pH was increased to 6 by dropwise addition of a KOH (2 M) solution. Subsequently, the solution was stirred at 50 °C and the pH was readjusted to 6 after 2 hours. After that, the reaction was continued for a total reaction time of 24 h. The excess of  $\text{GdCl}_3$  was removed by the addition of Chelex-100 resin. This was followed by filtration and lyophilisation of the filtrate, resulting in an off-white solid.

MS(ESI): m/z: 610.2 [M+H]<sup>+</sup>

#### *Three component reaction of 3-butyne-1-ol, cold sodium iodide and linear P(VBAz-co-OEGA)*

P(VBAz-co-OEGA) (20.0 mg,  $2.43 \times 10^{-6}$  mol) and sodium iodide (2.7 mg,  $1.8 \times 10^{-5}$  mol) were dissolved in 406  $\mu\text{L}$  DMSO with 74  $\mu\text{L}$   $\text{H}_2\text{O}$ . Copper(II) chloride (1.6 mg,  $1.2 \times 10^{-5}$  mol) was dissolved in 406  $\mu\text{L}$  DMSO in a second vial, and triethylamine (2.6  $\mu\text{L}$ ,  $1.8 \times 10^{-5}$  mol) was added, followed by 3-butyne-1-ol (0.92  $\mu\text{L}$ ,  $1.2 \times 10^{-5}$  mol). After five minutes, both vials were combined and the reaction mixture was stirred overnight (16 h) at 60 °C. The ratio between azide group, sodium iodide, copper(II) chloride, triethylamine, and 3-butyne-1-ol was 1 : 1.5 : 1 : 1.5 : 1. Next, the polymer was purified by dialysis (MWCO 3,500 Da) in water with three times solvent change, followed by lyophilisation. The resulting polymer was analysed by  $^1\text{H}$  NMR, SEC, and ATR-FTIR.

*Three component reaction of 3-butyn-1-ol, cold sodium iodide and P[P(VBAz-co-OEGA)-co-MBAA]*

P[P(VBAz-co-OEGA)-co-MBAA] (20.0 mg,  $4.11 \times 10^{-7}$  mol) and sodium iodide (2.7 mg,  $1.8 \times 10^{-5}$  mol) were dissolved in 406  $\mu$ L DMSO with 74  $\mu$ L H<sub>2</sub>O. Copper(II) chloride (1.6 mg,  $1.2 \times 10^{-5}$  mol) was dissolved in 406  $\mu$ L DMSO in a second vial, and triethylamine (2.6  $\mu$ L,  $1.8 \times 10^{-5}$  mol) was added, followed by 3-butyn-1-ol (0.92  $\mu$ L,  $1.2 \times 10^{-5}$  mol). After five minutes, both vials were combined and the reaction mixture was stirred overnight (16 h) at 60 °C. The ratio between azide group, sodium iodide, copper(II) chloride, triethylamine, and 3-butyn-1-ol was 1 : 1.5 : 1 : 1.5 : 1. Next, the polymer was purified by dialysis (MWCO 3,500 Da) in water with three times solvent change, followed by lyophilisation. The resulting polymer was analysed by <sup>1</sup>H NMR, SEC, and ATR-FTIR.

*Three component reaction of butyne-DOTA(Gd), cold sodium iodide and linear P(VBAz-co-OEGA)*

P(VBAz-co-OEGA) (2.0 mg,  $2.4 \times 10^{-7}$  mol, equals  $1.2 \times 10^{-6}$  mol azide groups) was dissolved in 40  $\mu$ L DMSO and sodium iodide (5  $\mu$ L of a 345 mM sodium iodide stock solution in DMSO ( $1.74 \times 10^{-6}$  mol)) was added.

Copper(II) chloride (12.0  $\mu$ L of a 96.9 mM CuCl<sub>2</sub> stock solution in DMSO ( $1.16 \times 10^{-6}$  mol)) was mixed in a second Eppendorf tube (1.5 ml) with triethylamine (4  $\mu$ L of a 436 mM triethylamine stock solution in DMSO ( $3.49 \times 10^{-6}$  mol)), and (4  $\mu$ L of a 145 mM butyne-DOTA(Gd) stock solution in water ( $1.16 \times 10^{-6}$  mol)).

After five minutes, both vials were combined inside the fume hood and the reaction mixture was heated overnight (16 h) at 90 °C, only heating the part of the Eppendorf tube that contains the reaction mixture. Next, the polymer was purified by dialysis (MWCO 3,500 Da) in water with three times solvent change, followed by lyophilisation. The resulting polymer was analysed by ICP-OES, SEC, ATR-FTIR and MRI.

*Three component reaction of butyne-DOTA(Gd), cold sodium iodide and P[P(VBAz-co-OEGA)-co-MBAA]*

P[P(VBAz-co-OEGA)-co-MBAA] (1.9 mg,  $3.4 \times 10^{-8}$  mol, equals  $1.2 \times 10^{-6}$  mol azide groups) was dissolved in 40  $\mu$ L DMSO and sodium iodide (5  $\mu$ L of a 345 mM sodium iodide stock solution in DMSO ( $1.74 \times 10^{-6}$  mol)) was added.

Copper(II) chloride (12.0  $\mu$ L of a 96.9 mM CuCl<sub>2</sub> stock solution in DMSO ( $1.16 \times 10^{-6}$  mol)) was mixed in a second Eppendorf tube (1.5 ml) with triethylamine (4  $\mu$ L of a 436 mM triethylamine stock solution

in DMSO ( $3.49 \times 10^{-6}$  mol)), and (4  $\mu$ L of a 145 mM butyne-DOTA(Gd) stock solution in water ( $1.16 \times 10^{-6}$  mol)).

After five minutes, both vials were combined inside the fume hood and the reaction mixture was heated overnight (16 h) at 90 °C, only heating the part of the Eppendorf tube that contains the reaction mixture. Next, the polymer was purified by dialysis (MWCO 3,500 Da) in water with three times solvent change, followed by lyophilisation. The resulting polymer was analysed by ICP-OES, SEC, ATR-FTIR and MRI.

#### *Three component reaction of 3-butyn-1-ol, iodine-125 and linear P(VBAz-co-OEGA)*

P(VBAz-co-OEGA) (4.0 mg,  $4.7 \times 10^{-7}$  mol, equals  $2.3 \times 10^{-6}$  mol azide groups) was dissolved in 80  $\mu$ L DMSO and iodine-125 (40  $\mu$ L from a 0.1 MBq/ $\mu$ L iodine-125 stock solution, diluted in DMSO (4.0 MBq)) was added inside a fume hood equipped with a lead brick wall and charcoal filter to limit exposure to iodine-125.

Copper(II) chloride (24.0  $\mu$ L of a 96.9 mM  $\text{CuCl}_2$  stock solution in DMSO ( $2.33 \times 10^{-6}$  mol)) was mixed in a second Eppendorf tube (1.5 ml) with triethylamine (8  $\mu$ L of a 436 mM triethylamine stock solution in DMSO ( $3.49 \times 10^{-6}$  mol)), and 3-butyn-1-ol (8  $\mu$ L of a 291 mM 3-butyn-1-ol stock solution in DMSO ( $3.49 \times 10^{-6}$  mol)).

After five minutes, both vials were combined inside the fume hood and the reaction mixture was heated overnight (16 h) at 60 °C in a heating module (Reacti-Therm I TS18821). Next, 20  $\mu$ L of the reaction mixture was diluted with SEC buffer and measured by radio-SEC. The remainder was purified by centrifugal filtration (Amicon Ultra-4 centrifugal filter unit with Ultracel-3 membrane and molecular weight cut-off 3,000 Da) for 20 min at 7,000 x g, washing three times with 3.5 ml water. The resulting polymer was again analysed by radio-SEC.

#### *Three component reaction of 3-butyn-1-ol, iodine-125 and P[P(VBAz-co-OEGA)-co-MBAA]*

P[P(VBAz-co-OEGA)-co-MBAA] (3.7 mg,  $6.6 \times 10^{-8}$  mol, equals  $2.3 \times 10^{-6}$  mol azide groups) was dissolved in 80  $\mu$ L DMSO and iodine-125 (40  $\mu$ L from a 0.1 MBq/ $\mu$ L iodine-125 stock solution, diluted in DMSO (2.0 MBq)) was added.

Copper(II) chloride (24.0  $\mu$ L of a 96.9 mM  $\text{CuCl}_2$  stock solution in DMSO ( $2.33 \times 10^{-6}$  mol)) was mixed in a second Eppendorf tube (1.5 ml) with triethylamine (8  $\mu$ L of a 436 mM triethylamine stock solution in DMSO ( $3.49 \times 10^{-6}$  mol)), and 3-butyn-1-ol (8  $\mu$ L of a 291 mM 3-butyn-1-ol stock solution in DMSO ( $3.49 \times 10^{-6}$  mol)).

After five minutes, both vials were combined inside the fume hood and the reaction mixture was heated overnight (16 h) at 60 °C in a heating module (Reacti-Therm I TS18821). Next, 20 µL of the reaction mixture was diluted with SEC buffer and measured by radio-SEC. The remainder was purified by centrifugal filtration (Amicon Ultra-4 centrifugal filter unit with Ultracel-3 membrane and molecular weight cut-off 3,000 Da) for 20 min at 7,000 x g, washing three times with 3.5 ml water. The resulting polymer was again analysed by radio-SEC.

*Three component reaction of butyne-DOTA(Gd), iodine-125 and linear P(VBAz-co-OEGA)*

P(VBAz-co-OEGA) (2.0 mg,  $2.3 \times 10^{-7}$  mol, equals  $1.2 \times 10^{-6}$  mol azide groups) was dissolved in 40 µL DMSO and iodine-125 (20 µL from a 0.1 MBq/µL iodine-125 stock solution, diluted in DMSO (2.0 MBq)) was added inside a fume hood equipped with a lead brick wall and charcoal filter to limit exposure to iodine-125.

Copper(II) chloride (12.0 µL of a 96.9 mM CuCl<sub>2</sub> stock solution in DMSO ( $1.16 \times 10^{-6}$  mol)) was mixed in a second Eppendorf tube with triethylamine (4 µL of a 436 mM triethylamine stock solution in DMSO ( $1.74 \times 10^{-6}$  mol)), and butyne-DOTA(Gd) (4 µL of a 145 mM butyne-DOTA(Gd) stock solution in water ( $1.16 \times 10^{-6}$  mol)).

After five minutes, both vials were combined inside the fume hood and the reaction mixture was heated overnight (16 h) at 90 °C in a heating module (Reacti-Therm I TS18821), only heating the part of the Eppendorf tube that contains the reaction mixture. Next, 20 µL of the reaction mixture was diluted with SEC buffer and measured by radio-SEC. The remainder was purified by centrifugal filtration (Amicon Ultra-4 centrifugal filter unit with Ultracel-3 membrane and molecular weight cut-off 3,000 Da) for 20 min at 7,000 x g, washing three times with 3.5 ml water. The resulting polymer was again analysed by radio-SEC.

*Three component reaction of butyne-DOTA(Gd), iodine-125 and P[P(VBAz-co-OEGA)-co-MBAA]*

P[P(VBAz-co-OEGA)-co-MBAA] (1.9 mg,  $3.4 \times 10^{-8}$  mol, equals  $1.2 \times 10^{-6}$  mol azide groups) was dissolved in 40 µL DMSO and iodine-125 (20 µL from a 0.1 MBq/µL iodine-125 stock solution, diluted in DMSO (2.0 MBq)) was added inside a fume hood equipped with a lead brick wall and charcoal filter to limit exposure to iodine-125.

Copper(II) chloride (12.0 µL of a 96.9 mM CuCl<sub>2</sub> stock solution in DMSO ( $1.16 \times 10^{-6}$  mol)) was mixed in a second Eppendorf tube with triethylamine (4 µL of a 436 mM triethylamine stock solution in DMSO

( $1.74 \times 10^{-6}$  mol)), and butyne-DOTA(Gd) (4  $\mu$ L of a 145 mM butyne-DOTA(Gd) stock solution in water ( $1.16 \times 10^{-6}$  mol)).

After five minutes, both vials were combined inside the fume hood and the reaction mixture was heated overnight (16 h) at 90 °C in a heating module (Reacti-Therm I TS18821), only heating the part of the Eppendorf tube that contains the reaction mixture. Next, 20  $\mu$ L of the reaction mixture was diluted with SEC buffer and measured by radio-SEC. The remainder was purified by centrifugal filtration (Amicon Ultra-4 centrifugal filter unit with Ultracel-3 membrane and molecular weight cut-off 3,000 Da) for 20 min at 7,000 x g, washing three times with 3.5 ml water. The resulting polymer was again analysed by radio-SEC.

## 4.3 Results and discussion

### 4.3.1 Preparation of P(VBC-co-OEGA) arm polymer

The arm-first approach was employed to synthesize core-cross-linked star polymers. First, a linear copolymer consisting of 4-vinylbenzyl chloride (4-VBC) and oligo(ethylene glycol) methyl ether acrylate (average  $M_n$  480 g mol<sup>-1</sup>) was synthesized via reversible addition-fragmentation chain transfer polymerization (RAFT) polymerisation using 3-(benzyl sulfanyl thiocarbonyl sulfanyl)-propanoic acid (BSPA) as the chain transfer agent. Arm-functionalities were chosen as these would result in the highest possible molecular MRI relaxivity. [29] BSPA was chosen as it is well suited for acrylates and acrylamides. The polymerization was carried out at 70 °C and the polymer molecular weight and composition were optimized by varying solvents, molar feed ratios, concentration and reaction time (see Table 4.14 and Figure 4.43).

The polymers were purified by careful precipitation in diethylether:petroleum spirit (1 :1 v/v %, boiling range 40 – 60 °C). <sup>1</sup>H NMR revealed that 4-VBC was preferentially incorporated over OEGA, resulting in a gradient copolymer with 4-VBC predominantly near the leaving R-group. This is beneficial as 4-VBC and as a result the conjugated gadolinium chelate will be present near the surface of the star resulting in optimal relaxation parameters, i.e. short water residency time and long rotational correlation times. [29] In addition, also 3-(trimethylsilyl)prop-2-yn-1-yl 2-((((3-propionic acid) thio)carbonothioyl) thio)propanoate) (TSPPA) was investigated as RAFT agent as the functional group could be exploited to introduce targeting moieties in future applications.

Table 4.14: Synthesis of P(VBC-co-OEGA) with different molecular weights by varying molar feed ratio of OEGA, solvent, concentration and reaction time. BSPA was utilized as RAFT agent for A-C and TSPPA for D.

	$M_{n,SEC}$ (g mol <sup>-1</sup> ) <sup>a</sup>	$M_{n,NMR}$ (g mol <sup>-1</sup> )	$\bar{D}_m$	$F_{OEGA}^b$	$F_{4-VBC}$	$f_{OEGA}^c$	$f_{4-VBC}^d$	Solvent	Solvent:OEGA	Time (h)
A	5500	4880	1.10	20	5	8	5	MeCN	3 : 1	7
B	7620	6800	1.15	40	5	12	5	Toluene	2 : 1	10
C	9480	8720	1.11	60	5	16	5	Toluene	2 : 1	10
D	7470	6890 <sup>e</sup>	1.11	50	5	12	5	Toluene	3 : 1	10

<sup>a</sup> Assessed by size-exclusion chromatography (SEC) in DMAc (0.03 % w/v LiBr) using a conventional calibration curve with narrow molecular weight distribution polystyrene standards.

<sup>b</sup> Initial molar feed ratio of each monomer per chain transfer agent.

<sup>c</sup> molar composition of OEGA per polymer

<sup>d</sup> molar composition of 4-VBC per polymer, <sup>1</sup>H NMR of the reaction mixture indicates over 90 % conversion for 4-VBC

<sup>e</sup> The trimethylsilylpropargyl RAFT end-group ( $\delta$  0.1 ppm) at 0.1 ppm was used as a reference.

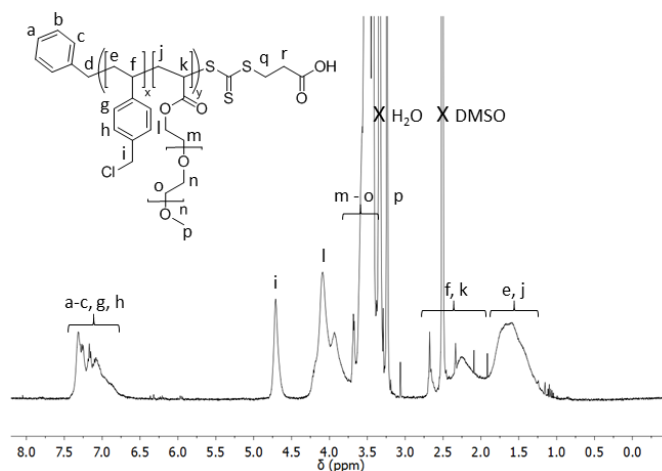


Figure 4.43:  $^1\text{H}$  NMR spectra of P(VBC-co-OEGA) recorded in  $\text{DMSO-d}_6$  showing successful incorporation of both 4-VBC and OEGA.

#### 4.3.2 Preparation of core-cross-linked star polymer

Core-cross-linked star polymers were obtained by chain-extending the copolymer P(VBC-co-OEGA) with a cross-linker, i.e. *N,N'*-methylenebis(acrylamide). Toluene was used as a solvent as the cross-linker and hence cross-linker core had a low solubility in this solvent leading to an assumed nano-phase separation including compartmentalisation of the polymerisation as was hypothesized by Davis and co-workers. [21]

Copolymers with different molecular weights were successfully employed to create a library of star polymers with a low polydispersity using toluene as solvent (see Table 4.15 and Figure 4.44). SEC did indicate incomplete arm-to-star conversions, but rigorous purification by a carefully designed precipitation method (arms are slightly more hydrophilic) resulted in the isolation of pure star products at high yields (see Figure 4.44B). The incomplete conversion is most likely caused by disproportionation and bimolecular termination of the propagating macro(radicals), leading to the formation of “dead” chains. [20] Interestingly, copolymers with higher molecular weights resulted in stars with a relatively similar molecular weight, but with a lower number of arms incorporated per star and hence less functional groups per star polymer.

Table 4.15: Synthesis of core-cross-linked star polymers using P(VBC-co-OEGA) copolymers with different molecular weights.

	$M_{n,SEC}$ (g mol <sup>-1</sup> )	$\bar{D}_{m,star}$	$D_H$ (nm)	$M_{n,SEC,arm}$ (g mol <sup>-1</sup> )	$\bar{D}_{m,arm}$	Arm incorporation	$N_{arms}$	$N_{4-VBC}$
A	49120	1.16	8	5500	1.10	90.9 %	8	40
B	48660	1.14	9	7620	1.15	81.0 %	6	30
C	56670	1.10	11	9480	1.11	89.3 %	5	25

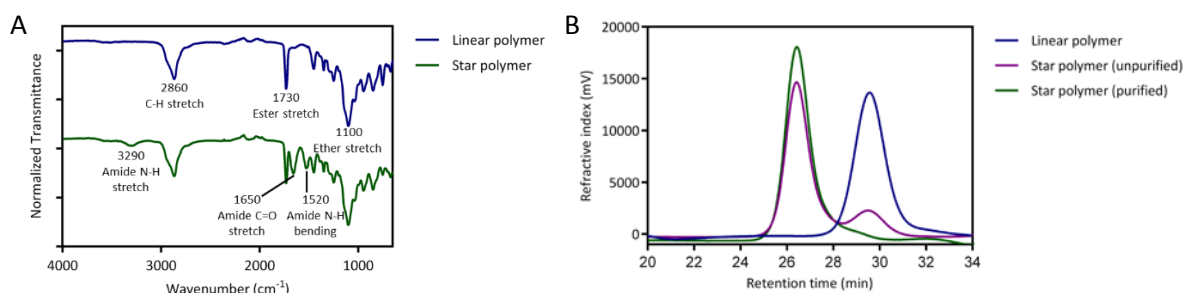


Figure 4.44: (A) ATR-FTIR spectra before and after core-cross-linking show the appearance of amide signals, indicating successful incorporation of the cross-linker (N,N'-methylenebis(acrylamide)). (B) Size-exclusion chromatograms of the linear copolymer (P(VBC-co-OEGA)), the reaction mixture after core-cross-linking, and after successful purification to remove unincorporated linear polymers.

### 4.3.3 Preparation of azide-functional polymers

An azide functionality was introduced into the star polymer via nucleophilic substitution of chloride by azide using sodium azide as a nucleophile, followed by purification by dialysis. Next to this, linear copolymer with azide functionality was also synthesized using the same reaction conditions. The purified products were analysed by ATR-FTIR and <sup>1</sup>H NMR. ATR FTIR showed the appearance of a signal at 2100 cm<sup>-1</sup> that can be attributed to azide stretch vibrations (see Figure 4.45A-B). In addition, the disappearance of the C-Cl stretch signal at 750 cm<sup>-1</sup> indicated successful substitution. Likewise, <sup>1</sup>H NMR showed an upfield shift of the methyl-benzylic proton signal from  $\delta$  4.55 to 4.30 ppm, also confirming full conversion to azide (see Figure 4.45C-D).

In preliminary experiments star-star coupling was observed after lyophilisation as indicated by a high molecular weight shoulder in SEC (PDI > 2) and even insoluble polymer (see Figure 4.46). The star-star coupling was attributed to azide photo-cross-linking by UV irradiation, which was further augmented by concentrating the solution. For example, the Gimes group used UV irradiation to core-cross-link micelles consisting of poly(ethylene oxide)-*b*-poly(vinylbenzyl azide). [43] As a result, all purifications

were carried out in darkness, and the products were stored in acetone until needed (see Figure 4.46 and Table 4.16).

Table 4.16: Effect of azide substitution on molecular weight distribution for both linear and star polymer as determined by size-exclusion chromatography in DMAc using polystyrene standards.

	Before azide substitution			After azide substitution		
	$M_{n,SEC}$ (g mol <sup>-1</sup> )	$\bar{D}_m$	$D_H$ (nm)	$M_{n,SEC}$ (g mol <sup>-1</sup> )	$\bar{D}_m$	$D_H$ (nm)
Linear	8930	1.16		9440	1.14	
Star	48660	1.14	9	53590	1.17	10

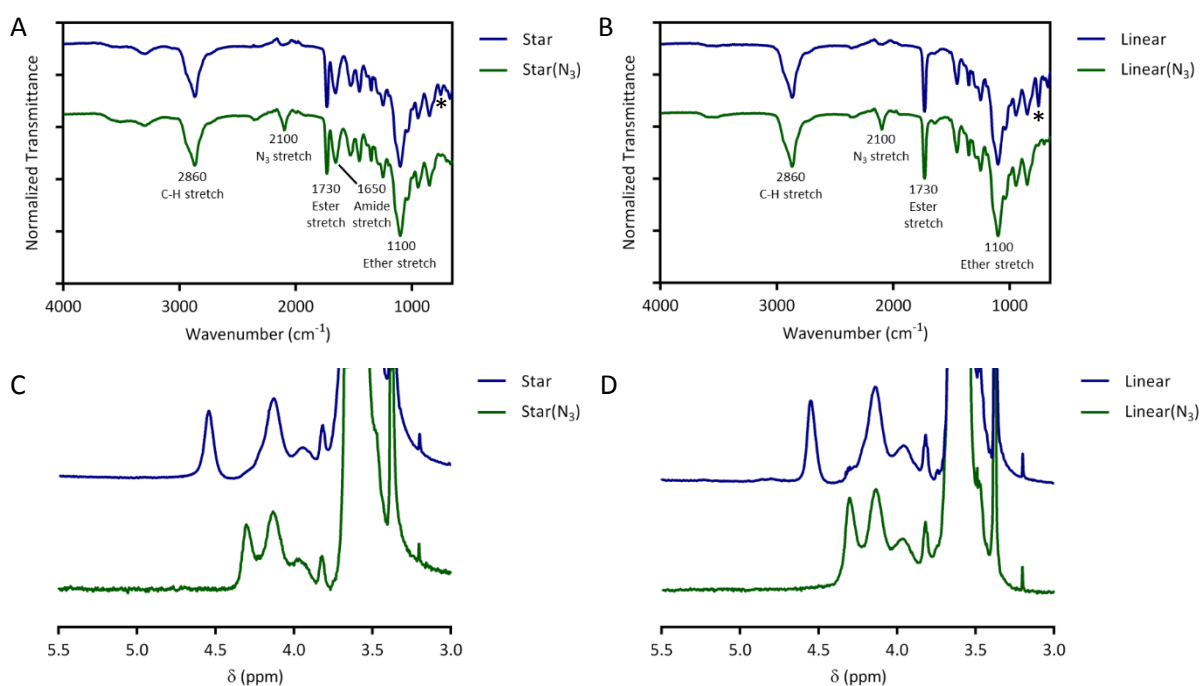


Figure 4.45: ATR-FTIR (A-B) and <sup>1</sup>H NMR spectra (C-D) demonstrate successful azide substitution. (A) FTIR spectra of the star polymer before and after nucleophilic substitution, showed the appearance of a signal at 2100 cm<sup>-1</sup> that belongs to azide stretch vibrations. In addition, the disappearance of the C-Cl stretch signal at 750 cm<sup>-1</sup> (see \*) further indicated successful substitution. (B) The FTIR spectrum of the linear copolymer also showed a clear azide stretch signal upon nucleophilic substitution accompanied by the disappearance of the C-Cl stretch signal. (C-D) <sup>1</sup>H NMR of the star (C) and linear (D) polymer before and after azide substitution as recorded in deuterated DMSO. The spectra showed a clear upfield shift of the methylbenzylic proton signal from δ 4.55 to 4.30 ppm upon azide substitution, which indicate full conversion for both star and linear polymer.

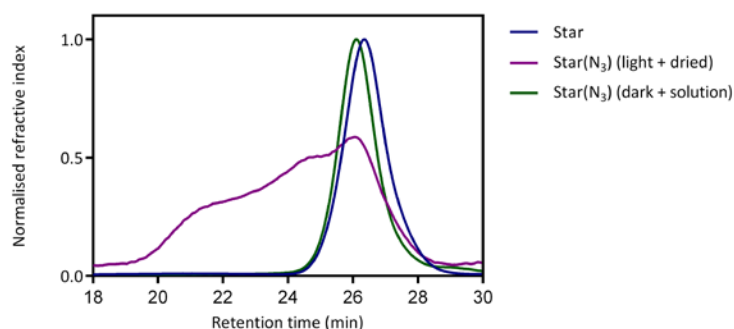
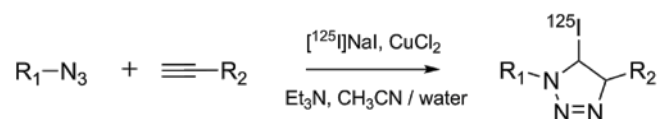


Figure 4.46: Size-exclusion chromatograms of the azide-substituted star polymers. Star-star coupling was observed upon purification by dialysis and lyophilisation. However, when performing the dialysis in darkness and only drying the compound when needed (acetone as solvent), no star-star coupling was observed.

#### 4.3.4 Investigation of three-component reaction for iodine labelling

The three-component reaction was based on earlier studies by the Årstad group in which a one-pot, three-component, copper(II)-mediated reaction of azide, alkyne, and  $[^{125}\text{I}]$ iodine yielded 5-  $[^{125}\text{I}]$ iodo-1,2,3-triazoles (see Scheme 4.15). [37, 40] In the first study the reactivity of azides and alkynes bearing aliphatic, benzylic, aromatic, and heterocyclic moieties was investigated [37] and in a follow-up study the three-component reaction was employed to combine a fluorescent group, a radioactive element, and a group for bioconjugation. [40]



Scheme 4.14: Synthesis of 5-  $[^{125}\text{I}]$ iodo-1,2,3-triazoles. [40]

In this chapter, the three-component reaction was applied to the highly complex star polymer architecture. Initially, a simplified system was designated to optimize the translation of the three-component reaction for macromolecular application. A linear copolymer P(VBAz-co-OEGA) was employed in combination with a simple alkyne, propargylamine, and sodium iodide was used as a source for cold iodine. The first amendment was a change of solvent system as the polymer was insoluble in acetonitrile : water (10 : 1 v/v %) and therefore DMSO : water (10 : 1) was used instead as reaction medium for all experiments. Water was incorporated as iodine-125 is supplied in water, but the amount should be kept to a minimum as an increasing water amount had a detrimental effect on the radiochemical yield (RCY). [37] Secondly, the reaction time was increased from 2 to 16 hours to take into account potential steric hindrance that could negatively affect the reaction rate. During the

explorative work, cold sodium iodide was used and reactions were carried out on a 10  $\mu\text{mol}$  (azide) scale.

Despite the modifications, initial reactions were unsuccessful and no (iodo)triazole formation was observed by  $^1\text{H}$  NMR nor ATR-FTIR. However, the supporting information of Yan *et al.* [37] noted detrimental effects of a colour change of the copper(II) chloride / triethylamine solution from burgundy to green that resulted in low RCYs and was attributed in their case to expired anhydrous acetonitrile. During the experiments, it was observed that the copper(II) chloride / triethylamine solution in DMSO had a stable burgundy colour, but addition of propargylamine lead to a colour change to green, indicating changes to the copper(II) complex. Therefore a different alkyne was employed, i.e. 3-butyne-1-ol, and no change of colour was observed upon addition of this compound. The three-component reaction to combine P(VBAz-co-OEGA), 3-butyne-1-ol, and sodium iodide was purified by dialysis (DMF and water) and analysed by  $^1\text{H}$  NMR, ATR-FTIR, SEC and DLS.

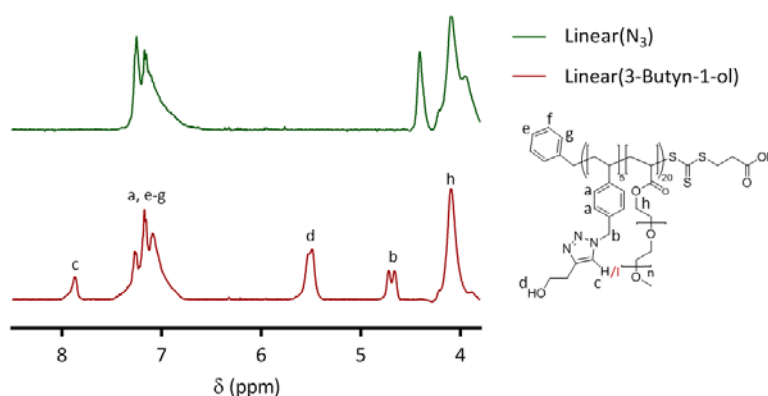


Figure 4.47:  $^1\text{H}$  NMR spectra of the linear polymer P(VBAz-co-OEGA) (top) and the reaction product of the three-component reaction of P(VBAz-co-OEGA) and 3-butyne-1-ol in the presence of sodium iodide (1.1 eq., bottom). The spectra were recorded in deuterated DMSO.

$^1\text{H}$  NMR spectra showed the presence of NMR signals that could be attributed to the successful triazole formation (see Figure 4.47), and the existence of a chemical shift at 7.86 ppm indicated that a proton was incorporated in the triazole. However, upon closer investigation of the intensities of the different signals it was noted that the proton-triazole NMR signal was lower than to be expected, indicating the partial formation of iodinated triazole (39%). This is further confirmed by the splitting of the other NMR signals near the triazole (b and d), signifying the presence of a mixed chemical environment containing both triazoles and iodotriazoles. Finally, the disappearance of the azidomethyl signal at 4.40 ppm indicated full conversion, which was confirmed by the disappearance of the azide stretch signal at  $2100\text{ cm}^{-1}$  in ATR-FTIR (see Figure 4.48A). Size-exclusion chromatography showed a small

decrease in retention time, and a relatively low polydispersity was maintained ( $M_n/M_w = 1.16$ , see Figure 4.48B).

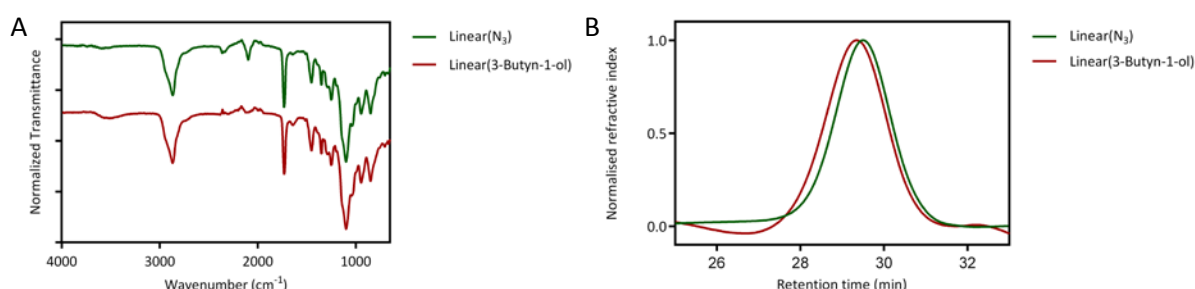
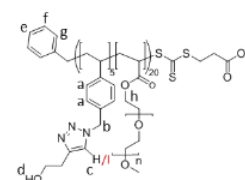


Figure 4.48: (A) ATR FTIR spectra of linear polymer before and after three-component reaction show the disappearance of the azide-stretch signal at 2100 cm<sup>-1</sup>. (B) Size-exclusion chromatograms of linear polymer display a small decrease in retention time after conjugation of 3-butyn-1-ol.

The same reaction was further explored in the absence of sodium iodide, as literature reported that the formation of the non-iodinated triazole was sluggish and the azide and alkyne would remain largely intact in the reaction mixture. [37] Surprisingly full triazole formation was achieved, indicating that the macromolecular system combined with modified reaction conditions resulted in different reaction kinetics. We further investigated this by adding different equivalents of sodium iodide, and indeed when increasing from 1.1 to 1.5 equivalents, the iodotriazole became more dominant (from 39 to 49 %). This provided the opportunity to fine-tune the iodine content of the macromolecule without limiting the number of alkyne groups (i.e. gadolinium chelates for MRI) in the macromolecular architecture as much less radio-iodine is required due to the higher sensitivity of PET. At the same time, full formation of iodotriazole could not be achieved as no further increase in iodotriazole formation was observed even when 5 equivalents of sodium iodide was used (see Table 4.17).

Table 4.17: Effect of different equivalents of sodium iodide on the formation of iodotriazole when combining linear P(VBAz-co-OEGA), 3-butyn-1-ol and sodium iodide. In the table, the signal intensities of the different relevant NMR signals were stated and the percentage of iodotriazole was calculated.

Eq. NaI	f <sub>c</sub>	f <sub>a, e-g</sub>	f <sub>d</sub>	f <sub>b</sub>	f <sub>h</sub>	Iodotriazole	Triazole
0	1.02	8.42	2.00	1.09	5.10	0 %	100 %
1.1	0.61	7.02	2.00	1.02	4.70	39 %	61 %
1.5	0.51	7.13	2.00	1.10	4.69	49 %	51 %
5	0.52	7.48	2.00	1.04	4.80	51 %	49 %



Next, the one-pot three-component reaction was studied for the more complex star polymer. The same reaction conditions were applied and reactions were again carried out on 10 μmol (azide) scale

using 3-butyn-1-ol as test alkyne.  $^1\text{H}$  NMR demonstrated successful triazole formation (see Figure 4.49) and analysis of the signal intensities again signified the formation of both iodotriazole and non-iodinated triazole. ATR-FTIR validated full conversion of the azide groups (see Figure 4.50A) and a small change in retention time was observed in SEC while maintaining a relatively low polydispersity ( $M_w/M_n = 1.20$ , see Figure 4.50B).

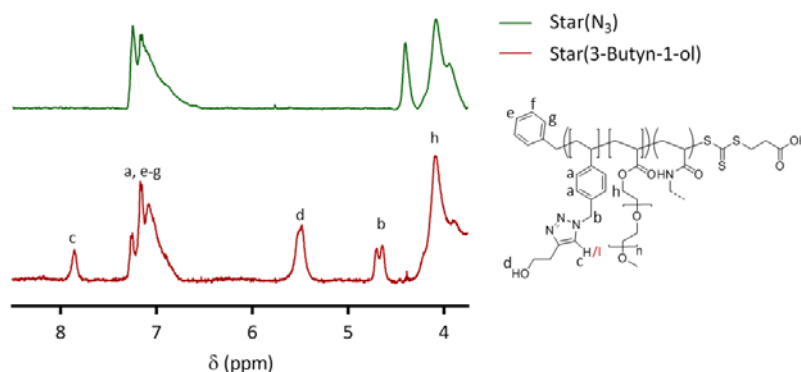


Figure 4.49:  $^1\text{H}$  NMR spectra of the star polymer  $\text{P}[\text{P}(\text{VBaz-co-OEGA-co-MBAA})]$  (top) and the reaction product of the three-component reaction of the azide-functional star polymer and 3-butyn-1-ol in the presence of sodium iodide (1.5 eq., bottom). The NMR spectra were recorded in deuterated DMSO.

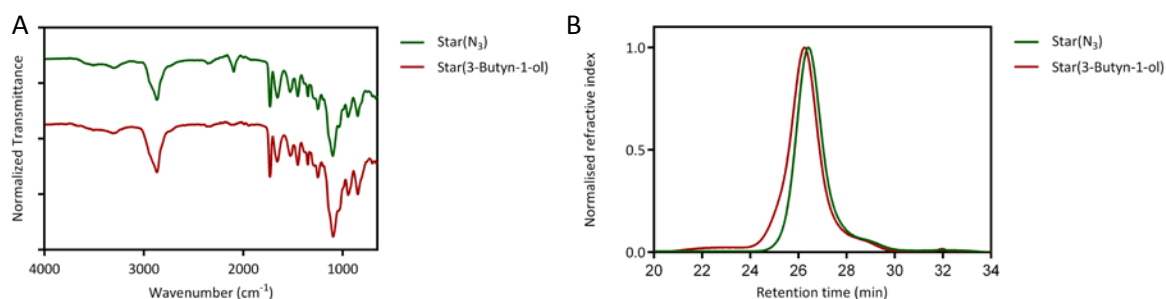
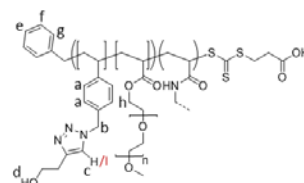


Figure 4.50: (A) ATR FTIR spectra of star polymer before and after three-component reaction show the disappearance of the azide-stretch signal at  $2100\text{ cm}^{-1}$ . (B) Size-exclusion chromatograms of star polymer display a small decrease in retention time after conjugation of 3-butyn-1-ol.

Similar to the linear polymer, the triazole was also formed in absence of sodium iodide, and the ratio of iodotriazole versus non-iodinated triazole could be varied by changing the amount of added sodium iodide to a maximum of around 46 % using the investigated conditions (see Table 4.18).

Table 4.18: Effect of different equivalents of sodium iodide on the formation of iodotriazole when combining star polymer P[P(VBAz-co-OEGA)-co-MBAA], 3-butyn-1-ol and sodium iodide. In the table the signal intensities of the relevant NMR signals were stated and the percentage of iodotriazole was calculated.

Eq. NaI	f <sub>c</sub>	f <sub>a, e-g</sub>	f <sub>d</sub>	f <sub>b</sub>	Iodo-triazole	Triazole
0	1.04	7.23	2.00	1.02	0 %	100 %
1.1	0.64	7.30	2.00	1.04	36 %	64 %
1.5	0.55	7.18	2.00	0.96	45 %	55 %
5	0.54	7.48	2.00	0.98	46 %	54 %



In summary, the star polymer and linear polymer were both successfully labelled with cold iodine using 3-butyn-1-ol as alkyne. The three-component reaction was carried out in DMSO for 16 hours at 60 °C to improve solubility and reaction efficacy. Both iodotriazole and non-iodinated triazole were formed simultaneously and the ratio could be fine-tuned by changing the amount of sodium iodide.

#### 4.3.5 Radiochemistry - Investigation of three-component reaction for radio-iodine labelling

Iodine-125 was selected to investigate radio-iodine labelling. It has a long half-life (59.4 days) and is relatively safe to handle due to a very low gamma energy (35 keV), [39] whereas iodine-123 emits gamma radiation with a much higher energy (159 keV) and iodine-131 decays by a combination of beta and gamma emission (364 keV). [39] The radiolabelling experiments were carried out at the radiochemistry laboratories of the Australian Nuclear Science and Technology Organisation (ANSTO, Lucas Heights, Australia). The labelling was assessed using an aqueous size-exclusion chromatography system comprising a refractive index detector, an absorbance detector and a radio-HPLC detector. An aqueous mobile phase was employed to facilitate stability studies in buffer or serum at a later stage.

Unfortunately, aqueous size-exclusion chromatography turned out to be more complicated than initially envisioned. The polymers (both linear and star) did not pass the column while the compounds were well soluble in the SEC buffer (0.10 mM phosphate buffer, 0.1 M sodium nitrate, pH 7.0) and similar POEGA-containing stars and polyethylene oxide standards were detectable by refractive index and absorbance (see Figure 4.51A). Different modifications to the system were investigated, such as increasing the salt content to prevent any ionic interactions, and adding organic solvent (10 % DMSO) to the mobile phase to limit possible hydrophobic interactions with the stationary phase. Eventually, adding 20 % DMSO to the phosphate buffer resulted in detectable peaks (see Figure 4.51B). It was hypothesized that even though only six benzyl-groups were present per linear polymer (on a molecular weight of 8930) and a similar fraction for the star polymers, the aromatic groups had strong interactions with the ultrahydrogel column. Unfortunately no molecular weight estimates could be made on the aqueous system as the polyethylene glycol standards had much shorter retention times

than the linear and star polymers. For example, the star polymer ( $M_{n,SEC\ DMac} = 53,590$  Da) had a maximum refractive index signal at 29.9 minutes, while the smallest polyethylene glycol standard ( $M_n = 19,100$ ) had a retention time of 29.2 minutes.

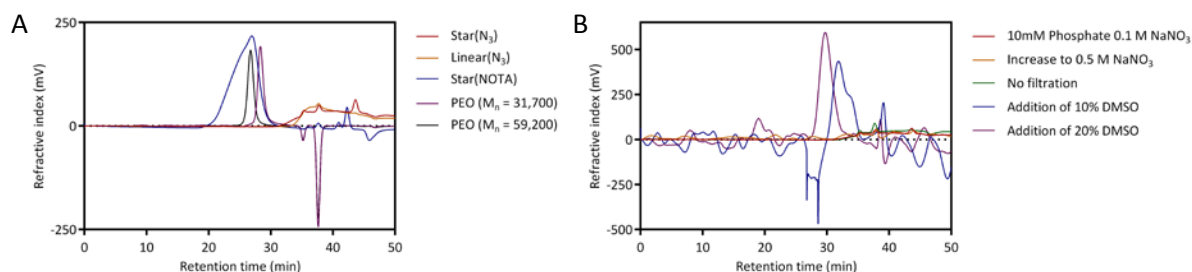


Figure 4.51: Aqueous size-exclusion chromatography was carried out using a Waters ultrahydrogel column. (A) The azide functional polymers did not give rise to any signal when using a mobile phase consisting of 0.10 mM phosphate buffer with 0.1 M sodium nitrate (pH 7.0), while a similar star polymer P[P(PFPA[NOTA]-co-OEGA)-co-MBAA] and polyethylene oxide standards were clearly detectable by refractive index. (B) Different buffer conditions were investigated for the star polymer and the introduction of an organic phase was required.

Iodine-125 was clearly detectable on the radio-HPLC detector and did not appear to have any irreversible interactions with the column. The radiochemical substance could also be identified using the refractive index detector. However as expected, no absorbance was detected at 256 nm (see Figure 4.52A), providing an alternative option to differentiate polymer from free iodine-125. As iodine-125 had a different retention time than both polymers, radio-HPLC was used to assess the radiochemical yield, and no gamma counter was required to determine the radioactivity of the purified product versus the residue containing free iodine-125.

Finally, the two-channel radio-HPLC detector was also fine-tuned to facilitate the measurement of both very high and low labelling efficacies. The loop-size was optimized (15 mm instead of 12 mm) and the channels were adjusted so that 1.0 MBq iodine-125 gave a signal of maximal 90 mV on the low sensitivity detector and overshoot the high sensitivity detector.

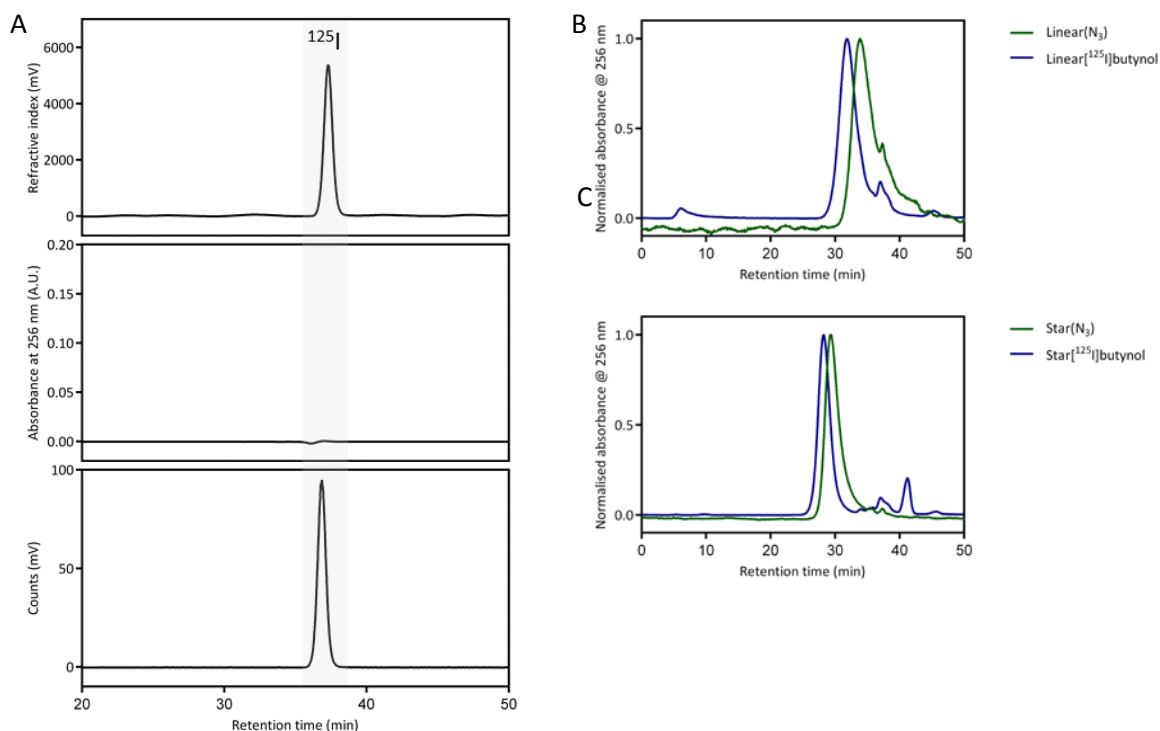


Figure 4.52: (A) Size-exclusion chromatogram of 1.0 MBq iodine-125: refractive index, absorbance at 256 nm and radioactivity count (optimized for both low and high sensitivity). On the right, size-exclusion chromatograms of the linear (B) and star polymer (C) (absorbance at 256 nm) before and after the three-component reaction with 3-butyn-1-ol and iodine-125 (before purification).

Next, radio-iodine labelling was investigated using either linear polymer P(VBAz-co-OEGA) or star polymer as azide source, 3-butyn-1-ol as alkyne and [<sup>125</sup>I]sodium iodide. Initially lower concentrations were employed as a higher reactivity was anticipated for radio-iodine, however very low radiochemical yields lead to a return to the previous reaction conditions. Reactions were carried out for 16 hours at 60°C on a 2.3 μmol (azide) scale in DMSO (160 μL) using 2.0 MBq iodine-125. The reactions were directly analysed by aqueous size-exclusion chromatography, followed by purification by centrifugal filtration (MWCO 3,500) and analysis by aqueous SEC.

Aqueous SEC showed a shift to a shorter retention time for both the linear and star polymer after reaction. This could indicate a higher molecular weight and thus successful conjugation (see Figure 4.52B and C) as was previously also observed for the three-component reactions with cold iodine. The refractive index detector showed the presence of two main peaks designated as the polymer and free iodine respectively (see Figure 4.53, top) and the polymers were clearly visible when measuring the absorbance at both 256 and 310 nm (data for 310 nm not shown).

Most importantly, the radioactivity detector showed a large signal at the same retention time as the polymer, indicating successful iodine-125 radiolabelling for both the linear and star polymer. Subsequently the radiochemical yield could be quantified by integrating both peaks (Table 4.19). The linear polymer had a higher RCY of 70.9 % compared to 46.7 % for the star polymer. The radio-detector also showed the presence of a small side product with a retention time of 34 minutes (RCY 2.9 % for star polymer reaction). Based on the hypothesized reaction pathways of the three-component reaction [40] and the long retention time, this peak was attributed to [ $^{125}\text{I}$ ]iodo-butynol, but the side-product could be easily removed by centrifugal filtration.

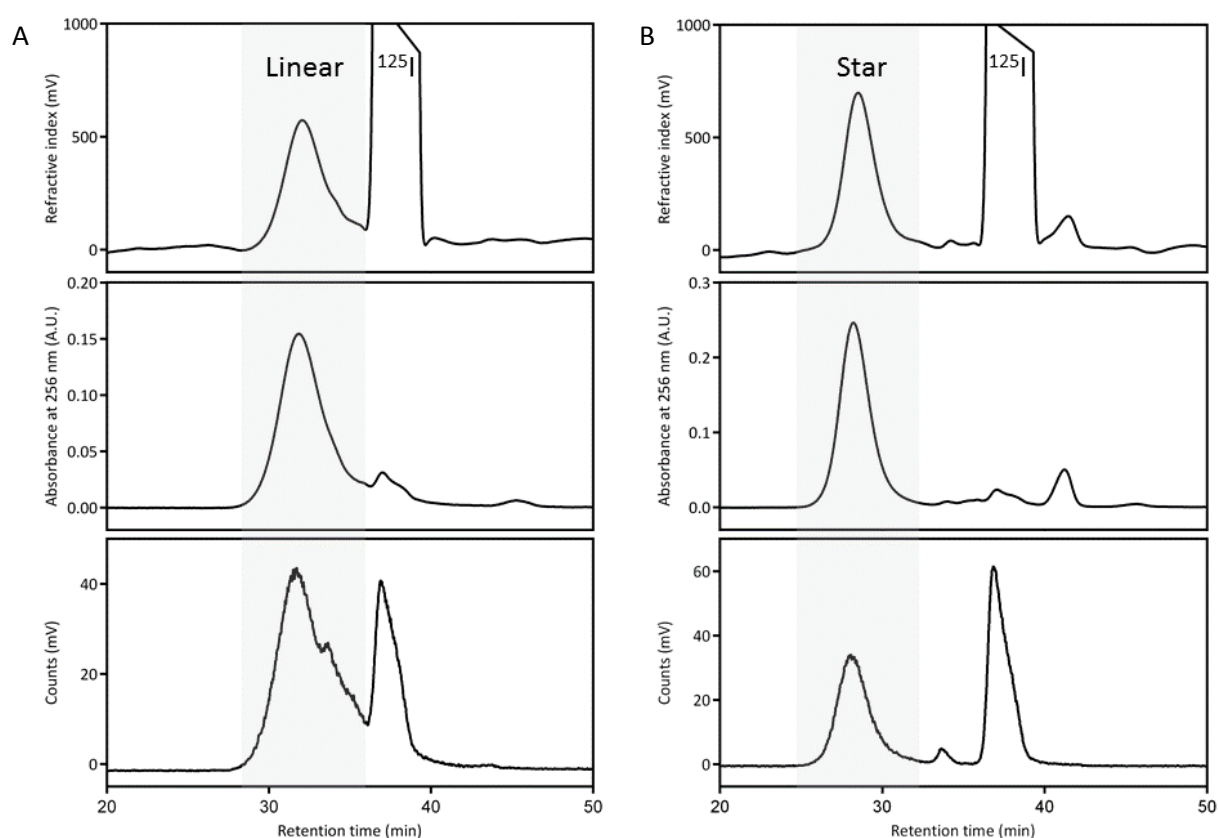
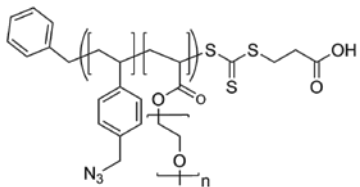
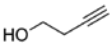
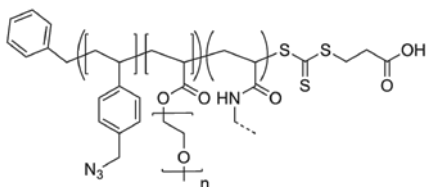
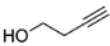


Figure 4.53: Size-exclusion chromatograms of the reaction mixtures after the three-component reaction of either linear polymer (A) or star polymer (B) with 3-butyn-1-ol and iodine-125. Top row, refractive index detector showed both the polymer and iodine-125; middle row, the absorbance at 256 nm showing the polymer only; and bottom row the radioactivity count rate, showing both iodine-125-labelled polymer and free iodine-125.

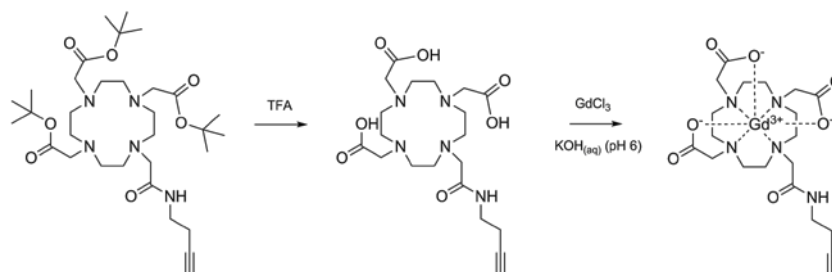
In summary, both the star polymer and the linear polymer were successfully labelled in a one-pot three-component reaction with iodine-125 and 3-butyn-1-ol, resulting in iodine-125-labelled polymers with a good radiochemical yield.

Table 4.19: Radiochemical yields (RCY) of the three-component reaction between linear or star polymer, 3-butyn-1-ol and iodine-125. The reactions were performed in DMSO for 16 hours at 60 °C.

Polymer	Alkyne	RCY (%)
<p>Linear(N<sub>3</sub>) polymer</p> 	<p>3-Butyn-1-ol</p> 	70.9
<p>Star(N<sub>3</sub>) polymer</p> 	<p>3-Butyn-1-ol</p> 	46.7

#### 4.3.6 Preparation of gadolinium-DOTA / (radio)iodine labelled polymers

After successfully optimizing the three-component reaction for the linear and star polymer and a small alkyne (3-butyne-1-ol), the reaction with the more complex butyne-functional gadolinium chelate (butyne-DOTA(Gd)) was investigated to open the pathway to bimodal MRI/PET imaging agents.



Scheme 4.15: Synthesis of butyne-functional gadolinium-chelate in two reaction steps.

Butyne-DOTA(Gd) was synthesized in two steps (see Scheme 4.16). First, butyne-DOTA-tris(*t*-butyl ester) was deprotected overnight in trifluoroacetic acid (TFA), followed by removal of TFA and the volatile side products by evaporation under reduced pressure. The deprotection was confirmed by <sup>1</sup>H NMR and ultra-high performance liquid chromatography - mass spectroscopy (UHPLC-MS). The NMR spectrum confirmed the disappearance of *tert*-butyl protons signal at  $\delta$  1.51 ppm (see Figure 4.54), while UHPLC-MS confirmed the presence of one main product with an  $m/z$  of 456.2 [M+H]<sup>+</sup> (see Figure 4.55A).

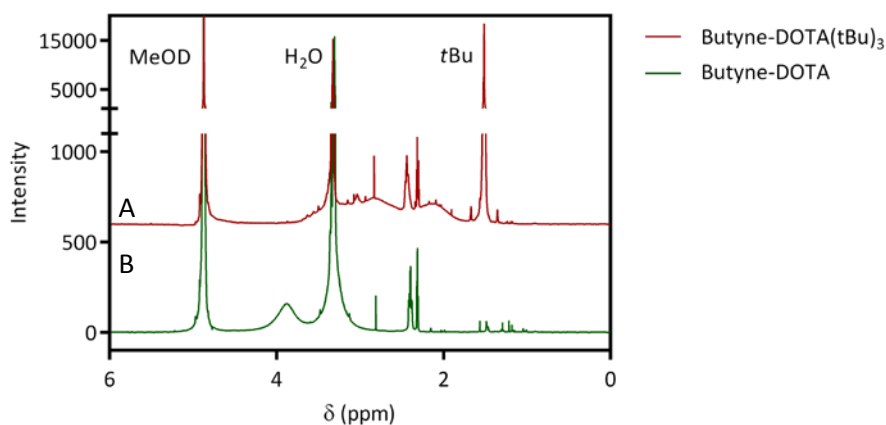


Figure 4.54: <sup>1</sup>H NMR spectra of (A) butyne-DOTA(*t*Bu)<sub>3</sub> and (B) deprotected butyne-DOTA as recorded in deuterated methanol (MeOD). The disappearance of the large *tert*-butyl NMR signal at  $\delta$  1.51 ppm confirmed successful deprotection.

In the second step, the chelate was incubated in the presence of gadolinium under slightly acidic conditions (pH 6) at 50 °C for 24 hours to facilitate complexation. Free gadolinium was removed using

a chelating material, Chelex 100, followed by filtration and lyophilisation to obtain an off-white solid. The final compound, butyne-DOTA(Gd), was successfully obtained and characterized by UHPLC-MS with an  $m/z$  of 610.2  $[M + H]^+$ .

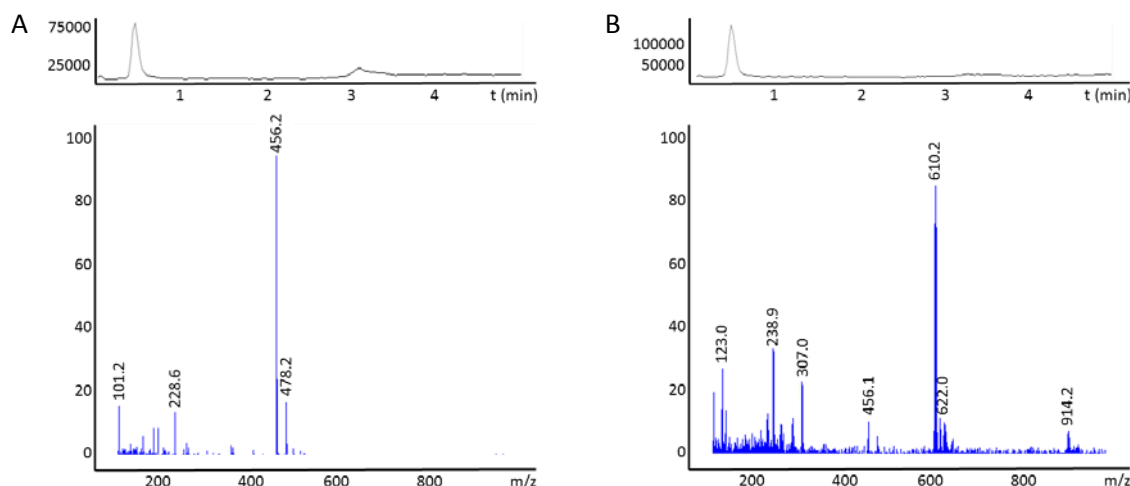


Figure 4.55: LC-MS spectra before (A) and after (B) gadolinium complexation of the deprotected butyne-DOTA chelate show an increase in  $m/z$  from 465.2 to 610.2, indicating successful gadolinium incorporation.

Next the three-component reaction using butyne-DOTA(Gd) as alkyne was investigated employing the previously used conditions. However the reactions with the linear or star polymer were unsuccessful and neither triazole nor iodotriazole was formed. Presumably the lower solubility of butyne-DOTA(Gd) in DMSO at 60 °C strongly limited the reaction efficacy. As a consequence, different solvents were investigated such as acetone, acetonitrile, *N,N*-dimethylacetamide, *N,N*-dimethylformamide, 1,4-dioxane, and tetrahydrofuran, however none was suitable for all reagents (azide functional polymer, butyne-DOTA(Gd), Cu(II)Cl<sub>2</sub>, triethylamine, and sodium iodide). All compounds were soluble in methanol, however a colour shift to green was observed for copper. This was previously observed to be indicative of an unsuccessful reaction, and indeed no decrease in SEC retention time was observed, nor any triazole formation in <sup>1</sup>H NMR.

The three-component reaction with butyne-DOTA(Gd) was further investigated using radio-iodine as this enabled the detection of very low conjugation efficacies. In a first reaction, standard conditions were employed using DMSO as solvent. Radio-HPLC showed a very low signal at the polymer retention time with an RCY << 0.1 % that was only detectable on the high sensitivity channel (see Figure 4.56A). Subsequently, attempts were made to increase the solubility of butyne-DOTA(Gd) in DMSO by increasing the temperature further and butyne-DOTA(Gd) was found to be more soluble at 90 °C. Hence, the three-component reaction was repeated at 90 °C. Unfortunately, no improvement in the

radio-labelling was observed (see Figure 4.56B). However, a second peak appeared in the radio-HPLC chromatogram at a retention time of 33.5 minutes (RCY 13.5 %), potentially signifying the presence of iodo-butyne-DOTA(Gd). This indicated that the solubility issues were at least partially resolved.

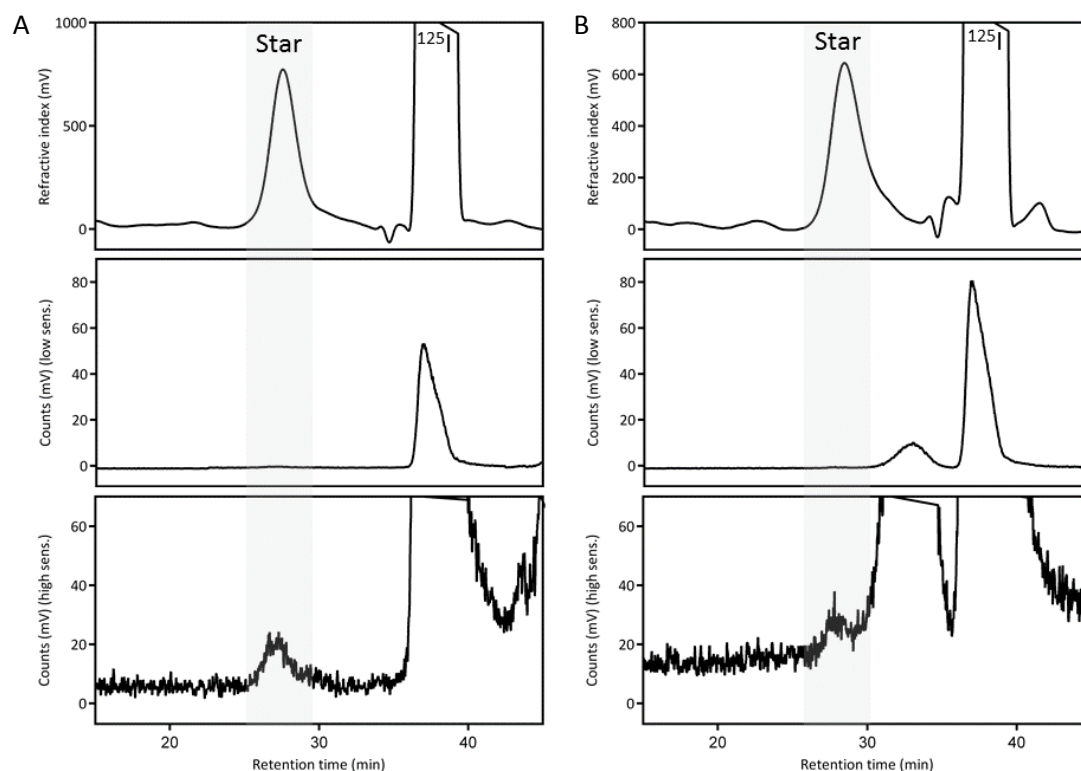


Figure 4.56: SEC chromatograms of three component reaction of azide-functional star polymer, butyne-DOTA(Gd) and iodine-125 in DMSO for 16 hours at (A) 60 °C, and (B) 90 °C.

The experiment was then repeated using both linear and star polymer to further study the three-component reaction. After the experiment, it was observed that the solvent was evaporated in one of the reactions, resulting in a blue solid on the bottom of the reaction vessel. Nevertheless, it was analysed to investigate the reaction and surprisingly iodine-125 labelled linear polymer was detected with a high radiochemical yield (RCY = 79.3 %, see Figure 4.57A). After several unsuccessful repeats, it was identified that the radiolabelling was pushed to completion by concentrating the reaction mixture; which in the present example was caused by a combination of evaporation and condensation near the top of the reaction vessel. As the reaction volume was very small (80  $\mu$ l), the condensation had a large effect on the solvent volume and thus reagent concentration (see Figure 4.58). Moreover, these conditions could be successfully repeated for the star polymer with an RCY of 58.2 % (see Figure 4.57B and Table 4.20) and the 125-iodine/DOTA(Gd) star polymer was successfully purified by centrifugal filtration (see Figure 4.59).

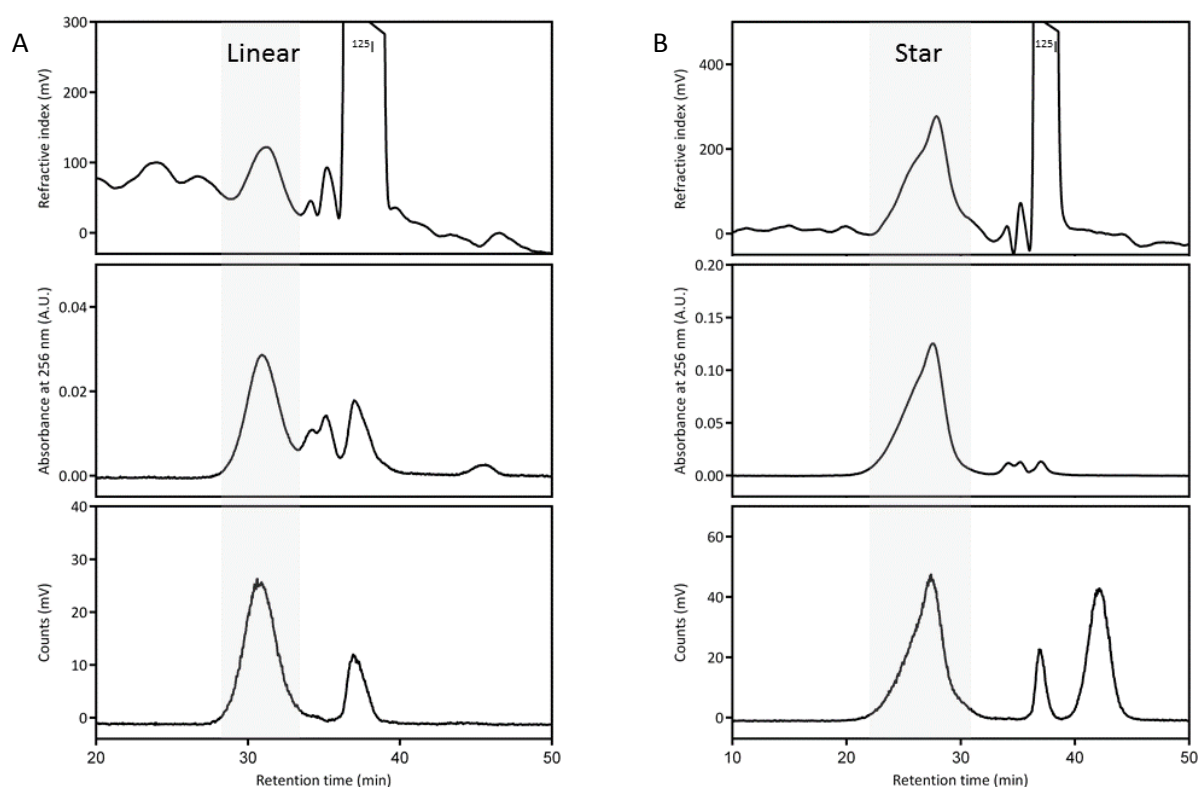


Figure 4.57: Size-exclusion chromatograms of the reaction mixtures after the three-component reaction of either linear polymer (A) or star polymer (B) with butyne-DOTA(Gd) and iodine-125. Top row, refractive index detector showed both the polymer and iodine-125 (the low signal for the linear polymer was caused by using a diluted sample for SEC); middle row, the absorbance at 256 nm showing the polymer only; and bottom row, the radioactivity count rate, showing both iodine-125-labelled polymer and free iodine-125.

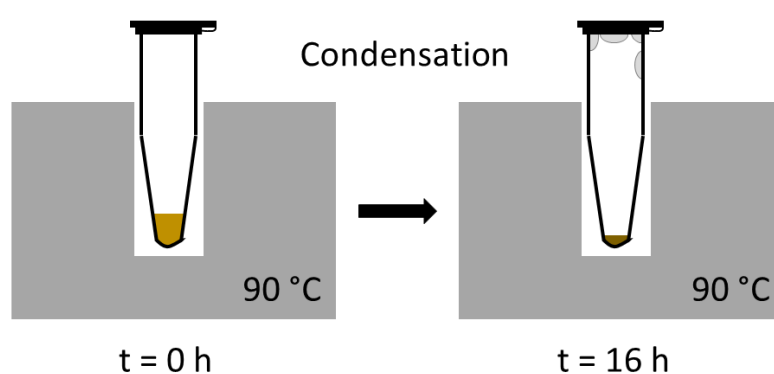
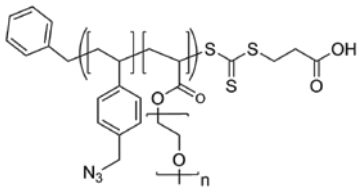
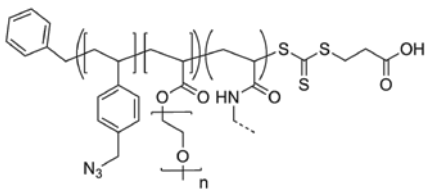


Figure 4.58: Proposed mechanism for increased concentration using experimental observations.

Table 4.20: Radiochemical yields (RCY) of the three-component reaction between linear or star polymer, butyne-DOTA(Gd) and iodine-125. The reactions were performed in DMSO for 16 hours at 90 °C, while concentrating by evaporation.

Polymer	Alkyne	RCY (%)
<p>Linear(N<sub>3</sub>) polymer</p> 	Butyne-DOTA(Gd)	79.3
<p>Star(N<sub>3</sub>) polymer</p> 	Butyne-DOTA(Gd)	58.2

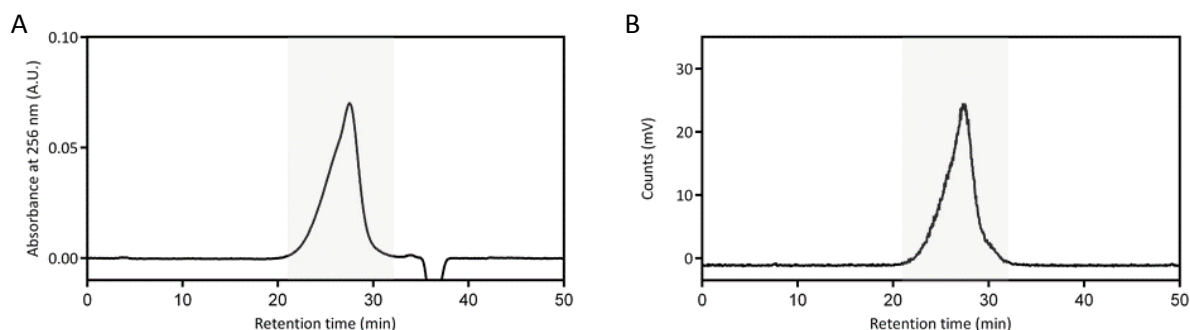


Figure 4.59: Size-exclusion chromatograms for purified iodine-125/DOTA(Gd) star polymer by centrifugal filtration with (A) absorbance at 256 nm and (B) gamma counts.

In summary, star and linear polymers were successfully labelled in a one-pot three-component reaction with both iodine-125 and butyne-DOTA(Gd) by modifying the previous reaction conditions and increasing the concentration by evaporation. This resulted in the efficient synthesis of a bimodal (Gd)DOTA-iodine-125 imaging agent with star architecture that could be easily purified.

## 4.4 Conclusion

In this chapter, a bimodal core-cross-linked star polymer was successfully developed that contains both an MRI contrast agent (Gd-DOTA) and a radio-isotope (iodine-125) using the three-component reaction (see Scheme 4.14), where iodine-125 can be replaced by iodine-124 for PET imaging, or potentially iodine-131 for radioimmunotherapy. First, a chloride-functional star polymer was synthesized using the arm-first method. This was followed by the substitution of chloride to azide post-polymerization, creating an azide-functional core-cross-linked star. Next the one-pot three-component (azide, alkyne, iodine) reaction was optimized for macromolecules using a model system comprising a linear azide functional polymer, a simple alkyne (3-butyne-1-ol) and cold sodium iodide, followed by applying the three-component reaction to the more complex star architecture. In the next step, both linear and star polymers were successfully labelled with iodine-125 using 3-butyne-1-ol or butyne-DOTA(Gd). This bimodal PET/MRI nanoparticle has a great potential to exploit the synergy between PET and MRI further, and also combine MRI with radioimmunotherapy, thus creating a theranostic particle.

## 4.5 References

- Kim, S., et al., *Hybrid PET/MR imaging of tumors using an oleanolic acid-conjugated nanoparticle*. Biomaterials, 2013. **34**(33): p. 8114-8121.
- Choi, J.S., et al., *A hybrid nanoparticle probe for dual-modality positron emission tomography and magnetic resonance imaging*. Angew Chem Int Ed Engl, 2008. **47**(33): p. 6259-62.
- Cheon, J. and J.H. Lee, *Synergistically integrated nanoparticles as multimodal probes for nanobiotechnology*. Acc Chem Res, 2008. **41**(12): p. 1630-40.
- Lee, H.Y., et al., *PET/MRI dual-modality tumor imaging using arginine-glycine-aspartic (RGD)-conjugated radiolabeled iron oxide nanoparticles*. J Nucl Med, 2008. **49**(8): p. 1371-9.
- Torres Martin de Rosales, R., et al., *Synthesis of  $^{64}\text{Cu}$ –Bis(dithiocarbamatebisphosphonate) and Its Conjugation with Superparamagnetic Iron Oxide Nanoparticles: In Vivo Evaluation as Dual-Modality PET–MRI Agent*. Angewandte Chemie International Edition, 2011. **50**(24): p. 5509-5513.
- Wong, R.M., et al., *Rapid Size-Controlled Synthesis of Dextran-Coated,  $^{64}\text{Cu}$ -Doped Iron Oxide Nanoparticles*. ACS Nano, 2012. **6**(4): p. 3461-3467.
- Delso, G., et al., *Performance Measurements of the Siemens mMR Integrated Whole-Body PET/MR Scanner*. Journal of Nuclear Medicine, 2011. **52**(12): p. 1914-1922.
- Vandenberghe, S. and P.K. Marsden, *PET-MRI: a review of challenges and solutions in the development of integrated multimodality imaging*. Physics in Medicine and Biology, 2015. **60**(4): p. R115.
- Matsumura, Y. and H. Maeda, *A new concept for macromolecular therapeutics in cancer chemotherapy: mechanism of tumoritropic accumulation of proteins and the antitumor agent smancs*. Cancer Res, 1986. **46**(12 Pt 1): p. 6387-92.
- Garcia, J., T. Tang, and A.Y. Louie, *Nanoparticle-based multimodal PET/MRI probes*. Nanomedicine (Lond), 2015. **10**(8): p. 1343-59.
- Yang, X., et al., *cRGD-functionalized, DOX-conjugated, and  $^{64}\text{Cu}$ -labeled superparamagnetic iron oxide nanoparticles for targeted anticancer drug delivery and PET/MR imaging*. Biomaterials, 2011. **32**(17): p. 4151-4160.
- Thorek, D.L.J., et al., *Non-invasive mapping of deep-tissue lymph nodes in live animals using a multimodal PET/MRI nanoparticle*. Nat Commun, 2014. **5**.
- Pellico, J., et al., *Fast synthesis and bioconjugation of  $(^{68}\text{Ga})$  core-doped extremely small iron oxide nanoparticles for PET/MR imaging*. Contrast Media Mol Imaging, 2016. **11**(3): p. 203-10.
- Notni, J., et al., *Convenient synthesis of  $(^{68}\text{Ga})$ -labeled gadolinium(III) complexes: towards bimodal responsive probes for functional imaging with PET/MRI*. Chemistry, 2013. **19**(38): p. 12602-6.
- Frullano, L., et al., *Bimodal MR&#8211;PET Agent for Quantitative pH Imaging*. Angewandte Chemie International Edition, 2010. **49**(13): p. 2382-2384.
- Park, J.-A., et al., *Heteronuclear Gd- $^{99\text{m}}\text{Tc}$  Complex of DTPA-Bis(histidylamide) Conjugate as a Bimodal MR/SPECT Imaging Probe*. ACS Medicinal Chemistry Letters, 2012. **3**(4): p. 299-302.
- de Smet, M., et al., *SPECT/CT imaging of temperature-sensitive liposomes for MR-image guided drug delivery with high intensity focused ultrasound*. Journal of Controlled Release. **169**(1–2): p. 82-90.
- Park, J.-A., et al., *Gadolinium Complex of 125I/127I-RGD-DOTA Conjugate as a Tumor-Targeting SPECT/MR Bimodal Imaging Probe*. ACS Medicinal Chemistry Letters, 2013. **4**(2): p. 216-219.
- Kryza, D., et al., *Biodistribution Study of Nanometric Hybrid Gadolinium Oxide Particles as a Multimodal SPECT/MR/Optical Imaging and Theragnostic Agent*. Bioconjugate Chemistry, 2011. **22**(6): p. 1145-1152.
- Ren, J.M., et al., *Star Polymers*. Chem Rev, 2016. **116**(12): p. 6743-836.
- Ferreira, J., et al., *Optimizing the generation of narrow polydispersity ‘arm-first’ star polymers made using RAFT polymerization*. Polymer Chemistry, 2011. **2**(8): p. 1671.
- Khor, S.Y., et al., *Molecular weight (hydrodynamic volume) dictates the systemic pharmacokinetics and tumour disposition of PolyPEG star polymers*. Nanomedicine, 2015. **11**(8): p. 2099-108.
- Syrett, J.A., et al., *Functional, star polymeric molecular carriers, built from biodegradable microgel/nanogel cores*. Chemical Communications, 2011. **47**(5): p. 1449-1451.
- Duncan, R. and R. Gaspar, *Nanomedicine(s) under the Microscope*. Molecular Pharmaceutics, 2011. **8**(6): p. 2101-2141.
- Boyer, C., V. Bulmus, and T.P. Davis, *Efficient Usage of Thiocarbonates for Both the Production and the Biofunctionalization of Polymers*. Macromolecular Rapid Communications, 2009. **30**(7): p. 493-497.

26. Boyer, C., et al., *Modification of RAFT-polymers via thiol-ene reactions: A general route to functional polymers and new architectures*. Journal of Polymer Science Part A: Polymer Chemistry, 2009. **47**(15): p. 3773-3794.
27. Boyer, C. and T.P. Davis, *One- pot synthesis and biofunctionalization of glycopolymers via RAFT polymerization and thiol-ene reactions*. Chemical Communications, 2009(40): p. 6029-6031.
28. Li, Y., et al., *Macromolecular Ligands for Gadolinium MRI Contrast Agents*. Macromolecules, 2012. **45**(10): p. 4196-4204.
29. Li, Y., et al., *The precise molecular location of gadolinium atoms has a significant influence on the efficacy of nanoparticulate MRI positive contrast agents*. Polymer Chemistry, 2014. **5**(7): p. 2592-2601.
30. Li, Y., et al., *Nanoparticles Based on Star Polymers as Theranostic Vectors: Endosomal-Triggered Drug Release Combined with MRI Sensitivity*. Advanced Healthcare Materials, 2015. **4**(1): p. 148-156.
31. Caravan, P., et al., *Gadolinium(III) Chelates as MRI Contrast Agents: Structure, Dynamics, and Applications*. Chem Rev, 1999. **99**(9): p. 2293-352.
32. Caravan, P., *Strategies for increasing the sensitivity of gadolinium based MRI contrast agents*. Chemical Society Reviews, 2006. **35**(6): p. 512-523.
33. Liu, J., et al., *Synthesis of Functional Core, Star Polymers via RAFT Polymerization for Drug Delivery Applications*. Macromolecular Rapid Communications, 2012. **33**(9): p. 760-766.
34. Welch, M.J., C.J. Hawker, and K.L. Wooley, *The advantages of nanoparticles for PET*. J Nucl Med, 2009. **50**(11): p. 1743-6.
35. Weissleder, R. and M.J. Pittet, *Imaging in the era of molecular oncology*. Nature, 2008. **452**(7187): p. 580-589.
36. Young, H., et al., *Measurement of clinical and subclinical tumour response using [<sup>18</sup>F]-fluorodeoxyglucose and positron emission tomography: review and 1999 EORTC recommendations*. European Journal of Cancer, 1999. **35**(13): p. 1773-1782.
37. Yan, R., et al., *One-Pot Synthesis of an <sup>125</sup>I-Labeled Trifunctional Reagent for Multiscale Imaging with Optical and Nuclear Techniques*. Angewandte Chemie International Edition, 2011. **50**(30): p. 6793-6795.
38. Jarrett, B.R., et al., *Synthesis of (<sup>64</sup>Cu)-Labeled Magnetic Nanoparticles for Multimodal Imaging*. Bioconjugate chemistry, 2008. **19**(7): p. 1496-1504.
39. Carlton, R.R. and A. McKenna-Adler, *Principles of Radiographic Imaging: An Art and A Science*. 5 ed. Vol. 1. 2012: Cengage Learning. 864.
40. Yan, R., et al., *A One-Pot Three-Component Radiochemical Reaction for Rapid Assembly of <sup>125</sup>I-Labeled Molecular Probes*. Journal of the American Chemical Society, 2013. **135**(2): p. 703-709.
41. Stenzel, M.H. and T.P. Davis, *Star polymer synthesis using trithiocarbonate functional  $\beta$ -cyclodextrin cores (reversible addition-fragmentation chain-transfer polymerization)*. Journal of Polymer Science Part A: Polymer Chemistry, 2002. **40**(24): p. 4498-4512.
42. Gottlieb, H.E., V. Kotlyar, and A. Nudelman, *NMR chemical shifts of common laboratory solvents as trace impurities*. The Journal of organic chemistry, 1997. **62**(21): p. 7512-7515.
43. Lê, D., et al., *Photo-Cross-Linked Diblock Copolymer Micelles: Quantitative Study of Photochemical Efficiency, Micelles Morphologies and their Thermal Behavior*. Macromolecules, 2014. **47**(7): p. 2420-2429.

## Chapter 5: Conclusions and Future Works

## 5.1 Conclusions

The overall objective of this dissertation was to develop novel methods to synthesize polymer-based nanoparticles with enhanced properties for both drug delivery and diagnostics.

**In chapter 2**, polymerisation-induced self-assembly was exploited to create a library of polymer-based nanoparticles with different sizes and shapes, and their efficacy as drug delivery vehicle was assessed to determine the optimal morphology. This was accomplished by synthesizing asymmetric functional POEGMA-*b*-P(ST-*co*-VBA) copolymers in methanol, yielding in one-pot polymerization: spherical micelles, worm-like micelles, rod-like micelles and vesicles. The presence of the aldehyde group was then exploited for cross-linking or to conjugate an anticarcinogen (doxorubicin) via pH-labile bonds (Schiff base or imine) onto the preformed nanoparticles. At physiological pH, only very limited drug release was observed, while drug release was enhanced at pH 5: a pH characteristic for late endosomes. The influence of the nanoparticle morphologies on uptake into the MCF-7 breast cancer cell line was investigated using flow cytometry and confocal microscopy. The results revealed a greater uptake for the worm-like and rod-like micelles over the spherical nanoparticles. Finally, the IC<sub>50</sub> of doxorubicin, following nanoparticle delivery, was studied, showing significant influence of the nanoparticle carrier morphology on therapeutic efficacy for breast cancer. Non-spherical drug-conjugated nanoparticles exhibited a lower IC<sub>50</sub>, demonstrating the advantages of filomicelles for drug delivery.

**In chapter 3**, first a method was developed to synthesize novel epoxide surface-functional nanoparticles by polymerization-induced self-assembly. Glycidyl methacrylate was utilized to prepare a short functional block, followed by chain extension with OEGMA to create the PISA macro-RAFT. Then a library of surface-functional self-assembled nanoparticles with different shapes was synthesized in a dispersion polymerization with styrene. A variety of sizes and shapes including micelles, filomicelles and vesicles could be routinely achieved by manipulation of the reaction stoichiometry and reaction time. The versatility of the epoxide groups for post-synthetic surface functionalization was then thoroughly tested using a primary thiol, primary amines and by ring opening with sodium azide followed by a CuAAC click reaction.

In the second part of the chapter, the use of the different shaped nanoparticles as positive MRI contrast was investigated by successfully conjugating a gadolinium chelate onto the self-assembled nanoparticles. A MRI relaxometry study demonstrated the advantages of filomicelles over the other shapes with possible applications as blood-pool contrast agents and in MR angiography.

Finally, in **chapter 4**, a novel bimodal MRI/PET imaging probe was designed making use of novel multicomponent chemistry to optimally exploit the synergy between MRI and PET. First, a chloride-functional core-cross-linked star polymer was synthesized, followed by nucleophilic substitution of chloride by azide to form an azide-functional star. Next, a three component reaction to simultaneously incorporate an alkyne and (radio)iodine (as PET tracer) was successfully investigated using a model system comprising an azide-functional linear or star polymer, a simple alkyne (3-butyne-1-ol), and cold iodine. This reaction was then successfully repeated using the more clinically relevant iodine-125 radioisotope. Lastly, an alkyne-functional gadolinium chelate (for MRI) was synthesized and successfully conjugated onto the azide-functional linear or star polymer via the three-component reaction with iodine-125, to successfully yield the final multimodal PET MRI star nanoparticle.

## 5.2 Future Works

**Chapters 2** and **3** established that RAFT-mediated polymerization-induced self-assembly is a facile method to prepare a library of nanoparticles with various sizes and shapes, with either functionalization of the core (3-vinylbenzaldehyde) or surface (glycidyl methacrylate). Moreover, applications in drug delivery and diagnostics (MRI) were successfully investigated, demonstrating the promise of filomicelles. It would very interesting to combine both applications and create a theranostic non-spherical nanoparticle. However, this would require the use of different orthogonal chemistries as both aldehydes and epoxides are reactive with amines.

One possible solution to introduce orthogonal functionalities is substituting glycidyl methacrylate for a different functional monomer, for example a 'clickable' monomer (e.g. 2-azidoethyl methacrylate) [1] or a thiol-reactive monomer (such as pyridyl disulfide ethyl methacrylate) [2]. The first option would also open up the opportunity to simultaneously include radioiodine by applying the three component reaction as presented in **chapter 4**. Furthermore, the orthogonality can also be exploited to incorporate targeting units, for example saccharides as in Basuki *et al.* [3] for the targeting of lung tumours. In addition, modification of the RAFT end-group could also be employed to introduce an active targeting moiety; however this would be limited to maximum one targeting group per polymer. [4]

An alternative option would be to incorporate a pre-synthesized prodrug monomer in the PISA process as this would avoid the necessity of two orthogonal functional groups. [5, 6] On the other hand, drugs could also be loaded via hydrophobic interactions during the PISA process. For example Karagoz *et al.*

showed that Nile red could be incorporated as a guest molecule without disturbing the morphology or the polymerization kinetics. [7]

In regards to **chapter 3**, although the nanoparticles showed considerable MR contrast, it would be beneficial to increase the number of gadolinium chelates per nanoparticle further for clinical applications. For example the clinically used Magnevist is administered at 0.1 mmol/kg, or 4.2 g for a 70 kg patient. To achieve a similar contrast enhancement at 1.5 T with the synthesized material, approximately 59 g of filomicelle is required. Although this is achievable (e.g. Doxil is administered at 50 g/m<sup>2</sup>), the injected amount can be significantly reduced by increasing the number of gadolinium per polymer (e.g. 5 – 10 per polymer). One approach would be to increase the conjugation efficiency using the two-step functionalization by first ring-opening with sodium azide and then applying the CuAAC click reaction (as explored in chapter 3) using an alkyne-functional gadolinium chelate (as synthesized in **chapter 4**). Alternatively, it would be interesting to further investigate preparing macro-RAFTs containing gadolinium-chelates, although preliminary tests showed that the RAFT end group can be affected in this process. Therefore, preparing gadolinium-chelate monomers could be an option too.

A disadvantage of PISA is the limited control over filomicelles as deviations in length and branched worms are sometimes observed. Sonication can be utilized to shorten long filomicelles, but at the moment no absolute control over filomicelle length can be achieved by PISA. So far only crystallization-driven self-assembly and particle replication in non-wetting templates can be used to prepare uniform filomicelles. [8] Nevertheless, PISA does offer a facile opportunity to create a library of uniform polymeric micelles with different sizes (20 to 70 nm), especially when using a high molecular weight macro-RAFT (over 12,000 Da). This could be further exploited to investigate the influence of size on biodistribution and intratumoral delivery.

Regarding the MRI relaxometry studies, measurements were carried out at a high magnetic field (7 T), however most clinically-used MRI scanners are operated at 1.5 or 3 T. Therefore it would be recommendable to measure T<sub>1</sub> relaxivity at these field strengths, especially as the relaxivity of gadolinium chelates is field dependent and higher relaxivities are observed at lower field strengths. [9] Furthermore, it would be interesting to determine the relaxation parameters (rotational correlation and water exchange rates) to assess the effect of morphology on these parameters.

**Chapter 4** presented a promising approach for the synthesis of a bimodal PET/MRI probe. However due to time constraints, MRI characterization has still to be performed. Nonetheless the  $T_1$  relaxivity is expected to be similar to previously published gadolinium-chelate containing core-cross-linked stars with a similar architecture. [10] Furthermore, the structural assignments of the iodotriazole can be further elucidated using  $^{13}\text{C}$  NMR. Finally, cytotoxicity studies are still outstanding to determine the biocompatibility of the probe, but no toxicity is to be expected based on literature. [11]

The currently designed star is not biodegradable, while this is recommendable as diagnostic agents should be preferably cleared as soon as desirable. This can be achieved by incorporating a biodegradable linker in the polymer structure, such as disulfide, acetal or ketal, which will afford the opportunity to precisely control the biodegradation of the star polymer. [12] These groups are biodegradable in the body according to different mechanisms; the disulfide can be reduced by the presence of glutathione in cytoplasm, while acetal and ketal groups are efficiently cleaved at the low pH found in the endosome. [12] Furthermore, preliminary studies were carried out using a RAFT agent with a protected alkyne group that could be exploited to introduce targeting groups onto the star polymer. Finally, it would be interesting to also develop a theranostic variant, for example by incorporating a drug in the core, [13] or alternatively using iodine-131 for radio immunotherapy. In each radioiodine application a different amount of iodine labelling is required. However, the flexibility of the iodo-click system enables this as the click reaction also occurs in the presence of a low amount of iodine, allowing tuning the star polymer iodine content without limiting the gadolinium content.

Several recommendations can also be made regarding the radiolabelling. First of all, it would be advisable to test the *in vitro* stability of the iodine-labelled stars by incubation in a buffer with or without bovine serum albumin. This can be investigated using radio size-exclusion chromatography. Secondly, so far only iodine-125 was incorporated as a proof of concept, however incorporation of iodine-124 is of course required for the creation of a true PET/MRI nanoprobe. Next, an important element to investigate is the fine-tuning of the radioiodine to gadolinium ratio as PET is several orders of magnitude more sensitive than MRI. [14] This can be realized by using less radioiodine (as the click reaction occurs in absence too) or alternatively by adding cold iodine to the radioiodine mixture. Lastly, it would of course be very informative to study the biodistribution of the star polymer in a small-scale *in vivo* study using intravenous injection. The evolution of accumulation in different organs could be assessed using PET/SPECT (depending on the isotope) and organs could be harvested, followed by the measurement of the radioactivity using a gamma counter.

In addition to above work, part of my PhD was focused on the development of environment-responsive MRI probes that exhibit MR contrast enhancement after an environmental change (e.g. pH) or upon drug release. Although these studies were not completed far enough to be included in this thesis, it is a very interesting concept that is worth exploring further and can lead to the design of the next generation of diagnostic and theranostic nanoparticles.

## 5.3 References

1. Li, Y., J. Yang, and B.C. Benicewicz, *Well-controlled polymerization of 2-azidoethyl methacrylate at near room temperature and click functionalization*. Journal of Polymer Science Part A: Polymer Chemistry, 2007. **45**(18): p. 4300-4308.
2. Wong, L., et al., *Synthesis of versatile thiol-reactive polymer scaffolds via RAFT polymerization*. Biomacromolecules, 2008. **9**(7): p. 1934-44.
3. Basuki, J.S., et al., *Magnetic nanoparticles with diblock glycopolymer shells give lectin concentration-dependent MRI signals and selective cell uptake*. Chemical Science, 2014. **5**(2): p. 715-726.
4. Boyer, C., et al., *Bioapplications of RAFT Polymerization*. Chemical Reviews, 2009. **109**(11): p. 5402-5436.
5. Hasegawa, U., et al., *Preparation of Well-Defined Ibuprofen Prodrug Micelles by RAFT Polymerization*. Biomacromolecules, 2013. **14**(9): p. 3314-3320.
6. Son, H.N., et al., *Chemotherapeutic copolymers prepared via the RAFT polymerization of prodrug monomers*. Polymer Chemistry, 2016. **7**(27): p. 4494-4505.
7. Karagoz, B., C. Boyer, and T.P. Davis, *Simultaneous Polymerization-Induced Self-Assembly (PISA) and Guest Molecule Encapsulation*. Macromolecular Rapid Communications, 2014. **35**(4): p. 417-421.
8. Truong, N.P., et al., *Polymeric filomicelles and nanoworms: two decades of synthesis and application*. Polymer Chemistry, 2016. **7**(26): p. 4295-4312.
9. Caravan, P., et al., *Influence of molecular parameters and increasing magnetic field strength on relaxivity of gadolinium- and manganese-based T1 contrast agents*. Contrast Media Mol Imaging, 2009. **4**(2): p. 89-100.
10. Li, Y., et al., *The precise molecular location of gadolinium atoms has a significant influence on the efficacy of nanoparticulate MRI positive contrast agents*. Polymer Chemistry, 2014. **5**(7): p. 2592-2601.
11. Li, Y., et al., *Macromolecular Ligands for Gadolinium MRI Contrast Agents*. Macromolecules, 2012. **45**(10): p. 4196-4204.
12. Syrett, J.A., et al., *Functional, star polymeric molecular carriers, built from biodegradable microgel/nanogel cores*. Chemical Communications, 2011. **47**(5): p. 1449-1451.
13. Li, Y., et al., *Nanoparticles Based on Star Polymers as Theranostic Vectors: Endosomal-Triggered Drug Release Combined with MRI Sensitivity*. Advanced Healthcare Materials, 2015. **4**(1): p. 148-156.
14. Weissleder, R. and M.J. Pittet, *Imaging in the era of molecular oncology*. Nature, 2008. **452**(7187): p. 580-589.